# Application of Sensitive API-Based Indicators and Numerical Simulation Tools to Advance Hot-Melt Extrusion Process Understanding

**Dissertation**

zur

Erlangung des Doktorgrades (Dr. rer. nat.)

der

Mathematisch-Naturwissenschaftlichen Fakultät

der

Rheinischen Friedrich-Wilhelms-Universität Bonn


vorgelegt von

**Rachel Catherine Evans**

aus

Salt Lake City, Utah, USA


**Bonn 2019**

Angefertigt mit Genehmigung der Mathematisch-Naturwissenschaftlichen Fakultät der Rheinischen Friedrich-Wilhelms-Universität Bonn

Promotionskommission:

Erstgutachter: Prof. Dr. Karl-Gerhard Wagner
Zweitgutachter: Prof. Dr. Alf Lamprecht
Fachnaher Gutachter: Prof. Dr. Gerd Bendas
Fachfremder Gutachter: Prof. Dr. Robert Glaum

Tag der Promotion: 17. Juli 2019
Erscheinungsjahr: 2019

*Significant portions of Chapter 4 were previously published in an article entitled "Development and Performance of a Highly Sensitive Model Formulation Based on Torasemide to Enhance Hot-Melt Extrusion Process Understanding and Process Development", Evans, et.al., AAPS PharmSciTech, 2018.*

*Significant portions of Chapters 2 and 5 were submitted for publication in an article entitled "Holistic QbD Approach for Hot-Melt Extrusion Process Design Space Evaluation: Linking Materials Science, Experimentation and Process Modeling", Evans, et.al. to the European Journal of Pharmaceutics and Biopharmaceutics.*

# Acknowledgements

I would first like to thank Prof. Dr. Karl G. Wagner for both his scientific advice as well as for his carefully considered and unwavering support and guidance throughout the supervision of my PhD thesis. From the AbbVie side, I would like to thank Dr. Samuel Kyerematenge and Andreas Gryczke for their scientific mentorship, enthusiastically sharing their knowledge and expertise and for always being available for technical discussions. Also invaluable, I would like to thank Esther Bochmann for generously sharing her knowledge and expertise in melt rheology and for being an eager and engaging research partner.

I would also like to acknowledge and thank many AbbVie colleagues for helpful and productive conversations over the last few years. I greatly appreciate the early input and advice from Dr. Jörg Rosenberg and Dr. Geoff Zhang which shaped my approach to the research, especially in the selection of model compounds and polymers. Mirko Pauli, Constanze Schmidt and Norbert Steiger introduced me to small-scale extrusion and formulation considerations and were helpful discussion partners throughout. Ute Lander generously taught me large-scale extrusion and was a vital partner during the last stage of experiments. Thomas Keßler was always available to discuss the complexities of hot-melt extrusion, advising extruder and screw configuration design, and pointing out aspects of my results that would be interesting for further study. I greatly enjoyed productive discussions with Dr. Kristin Lehmkemper about extrusion theory and collaborating with her on the sensitivity analysis, especially the impact of material properties. Both Dr. Mario Hirth and Dr. Frank Theil helped me to reason through various aspects of the research and to, on occasion, keep me grounded.

I very much appreciate the experimental assistance and support of Teresa Dagenbach, Amelie Wirth, Max Frentzel and Alex Castillo with material property analysis and sample characterization. For their analytical expertise and advice, I would like to recognize and thank David Geßner, Stefan Weber, Karlheinz Rauwolf, Dirk Remmler, Dr. Benjamin-Luca Keller and Dr. Christian Schley. I would also like to thank Ines Mittenzwei, Michael Preiß, Michael Gali and Jannik Mohr for their experimental assistance with large-scale extrusion.

Support for my PhD research would not have been possible without the initiation of the collaboration between AbbVie and the University of Bonn by Dr. Martin Bultmann, Dr. Matthias Degenhardt and Dr. Gunther Berndl. In addition, I greatly appreciate my AbbVie managers, Dr. Lutz Asmus, Dr. Matthias Degenhardt, Dr. Mike Hoffman and Andreas Gryczke, for supporting my research activities while also arranging my part-time AbbVie responsibilities so that I could both focus on the scientific aspects of research while still contributing to AbbVie's business objectives. I would especially like to thank Andreas Gryczke for supporting my goal in the last year and aligning my AbbVie and PhD work around one topic; both mutually benefitted from this.

Experimental facilities and infrastructure support and were provided by AbbVie, NCE-Formulation Sciences and Maintenance and Engineering departments, and particular thanks go to the teams of mechanics and electricians and Zija Islamovic for pilot-plant equipment setup and cleanup. Special thanks go to Roger Kubitschek and Ralf Heilmann, as well as Rainer van Deursen from Schneider Electric / Eurotherm, for prioritization and realization of extruder upgrades.

From Sciences Computers Consultants, I wish to thank the entire team for training, support, helpful discussions and upgrades to the Ludovic® software, especially Batch Mode.

I would also like to thank Chrissi Lekić, Dr. Sheetal Pai-Wechsung, Esther Bochmann, Dr. Ariana Low, Karola Rau, Dijana Trajkovic and Ekaterina Sobich for friendships begun in Germany, in particular for frequent chats, sometimes daily and sometimes after hours. I also wish to thank my parents, brother, sister-in-law and nieces, and long-time friends Dr. Nihan Yönet-Tanyeri, Kate Ferrario, Dan Ferrario, Dr. Noelle Patno, Dr. Dorothea Sauer, Millán Díaz-Aguado and Mihaela Iordanova for their moral support from across the ocean.

I wish to express tremendous gratitude to Ingrid Hölig and her family for welcoming me and a very special little dog named Cherry into their lives and making us feel at home in Wächtersbach. And last but definitely not least, I would like to thank my dear Peter for sharing the best of his homeland, keeping me culturally entertained as well as physically fit with hikes and bike trips to visit our favorite fields of wild flowers.

*For my friends and family, both near and far*

The highest reward for a person’s toil is not what they get for it,
but what they become by it.

*John Ruskin*

# TABLE OF CONTENTS

# Nomenclature

## Symbols

| | |
|---|---|
| 1D | one-dimensional |
| 3D | three-dimensional |
| $a$ | Yasuda constant |
| a | extruder center line |
| $a_T$ | WLF shift factor |
| $A$ | surface area |
| $C$ or $c$ | concentration |
| $C_1$ | WLF equation constant 1 |
| $C_2$ | WLF equation constant 2 |
| $c_P$ | heat capacity |
| $c_{PL}$ | liquid phase heat capacity |
| $c_{PS}$ | solid phase heat capacity |
| $C_s$ | saturation solubility |
| $d_{10}$ | diameter at which 10% of particle are smaller |
| $d_{50}$ | diameter at which 50% of particle are smaller |
| $d_{90}$ | diameter at which 90% of particle are smaller |
| $D$ | barrel diameter or diffusion coefficient |
| $D_o$ | outer screw diameter |
| $D_i$ | inner screw diameter |
| DeltaT or ΔT | difference in temperature between barrel and melt |
| $E(t)$ | the exit age function of the residence time distribution |
| $h$ | boundary layer thickness |
| $k_B$ | Boltzmann constant |
| L | extruder length |
| L/D | extruder length:diameter ratio |
| $M_d$ | extruder screw torque limit |
| MW | molecular weight |
| $n$ | power law index |
| $N$ | screw speed [rpm] |
| $Q$ | throughput [kg/h] |

| | |
|---|---|
| $r$ | radius |
| $t$ | time |
| $t$ > 115 °C | time that melt temperature is greater than 115 °C |
| $T$ | temperature |
| $T_d$ | degradation onset temperature |
| $T_g$ | glass transition temperature |
| $T_m$ | melting temperature |
| $T_{max}$ | maximum simulated melt temperature, typically at end of 2nd BW kneading block |
| $\Delta T_{max}$ | $T_{max}$ at high screw speed minus $T_{max}$ at low screw speed |
| $T_p$ | processing temperature (melt temperature, not barrel) |
| $T_s$ | solubility temperature |
| $T_0$ | reference temperature |
| $V$ | volume |
| $V_{free}$ | extruder free volume [$dm^3$] |
| $\dot{\gamma}$ | shear rate |
| $\dot{\gamma}_C$ | shear rate in the screw channel |
| $\dot{\gamma}_O$ | shear rate in the overflight region |
| $\delta_C$ | channel depth |
| $\delta_{CL}$ | screw clearance (or leakage) |
| $\eta$ | shear melt viscosity |
| $\eta_0$ | zero-shear rate viscosity |
| $\eta_\infty$ | infinite-shear rate viscosity |
| $\eta_T$ | shear viscosity at extrapolated temperature |
| $\lvert\eta^*\rvert$ | complex viscosity |
| $\lambda$ | characteristic time |
| $\lambda_T$ | characteristic time at extrapolated temperature |
| $\lambda_0$ | characteristic time at reference temperature |
| $\tau$ | torque [N·m] or shear stress [Pa] |
| $\tau_F$ | filled torque (when process is running) [N·m] |
| $\tau_E$ | empty torque (but screws turning) [N·m] |

**Abbreviations**

| | |
|---|---|
| API | active pharmaceutical ingredient |
| ASD | amorphous solid dispersion |
| BW | backward |
| COP | copovidone |
| CQA | critical quality attribute |
| C-Y | Carreau-Yasuda (equation) |
| DoE | design of experiments |
| DPD | dipyridamole |
| DSC | dynamic scanning calorimetry |
| f(t) | function of time |
| FW | forward |
| f(x) | function of position |
| HME | hot-melt extrusion |
| HPLC | high-performance liquid chromatography |
| HPLC-MS | high-performance liquid chromatography – mass spectrometry |
| HSS | high screw speed |
| IR | infrared |
| KB | kneading block |
| LCE | local conducted energy |
| LOD | loss-on-drying |
| LSS | low screw speed |
| MRT | mean residence time |
| MST | materials science tetrahedron |
| NoR | average number of revolutions experienced by a unit of material |
| PA% | peak area percent |
| PAT | process analytical technology |
| PEG | polyethylene glycol |
| PID | proportional–integral–derivative control |
| PLM | polarized light microscopy |
| PSD | particle size distribution |
| QbD | quality by design |
| RT | retention time |

| | |
|---|---|
| RTD | residence time distribution |
| SA:V | surface area to volume ratio |
| SAOS | small angle oscillatory shear |
| SFL | specific feed load |
| SME | specific mechanical energy |
| SOL | Soluplus® |
| Span® 20 | sorbitan monolaurate |
| TCE | total conducted energy |
| TEC | triethyl citrate or thermal exchange coefficient |
| TEL | telmisartan |
| TGA | thermogravimetric analysis |
| TOR | torasemide |
| TPE | total product energy |
| TSE | twin-screw extruder |
| TW80 | Tween® 80 (polysorbate 80) |
| VSFL | volume-specific feed load |
| WLF | Williams-Landel-Ferry (equation) |
| wt% | weight percent |
| XRPD | x-ray powder diffraction |
| ZSK18 | 18 mm extruder |
| ZSK26 | 26 mm extruder |
| ZSK40 | 40 mm extruder |

# 1 Introduction

The process of hot-melt extrusion (HME) in the pharmaceutical industry via a twin-screw extruder (TSE) was adapted from the plastics industry more than 35 years ago for the purpose of generating amorphous solid dispersions (ASDs) of poorly water-soluble active pharmaceutical ingredients (APIs) in polymeric matrices (1–5). It has since become an established unit operation for more than 10 APIs in commercial amorphous drug products (6–8). HME is efficient in that TSEs have a relatively small physical footprint and can potentially be run continuously (9,10). The process is primarily performed to enhance the bioavailability of poorly-water soluble drug substances (2,11). By imparting thermal and mechanical energy to material being processed, the crystalline API is transformed into a high-energy amorphous state, dissolved or melted and dispersed in the surrounding stabilizing polymer matrix (8). As a result, the energetic barrier for dissolving into aqueous fluids is overcome.

Over the years, HME using various polymer matrices has been used to produce a wide range of commercial medicinal products such as oral tablets and has extended to parenteral implants (3,6,7). It has also been used to show the feasibility of production of films, granules and pellets (2,5,11). For such a widely-used process as HME, both in the development of new drug products as well as in the production of commercial products, it is imperative that pharmaceutical scientists and engineers possess a solid understanding of the process and its relationship to critical quality attributes (CQAs) such as degradation and residual crystallinity. Despite many years and much effort spent to research HME, even at present, there are many gaps in HME process understanding.

Generally, the process involves a number of inter-related steps which can be considered sub-unit operations within the extruder barrels (Figure 1.1). Typically a co-rotating TSE is used for pharmaceutical applications (12). A powder-based mixture composed of at least API and polymer matrix are fed at constant feed rate into the TSE onto rotating screws containing at least one section of mixing elements. Melting or softening of the matrix occurs due to heat rise resulting from conduction from the barrel housing or by viscous dissipation from the shear imparted by conveying and mixing screw elements. Ideally, through this mixing and temperature

rise, the API melts or dissolves into the matrix and distributes to form a homogeneous single phase. Lastly, the material may be degassed prior to being extruded through the die, formed and cooled.

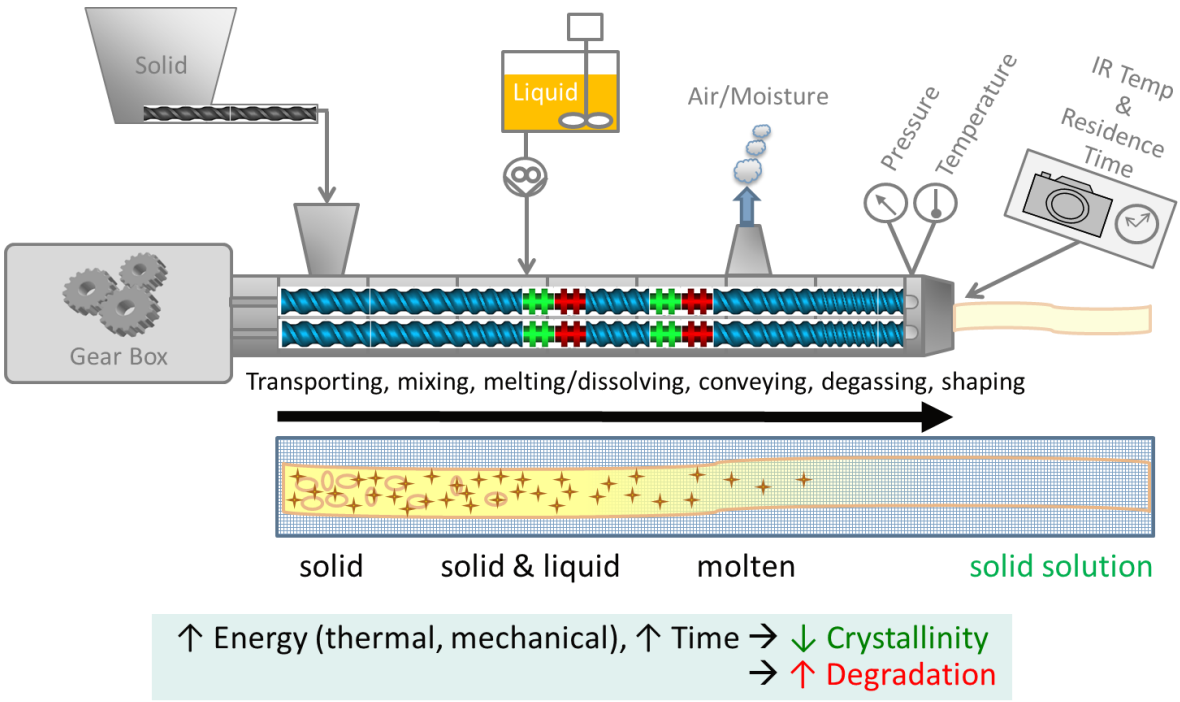


Figure 1.1 *Hot-melt extrusion for the formation of ASDs.*

Detailed analysis of the HME process is a challenging endeavor due to the "black-box" nature of the equipment; many measures of the process are challenging to access accurately. For example, standard thermocouples for measuring the melt temperature are heavily influenced by heat transfer from the surrounding barrels. While promising advancements have been made to precisely measure the melt temperature, such as with a thermocouple mesh (13) or by optical infrared (IR) sensors (14), the new methods are complex to implement, require extensive calibration, and in the case of IR, still fail to capture the 3D gradients in temperature. The torque, a quantity needed to calculate the mechanical energy input and to compare processes at different scales, can also be inaccurate due to losses in the gear box of the extruder drive (9,15). Other aspects of process monitoring or process analytical technology (PAT) have been investigated such as the energy monitoring (16), in-line methods such as rheometry to measure melt viscosity and spectroscopic techniques to measure chemical transformations. These methods show promising

results but are not yet routinely implemented in the pharmaceutical industry (9,10,17,18).

The materials being processed have complex properties and behavior which are both intrinsic but also dependent upon the process conditions and extent of processing. Typical matrix polymers used for HME often exhibit non-Newtonian viscoelastic flow behavior, meaning that the melt viscosity is a function of both temperature and shear rate. APIs often plasticize the matrix, and additives such as surfactants may also impact the rheology (19,20). Further, because the purpose of HME is to form a single phase from multiple discrete starting materials, the structure and therefore properties of the material inside the extruder evolve along the screw, a type of reactive extrusion (21).

Although HME can be run continuously, scaling is required at different stages during product and process development. For example, in early stages or for research or troubleshooting purposes, small scales may be used, while larger scales are used when larger quantities of API are available and for commercial production. Despite approaches to maintain geometric similarity across scales, differences in performance arise due to the inherent and fundamental difference of the ratio between barrel surface area and volume and different barrel heating and cooling designs among vendors, even within scale (22). Many guidelines and recommendations have been written regarding scaling of pharmaceutical HME (23–26), but few scholarly investigations have been published studying relevant scaling approaches or evaluating the success of the approaches.

Process modeling in multiple dimensions, not just 1D but also 3D, can supplement the lack of accurate experimental data (15). One-dimensional simulation can compute global mechanical and conducted energy values, residence time distribution values, local temperature, pressure, melt viscosity, shear stress, residence time and viscous dissipation (27). Three-dimensional approaches such as computational fluid dynamics and smoothed particle hydrodynamics can compute gradients in many of these local values, but high computational burden limits the study of the entire extruder (28,29). However, a challenge for validating these models exists in the form of quantitative correlations of the process with critical quality attributes. While residual

crystallinity, for example, can be quantified and correlated, degradation of the API resulting from excess thermal energy is often negligible or overshadowed by analytical method error. The reason for this is that most poorly-water soluble APIs are screened for suitability, primarily thermal stability, long before an API is available in large enough quantities for a hot-melt extrusion experiment. As a result, and as is also the case for attempts to understand the process through purely empirical approaches, there is little way of measuring the success of the process; it has a certain level of robustness built-in. For these reasons there is a need for correlating the experimental results with simulated results. One way to address this is through measurement of the sum total outcome of the process via an indirect method, namely with a process indicator. The focus of this thesis is the use of both simulation approaches and the use of APIs as sensitive process indicators to gain deeper insights into the HME process.

# 2 Theoretical Background

## 2.1 Application of the Materials Science Tetrahedron to HME

The complex nature of HME and the transformation of the input material through extrusion can be captured by the application of the materials science tetrahedron (MST). Its origin and applicability to drug product development was explained with several examples by Sun, primarily focusing on tablet compression (30). This concept is interpreted and applied for HME and presented in Figure 2.1. The corners of the tetrahedron are represented by the material structure, material properties, process parameters and process performance. Similar to interstitial sites in a crystal lattice, characterization and process simulation are placed at the core of the tetrahedron. The value in describing a process using the MST is that all of the inter-dependent relationships can be holistically described and analyzed.

Inherent to any process, variation of a number of independent and dependent variables influence the final material produced by the process. In HME, the independent variables are both continuous and discrete. When an HME process is analyzed via a design of experiment (DoE), a regression equation describing the relationship between a given response and the independent variables typically contains terms with not only main effects but also interactions (31). The existence of these interactions suggests that the more important factors in the process may be dependent variables. Process performance responses are typically defined by the critical quality attributes, the most important of which for HME are the residual crystallinity and degradation as they determine the amount and form of solubilized API available to contribute to enhanced bio-performance. Other important CQAs also include assay and uniformity, as well as moisture content, which is important for physical and potentially chemical stability of the ASD.

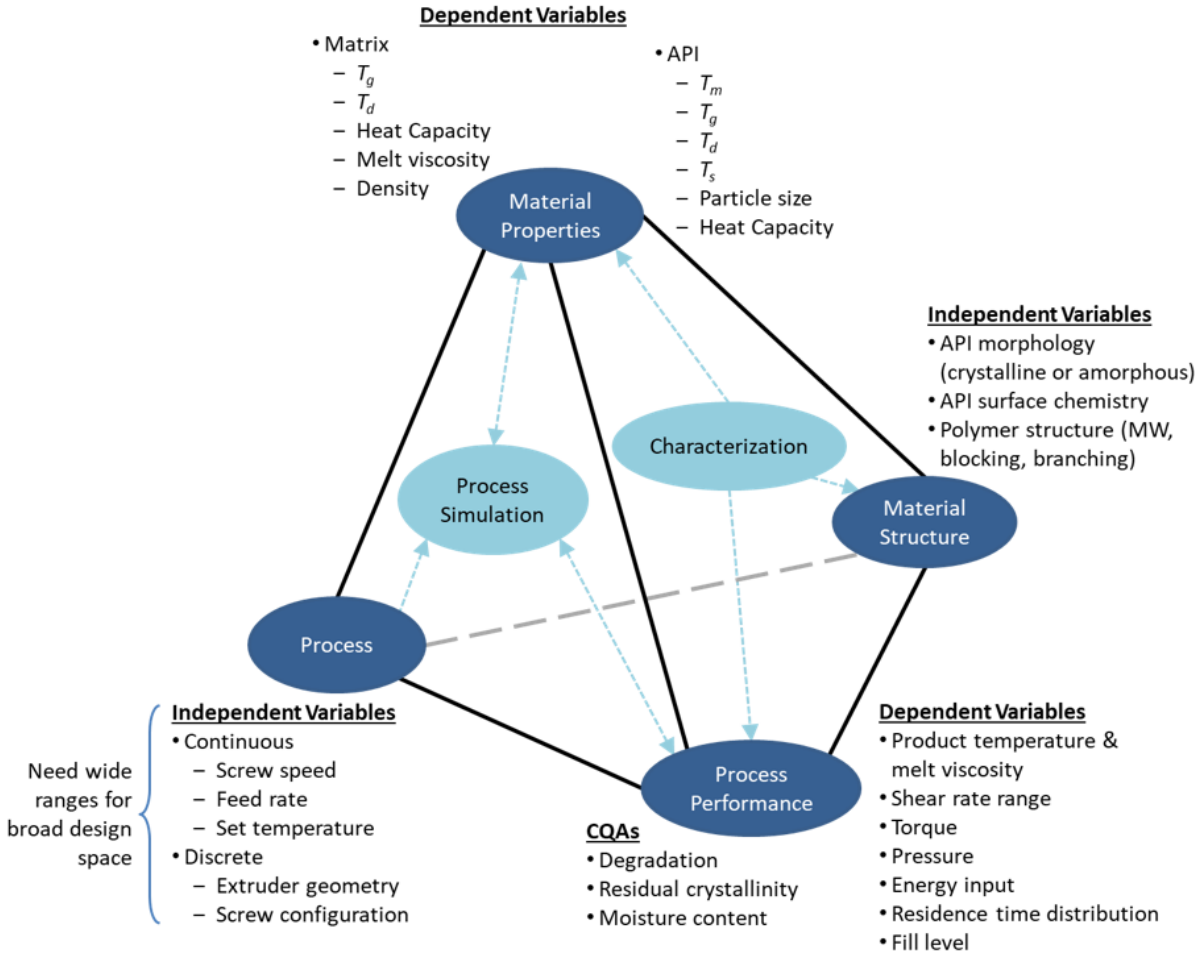


Figure 2.1 *The materials science tetrahedron (MST) as applied to HME for ASD formation. Important temperatures: $T_g$ = glass transition, $T_m$ = melting, $T_d$ = degradation, $T_s$ = solubility (temperature at which a given concentration of API is thermodynamically soluble in the matrix). MW = molecular weight.*

## 2.2 Process Parameters

The process parameters for HME are a combination of discrete and continuous independent variables. Continuous independent variables in HME are the screw speed, feed rate, barrel temperature and vent pressure. Discrete independent variables are the extruder scale, screw configuration, barrel length, die geometry and API and matrix properties. All dependent variables are impacted by more than one independent variable, leading to the high degree of interactions and complex relationships between the process parameters and the CQAs (Figure 2.2).

The most important aspects of extruder geometry are related to barrel and screw element design, shown for a double-flighted TSE in Figure 2.3. The center line, screw outer and inner diameters, channel depth and screw clearance define the process performance behavior. For example, the ratio of the screw diameters $D_o/D_i$ has important implications on fill level in the screw channel and shear rate (15,32). Also, strongly impactful for shear rate is the clearance, that is the distance between screw tip and barrel wall. Two primary types of elements used in TSE are conveying elements (Figure 2.4a), defined by the length and pitch, and kneading blocks (Figure 2.4b), defined by disk offset angle, direction of rotation, thickness and number. As the name implies, conveying elements serve to transport material in the axial direction and can be configured to move material both forward, towards the die, as well as backwards, perhaps to extend residence time in a mixing zone. Kneading blocks shear the material more intensively than conveying elements and can initiate polymer melting or softening as well as mix components to encourage the formation of a homogeneous and/or single phase.

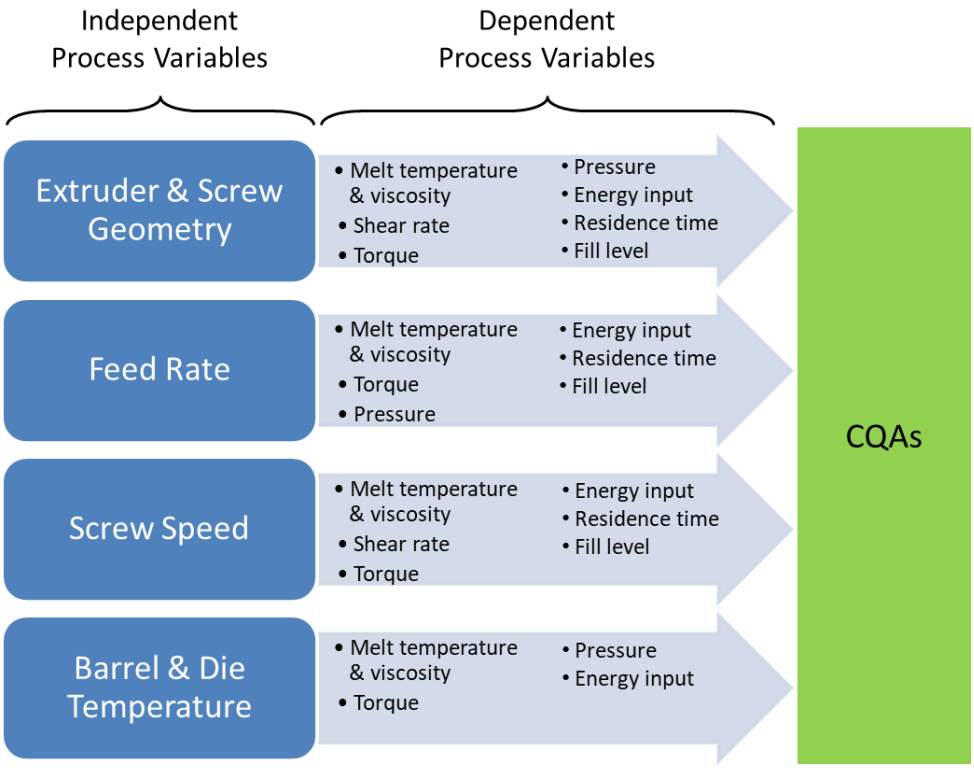


Figure 2.2 *Sorted impact of independent variables on dependent variables in HME.*

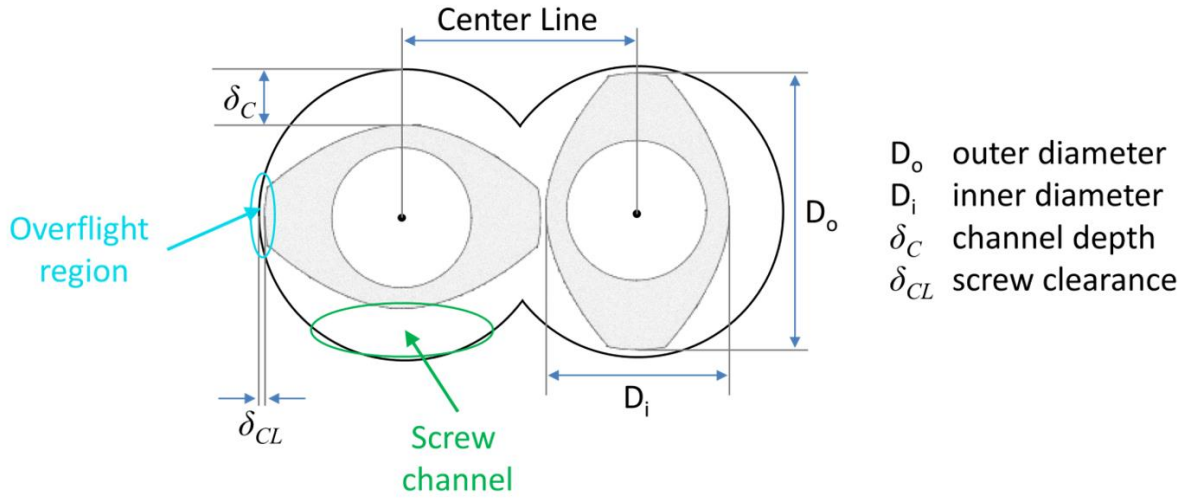


Figure 2.3 *Twin-screw extruder 2-flighted barrel and screw shaft geometry.*

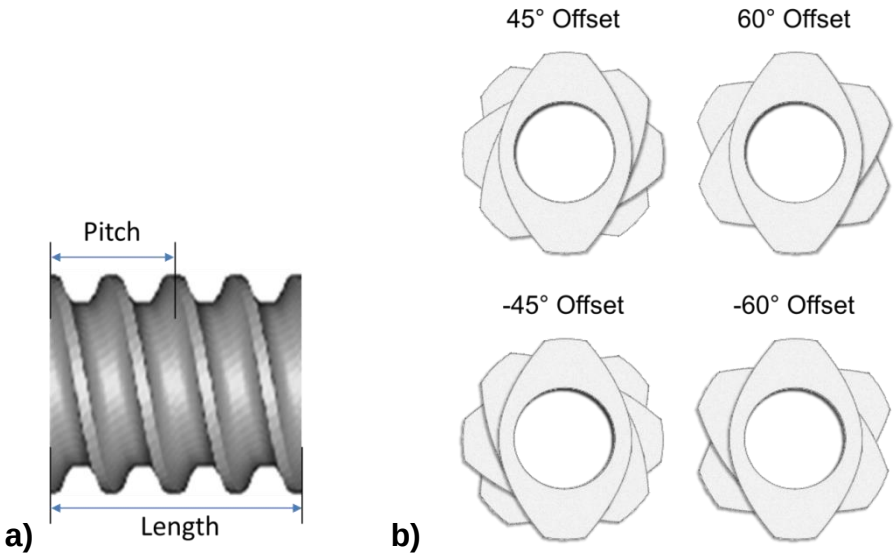


Figure 2.4 *Conveying (a) and kneading block (b) element geometry. (Conveying screw element image was modified from Ludovic®. Conveying element is depicted from side view, while kneading elements are depicted from axial view.)*

## 2.3 Material Properties

In addition to the influence of process parameters, the way in which a material performs during processing is dependent upon the raw material properties. The material properties can be considered dependent variables, determined by the raw material chemical and physical structure (26). The material properties of a given

formulation, especially their thermal properties, determine processing behavior and potentially also the product's final quality. The appropriate material properties will enable optimal processing with a broad design space and optimal product quality and vice versa. Knowledge and understanding of the material properties and their significance can facilitate working with and not against the natural behavior of the formulation. For HME, understanding the thermal properties and the role of the matrix rheological properties is essential to designing and controlling the process and the resulting product quality. Specifically, some of the most important material properties are the API particle size, matrix polymer and API glass transition temperatures ($T_g$), the API melting and solubility temperatures ($T_m$ and $T_s$), the API and matrix degradation temperatures ($T_d$), and the matrix melt viscosity as a function of temperature and shear rate. Smaller API particle size will increase the dissolution rate due to greater surface area (33). Characterization of the matrix $T_g$ and melt viscosity can be used to identify the minimum processing temperature and extruder torque limitation (34–41). Because the formation of an ASD via HME involves physical transformation of the raw materials, sometimes considered to be a type of reactive extrusion (21), the material properties of the product being processed can change as a function of the position along the length of the extruder. For example, an API, which is soluble in the polymer matrix and has $T_g$ much lower than that of the matrix, will plasticize the matrix upon dissolution and mixing (19). This effect will reduce the melt viscosity and therefore reduce viscous dissipation. However, an API can also anti-plasticize the matrix if its $T_g$ is higher than that of the matrix, leading to potentially more viscous dissipation (42).

Any rise in product temperature can result in degradation of the constituent materials, depending on their degradation temperatures and the respective temperature realized by the process. This potential for thermal degradation is one of the most commonly cited concerns in the HME process. It is commonly assumed that HME cannot be used to process high melting point APIs for the formation of ASDs (43,44). This assumption leads to the thinking that the product temperature must exceed the melting point of the crystalline API in order to form an ASD (6,45). For high melting point APIs, this temperature can exceed the thermal stability of the API or even the matrix. Further, as a remedy, the common thinking is that a plasticizer should be

added to the formulation to reduce the viscosity and consequently shift the temperature processing window to lower values, below the degradation temperature of the thermo-labile species (46,47).

However, this rationale is flawed primarily due to a lack of wide-spread understanding of the relevant material properties such as the influence of intermolecular interactions between API and polymer which affect the phase diagram of the ASD system. An ASD can be produced below the melting point of the pure API if the solubility temperature for a given drug loading is within an accessible temperature range (26,48). This temperature may be substantially lower than the melting point and well within a range in which no degradation occurs. In addition, too much plasticization and reduction in processing temperature could lead to incomplete formation of the ASD, aka presence of residually crystalline API in the matrix. In this way, the phase diagram can function as a processing map, with the processing temperature, $T_p$, indicated for a drug loading of 10 %w/w (Figure 2.5).

Based on these complex and inter-dependent relationships between the material properties and the process, and the evolution of the material properties that can occur during processing, a thorough understanding of both the thermodynamic and melt viscosity properties of the materials is essential. The thermodynamic aspects were discussed recently by Moseson and Taylor (48), and by others in the past (26).

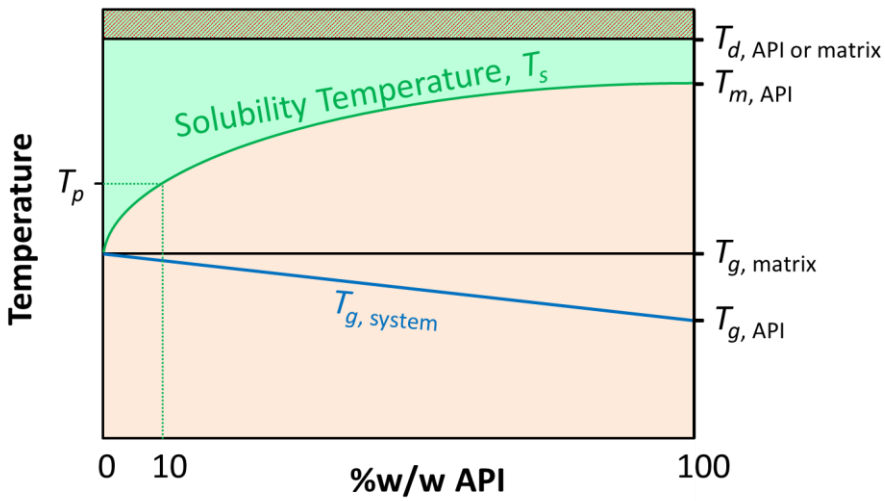


Figure 2.5 *API-matrix solubility phase diagram as a process design space map.*

The complex non-Newtonian behavior, specifically the temperature and shear-rate dependency, can be described by a number of empirical models, for example the Cross model (49) or, in these studies, the Carreau-Yasuda (C-Y) model (50,51). The Carreau-Yasuda (C-Y) model in combination with the with temperature dependency described by the Williams-Landel-Ferry (WLF) equation (52) can account for both Newtonian and non-Newtonian rheological behavior. The basic form of the C-Y equation expressing the melt viscosity as a function of shear rate is shown in equation 2.1:

$$\eta = \eta_\infty + (\eta_0 - \eta_\infty) \cdot [1 + (\lambda\dot{\gamma})^a]^{\frac{n-1}{a}} \quad (2.1)$$

where $\eta$ is the viscosity as a function of temperature and shear rate, $\dot{\gamma}$, $\eta_0$ is the melt viscosity at zero shear rate, $\eta_\infty$ is the melt viscosity at infinite shear rate, $\lambda$ is the characteristic time, $n$ is the Power law index and $a$ is the Yasuda constant. The characteristic time is related to the relaxation behavior of the specimen over time. Both the zero-shear rate viscosity and the characteristic time are functions of temperature. If $\eta_\infty$ is assumed zero, the equation simplifies to equation 2.2:

$$\eta = \eta_0 \cdot [1 + (\lambda\dot{\gamma})^a]^{\frac{n-1}{a}} \quad (2.2)$$

Both the zero-shear rate viscosity, $\eta_0$, and the characteristic time, $\lambda$, are strong functions of temperature for amorphous pharmaceutical polymers, especially near the $T_g$ of the polymer, roughly $T_g < T < T_g$+100 °C (15,52,53). This temperature dependency can be accounted for by use of the WLF equation, equation 2.3:

$$\log(a_T) = \frac{-C_1 (T - T_0)}{C_2 + (T - T_0)} \quad (2.3)$$

where $a_T$ is a shift factor resulting from time-temperature superposition processing of rheological data, $T$ is the target temperature, $T_0$ is the reference temperature, and $C_1$ and $C_2$ are constants. Equations 2.4 and 2.5 are used to calculate the melt viscosity and characteristic time at temperatures other than the reference temperature:

$$a_T = \frac{\eta_T}{\eta_0} \quad (2.4)$$

$$a_T = \frac{\lambda_T}{\lambda_0} \tag{2.5}$$

where $\eta$ and $\lambda$ are the viscosity and characteristic time from the Carreau-Yasuda equation, and the subscripts $T$ and 0 refer to the desired and reference temperatures, respectively.

## 2.4 Process Performance

Process performance can be characterized by two categories of measures of the process: the dependent variables and the product CQAs. Dependent variables for HME have been identified as the melt temperature, residence time, energy input, and fill level (9,54,55). Additional measures of the process not considered to be dependent variables are the product CQAs, namely degradation, residual crystallinity and moisture content. These aspects of process performance are discussed in more detail below, as well as how they are measured or calculated.

### 2.4.1 Melt Temperature and Melt Viscosity

The temperature of the melt is a measure of the amount of energy input into the processed material resulting from either conductive heat transfer or mechanical energy. The most common method to measure the melt temperature is via thermocouples inserted into the extruder barrel and die. They are flush mounted to prevent melt flow disruption and, due to insufficient insulation of the thermocouple junction, the measured values are known to be highly influenced by the barrel itself and therefore inaccurate (14). An alternative is infrared thermography in which an IR camera is used to measure the radiation emitted by the melt exiting an extruder die. The IR intensity is material dependent, characterized by the thermal emissivity, which itself varies as a function of wavelength and temperature. The emissivity for polymeric materials can be approximated with a value of 0.9 (56). While the measurement is limited by the fact that it takes place at the end of the extruder and at the surface of the melt, and therefore may be influenced by heat loss to the environment, it has proved to be more informative and relevant than measurements by thermocouples. This means that IR thermography cannot measure the temperature of the melt along the screw. Traditional thermocouples can be inserted into bores placed at any point along the screw, but again, the measurement is highly

influenced by the barrel temperature. As discussed in section 2.3, the material melt viscosity is a strong function of temperature and will change as the temperature of the melt changes.

### 2.4.2 Residence Time Distribution

The residence time distribution (RTD) is a measure of the time a unit of material spends inside the extruder. It provides valuable information about the degree of axial mixing and is also an input for reaction kinetics related to dissolution and degradation. Measurements are performed at steady state with the addition of a low concentration pulse of tracer substance added to the feed stream. The concentration of the tracer substance, typically a pigment, is measured or monitored at the extruder die exit over time. The concentration can be characterized by the exit age distribution (57) given by equations 2.6 and 2.7:

$$\int_0^\infty E(t)dt = 1 \tag{2.6}$$

$$E(t) = \frac{c}{\int_0^\infty c dt} = \frac{c}{\sum_0^\infty c\Delta t} \tag{2.7}$$

where *c* is the tracer concentration at a given time *t* and *E(t)*, the exit age function, has units of 1/s or %.

The mean residence time (MRT), defined as the time that a unit of material which was added at time *t* = 0 leaves the process with a 50% probability, can be calculated by equation 2.8.

$$t_{mean} = \frac{\int_0^\infty tcdt}{\int_0^\infty cdt} = \frac{\sum_0^\infty tc\Delta t}{\sum_0^\infty c\Delta t} \tag{2.8}$$

### 2.4.3 Mechanical Energy Input

#### 2.4.3.1 Shear Rate and Shear Stress

The average shear rate in an extruder can be calculated using a simple relationship considering the extruder geometry, screw geometry and the screw speed (15,58,59).

These equations assume that the shear rate is independent of the melt viscosity of the material being sheared. This assumption is appropriate for an average calculation due to the typically starved feeding operation of a twin-screw extruder and therefore substantial portions of the screw being only partially filled (60). Therefore, shear due to pressure flow can be neglected, leaving only drag flow (screws turning) contributing to shear rate. However, shear rate due to pressure-driven flow is a function of melt viscosity. Average shear rate can be calculated in two locations, in the screw channel $\dot{\gamma}_C$ (equation 2.9) or in the overflight region $\dot{\gamma}_O$ (equation 2.10):

$$\dot{\gamma}_C = \frac{D*\pi*N}{\delta_C*60} \quad [1/s] \tag{2.9}$$

$$\dot{\gamma}_O = \frac{D*\pi*N}{\delta_{CL}*60} \quad [1/s] \tag{2.10}$$

where $D$ [mm] is the barrel diameter, $N$ [rpm] is the screw speed, $\delta_C$ [mm] is the channel depth, and $\delta_{CL}$ [mm] is the screw clearance. If the $D_o/D_i$ ratio is constant, the $\dot{\gamma}_C$ will be the same across scales. If this is not the case, for scaling purposes, the screw speed can be back-calculated to maintain constant shear rate. The shear rate in the overflight region is more sensitive to the potentially differing screw clearance for different screw diameters and therefore can change even if $D_o/D_i$ remains constant. It is also highly sensitive to accurate measurements of clearance, which can be challenging and vary over time as an extruder wears over time.

The shear stress is simply the product of the viscosity and the shear rate given in equation 2.11:

$$\tau = \dot{\gamma} * \eta \quad [Pa] \tag{2.11}$$

where $\dot{\gamma}$ [1/s] is the average shear rate and $\eta$ [Pa·s] is the shear viscosity.

Because the viscous heat generation is proportional to the melt viscosity multiplied by the square of the shear rate (61), the shear rate itself strongly impacts the temperature rise in the melt.

#### 2.4.3.2 Torque

The torque for a given process condition is given by equation 2.12:

$$\tau = \tau_F - \tau_E \quad [\text{N·m}] \tag{2.12}$$

where $\tau_F$ [N·m] is the torque reading from the extruder when the process is running minus $\tau_E$ [N·m] the empty torque, or the torque reading from the extruder when no material is in the extruder, at the identical screw speed.

#### 2.4.3.3 SME

The specific mechanical energy can be calculated using multiple equations, but the one selected for use in this thesis is given by equation 2.13 (62):

$$SME = \frac{2*\pi*N*\tau}{Q} \quad \left[\frac{kWh}{kg}\right] \tag{2.13}$$

where $N$ [rpm] is the screw speed, $\tau$ [N·m] is the torque and $Q$ [kg/h] is the throughput.

### 2.4.4 Conducted Energy Input

The conducted energy describes the thermal energy that is transferred between the extruded material and the temperature regulated barrel housing. Conducted energy can be approximated by measuring the heating and cooling activity occurring in the various barrel segments in an extruder. The heating and cooling activity is recorded by logging the occurrence and duration of heating element activity and water valve opening. Additional aspects of this topic are discussed in Chapter 6.

### 2.4.5 Measures of Fill

#### 2.4.5.1 Specific Feed Load and Volume Specific Feed Load

The rate of feeding an extruder screw can be calculated and somewhat visualized by using the equation for the specific feed load, equation 2.14:

$$SFL = \frac{Q*1000}{N*60} \quad \left[\frac{g}{rev}\right] \tag{2.14}$$

where $Q$ [kg/h] is the throughput and $N$ [rpm] is the screw speed. The SFL can be normalized by the extruder free volume, known as the volume specific feed load (62), equation 2.15:

$$VSFL = \frac{Q*1000}{N*60*V_{free}} \quad \left[\frac{g}{rev \cdot dm^3}\right] \tag{2.15}$$

where $V_{free}$ [dm$^3$] is the extruder free volume not including the die. This equation is useful for scaling purposes or when the extruder free volume varies within scale.

#### 2.4.5.2 Fill Level

The fill level of the extruder, meaning total amount of material present in the extruder, neglecting the die, can be estimated by equation 2.16:

$$Fill\ Level = VSFL * NoR = \frac{Q*MRT*1000}{3600*V_{free}} \left[\frac{g}{dm^3}\right] \tag{2.16}$$

where the $NoR$ is the average number of revolutions experienced by a unit of material and can be estimated by equation 2.17:

$$NoR = \frac{N*MRT}{60} \quad [rev] \tag{2.17}$$

where $N$ [rpm] is the screw speed and $MRT$ [s] is the mean residence time. The simplified form of the equation for fill level is similar to equations found in the literature (63,64) and is sometimes normalized by material melt density.

#### 2.4.5.3 Pressure

Pressure is typically measured in the die by a pressure transducer as a safety mechanism (61). Rise in pressure can be related to high water content, but in pharmaceutical extrusion, material is often degassed in the barrel segment prior to the die. In the case of starved-fed extruders in pharmaceutical extrusion, the pressure rarely exceeds 1 bar and has not been observed to vary as a function of processing conditions in these studies. Therefore, pressure was not considered to be an important measure of the process.

### 2.4.6 Critical Quality Attributes

#### 2.4.6.1 Degradation

Degradation of both the API and the matrix components are undesirable results for an HME process. Thermal degradation is a primarily concern for the API because

most polymer matrices are thermoplastic in nature and require processing temperatures to be set above the $T_g$ at which the material will flow, typically with melt viscosity between 100 to 10,000 Pa·s (22). Other degradation reactions such as hydrolysis can also occur during HME processing. Corrective measures to reduce the melt temperature include reduction of the mechanical energy input, e.g. decreasing melt viscosity or decreasing screw speed, or reduction of conductive energy from the barrels, e.g. reducing barrel temperature. However, below a certain barrel temperature, the melt will be highly viscous, leading to heat generation by viscous dissipation. The degradation of API can be quantified by chromatographic techniques such as HPLC.

#### 2.4.6.2 Residual Crystallinity

Residual crystallinity is a measure of the success of the formation of the ASD. It can be quantified by peak height and/or area in x-ray powder diffraction (XRPD) or by integration of the melting endotherm in differential scanning calorimetry (DSC), if the API does not recrystallize upon heating or dissolve before melting. Another aspect of crystallinity present in an ASD is that of recrystallization but was outside the scope of this work. It can occur over time or at elevated temperatures and moisture content at which the molecular mobility within the matrix enables API molecules to reconfigure and crystallize.

#### 2.4.6.3 Moisture content

The moisture content is an important CQA because it can impact physical stability, most importantly the presence of crystallinity (65). Often the starting materials contain moisture or may be somewhat hygroscopic, especially the matrix polymers. The resulting moisture content can be variable based on heat exposure and vacuum pressure applied during processing. It can be measured by common loss-on-drying for a quick readout or by Karl Fischer titration for more accuracy. However, because the physical stability of the materials was not considered in this thesis, the resulting moisture content was not measured.

## 2.5 Process Modeling and Simulation

In addition to building relationships via laboratory experiments, process modeling can help to establish the relationships within the tetrahedron and provide deeper insight. Process models take into account the relevant properties of the material being processed in relation to the process parameters and equipment geometries, even accounting for evolution of the properties as a function of location in the process and feeding that back into the computation by way of numerical methods. Upon variation of any input parameter, process models are particularly useful for the generation of qualitative estimates and rank ordering, identifying the most influential variables. In this way, better experiments can be designed upfront, with perhaps a reduced number of variables to be tested. In addition, a synergistic approach utilizing both process modeling and relevant experimentation can yield answers to the gaps in understanding on both sides (66). With a validated model, gaps in experimental data can be supplemented with simulated data or design spaces can be supported. However, because not all experimental factors can be modeled, at least not at the present, quantitative predictions are not always feasible for every scenario. In the end, the requirements of quality by design (QbD) can be fulfilled by a combination of experimentation and modeling to rationally select formulation components based on their material properties to ensure product performance, quality, and even processing performance.

Process modeling has been applied to twin-screw extrusion through the development of a number of 1D simulation software programs (27,67–69) and a number of studies in the polymer and food industries have been reported (15,70–79). However, scholarly articles applying it to pharmaceutical HME are still limited. Studies with 1-dimensional simulation of the twin-screw extrusion process have shown agreement with the main effects of process parameters, that it can be used to optimize screw configurations during process scaling, as well as provide insight into the energetics of the process and study and optimize sources of heat generation during scaling (22,38). More recently, advancements to ease the use of HME simulation in early-stage formulation development have been made with the development of a model for ASD melt viscosity based on simpler measurements of the matrix melt viscosity and the $T_g$ of the ASD (80,81). Other researchers have focused on performing 3D

simulations based on smoothed particle hydrodynamics, reducing them to 1D models with the goal of applying them to pharmaceutical HME (28,29,82–84). Studies specifically related to the modeling of pharmaceutical HME include, for example, the development of a new model of the residence time distribution and the time to dissolution (85,86).

# 3 Aims and Scope of Work

The aim of this work was to gain deeper insight into the process of hot-melt extrusion by use of sensitive indicator substances and process simulation. Specifically, the work should establish links between material properties, process parameters, process performance and scaling behavior. Particular emphasis should be placed on relevant CQAs for the HME process as well as the process energetics.

In order to do this, indicator substances would need to be identified and fit-for-purpose formulations developed. Ideally, at least in the scope of this work, the indicator substances should not modify the formulation material properties, e.g. $T_g$ or melt viscosity, so as to simplify description of the system to the simulation model. Specifically, two APIs, torasemide and telmisartan, were selected for use as the indicator substances because it was found that as a function of processing, due to their physicochemical properties, they could yield measurable and relevant CQA responses, i.e. degradation and/or residual crystallinity. The formulations were developed and selected for their processing performance to exhibit the desired material properties such as processing window or melt viscosity characteristics. The formulations were not designed to be viable in terms of bioavailability enhancement or chemical and physical stability. Accordingly, neither the drug release / bio-performance nor the product stability was analyzed.

In terms of the HME process, in-scope was the study and characterization of the HME process from extruder inlet to die, including design of the extruder, process and measurements in-line and at-line. Reasons for this decision were based on 1) the ASD is formed within the extruder and not after exiting the die and 2) because the chosen simulation software, Ludovic®, only considers the process in this zone. As a result, any aspects of the process after the melt exits the die, aside from melt temperature measurement, or downstream processing were not considered. Samples were of course cooled quickly and stored in a controlled humidity and temperature environment so as to preserve their physical and chemical state at die exit.

# 4 Development and Performance of a Highly Sensitive Model Formulation Based on Torasemide to Enhance Hot-Melt Extrusion Process Understanding and Process Development

## 4.1 Introduction

Process understanding of HME can be defined in several ways, and includes the knowledge of the design and functional aspects of processing equipment, the impact of process parameters and process conditions on the final product attributes, material properties that may impact certain process conditions, accurately scaling the process, and the value and application of models or simulation tools to optimize a design space, just to name a few. A recent review discussed the basic impact of common process parameters and the use of design of experiments to identify critical formulation and process factors as well as define design spaces, and basic strategies for scale-up of the HME process (64). However, fully understanding and simulating the HME process is a challenging task due to the known complexities of the twin-screw extruder, such as heat-transfer, heat-generation and variable geometry (32,82).

Nevertheless, generation of an amorphous solid dispersion (ASD) via the process of HME involves a complex series of inter-related unit operations within one piece of equipment (1,87,88). The process is further complicated by the dynamic aspect of the chemical and physical composition of the material being processed. In the case of pharmaceutical HME, which can be considered a type of reactive extrusion, an amorphous or semi-crystalline polymer serves as a matrix, sometimes in combination with a plasticizer or surfactant, into which a solid drug substance melts or dissolves into a molecularly dispersed state throughout the process (2,21,33). This means that the phase-composition of the material, and potentially its bulk material properties, evolves over the length of the extruder. The successful formation of an ASD, as determined primarily by drug substance degradation and residual crystallinity CQAs, is thus dependent on many factors such as the properties of the materials and their interactions with one another, as well as the interplay between process conditions such as temperature, time and shear.

On the one hand, the above-mentioned process variables enable the formation of an ASD, but on the other hand, they can also induce degradation of thermo-labile APIs. When the processing of thermo-labile APIs via HME is discussed in the literature, strategies for mitigating this challenge are usually presented. Such examples include plasticization of the melt (89), drug-polymer interactions (90), formation of an amorphous form prior to extrusion (91), co-crystal formation (92), adjusting the process parameters or setup (93–95), adjusting the chemical microenvironment (95), or utilizing alternative approaches such as melt fusion (25,96), solvent-based approaches (97) or spray congealing (98). Residual crystallinity, as a measure of the success of ASD formation, has been discussed in a similar fashion; strategies related to process setup, namely screw configuration, have been presented to fully melt or dissolve the API (33,99). Alternatively, two studies have been reported utilizing the degradation of model substances to better understand the process, one to investigate the thermal history of material processed and another to calibrate in-line Raman spectroscopy as a prediction tool for the final product properties (31,100). This work builds on and adds to the idea of using a sensitive indicator substance and allows for correlation of the degradation and residual crystallinity, two of the most important CQAs for hot-melt extrusion, with processing conditions.

## 4.2 Aims of Work

The aim of this work was to investigate the use of torasemide as a highly sensitive indicator substance, develop a formulation suitable for studying the effect of a wide range of process parameters on typical HME CQAs, specifically drug substance degradation and residual crystallinity, and to identify links between the observed relationships and HME simulation-derived results. It was not the goal to produce a viable ASD formulation of torasemide in which the substance is completely dissolved and not degraded. In fact, in preliminary unpublished experiments, torasemide showed a rather pronounced level of degradation, even up to 100% of the initial drug substance, depending on the processing conditions. It was also observed that at lower main barrel and die temperatures, extrudates with both residual crystallinity and degradation could be produced. Based on these findings, the idea of utilizing torasemide as a process indicator was conceived.

## 4.3 Experiment Design

Off-line characterization of the thermal properties of torasemide (TOR) and the torasemide-containing formulations was performed using neat drug substance and physical mixtures, discussed in section 4.4.1. The extrusion experiments in this study were performed in two parts (Table 4.1). The first part, discussed in section 4.4.2, involved selection of the matrix composition by varying the PEG 1500 concentration in Soluplus® (SOL) in order to optimize the extrusion processing space and enable observation of the degradation and residual crystallinity CQAs. The second part, discussed in sections 4.4.3 and 4.4.4, studied the performance of the selected formulation and investigated the impact of the screw configuration, screw speed and blend moisture content on the CQAs. Following experimental work, retrospective analysis of the process was performed using Ludovic® simulation software to correlate the CQAs with a simulation-derived process characteristic, discussed in section 4.4.5.

Table 4.1 *Extrusion study design – experiment design parameters and ranges.*

| | | **Study 1 – Selection of Matrix Composition** | **Study 2 – Performance of Selected Formulation** |
|---|---|---|---|
| Process Variable | Main Barrel and Die Temperature | 105 to 155 °C in 10 °C increments | 105 to 135 °C in 10 °C increments |
| | Feed Speed | 10 to 20 rpm in 5 rpm increments, resulting in feed rates ranging from 1.75-5 g/min | 10 to 25 rpm in 5 rpm increments, resulting in feed rates ranging from 1.5-5 g/min |
| | Screw Speed | 150 rpm (constant) | Standard: 150 rpm<br>(One study compared the standard option with 125 vs. 175 rpm) |
| | Venting<br>(port open to atmosphere) | Configuration 1: fully closed (constant) | Configuration 1: fully closed (standard unless otherwise noted)<br>Configuration 2: vent 1 open, vent 2 closed (aka early open-end closed)<br>Configuration 3: vent 1 open, vent 2 open (aka early open-end open)<br>Note: only 1-mixing zone screw used |
| | Screw Configuration | Primarily 1-mixing zone screw, but 2mix5disk60degFWBW was used for one study with 15 %w/w PEG 1500 (see Figure 4.2 for more details) | Primarily 1-mixing zone screw, and 2mix5disk60degFW-5disk60degFWBW were used, with one comparison to 2mix5disk60degFW (see Figure 4.2 for more details) |
| Formulation Variable | Torasemide concentration | 10 %w/w (constant) | 10 %w/w (constant) |
| | PEG 1500 concentration | 0, 5, 10 and 15 %w/w | 10 %w/w (constant) |
| | Blend moisture content | 2 %w/w (constant) | 2 vs. 2.5 %w/w<br>Note: only 1-mixing zone screw used |

The experimental processing train for extrudate preparation is shown in Figure 4.1, more details in section 7.2.2.2. The various screw configurations and venting options studied with torasemide are shown in Figure 4.2.

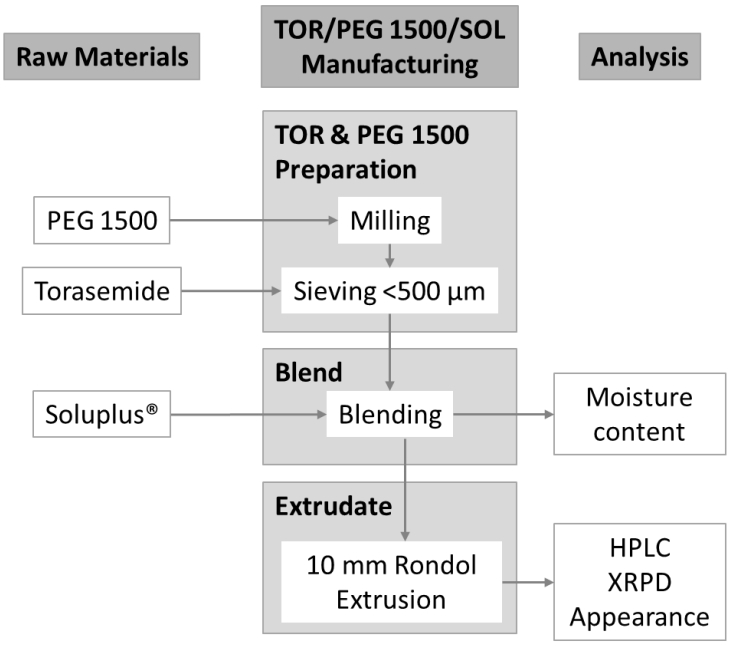


Figure 4.1 *Experiment processing train and corresponding analysis.*

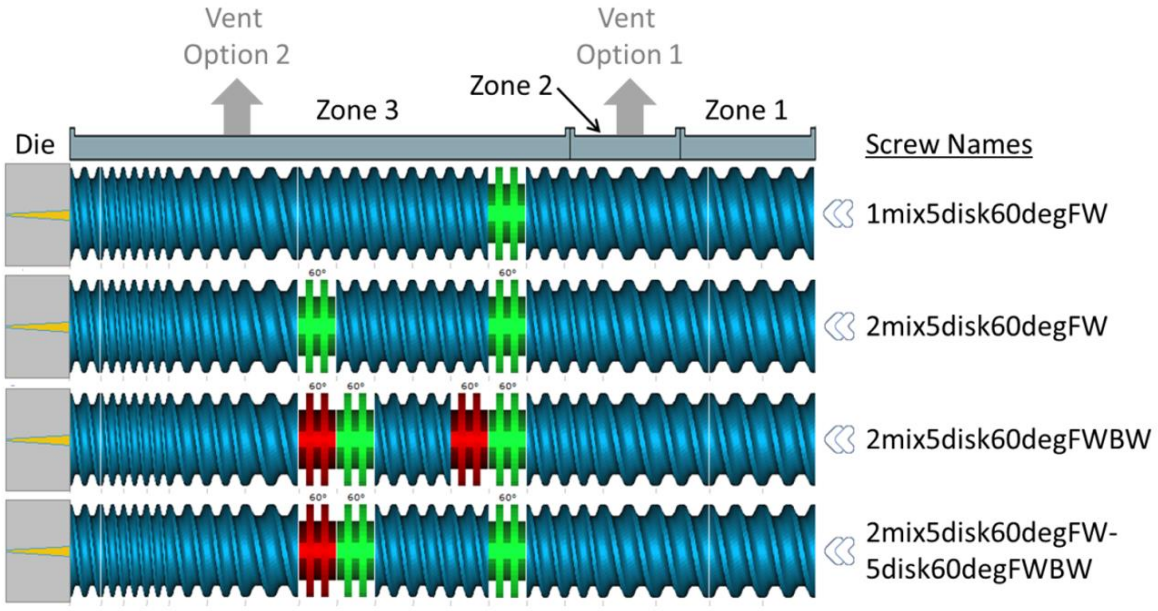


Figure 4.2 *Extruder geometry and screw configurations. Note: die and screw depictions are not to scale. Drawings prepared with Ludovic® v.6.0 software. Green kneading blocks are 60° forward and red kneading blocks are 60° backward.*

## 4.4 Results

### 4.4.1 Thermal Characterization of Torasemide and Physical Mixtures

Heating studies via TGA and DSC with neat torasemide were performed to better understand its degradation behavior. Melting of torasemide begins at approximately 160 °C and a weight loss of ~0.6 wt% is observed throughout this transition (Figure 4.3a). HPLC analysis of samples heated to intermediate temperatures between 100 to 180 °C showed that degradation began only upon melting (Figure 4.3b). Two degradants were observed, and less than 10 PA% of torasemide was remaining at 180 °C. The primary degradant was the thermal degradant, confirmed by HPLC-MS (Appendix 10.1), and the second was the hydrolysis degradant (Figure 4.4). A comparison of pierced and hermetically sealed pans showed little difference in the formation of the thermal versus hydrolysis degradants.

Preliminary extrusion experiments showed substantial degradation at main barrel and die temperatures below the melting point of torasemide (data not shown). Therefore, DSC experiments similar to those with neat torasemide were conducted to investigate the degradation process in physical mixtures. HPLC analysis showed that in the case of sealed pans, both the thermal and hydrolysis degradants start to form at temperatures between 110-120 °C (Figure 4.5a). In the case of pierced pans, only the thermal degradant is formed. The DSC thermogram in Figure 4.5b for a pre-dried extrusion blend shows 3 thermal events. The first is melting of the PEG 1500 at 45 °C. The second is glass transition of the mixture formed up to that point, dominated by SOL softening at ~70 °C. The third is a dissolution endotherm of the torasemide dissolving into the matrix. The dissolution process begins at ~115 °C, as clearly seen in the first derivative of the thermogram (Figure 4.5b). Control experiments of binary mixtures of TOR and PEG 1500 showed degradation occurring at similar temperatures (data not shown). Moreover, when extrudates with a substantial amount of residual crystallinity were heated on a hot-stage polarized light microscope (PLM), crystals were visually observed to lose birefringence also at ~115 °C, indicating onset dissolution of the crystals (data not included). The progression of degradation over time for samples heated to 140 °C at a heating rate

of 10 K/min clearly show the effect of moisture, and in both sealed and pierced pans, both degradants reach a plateau between 5 and 10 min hold time (Figure 4.5c).

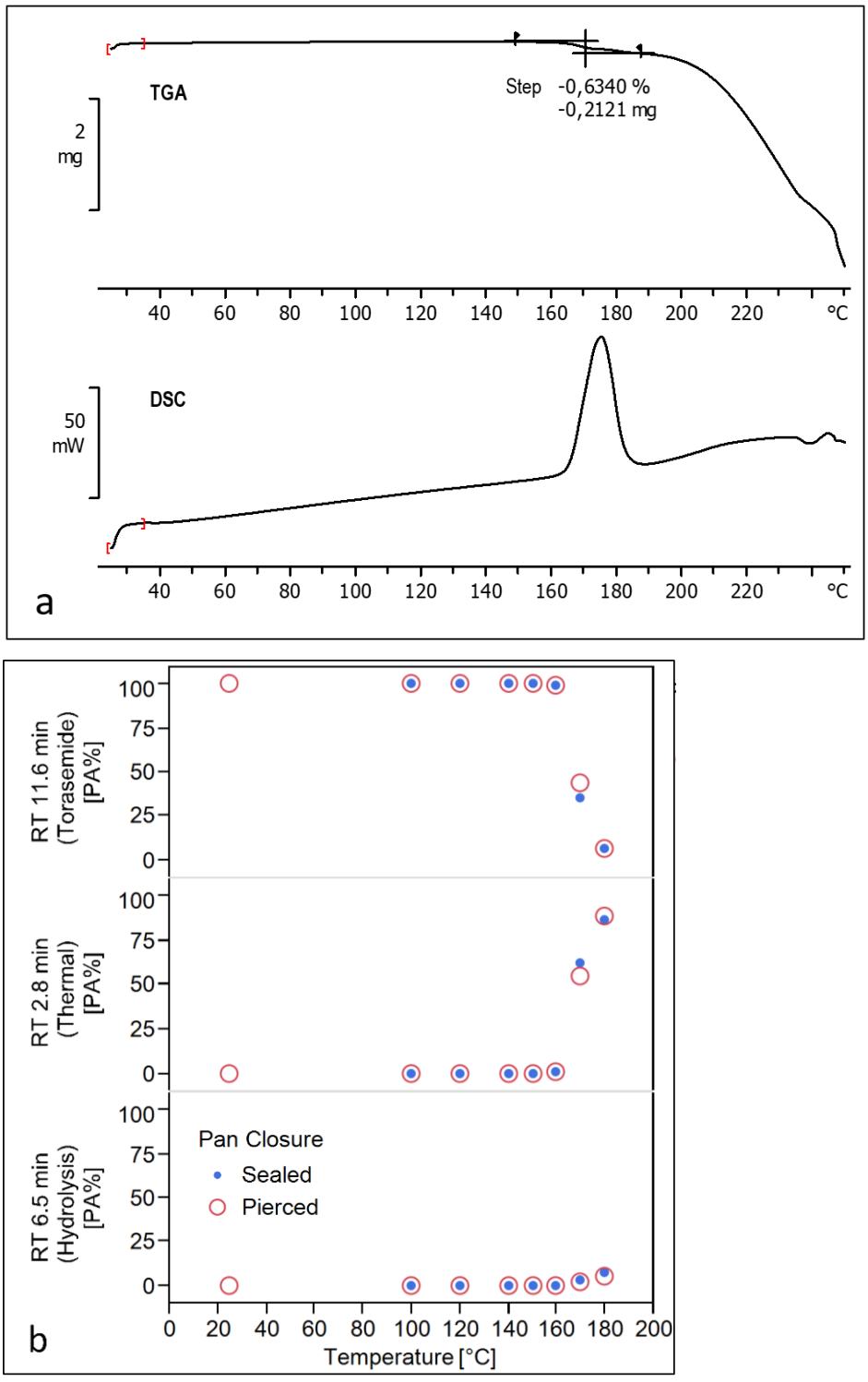


Figure 4.3 *Thermal analysis of neat torasemide. a) TGA and DSC curves of torasemide (endo up), b) torasemide and degradants levels after thermal exposure.*

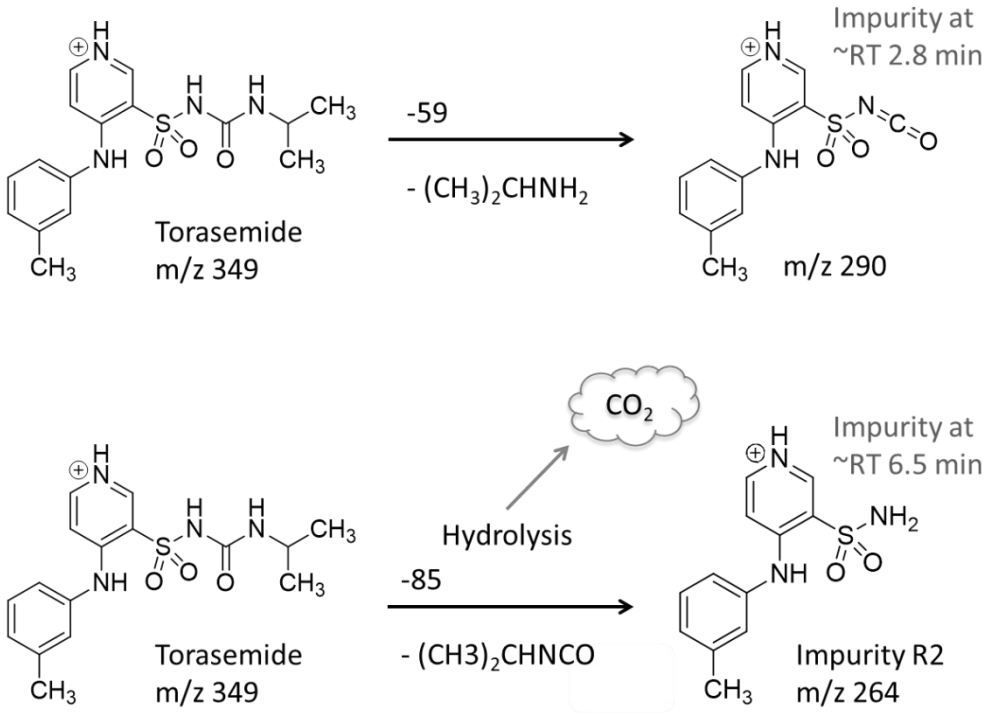


Figure 4.4 *Molecular structures of torasemide and its reaction products for thermal (upper) and hydrolysis (lower) degradation. Designation of hydrolysis impurity as R2 is in reference to study by Jovic, et.al.* (101).

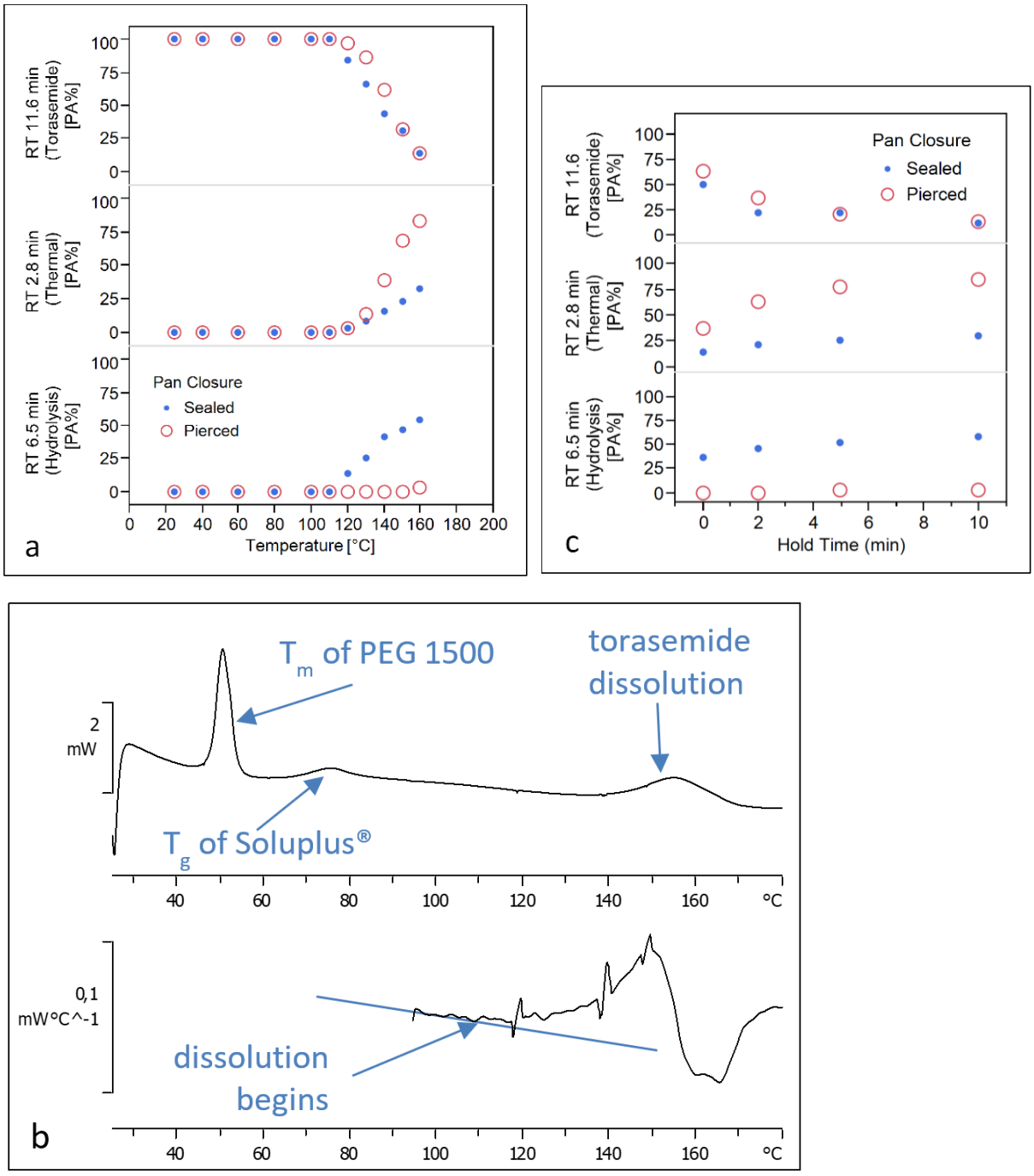


Figure 4.5 *Thermal analysis of physical mixtures of torasemide. a) torasemide and degradant levels after thermal exposure, b) DSC curves of extrudate blend (endo up), c) progression of torasemide and degradant levels with time at a hold temperature of 140 °C.*

### 4.4.2 Selection of Matrix Composition for Optimal Extrusion Processing Space and Observation of CQAs

For studies exploring matrix composition, the process parameters were chosen such that the primary independent variables were main barrel and die temperature and feed rate. However, because the screw speed was held constant and only the 1-mixing zone screw was used (Figure 4.2), the feed rate directly impacted the MRT (Figure 4.6). The MRT decreases with increasing feed rate, as expected, and tends toward a plateau at both low and high feed rates. Because the extruder used is equipped with a volumetric feeder, it is challenging to keep the feed rate constant while other variables, in particular formulation composition, are studied. As such, the MRT was used as a dependent variable in these studies.

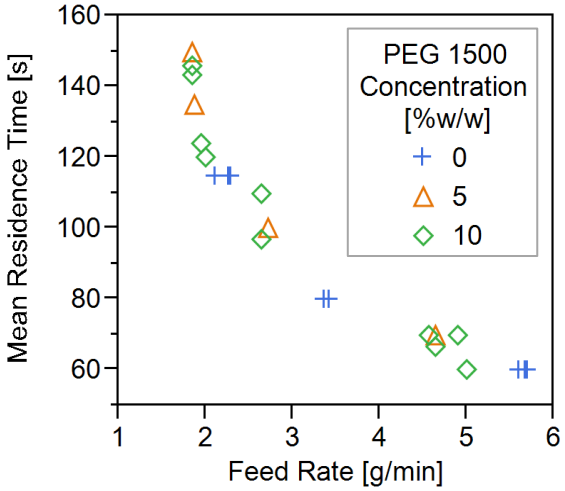


Figure 4.6 *Relationship between feed rate and mean residence time for selected processing conditions: varied temperature but constant screw speed of 150 rpm and 1-mixing zone screw configuration.*

#### 4.4.2.1 Effect of Plasticizer Concentration on Ranges of Processing Space and CQAs Observed

The plasticizer concentration had a direct impact on the investigable processing space, in particular the main barrel and die temperature range. The torque increased when the main barrel and die temperature was too low for a given plasticizer concentration, and measured barrel temperature in the last heated zone rose above the set point at lower temperatures (data not shown). Therefore, with increasing plasticizer concentration, the main barrel and die temperature could be decreased

(Figure 4.7). The minimum possible main barrel and die temperature decreased from 135 °C with 0 %w/w PEG 1500 step-wise down to 95 °C with 15 %w/w PEG 1500. Melt temperatures at die exit were always 10-20 °C above the main barrel and die temperature. The feed rate, and therefore MRT, was not impacted by the concentration of plasticizer. However, the feed rates selected allowed for the same range of MRTs to be investigated for all formulations (Figure 4.8).

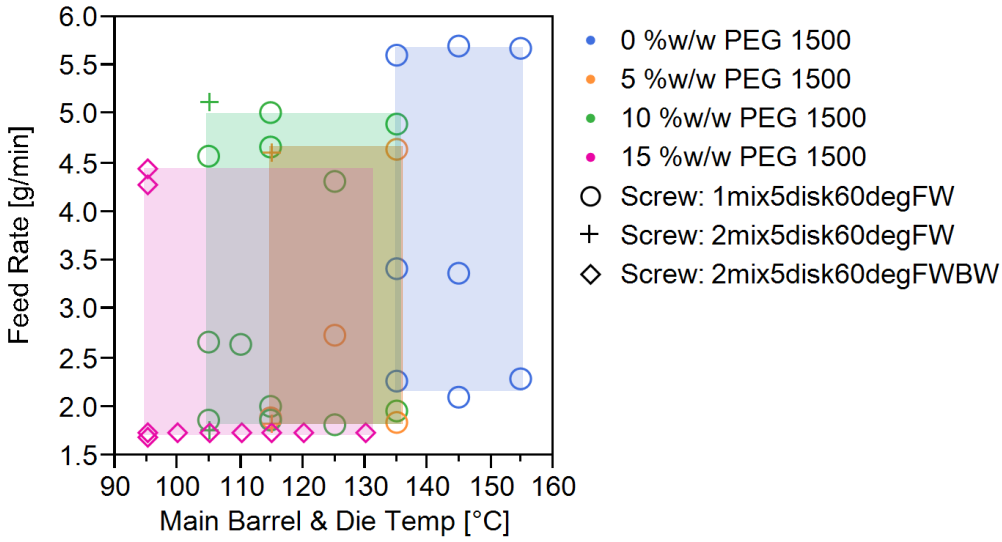


Figure 4.7 *Effect of PEG 1500 concentration on processing space. Colors indicate PEG 1500 %w/w concentration while symbols indicate screw configuration used.*

The plasticizer concentration also had an impact on the range of observable CQAs, specifically the total amount of drug substance degradation and the residual crystallinity. The range of degradation decreased with increasing plasticizer concentration (Figure 4.8a). However, within the processing space studied for each formulation, the amount of degradation increased with both increasing residence time and increasing main barrel and die temperature. Correspondingly, the range of observed residual crystallinity increased with increasing plasticizer concentration (Figure 4.8b). Again, within the processing space studied for each formulation, the amount of residual crystallinity decreased with increasing residence time and increasing main barrel and die temperature. However, the investigable processing space for the 5 %w/w PEG 1500 formulation was limited by low levels of measurable residual crystallinity approaching 0 %w/w at increased temperatures. In the case of 0 %w/w PEG 1500, the processing space was limited by degradation levels

approaching 100 %w/w as higher temperatures had to be applied for extrusion. Residual crystallinity was not quantified by XRPD for the samples without PEG 1500, but almost no residual crystallinity was observed via polarized light microscopy (results not shown).

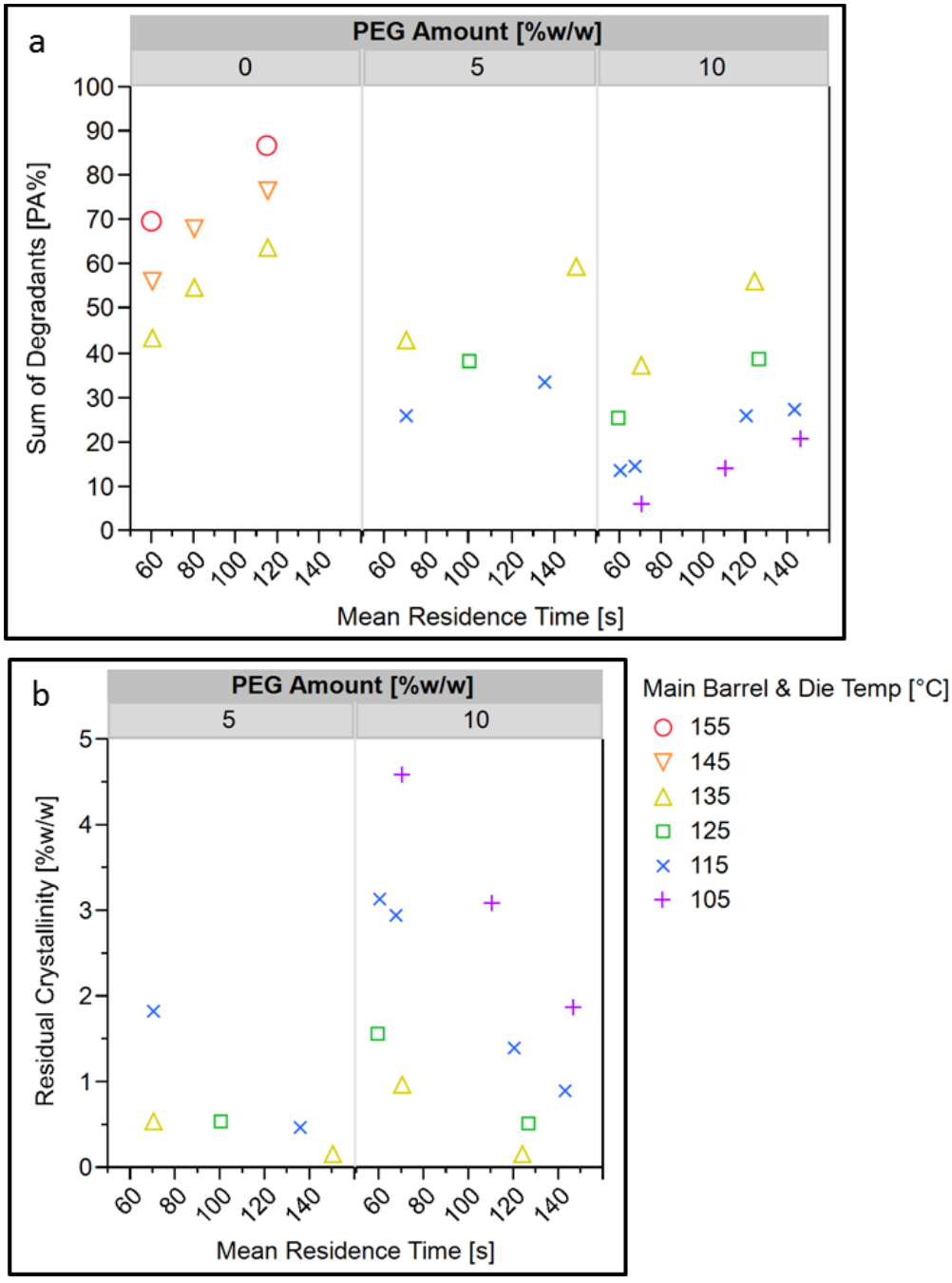


Figure 4.8 *Range of a) total degradants observed [PA%] and b) residual crystallinity [%w/w of formulation] with different concentrations of PEG 1500. Screw speed was constant at 150 rpm and the 1-mixing zone screw was used.*

The amount of degradation and residual crystallinity also showed a dependency on PEG 1500 concentration, even when similar processing conditions were used (Figure 4.8). At main barrel and die temperatures between 115 and 135 °C, the amount of degradation decreased slightly with increasing PEG 1500 concentration. Within the same temperature range, the amount of residual crystallinity was higher with 10 %w/w PEG 1500 than with 5 %w/w PEG 1500.

The residual crystallinity is shown visually for the 10 %w/w PEG 1500 formulation in Figure 4.9 for a selection of process conditions, along with photographs of the extrudates. The residual crystallinity decreases as expected with both time and temperature, and ranges from an uncountable number of crystals to only very few, corresponding to 4.6 to 0.17 %w/w as measured by XRPD. The transparency increases as expected with time and temperature, and ranges from very turbid to translucent to visually transparent. Air bubbles are present in some extrudates due to the absence of venting on the extruder during these experiments. The transparency, or turbidity, of the 1 mm thick extrudate samples was further quantified and compared to the measured residual crystallinity (Figure 4.10). The turbidity is almost unchanged for samples with residual crystallinity above 2 %w/w, but gradually decreases as residual crystallinity decreases. Some noise in the turbidity values may be related to bubbles present in the extrudates, which can be eliminated with the use of venting on the extruder.

The formulation with 10 %w/w PEG 1500 exhibited a processing space with main barrel and die temperature beginning at 105 °C, below the onset dissolution temperature of torasemide into the matrix, which demonstrated the widest range of observable degradation and residual crystallinity CQAs. It is also apparent from these data that at least a fraction of crystalline torasemide was dissolving into plasticized matrices composed of SOL-PEG 1500.

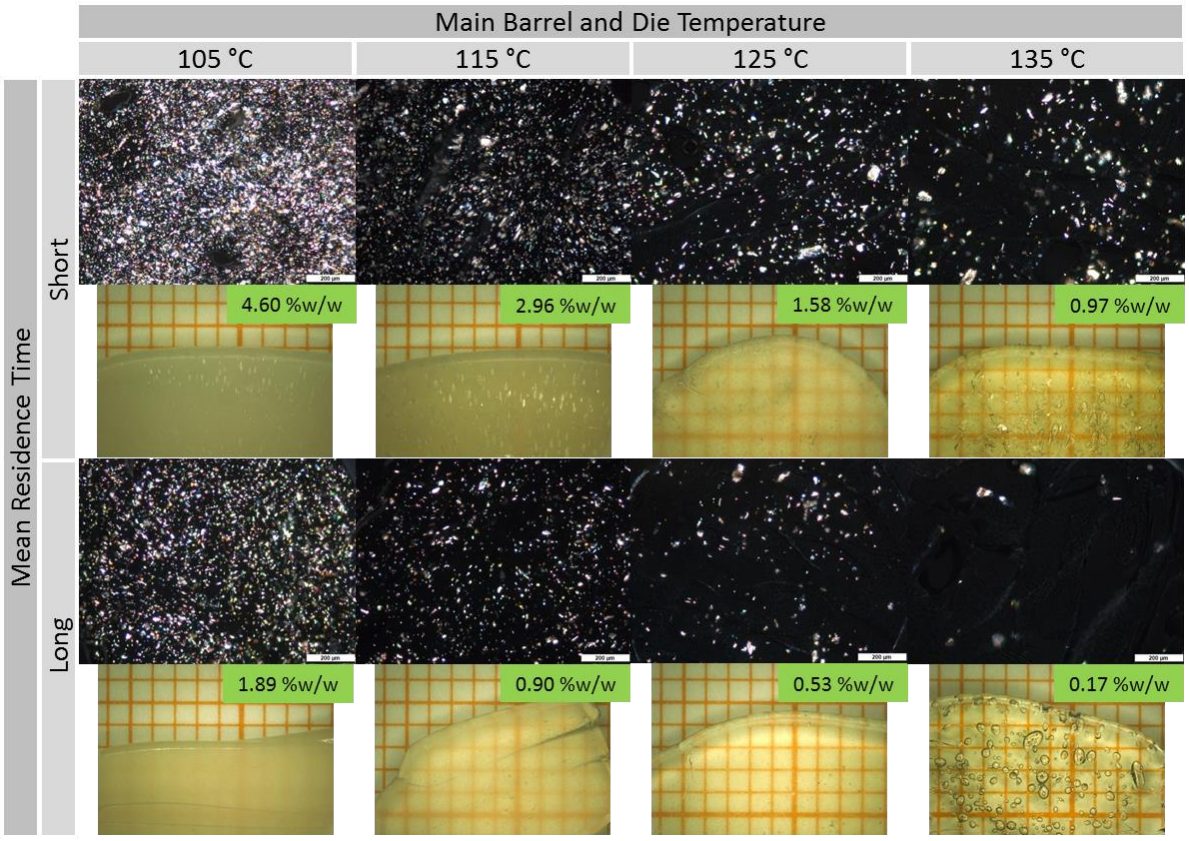


Figure 4.9 *Residual crystallinity [%w/w of formulation] and extrudate transparency for selected 10 %w/w PEG 1500 samples. (PLM scale bar represents 200 µm and orange grid paper represents 1 mm line spacing).*

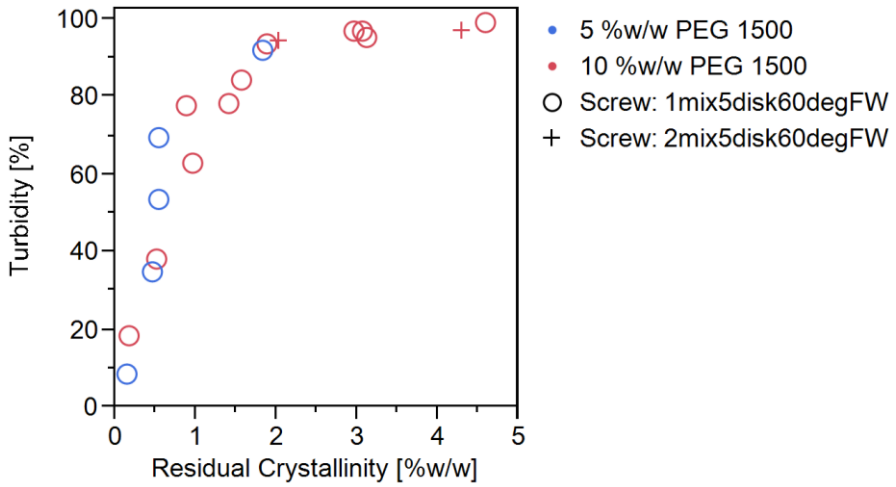


Figure 4.10 *Comparison of extrudate turbidity and residual crystallinity for two concentrations of PEG 1500 and two screw configurations.*

#### 4.4.2.2 Effect of System Composition on Extrudate Melt Viscosity

Measurement of the melt viscosity and $T_g$ via DSC of various compositions of SOL with 0, 5 and 10 %w/w PEG 1500 and 0 and 10 %w/w TOR showed a plasticizing effect by PEG 1500 but little impact of the TOR (Figure 4.11 and Figure 4.12). It was observed during melt viscosity measurement that the formulations with TOR flowed at lower temperatures in comparison to the corresponding placebo. As a result, the melt viscosity was measured at different set temperatures, leading to sets of master curves at different temperatures. However, upon extrapolation to the same temperature, 125 °C or 135 °C, the presence of TOR has a negligible impact on the melt viscosity (Figure 4.13).

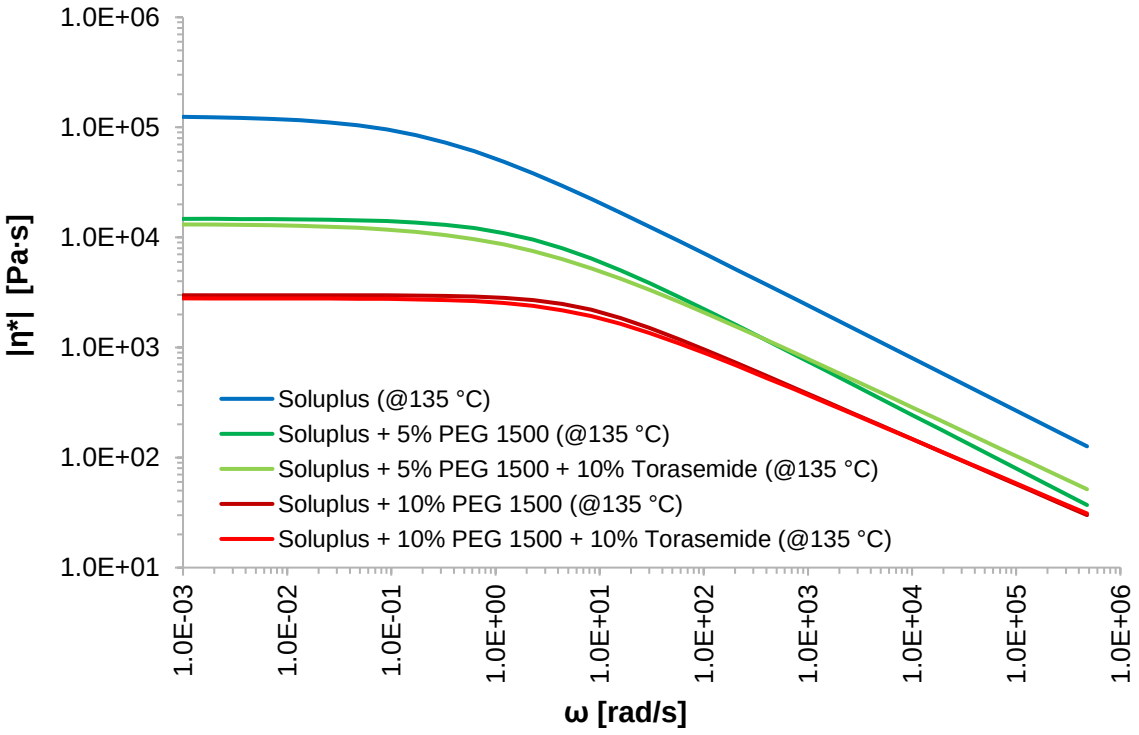


Figure 4.11 *Formulation melt viscosity as a function of PEG 1500 concentration and torasemide presence (extrapolated to temperature of 135 °C).*

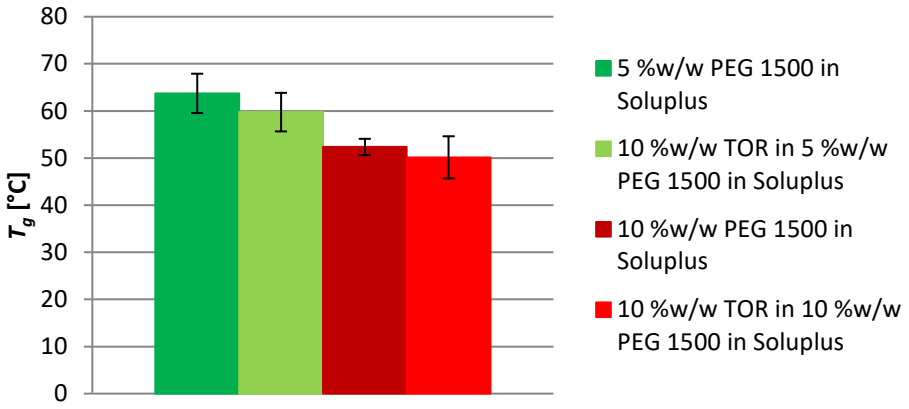


Figure 4.12 *Formulation $T_g$ as a function of PEG 1500 concentration and torasemide presence. Error bars indicate the standard deviation from n=3 measurements.*

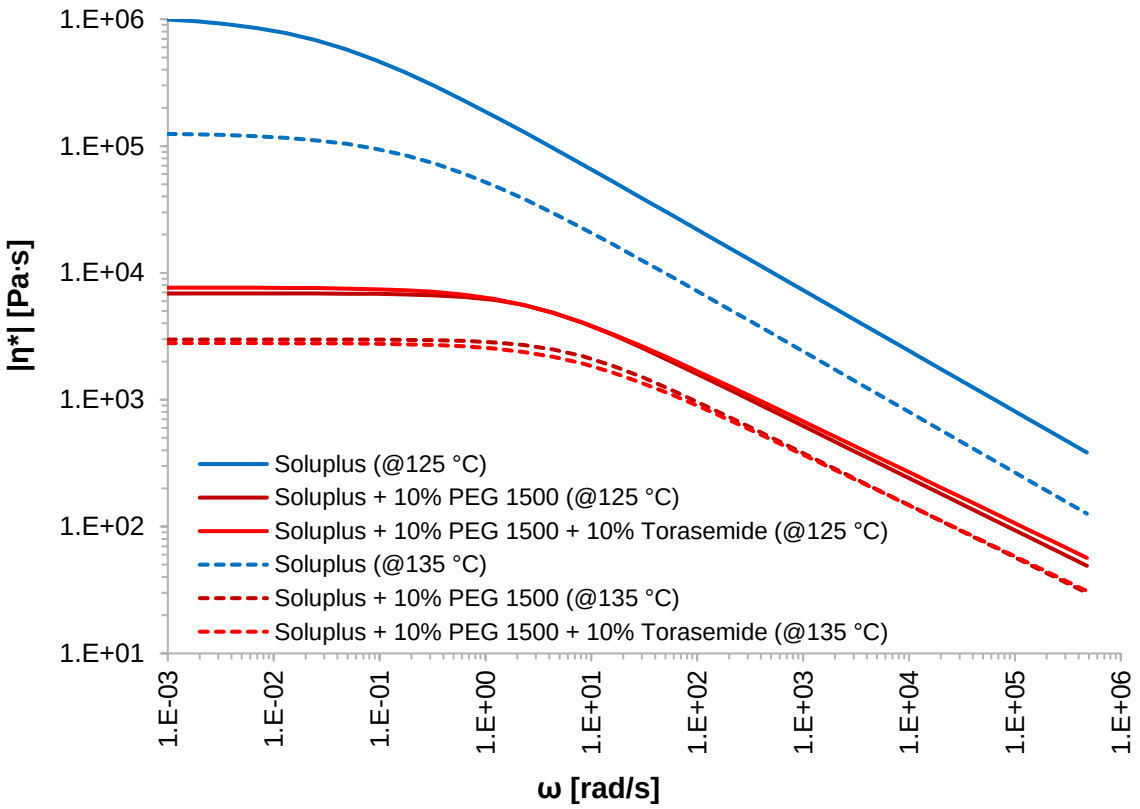


Figure 4.13 *Formulation melt viscosity as a function of PEG 1500 and torasemide presence and temperature (extrapolated to temperatures of 125 °C and 135 °C).*

### 4.4.3 Performance of Torasemide-Based Indicator System with 10 %w/w PEG 1500 Formulation

Based on the wide range of CQAs that can be observed with the model formulation with a 10 %w/w concentration of PEG 1500, additional process variables such as the effect of screw configuration, screw speed and moisture content were studied.

#### 4.4.3.1 Effect of Screw Configuration

Three screw configurations were studied with varied numbers of mixing zones (one or two) and different combinations of forward and backward 60° kneading disks (Figure 4.2). The screw configuration had only a minor impact on the total degradation within the mean residence time range of 80-160 s, while temperature and mean residence time showed more prominent effects (Figure 4.14a). No difference in degradation was seen between the two screws composed of only forward kneading blocks; the MRTs were nearly identical (Figure 4.14c). The backwards kneading blocks in the more complex screw increased the MRT for a given feed rate (Figure 4.14c). However, when the MRT was the same as for the 1-mixing zone screw, approximately 90-160 s, degradation levels were similar (Figure 4.14a).

Conversely, the amount of residual crystallinity was impacted by screw configuration, especially at lower temperatures and shorter residence times (Figure 4.14b). The extrudates manufactured with the harsher screw contained less residual crystallinity than those manufactured with the simple screw.

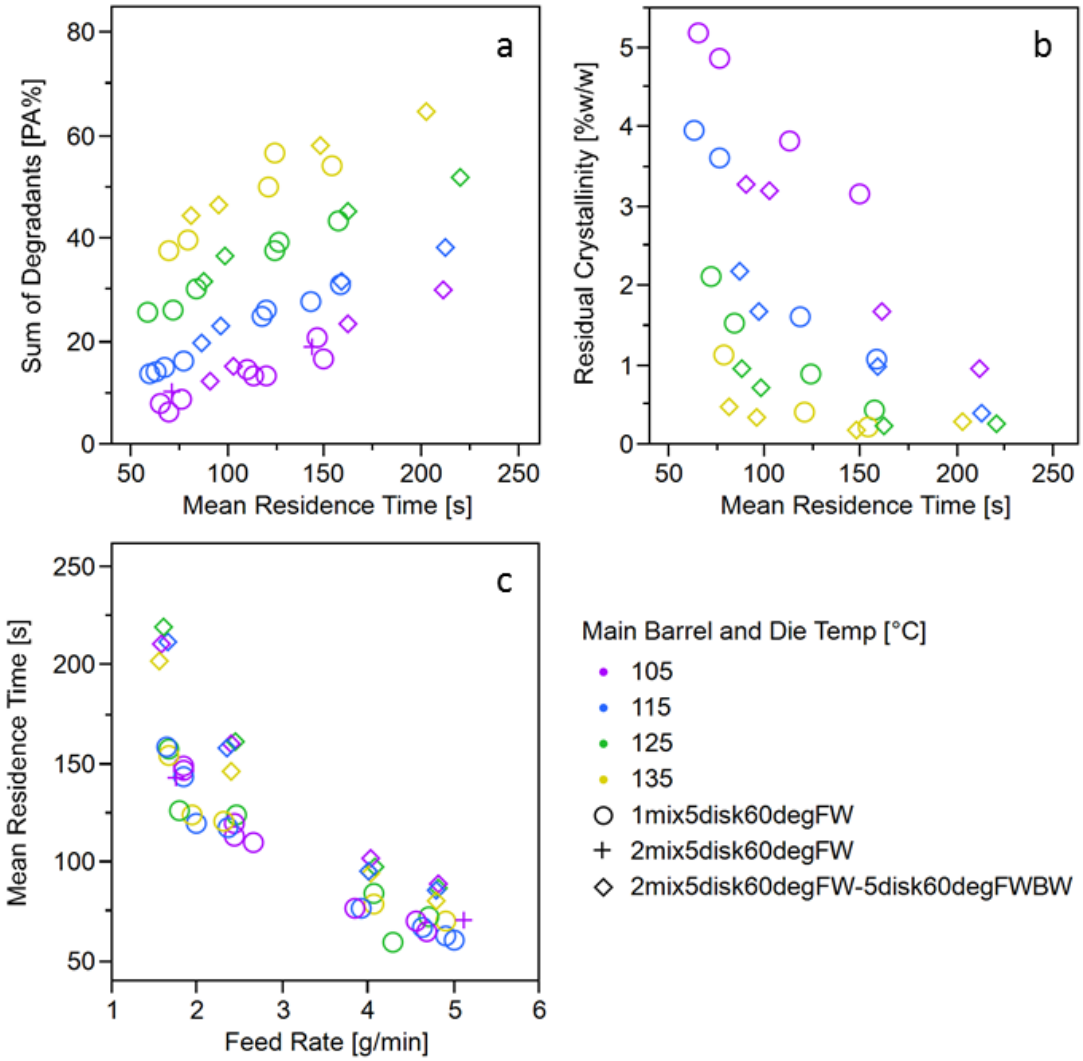


Figure 4.14 *Effect of screw configuration on a) torasemide degradation, b) residual crystallinity and c) mean residence time vs. feed rate for constant screw speed of 150 rpm.*

### 4.4.3.2 Impact of Screw Speed

The impact of screw speed was studied in order to assess the shear sensitivity of the CQAs. The standard screw speed of 150 rpm was compared with 125 and 175 rpm. The lower limit was selected based upon prior knowledge that back mixing can occur at a low screw speed of 100 rpm. The upper limit was selected based upon observations of barrel over-heating when a screw speed of 200 rpm is used. With increasing screw speed, the degradation level increased slightly while residual crystallinity decreased, but the predominant factor was the main barrel and die

temperature (Figure 4.15). In addition, higher degradation and lower crystallinity were seen with the more aggressive screw (Figure 4.2).

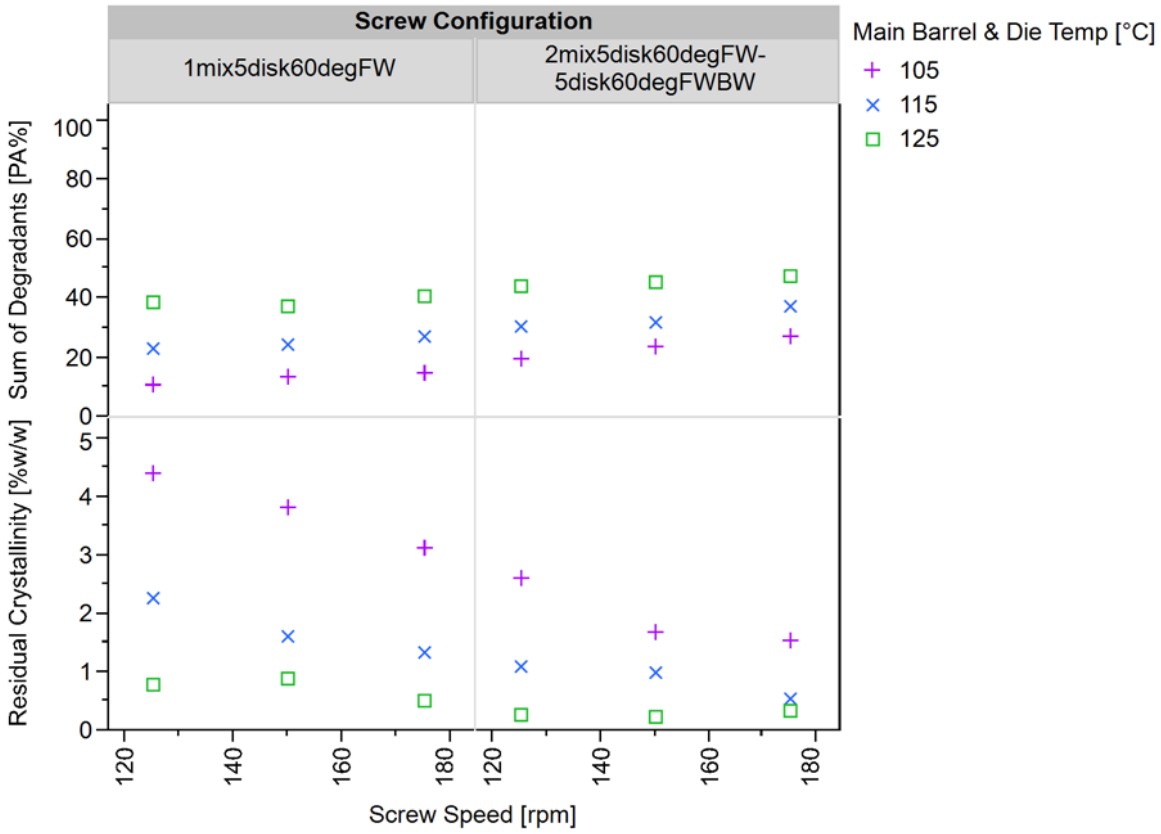


Figure 4.15 *Effect of screw speed on CQAs as a function of screw design and process temperature. Throughput was constant at ~2.4 g/min via feeder screw speed of 15 rpm. MRT for 1-mixing zone screw was ~115 s while MRT for 2-mixing zone screw was ~150 s.*

The melt temperature at the die exit did not differ between the two screw configurations when the main barrel and die temperature was set to 115 and 125 °C, but for 105 °C, the melt temperature was noticeably higher for the screw with only one mixing zone (data not shown).

#### 4.4.3.3 Influence of Moisture on Torasemide Degradation

Due to the propensity for hydrolysis degradation with torasemide, the impact of moisture was also studied. In a head-to-head study varying the main barrel and die temperature and MRT, blends with 2 and 2.5 %w/w moisture were evaluated based on the observed moisture content of packaged SOL. Within this range, the effect of

the initial moisture content of the blend was found to be insignificant on hydrolysis degradant levels (data not included).

Multiple venting configurations were compared to investigate the potential utility of torasemide to study the effect of the transient amount of moisture in a HME formulation on process performance and resulting extrudate quality. The blend used for this study contained an initial amount of 2.5 %w/w moisture. Three venting configurations were studied utilizing two available vent ports on the extruder (Figure 4.2). The three venting configurations studied were 1) early closed-end closed, 2) early open-end closed, and 3) early open-end open. In this experiment, the main barrel and die temperatures were kept constant at 115 °C, the screw speed was held constant at 150 rpm, the 1-mixing zone screw was used, and the feed rate was varied in order to observe the progression of degradation over time spent in the extruder.

The torasemide degradation as a function of venting and residence time is shown in Figure 4.16. The highest amount of hydrolysis degradation was seen when both vent ports were closed (Figure 4.16, middle graph). However, the same amount of hydrolysis degradant was seen independent of the number of open vent ports. This observation was surprising due to quite different experimental observations of the two venting configurations. Very little moisture was detected escaping from the first port, partly due to material filling and plugging the opening. In contrast, a substantial amount of moisture and potentially other vapors, visualized by placing a glass beaker over the port for a short period of time, was seen escaping from the second port.

With regards to thermal degradation, little difference was seen between venting configurations 1 and 2 (Figure 4.16, top graph). However, the amount of thermal degradation produced, especially at longer residence times, was distinctly different for venting configuration 3. The torque was observed to increase slightly when the second vent port was open. It was also observed that the extrudates produced with venting configuration 3 contained fewer bubbles than those produced with a closed 2$^{nd}$ vent port. Overall, venting configuration 2 produced extrudates with the least amount of total degradation (Figure 4.16, bottom graph).

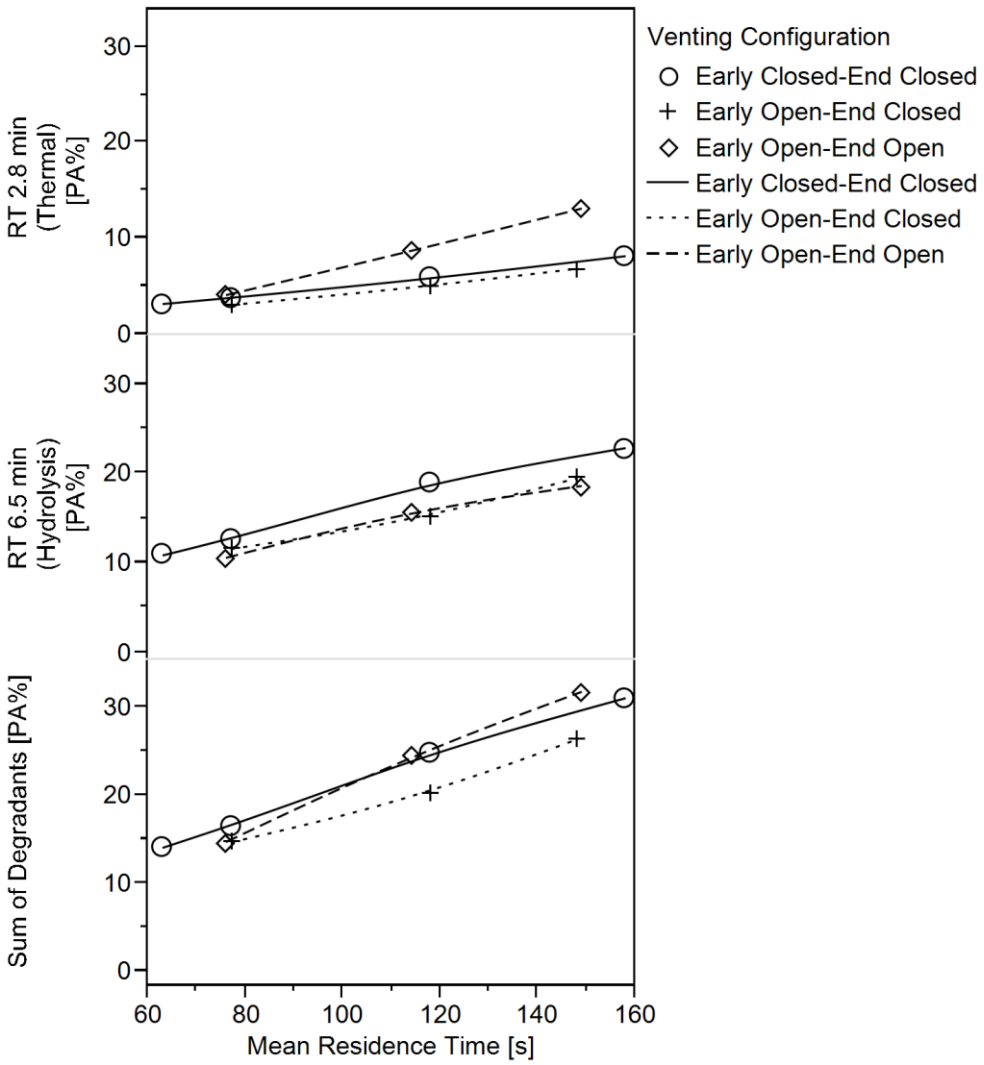


Figure 4.16 *Effect of venting configuration on torasemide degradation at various feed rates. Main barrel and die temperature held constant at 115 °C and constant screw speed of 150 rpm with 1-mixing zone screw.*

### 4.4.4 Chemical Composition of Torasemide-Containing Extrudates

The torasemide CQAs showed the expected behavior for a dissolving API in a polymer matrix: degradation increased with time and temperature while residual crystallinity decreased with time and temperature. It was also deduced that the extrudates were composed of a combination of torasemide in the crystalline form, thermal and hydrolysis degradants, and potentially also dissolved torasemide. Evidence for this was shown in Figure 4.8 and Figure 4.14, and is again presented for a larger set of data, including for several screw configurations, in Figure 4.17.

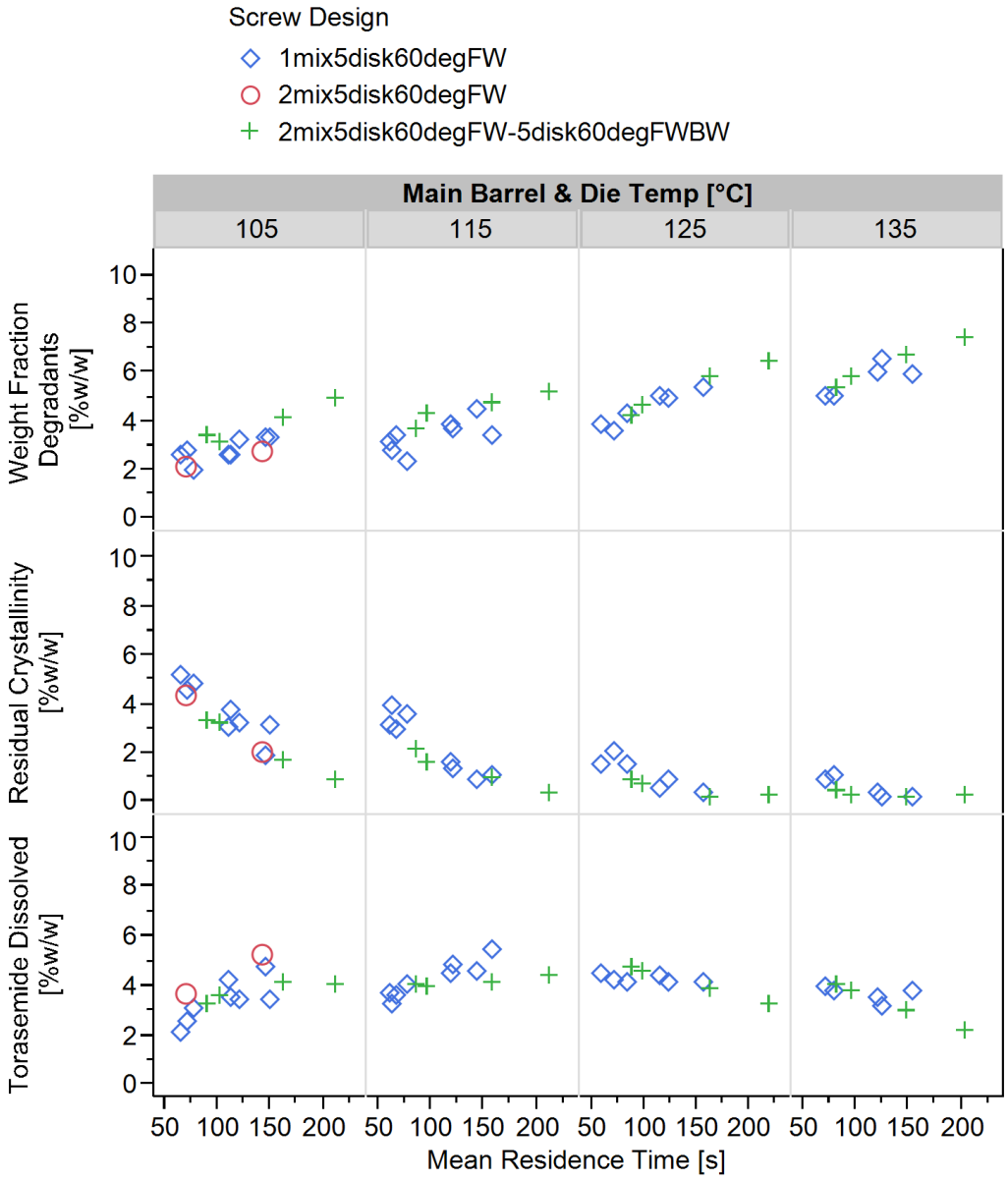


Figure 4.17 *Evolution of dissolution and degradation processes as a function of time and process temperature for the 10 %w/w PEG 1500 formulation. All quantities are in %w/w of formulation and 10 %w/w is equivalent to 100 %w/w of initial API.*

Because HPLC does not distinguish between un-degraded torasemide in the crystalline form versus in the dissolved state, it was unclear whether torasemide degraded immediately upon dissolution or if it could be present molecularly dissolved and remain un-degraded. Therefore, this time, the degradation is presented as a weight fraction of the formulation, and the weight fraction of dissolved torasemide is also included. The weight fraction of degradants increased with time and temperature

while the crystalline fraction of torasemide simply decreased with time and temperature (Figure 4.17). However, the dissolved fraction of torasemide increased at low main barrel and die temperatures, reached a plateau at intermediate temperatures when the rates of dissolution and degradation were roughly equal, and simply decreased with time at high temperatures. Slight differences were observed in the slopes of the evolution of these species over temperature and time for the different screw configurations.

With the torasemide system, the amount of degradation and residual crystallinity were strongly correlated (Figure 4.18). For a wide range of process conditions in which temperature, residence time and screw configuration were varied, extrudates with a given amount of residual crystallinity resulted in a relatively tight range of degradation, roughly within ±5 PA%.

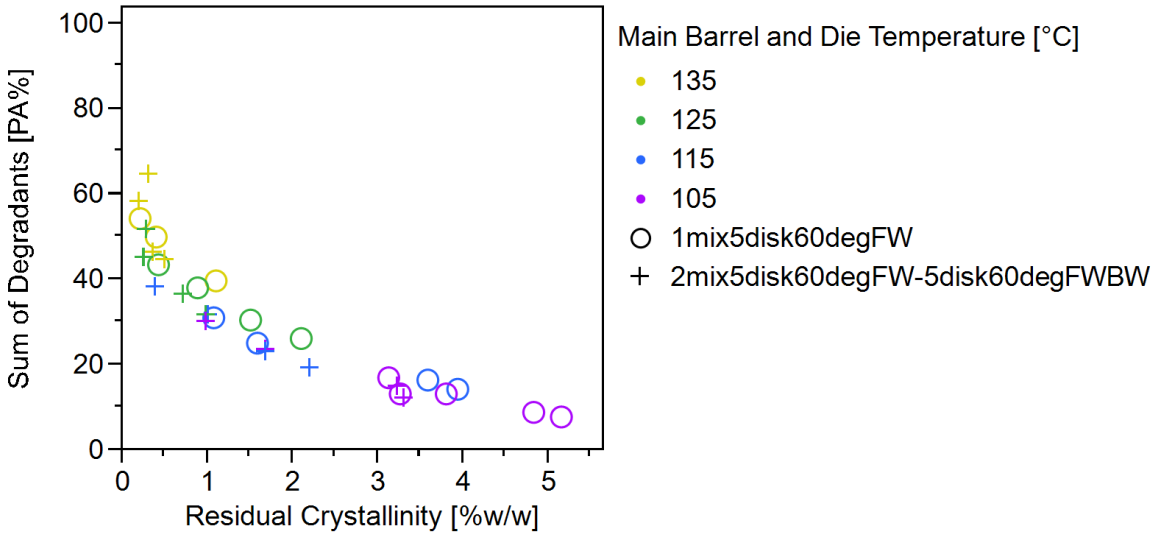


Figure 4.18 *Relationship between torasemide degradation and residual crystallinity for a range of process conditions, for the 10 %w/w PEG 1500 formulation. Feed rate was varied, but screw speed was kept constant at 150 rpm.*

### 4.4.5 Numerical Simulation and Correlation of CQAs with Dimulation-Derived Process Characteristic

Further investigation of the relationship between CQAs, process parameters and performance via simulation yielded a new way to quantify the relationship between the already highly-correlating sum of degradants and residual crystallinity. For this evaluation, only the set of data generated with the 10 %w/w PEG 1500 formulation

and 2mix5disk60degFW-5disk60degFWBW screw design (Figure 4.2) was used. The material properties used for simulation are shown in Table 4.2.

Table 4.2 *Material Properties of 10 %w/w TOR / 10 %w/w PEG 1500 / SOL.*

| **Carreau-Yasuda and WLF Equation Parameters** | | **Thermal Properties** | |
|---|---|---|---|
| $T_0$ | 115 | Solid $c_p$ (J/kg/°C) | 1686 |
| $\lambda$ | 1.18 | Solid Density (kg/m$^3$) | 560 |
| $n$ | 0.6 | Solid Thermal Conductivity (W/m·K) | 0.2 |
| $\eta_0$ | 21886 | Liquid $c_p$** (J/kg/°C) | f(T); at 135 °C = 2068 |
| $\eta_\infty$ | 0 | Liquid Density (kg/m$^3$) | 1400 |
| $a$ | 0.86 | Liquid Thermal Conductivity (W/m·K) | 0.2 |
| $C_1$ | 21.17 | $T_g$ as Melting Temperature (°C) | 50 |
| $C_2$ | 300 | Melting Enthalpy (kJ/kg) | 0 |

* For master curve at 115 °C reference temperature
** In Ludovic® software, the liquid $c_p$ was entered as a function of temperature, data not shown

The Ludovic® model provided simulated results which were in fairly good agreement with experimental results. While the absolute agreement for melt temperature was slightly off, the correlation was strong (Figure 4.19). Many attempts to improve the agreement were unsuccessful, for example by adjusting the thermal exchange coefficients or the WLF parameters, data not shown. It was possible to raise or lower the melt temperature, but occasionally the melt temperature, especially the maximum, resulted in an unreasonably high value, for example above the melting temperature of torasemide, 162 °C. Because residual crystallinity was observed in all samples, it is unlikely that the melt temperature exceeded this temperature. In this way, the maximum melt temperature in relation to the API melting temperature was also used to tune the simulations. Based upon this analysis, it may be that there is error in the measured melt temperature values. Unfortunately, it was not possible to measure the solubility of TOR in the matrix due to substantial degradation; data regarding the temperature at which 10 %w/w torasemide is soluble in the matrix could have guided the model validation efforts. The measured and simulated residence time distributions RTDs and mean residence times MRTs showed nearly perfect agreement (Figure 4.20 and Figure 4.21).

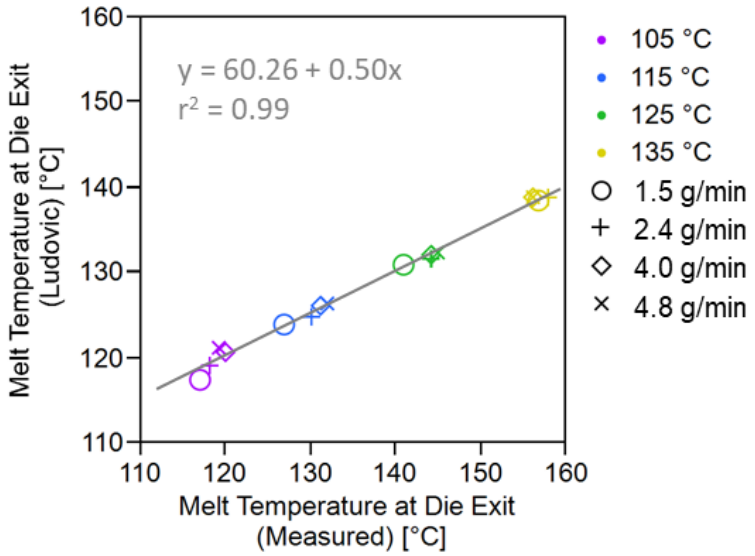


Figure 4.19 *Correlation of measured vs. simulated melt temperature at die exit.*

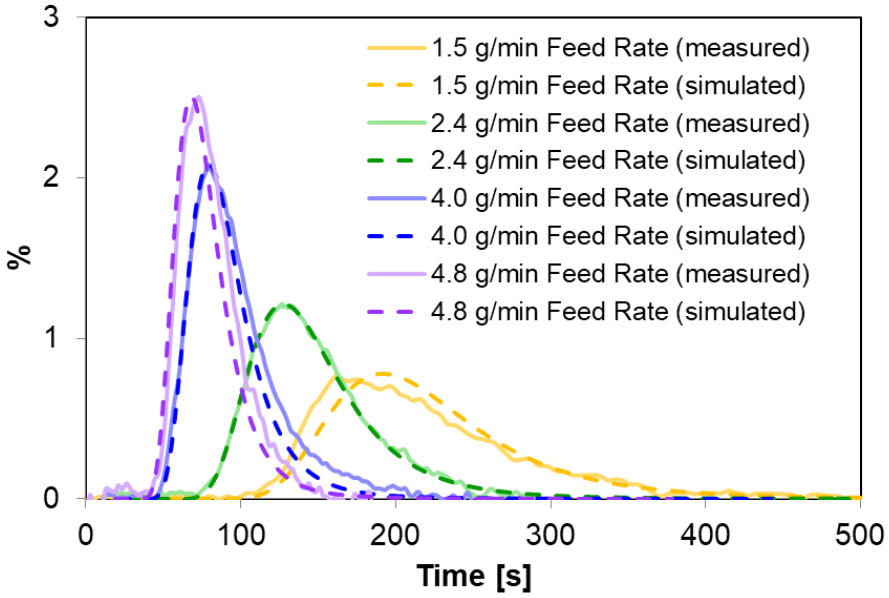


Figure 4.20 *Example of agreement between measured and simulated RTD (screw speed constant at 150 rpm and main barrel and die temperature constant at 135 °C).*

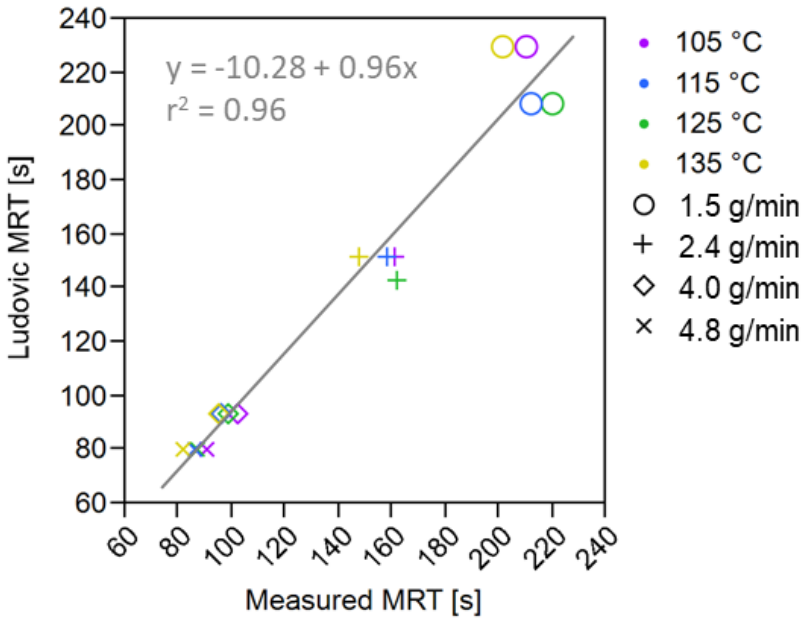


Figure 4.21 *Correlation of measured and simulated MRT.*

Based upon sufficient model validation, further analysis of the process was conducted. Among all simulated responses, namely the viscous dissipated energy from the screw, the specific mechanical energy, the total conducted energy, the total product energy, the time above 115 °C (t > 115 °C), and the integral of the temperature as a function of time, the last visually correlated the best. The integral of the *t* > 115 °C, i.e. area below the temperature vs. MRT curve but above 115 °C (Figure 4.22), was calculated for each process condition, assigned a color value and used to label the individual data points in the sum of degradants vs. residual crystallinity plot (Figure 4.23). Regardless of the processing condition applied, smaller integrals corresponded to higher levels of residual crystallinity and less degradation while larger integrals corresponded to lower levels of residual crystallinity and much more degradation.

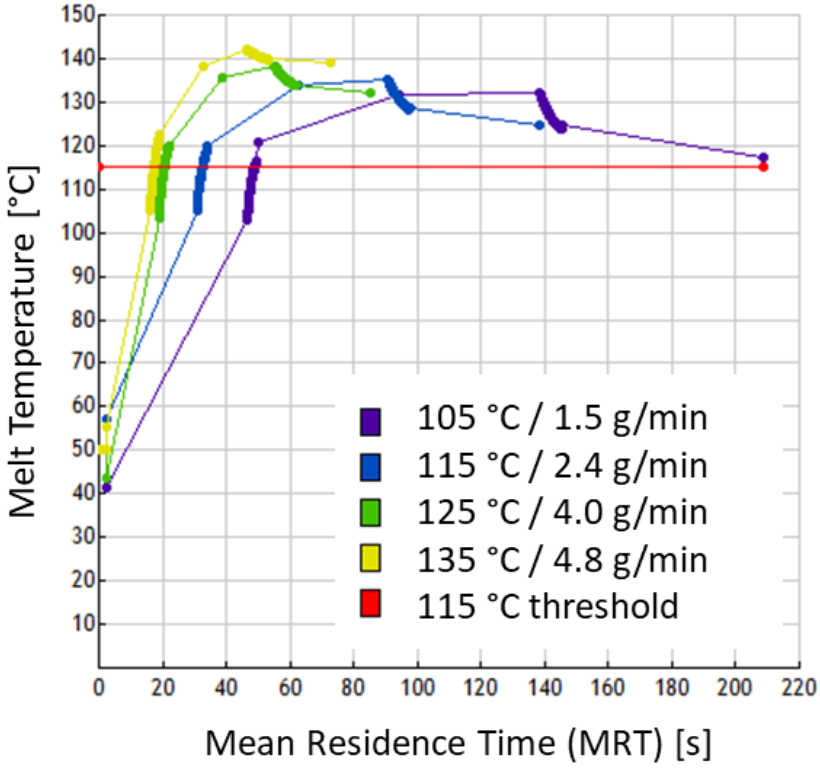


Figure 4.22 *Simulated melt temperature as a function of time for selected cases (red line indicates onset dissolution temperature of torasemide at 115 °C).*

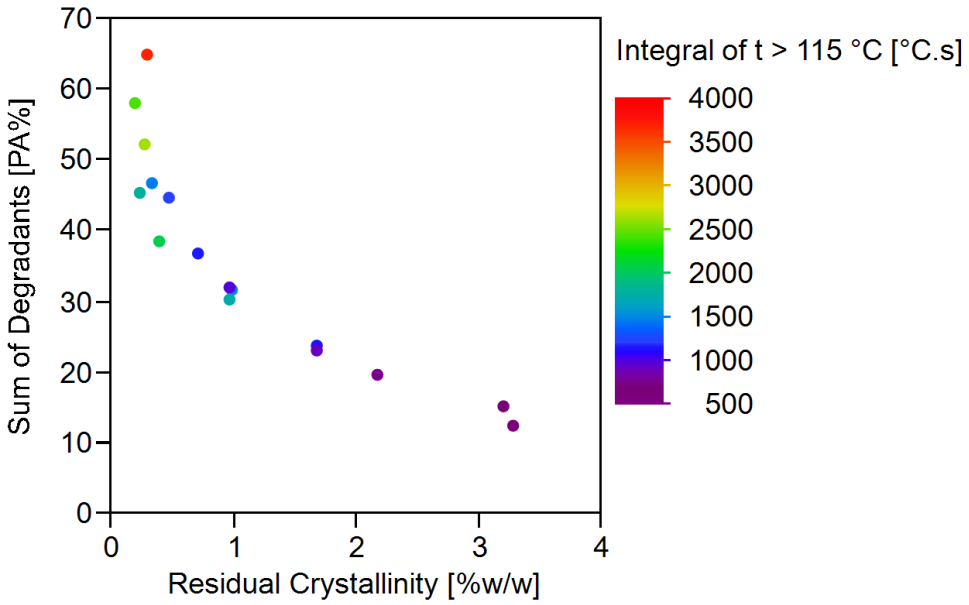


Figure 4.23 *Correlation of CQAs with integral of simulated average time the melt temperature is above 115 °C.*

## 4.5 Discussion

HME, as a process technology with a long history of use in the formation of ASDs, brings thermal and mechanical energy to the material being processed. However, determining the specific impact of the process on the final product CQAs is challenging due to the fact that most APIs are screened for thermal stability, as well as their likelihood of forming a solid solution via molecular interactions or solubility in the polymer matrix (45,102). Therefore, most products have an inherently wide process design space. Nevertheless, in a regulated industry, pharmaceutical scientists must demonstrate the impact of the process on the final product (103). These studies with torasemide and the development of a formulation with a tailored processing window indicate potential for deeper understanding of the HME process. With one system, two CQAs, degradation and residual crystallinity, can be related to process conditions such as the thermal and shear environment, as well as the residence time.

The torasemide formulation based on SOL and PEG 1500 enables the study of both degradation and residual crystallinity due to its dissolve-then-degrade mechanism. Thermal characterization of neat torasemide via weight lost during TGA alone did not explain the substantial amount of degradation observed when torasemide was extruded at main barrel and die temperatures well below its melting point (Figure 4.3). However, when combined with HPLC-MS analysis, the degradation products were revealed to be very similar in molecular weight to torasemide itself and therefore not likely to be volatile (Figure 4.4 and Appendix 10.1). In addition, torasemide underwent no degradation until melting was initiated but was nearly 100% degraded by the time it had completely melted (Figure 4.3), or 20 °C above the initial melting temperature and after only 2 minutes of additional heating. This observation indicated rapid degradation kinetics and that melt quenching attempts to prepare an amorphous form of torasemide are futile. It also indicated that torasemide is highly susceptible to degradation, specifically thermal and hydrolysis, when not stabilized by a crystalline lattice. This instability at elevated temperatures in the non-crystalline state was confirmed by controlled heating of the physical mixture and the correlation between onset dissolution temperature and by the temperature at which degradation products were detected (Figure 4.5).

Extrusion experiments (Figure 4.8, Figure 4.14 and Figure 4.15) and the high degree of correlation between degradation and residual crystallinity (Figure 4.17 and Figure 4.18) also confirmed the dissolve-then-degrade mechanism. The torasemide system, as already demonstrated in this study on a standard design twin-screw extruder with various kneading block screw configurations, showed a wide and measurable range of degradation and residual crystallinity within typical residence times for twin-screw extrusion. This rate of dissolution and degradation occurring within a more representative range of residence time in the torasemide system is an advantage over the spironolactone system studied by Vigh, *et.al*. For that system, materials were extruded in recirculation mode on a Haake® Mini-lab extruder in which processing times of up to 25 min were required to see the evolution of degradation and residual crystallinity (31). In fact, the residence time data in this TOR study, for a given screw speed and configuration, showed that the MRT was a strong function of feed rate and reached both maximum and minimum limits (Figure 4.6), which agrees with the literature (104). The MRT reached a maximum limit of about 150 s at low feed rates and a minimum limit of about 60 s at high feed rates, which can be explained by the MRT's dependency on extruder free volume and fill ratio (104). Given this dependency and the practical desire for process efficiency enabled by high throughputs, an indicator system like torasemide which shows sensitivity within practical and realistic process boundaries is advantageous. The MRT, as well as the residence time distribution, could be increased and/or adjusted by introducing more mixing or backwards conveying elements to the screw configuration, but not without causing considerable changes to other process conditions.

Measurement and quantification of the residual crystallinity in this TOR system was only feasible by XRPD. Utilization of the melting endotherm via DSC was not possible because none was detected (data not included), indicating that torasemide fully dissolved before melting. This observation has been described previously and the present work corroborates this finding (3,31).

The high degree of correlation shown between torasemide degradation and residual crystallinity over a wide range of different process parameter combinations (Figure 4.18) also indicates that a more general process condition, rather than several independent process variables, is responsible for the evolution of the CQAs. In this

case, the integral of the time > 115 °C correlated well with the relationship between residual crystallinity and sum of degradants (Figure 4.23). This approach neglects the kinetics of the reaction, namely that the API will both dissolve and degrade at a faster rate at higher temperatures. In fact, due to the dissolve-then-degrade mechanism of TOR in this system, and absent of a method to quantify the dissolution rate of TOR into the matrix, development of a coupled dissolution and degradation kinetics relationship is at present not feasible. However, the integral approach is a preliminary attempt to identify a general process characteristic which correlates with multiple CQAs which could also guide scaling. If confirmed for other systems, it could be highly efficient to design extrusion development and scale-up studies around varying this type of general process characteristic, or perhaps another type of imparted energy and residence time distribution, for example. This concept has been discussed in the literature, and the present data confirms and supports this approach towards process understanding and development (9).

The plasticizing effects of torasemide and the presence of its degradants on the overall system melt viscosity are not fully understood. Due to the high concentration of degradants and potentially yet-to-be degraded torasemide present in the extrudate samples, it was important to investigate the impact of their presence on the melt viscosity of the system. Pure un-extruded Soluplus® was compared to extruded placebo and active-containing extrudates with 5 and 10 %w/w PEG 1500 (Figure 4.11). The placebos and active formulations were extruded to ensure mixing of the matrix components as well as to ensure the presence of dissolved and degraded torasemide. These formulations were considered to be extremes in sample composition and should indicate the maximum extent that plasticization by dissolved and degraded torasemide could have on the system, if indeed there were to be an observable difference in melt viscosity. The extremes in sample composition were tested, rather than for example low, middle and high amounts of degradation, due to the time-dependent nature of rheological experiments. It is impossible to eliminate the time component from such testing because samples must be thermally equilibrated, and the frequency sweeps also last at least a few minutes. This is an important consideration for measuring the rheology of reactive systems. Although feasible temperature windows for rheological measurements differed for placebo vs.

active, the melt viscosity data and $T_g$ analysis indicate that the concentration of PEG 1500 strongly plasticized the SOL, while the presence of torasemide and its degradants had a minor impact (Figure 4.11, Figure 4.12 and Figure 4.13). Further, the glass transition temperature of SOL, approximately 70 °C (62) is similar to that of torasemide, approximately 80 °C (105). Therefore, it is expected that torasemide will modify the melt viscosity of the system to a lesser extent than PEG 1500 as the torasemide dissolves into the surrounding matrix, assuming no specific interaction, and hence the Gordon-Taylor law would apply. SOL as a matrix polymer was chosen in part for this exact reason, to avoid a reactively-plasticizing effect of the API on the matrix. Moreover, the similarity of the degradants' molecular structures to that of torasemide might also result in a non-plasticizing effect. If this is the case, the extent of reaction of torasemide dissolving and then degrading may not substantially impact the overall melt viscosity of the system. These attributes lend the system well to the study of melt viscosity as a function of plasticizer content as well as the study of shear in the extruder.

The effect of plasticization was seen as the processing space was adjusted exclusively via the PEG 1500 concentration (Figure 4.7). The minimum main barrel and die temperature for each formulation was limited by high torque due to higher material melt viscosity at lower temperatures. However, when processed at the same temperature, formulations with varying PEG 1500 concentration showed almost the same amount of degradation, indicating that in this small extruder, material temperature was controlled more by barrel heat conduction than viscous dissipation (Figure 4.8). This conduction-dominated heating was also apparent when two different screw configurations were compared (Figure 4.14) as well as when screw speed was varied, although the screw speed range was limited by equipment constraints (Figure 4.15). On the other hand, residual crystallinity levels varied both with PEG 1500 concentration and screw configuration (Figure 4.8 and Figure 4.14). Lower residual crystallinity levels at lower PEG 1500 concentration can be explained by a higher level of viscous dissipation. For screw configuration, more shear simply led to fresh surfaces of the torasemide crystals which could more readily dissolve into the surrounding matrix. However, some of these relationships, particularly the conduction dominated heating, may not be the case at larger scales when shear

rates are higher, especially at the outer diameter of the screws near the barrel wall, and as the surface area to volume ratio decreases. Lastly, the fact that a difference in residual crystallinity is observed but little difference in degradation corroborates the finding that torasemide does not immediately degrade once dissolved, as shown in Figure 4.17.

Overall, the loss in crystallinity and degradation at main barrel and die temperatures lower than the onset dissolution temperature of torasemide (115 °C) is indicative of at least some viscous dissipation, regardless of the plasticizer concentration. The presence of viscous dissipation is also supported by two observations: 1) melt temperatures at die exit were higher than the main barrel and die temperatures for all process conditions and 2) the measured barrel temperature in the last heated zone of the extruder rose above the set temperature at the lowest temperature settings. However, comparison of the melt temperature at die exit to barrel and die set temperatures does not reveal the melt's complete thermal history. On the other hand, the use of torasemide as an indicator can support process understanding and provide an indirect view of the effect of processing conditions, since the degradation is a function of the entire thermal history. In addition, the highly plasticized 15 %w/w PEG 1500 formulation offered no advantage in terms of minimizing the main barrel and die temperature to limit degradation due to the fact that processing at a temperature, for example 95 °C, below the onset dissolution temperature of torasemide (115 °C; note: not melting point) would lead to no dissolution. Therefore, before processing a new API via HME which exhibits a dissolving mechanism for ASD formation, it is useful to know its onset dissolution temperature, in addition to other material characteristics such as melt viscosity and degradation temperatures.

The combination of both thermal and hydrolytic degradation mechanisms in the torasemide system offers a unique opportunity to study the impact of moisture as well as transient plasticization via moisture on the extrusion process. The fact that the most thermal degradation was observed when the extruder was fully vented (Figure 4.16) indicates that moisture was serving as a plasticizer. Removing the moisture near to the exit of the extruder resulted in a strong increase in melt viscosity, which lead to increased viscous dissipation, increased melt temperature and therefore thermal degradation. The expected rise in torque also supported this conclusion.

These findings are in agreement with the observations regarding torque and extrudate appearance, namely the presence of bubbles, reported previously (95,106). Furthermore, the present data links these observations to important degradation CQAs by adjusting the process setup to limit hydrolysis degradation. In addition, the effect of moisture, in particular residual moisture in a finished product, is important to understand as it could result in reduced physical stability, due to the reduction in glass transition temperature and elevated molecular mobility favoring recrystallization (65,102).

In these studies, the blend moisture content within the range of 2-2.5 %w/w resulted in negligible differences in thermal and hydrolysis degradation levels. However, in preliminary studies (data not included), 10 %w/w drug load torasemide in SOL blends prepared with SOL artificially equilibrated to contain 0.5 and 6 %w/w moisture did show considerable differences. In this case, the ratio of thermal to hydrolysis degradants was reversed, similar to in the DSC study (Figure 4.5). The presence of a hydrolysis degradation mechanism is certainly a complicating aspect of this model formulation, especially in terms of normal processing. However, open-pan controlled heating DSC experiments showed that it is possible to eliminate the hydrolysis degradation pathway, if water is removed. Further, isolated feeding systems capable of drying feed material and controlling ambient moisture are available on the market. Such systems are used in the extrusion of polyethylene terephthalate and poly(lactic acid), for example, which are highly hygroscopic and hydrolysis in the melt phase can lead to a reduction in molecular weight (107–109).

## 4.6 Conclusions

In this work, a highly sensitive indicator, crystalline torasemide modification I was identified and studied. Torasemide degrades not only as a function of heat but also moisture content, and the degradation level is a function of the extent to which the indicator substance has dissolved into the surrounding matrix. This means that both degradation and residual crystallinity, two common CQAs in HME products, can be monitored with the same system.

The degradation mechanism of torasemide was described and the development of the complete model formulation as well as its performance under different processing

conditions was discussed. Torasemide in a PEG 1500-plasticized SOL matrix was found to be a highly sensitive model to show the impact of thermal and temporal process events in the HME process. Crystalline torasemide begins dissolving into the polymer matrix at approximately 115 °C and subsequently decomposes into thermal and hydrolysis degradants. Depending on the process conditions, varying amounts of residual crystalline torasemide, dissolved but un-degraded torasemide, thermal degradant and hydrolysis degradant are present. Depending on the amount of plasticizer present, the feasible processing window can be shifted, resulting in measurable quantities of residual crystallinity and degradants. Furthermore, a wide range of degradation and residual crystallinity levels are observable within typical processing ranges, especially with respect to processing times. In addition, the hydrolysis-sensitivity of torasemide was exploited to study the effectiveness of venting systems. Correlations between the CQAs and process parameters and conditions reflect the current understanding of the HME process, justifying this model system as highly relevant and informative for further studies of the HME process and optimizing process development.

Despite the unique insights the torasemide indicator system delivered, there are a few drawbacks as well. In particular, torasemide is unsuitable for correlating the degradation kinetics with simulation due to the dependency of degradation on dissolution into the matrix. If a method could be developed which accurately measures the dissolution kinetics of API in the matrix polymer, a coupled kinetic relationship could be generated. In addition, although the API and matrix polymer were selected to have similar $T_g$, there was some uncertainty in the melt viscosity characterization of the system, primarily due to its reactive nature. Due to the similarity between the time-scale of rheological experiments and reactions occurring within the formulation, it is challenging to identify the precise material properties as a function of time or extent of reaction. This aspect of HME, though, can be important because the material properties evolve as a function of the process.

However, the idea of identifying a process design space within which substantial levels of CQAs can be generated, facilitated by a sensitive indicator such as the API itself, can be applied to other systems. The telmisartan-copovidone system is one such system and is the subject of the remainder of this thesis.

# 5 Melt Viscosity Design Space Evaluation using Telmisartan as a Low-Solubility API-in-Polymer Indicator and Process Modeling

## 5.1 Introduction

Knowledge of the material properties and their relationship to processing characteristics is fundamental to successful development of broad design spaces and implementation of Quality-by-Design (QbD) (103). In particular, the formulation melt viscosity has a substantial impact on HME process performance, especially the melt temperature evolution (Figure 7.3). The rheological behavior of polymer melts and the importance of their relationship to some of the critical aspects of HME process performance was the subject of a review by Aho, et.al. (37). In addition, there has been interest in recent years to utilize rheological data to estimate or even predict starting process parameters (34–36,40,41). Further, pharmaceutical systems tend to exhibit well-described viscoelastic behavior and can be modeled. For example, the complex non-Newtonian behavior, specifically the temperature and shear-rate dependency, can be described by a number of empirical models. In this study, the Carreau-Yasuda equation (equation 2.2) with WLF temperature dependency (equation 2.3) was used to model the melt viscosity.

A schematic representation of the melt viscosity as a function of shear rate is shown in Figure 5.1. The effects of both the zero-shear rate viscosity $\eta_0$ and the power law index $n$ are depicted. The $\eta_0$ is both a function of the composition and the temperature of the material, and has been shown to correlate with $T_g$ (110). The $n$ describes the extent of shear thinning that can occur for a particular material (111,112), with a value of 1 for Newtonian behavior and a value between 0 and 1 for materials exhibiting shear thinning behavior. Both of these parameters can vary from polymer-to-polymer and from formulation-to-formulation (41,110,113). Depending on the shear rate range of the process, with range typically between 100 to 10,000 1/s (15), either or both of these parameters can influence the resulting melt viscosity. In addition to being a function of temperature and shear rate, the matrix melt viscosity can also be a function of additional components incorporated within it, such as moisture content, undissolved and dissolved API, surfactant, plasticizer, depending on relative concentrations (19,20,37,39,110,112,114–127).

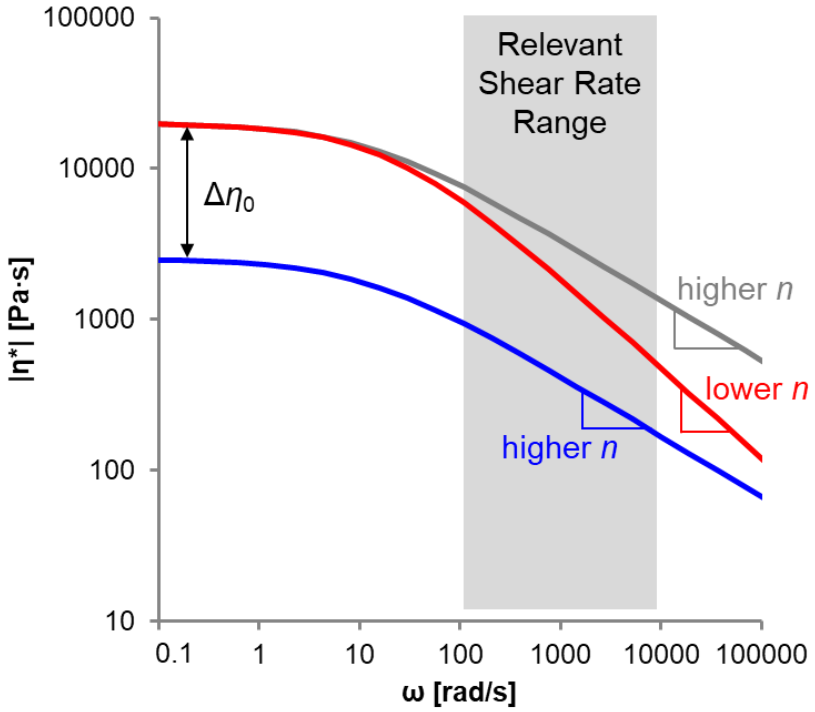


Figure 5.1 *Schematic representation of the melt viscosity as a function of shear rate, showing effect of $\eta_0$ and n.*

## 5.2 Aims of Work

The motivation for this study came from an observation during the measurement of the melt viscosity of a variety of copovidone-surfactant mixtures, data unpublished. It was observed that, in addition to a reduction in the $\eta_0$ with surfactant present, the $n$ for pure copovidone was always lower than for copovidone-surfactant mixtures. With the understanding that the power law index, $n$, relates to a material's tendency for shear thinning (15), it was hypothesized in this study that the processing design space with respect to screw speed for a formulation with surfactant present should be less sensitive to screw speed and therefore more broad. The objective for this work was to test this hypothesis in order to better understand the role of the matrix melt viscosity properties in HME while simultaneously relating the findings to a measurable CQA, namely residual crystallinity. Because of this latter objective, out of scope was the generation of a crystal-free ASD; instead a processing space was explored within which residual crystallinity of the API telmisartan could be utilized as an indicator of the HME process' ability to form an ASD.

The reasons for focusing on residual crystallinity are two-fold. First, the primary objective of solubility enhancement via the formation of an ASD is to break down the crystal lattice and transform the crystalline API into an amorphous form. Second, degradation of the API is also an important CQA, but as has been observed in a few cases, this may not occur until the API has first dissolved (31,128). In addition, any analysis of the solubility enhancement of the model API as a result of formation of an amorphous form, as an ASD or not, was also out of scope, as this has already been demonstrated (42,129,130). Along with the analysis of the rheological properties of the model system, and in order to fully interpret the findings, the CQA results were related back to the thermodynamic properties, that is, the temperature-dependent API solubility phase diagram. Lastly, process simulation was used to gain access to non-measurable processing characteristics for additional interpretation of the findings.

## 5.3 Experiment Design

Two formulations containing 10 %w/w telmisartan, 0 or 5 %w/w polysorbate 80 (Tween® 80 or TW80), and copovidone (COP) were compared in these studies. The experimental processing train is shown in Figure 5.2, more details in 7.2.2.2, with the primary difference being pre-extrusion of the TW80 / COP matrix. Process parameters for the laboratory extrusion experiment are listed in Table 5.1 and they were also used for simulations for executing and validating the corresponding Ludovic® model according to the method outlined in Figure 7.7. An expanded set of processing conditions was simulated using the validated model (Table 5.2) to further evaluate and compare the process design space as a function of formulation. To supplement the study, a simulated sensitivity analysis of the effect of the rheological parameters, $n$ and $\eta_0$ in the Carreau-Yasuda equation, on melt temperature as a function of barrel temperature and screw speed was also performed (see section 7.2.6.3 for more details).

In all simulations in this chapter, the effect of screw speed on melt temperature evolution was quantified by calculating the difference in maximum melt temperature, $\Delta T_{max}$, in this case corresponding with a position in the reverse kneading block, in red color (Figure 5.3), between high and low screw speeds.

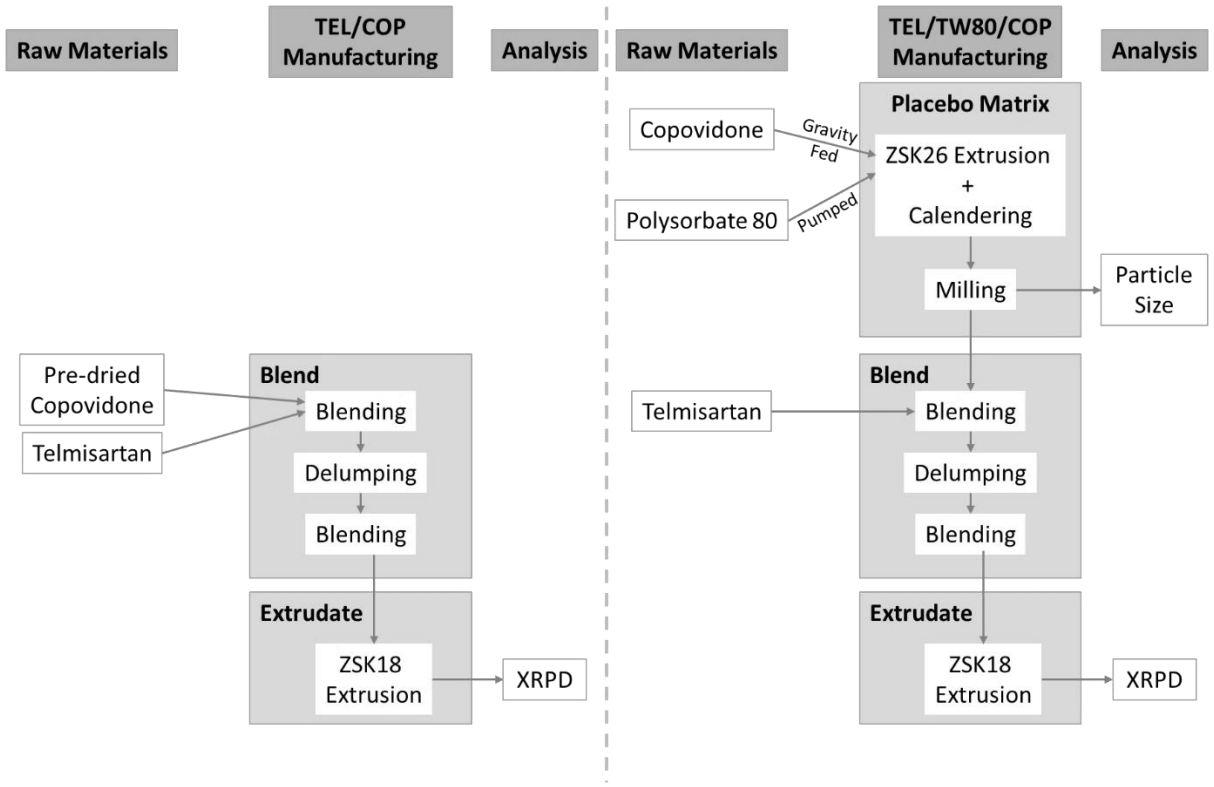


Figure 5.2 *Experimental processing train for binary formulation (left) and ternary formulation (right) and corresponding material analysis.*

Table 5.1 *Laboratory extrusion experiment design.*

| **Parameter** | **Set Points** |
|---|---|
| Barrel and Die Temperature [°C] | 170, 190, 200 |
| Screw Speed [rpm]* | 100, 400 |
| Feed Rate [kg/h]* | 0.5, 2.0 |
| Formulation | TEL / COP, TEL / TW80 / COP |
| * feed rate and screw speed were adjusted together to maintain constant fill level | |

Table 5.2 *Simulation experiment design.*

| **Parameter** | **Set Points** |
|---|---|
| Barrel Temperature* [°C] | 177, 187, 197, 207 |
| Die Temperature [°C]** | 170, 180, 190, 200 |
| Screw Speed [rpm] | 100, 200, 300, 400 |
| Feed Rate [kg/h]*** | 0.5, 1.0, 1.5, 2.0 |
| Formulation | TEL/COP, TEL/TW80/COP |
| * Barrel temperature near the screws was actually ~ 7 °C above set temperature, and so this higher temperature was used as the barrel temperature for more accurate simulation<br>** Barrel temperature and die temperature were varied together<br>*** Feed rate and screw speed were varied together to maintain constant fill level | |

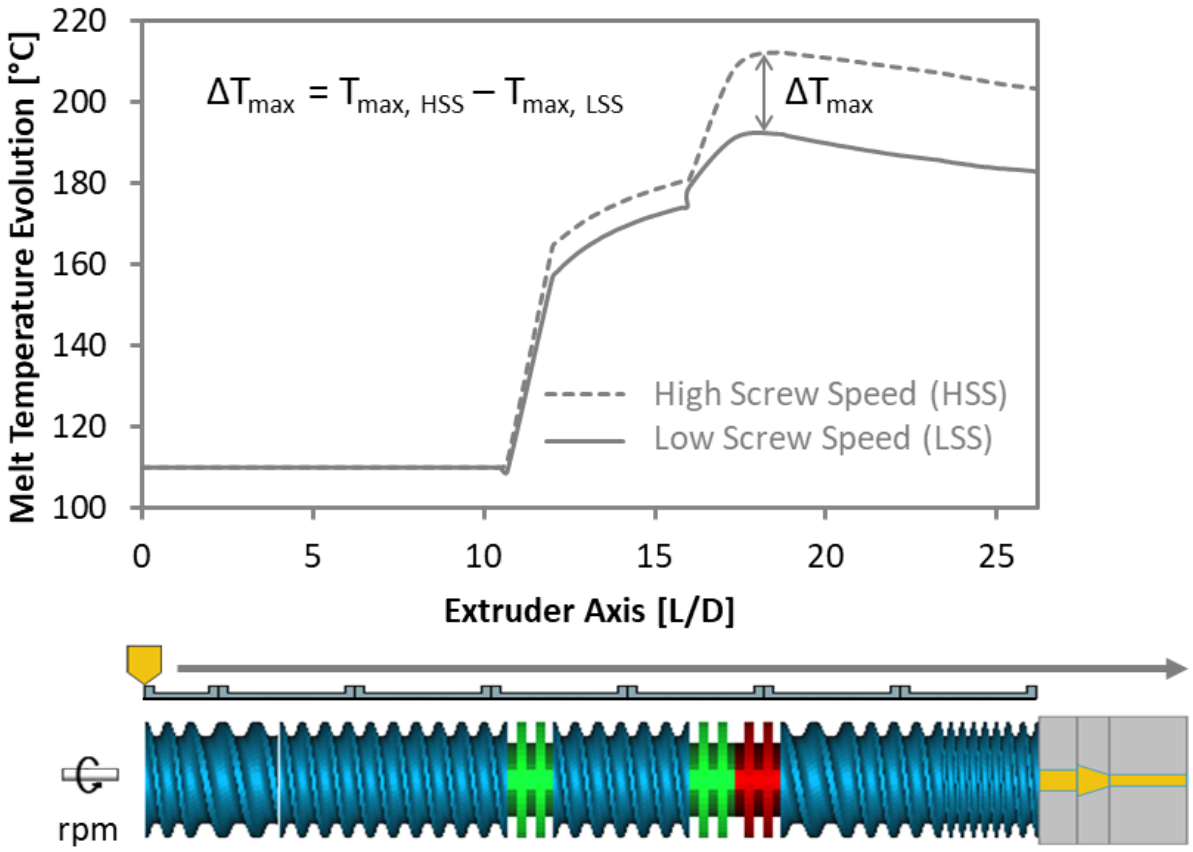


Figure 5.3 *Schematic representation of the melt temperature evolution along the screw profile from simulated data and calculation of* $\Delta T_{max}$*. Note: die channel (light orange) is not to scale in relation to the screw diameter.*

## 5.4 Results

### 5.4.1 Selection of Model System – Material Properties

In order to test the hypothesis that the processing design space with respect to screw speed should be broader with plasticizing surfactant present, an appropriate model system needed to be identified. Such a system would require unique material properties for both the model API and surfactant with plasticizing behavior. To focus on the plasticization induced by the surfactant, the API should also not substantially alter the $T_g$ of the matrix polymer. In addition, the API should not be highly soluble in the polymer matrix, in order to monitor residual crystallinity, and should be thermally stable as degradation could also potentially alter the viscosity of the system. The surfactant should also be thermally stable and non-volatile, not alter the API's solubility in the overall matrix, and be miscible at the selected concentration. Non-scientific considerations were also the potency of the API so that special handling or equipment containment were not required, as well as the API's affordability and sourceability. After screening of various APIs and surfactants, telmisartan (TEL) was selected as model API, polysorbate 80 (TW80) as model surfactant/plasticizer and copovidone (COP) as matrix polymer as these substances fulfilled the above-mentioned requirements.

#### 5.4.1.1 Thermal Properties and Phase Diagram

TEL is thermally stable and exhibited moderate solubility in COP and COP / TW80 matrices, independent of matrix composition up to 5 %w/w TW80. TEL melts at 269 °C, begins to thermally decompose at ~280 °C (data not shown) and has an amorphous $T_g$ of 129 °C. According to the API solubility phase diagram, the solubility temperature, $T_s$, of TEL in COP is unchanged when 5 %w/w TW80 is present (Figure 5.4). Experimentally determined $T_s$ at 20 %w/w TEL in matrices was used to construct the solubility curve according to the Kyerematen model and method (102). Additional $T_s$ data at 5 and 10 %w/w TEL were generated to independently confirm the predicted solubility by the model. Based on these results, 5 %w/w TEL should be thermodynamically soluble at 197 °C, 8 %w/w at 203 °C, and 10 %w/w at 213 °C. TEL thermal stability in COP was confirmed by HPLC analysis of preliminary ASDs extruded at temperatures up to 230 °C (see Appendix 10.2). In addition, DSC

analysis of the extrudates with residual crystallinity shows the onset of the dissolution process to initiate between 170-180 °C, indicated by the dissolution endotherm, data not shown.

TEL had the tendency to anti-plasticize the COP or TW80 / COP matrix, but at the 10 %w/w concentration used, the effect is minimal or even negligible. The matrix polymer, COP, had a dry $T_g$ of 107 °C while the $T_g$ of TEL was 129 °C. The measured $T_g$ of a 20 %w/w of TEL in COP was 108.5 °C. TEL exhibited a slight anti-plasticizing effect on COP, however, at 10 %w/w drug load, this effect was negligible as the $T_g$ (107.8 °C) is close to that of COP. The $T_g$ of the ternary system 20 %w/w TEL / 5 %w/w TW80 / COP was 95 °C, slightly lower than the binary mixture, indicating a plasticizing effect of the TW80. The $T_g$ of the ternary system with 10 %w/w TEL / 5 %w/w TW80 / COP was 92 °C.

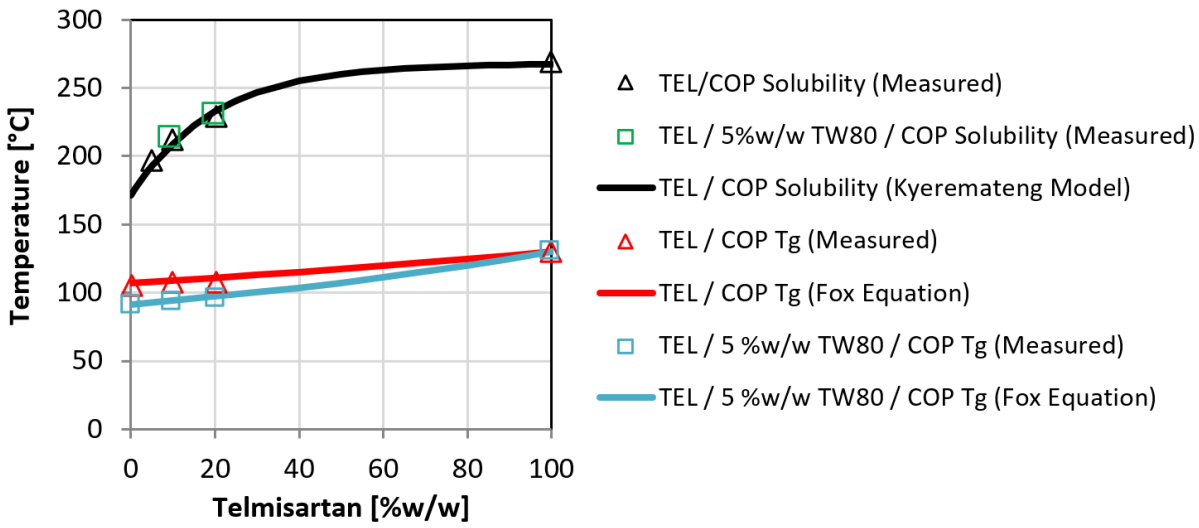


Figure 5.4. *Phase diagram of telmisartan in copovidone with and without TW80. The black line is the solubility curve and indicates the temperature at which a given concentration of TEL is soluble in the polymer matrix. The red and blue lines indicate the glass transition temperature as a function of the concentration of TEL in a COP matrix or a 5 %w/w TW80 / COP matrix, respectively.*

### 5.4.1.2 Blend Powder Properties

The blends were designed to be as identical as possible in terms of powder properties so as to provide a similar environment into which the TEL could incorporate and dissolve, albeit with different melt rheological properties. The

properties of the matrix considered were the bulk density, the particle size distribution (PSD) and the moisture content and were kept constant (Table 5.3).

Table 5.3 *Blend Powder Properties.*

| **Formulation** | **Blend Bulk Density [g/mL]** | **Matrix PSD** | | | **Blend Loss-on-Drying [%]** |
|---|---|---|---|---|---|
| | | **$d_{10}$ [µm]** | **$d_{50}$ [µm]** | **$d_{90}$ [µm]** | |
| 10 %w/w TEL / COP | 0.36 | 24.0 ± 0.4 | 79.3 ± 1.2 | 184 ± 1 | 0.86 |
| 10 %w/w TEL / 5 %w/w TW80 / COP | 0.42 | 22.1 ± 0.3 | 81.3 ± 1.1 | 181 ± 0 | 1.26 |

5.4.1.3 Rheological Properties

*Model Formulations*

The melt viscosity as a function of angular frequency at a reference temperature of 170 °C of the two formulations, 10 %w/w TEL / COP and 10 %w/w TEL / 5 %w/w TW80 / COP, shows the plasticizing effect of the TW80 in the TEL / TW80 / COP formulation (Figure 5.5a), described and captured by the difference in $\eta_0$, the zero-shear rate viscosity (Table 5.4). For comparison, the melt viscosity profiles of pure COP and a plasticizer / COP mixture (3 %w/w TEC / COP) are included. The $T_g$ of the 3 %w/w TEC / COP system was measured to be 95 °C, and this value was used as an input value into the melt viscosity prediction model (110). The plasticization effect by the surfactant TW80 was similar to that of a common plasticizer, TEC. The melt viscosity for both TEL formulations is also a function of temperature (Figure 5.5b). The expected reduction in melt viscosity as temperature increases is seen for three reference temperatures, 150 °C, 160 °C, and 170 °C.

Another potentially interesting behavior is the slight difference in shear-thinning tendency, seen as the slope in the power law region of the melt viscosity profile and described by the power law index, $n$. The power law index is higher for the formulation with TW80 (Table 5.4), potentially indicating that this formulation is less susceptible to shear thinning than the TEL / COP binary mixture. This observation and its effect on melt temperature evolution is further explored via a sensitivity analysis simulation study (see next sub-section). Other differences include the variation of the Yasuda constant, $a$, and the characteristic time, $\lambda$, which is related to

the relaxation behavior of the material over time. The observed range of the Yasuda constant results in a minor impact on the melt viscosity profile, namely the curvature of the transition region. In addition, within the shear rate range expected in the extruder, between 10 to 1000 1/s or rad/s and even up to 10,000 1/s at high screw speeds (15), depending on the screw clearance, the difference in $\lambda$ can also be neglected because the processing region is almost fully in the power law region of the melt viscosity profile.

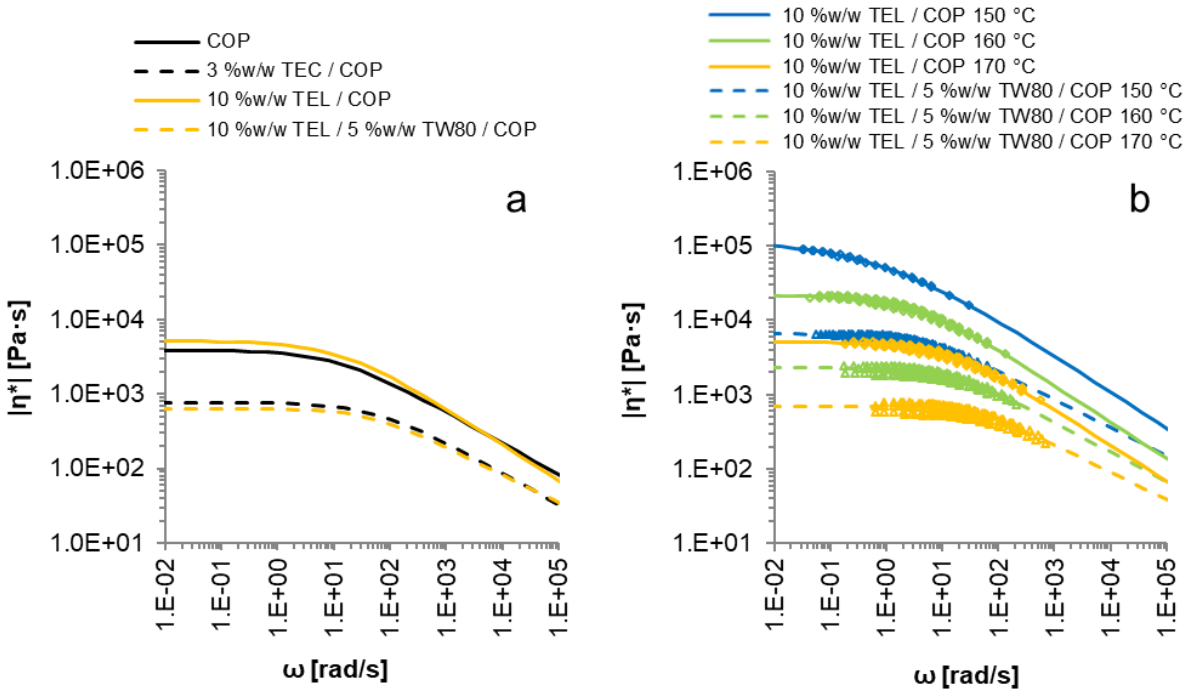


Figure 5.5 *Plotted master curves for various formulations a) at 170 °C and b) as a function of temperature. Master curves in a) are modeled data.*

Table 5.4 *Carreau-Yasuda and WLF equation parameters for master curves at 170 °C reference temperature.*

| Formulation | 10 %w/w TEL / 5 %w/w TW80 / COP | 10 %w/w TEL / COP | COP | 3 %w/w TEC / COP |
|---|---|---|---|---|
| $T_0$ [°C] | 170 | 170 | 170 | 170 |
| $\lambda$ [s] | 0.024 | 0.071 | 0.085 | 0.017 |
| $n$ | 0.630 | 0.514 | 0.577 | 0.577 |
| $\eta_0$ [Pa·s] | 629.3 | 5134 | 3843 | 771.7 |
| $\eta_\infty$ [Pa·s] | 0 | 0 | 0 | 0 |
| $a$ | 0.965 | 0.708 | 0.757 | 0.757 |
| $C_1$ | 6.2 | 10.74 | 8.86 | 8.86 |
| $C_2$ [°C] | 146 | 190.2 | 167.6 | 167.6 |

*Ludovic® Sensitivity Analysis of Shear Thinning, n, and Plasticization, $\eta_0$, on Melt Temperature Evolution*

Sensitivity analysis of the rheological properties showed that the zero-shear rate viscosity, $\eta_0$, has a more pronounced effect on the melt temperature evolution than the power law index, *n*, within the ranges of barrel temperature and screw speed tested (Figure 5.6). At low barrel temperature, screw speed strongly impacted the melt temperature (higher $\Delta T_{max}$ values). At increasingly higher barrel temperatures, screw speed had a diminishing impact (lower $\Delta T_{max}$ values). Regardless of the processing condition, *n* impacted the melt temperature less than $\eta_0$ did, but the *n* or $\eta_0$ value corresponding to higher intrinsic melt viscosity led to higher melt temperature. In other words, high *n* and $\eta_0$ (blue) resulted in higher melt temperature while low *n* and $\eta_0$ (red) resulted in lower melt temperature.

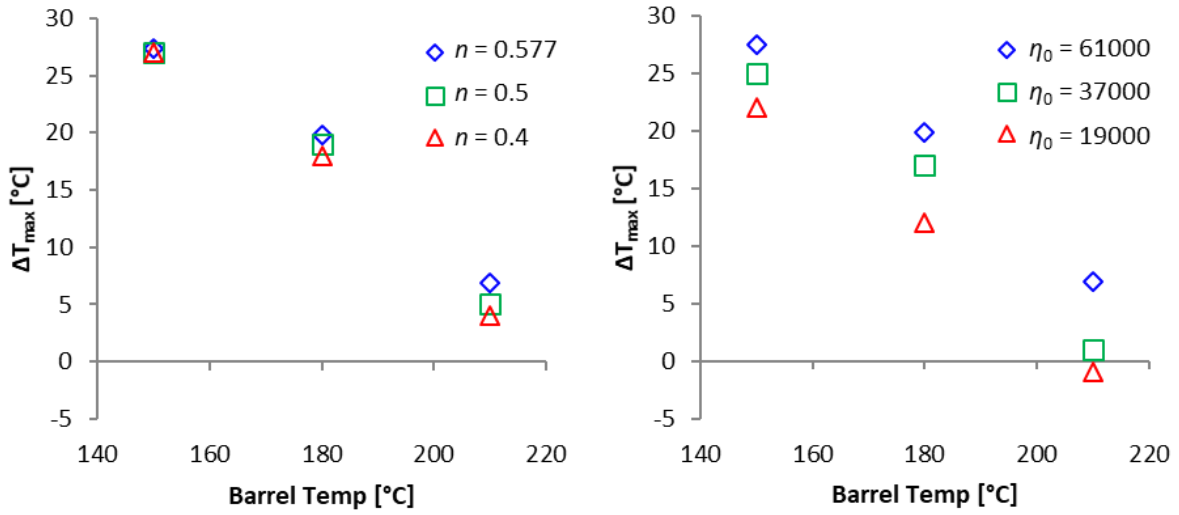


Figure 5.6 *Extent of melt temperature rise as a function of screw speed for different barrel temperatures and values of n and $\eta_0$. See* Figure 5.3 *for explanation of* $\Delta T_{max}$ *and relationship to screw speed.*

### 5.4.2 Experimental Extrusion – Produce Data to Build and Validate Ludovic® Model

A reduced laboratory extrusion experiment was conducted to investigate and quantify the relationship between processing parameters, formulation matrix composition and CQA, in this case residual crystallinity. All processing conditions yielded extrudates with measurable residual crystallinity. The amount of residual crystallinity depended

on the matrix composition and on the processing conditions (Figure 5.7). As expected, less residual crystallinity was observed with both higher temperatures and higher screw speeds. However, despite the same processing conditions being applied to both formulations, for all conditions, more residual crystallinity was observed in the formulations containing TW80. Die exit melt temperature increased with increasing barrel temperature and increasing screw speed, and was generally higher for the un-plasticized formulation, especially at lower barrel temperatures.

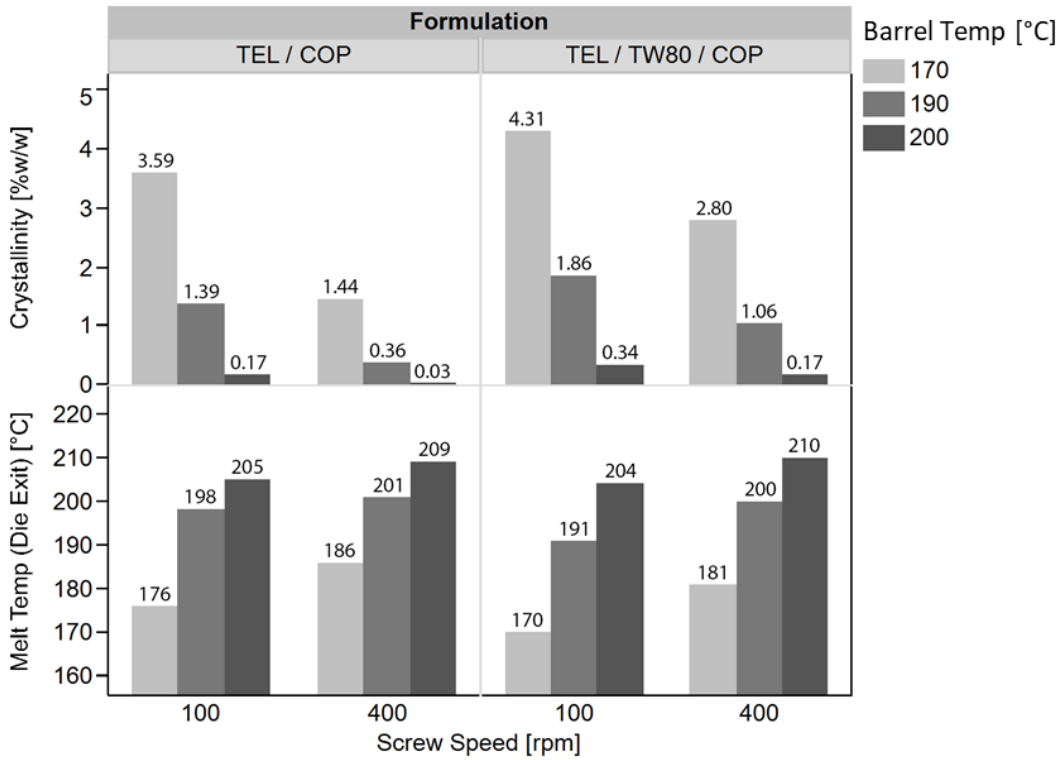


Figure 5.7 *Residual crystallinity (in %w/w of formulation) in extrudate product and measured die-exit melt temperature.*

When all process conditions were analyzed by formulation, the residual crystallinity correlated strongly with the measured die-exit melt temperature (Figure 5.8a). The linear regression equations for the two formulations were similar. The residual crystallinity varied more as a function of screw speed at lower barrel temperatures than at higher barrel temperatures. When the Ludovic® model was applied to simulate the laboratory extrusion experiments, utilizing the measured material property inputs given in Table 5.4 and Table 5.5, the simulated and measured die-exit melt temperatures were found to be strongly correlated across all formulations

and process conditions (Figure 5.8b), with regression equation given in the figure. Thus, the model was validated, showing that the 1D Ludovic® simulation software is capable of determining experimental extrusion process characteristics.

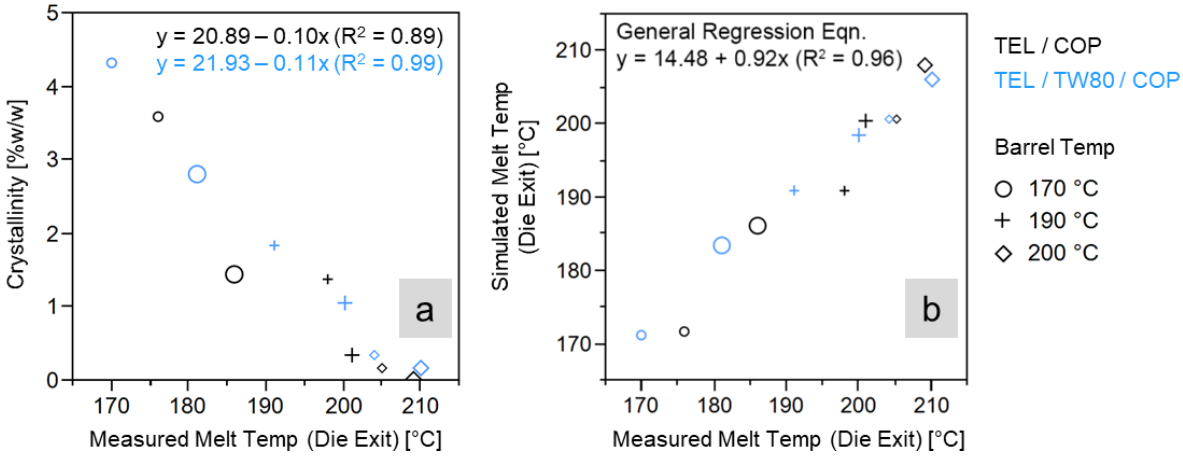


Figure 5.8 *Correlation of a) residual crystallinity and measured die-exit melt temperature and b) simulated and measured die-exit melt temperatures. Small symbols are for screw speeds of 100 rpm while large symbols are for 400 rpm.*

Table 5.5 *Material property inputs for simulation.*

| **Formulation** | **TEL / TW80 / COP** | **TEL / COP** |
|---|---|---|
| Solid $c_p$ [J/kg/°C] | 1000 | 1000 |
| Solid Density [kg/m$^3$] | 400 | 400 |
| Solid Thermal Conductivity [W/m·K] | 0.19 | 0.19 |
| Liquid $c_p$* [J/kg/°C] | f(T), at 170 °C = 1763 | f(T), at 170 °C = 1822 |
| Liquid Density [kg/m$^3$] | 1150 | 1150 |
| Liquid Thermal Conductivity [W/m·K] | 0.19 | 0.19 |
| $T_g$ as Melting Temperature [°C] | 92 | 110 |
| Melting Enthalpy [kJ/kg] | 0 | 0 |
| * In Ludovic® software, the liquid $c_p$ was entered as a function of temperature, data not shown | | |

### 5.4.3 Deeper Insight via Process Modeling

Based on good correlation between the residual crystallinity and measured die-exit melt temperature and based on the good correlation between measured and

simulated die-exit melt temperatures, the validated Ludovic® model was used for further process analysis. In addition, the model was applied to conduct a simulated full-factorial experiment in order to fill in gaps in laboratory experimental data and confirm observations about the design space.

#### 5.4.3.1 Impact of Matrix Melt Viscosity on Maximum Melt Temperature

Process modeling enabled analysis of the melt temperature inside the extruder, in particular the maximum melt temperature, which is a difficult quantity to measure via typical temperature sensing methods (Figure 5.3). As was seen for the experimental melt temperature at die exit, the simulated maximum melt temperature increased with both increasing screw speed and increasing barrel temperature (Figure 5.9a). At a screw speed of 400 rpm and barrel temperature of 200 °C, both formulations reached simulated max temperatures greater than the solubility temperature of 10 %w/w TEL in the matrix, 213 °C. It was at these same processing conditions that almost no residual crystallinity was observed (Figure 5.7 and symbols marked with an asterisk, *, Figure 5.9a). Little residual crystallinity, namely less than 0.5 %w/w, was also observed for the TEL / COP formulation processed at barrel temperature of 190 °C and screw speed of 400 rpm as well as for both formulations processed at barrel temperature of 200 °C but only 100 rpm screw speed. For the two formulations extruded at 200 °C and 100 rpm, the maximum melt temperature was slightly below the API solubility temperature. In comparison to the melt temperature measured at die exit (Figure 5.7), a greater distinction can be made between the two formulations in the maximum melt temperature in the extruder. Namely, for a given processing condition, a higher maximum melt temperature was always observed for the un-plasticized TEL / COP formulation. Furthermore, as was seen with the melt viscosity parameter sensitivity analysis, the higher intrinsic melt viscosity formulation, TEL / COP, reached higher melt temperatures within the same range of screw speeds, independent of barrel temperature setting (Figure 5.9b). In addition, the screw speed sensitivity $\Delta T_{max}$ was decreased for both formulations as barrel temperature was increased, corroborating the observations that residual crystallinity was less sensitive to changes in screw speed at higher temperatures.

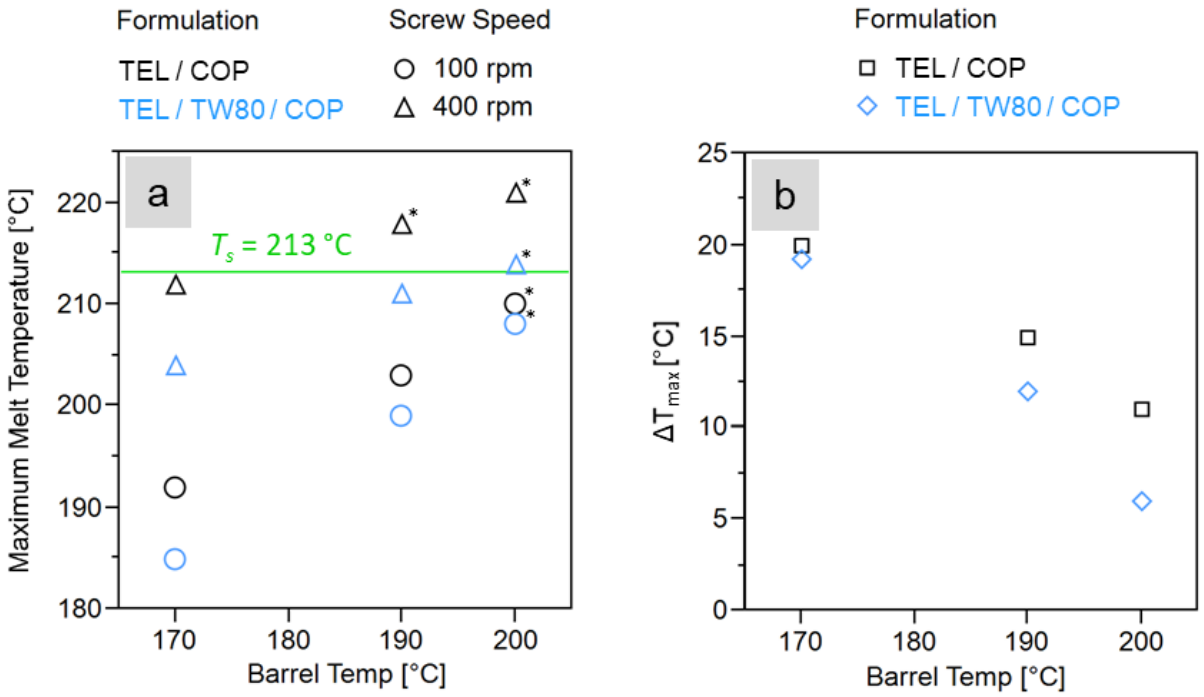


Figure 5.9 *Simulated maximum melt temperature (a) and extent of melt temperature rise as a function of screw speed* $\Delta T_{max}$ *(b) for different barrel temperatures and formulations. The API solubility temperature,* $T_s$*, for 10 %w/w TEL in the matrices is designated in (a) and extrudates with less than 0.5 %w/w residual crystallinity are indicated with an asterisk (*).*

### 5.4.3.2 Simulated Full-Factorial Experiment and Impact of Rheology on Design Space

The findings from the reduced laboratory extrusion experiment were supplemented by a full-factorial simulated experiment. The melt temperature evolution, in particular the range of maximum melt temperature as a function of screw speed, differs more for the TEL / COP formulation than for the TEL / TW80 / COP formulation (Figure 5.10). The range of maximum melt temperature is broader for lower barrel temperatures than higher barrel temperatures. In addition, the melt temperature approaches the set barrel temperature at higher barrel temperatures, especially at lower screw speeds and for the TEL / TW80 / COP formulation, e.g. at 200 °C.

According to the approach described in Figure 5.3, these effects were further quantified by calculating the difference in maximum melt temperature between high and low screw speeds, $\Delta T_{max}$ (Figure 5.11). As barrel temperature is increased, the

screw speed had less and less of an impact on temperature rise (Figure 5.11), as also observed in the rheology sensitivity analysis study (Figure 5.6) and for the simulations of the reduced experimental data set (Figure 5.9b). Especially in comparison to the experimental data set, the results are the same except for the addition of data simulated for barrel temperatures of 180 °C. In this representation, it is clearly seen that the melt temperature rise is more sensitive to screw speed for the TEL / COP formulation than for the TEL / TW80 / COP formulation.

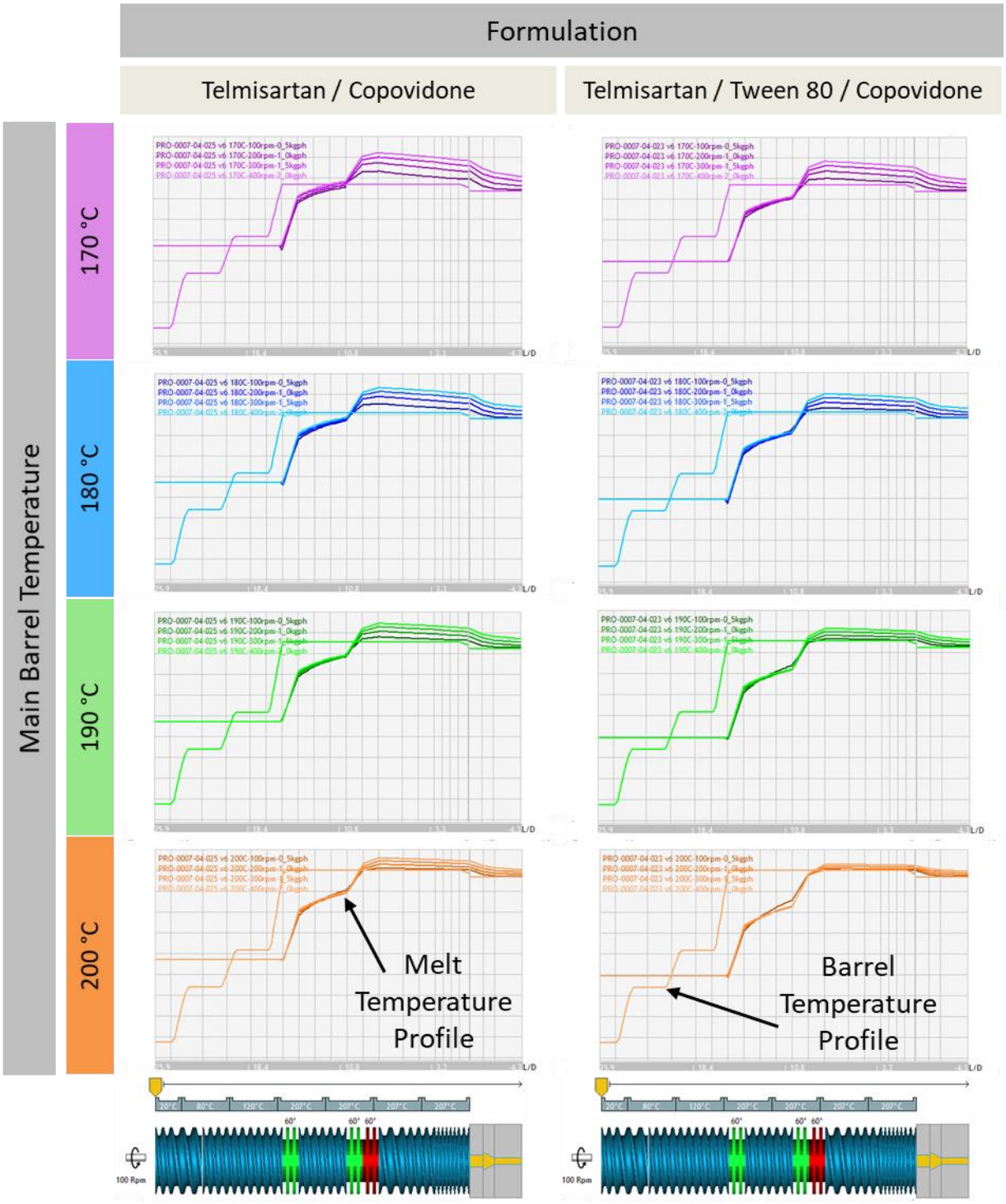


Figure 5.10. *Evolution of simulated melt temperature vs. extruder length as a function of barrel set temperature (color), screw speed (shade, low is darker shade) and formulation (column). Screw profile and die shown below graphs, die not to scale. The step-wise increasing line in each graph depicts barrel set temperature for comparison with the evolved melt temperatures. The y-axis in each plot ranges from 0 to 230 °C.*

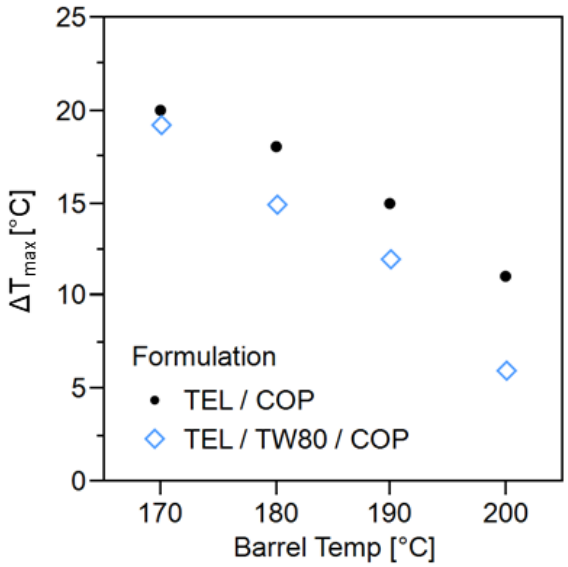


Figure 5.11. *Extent of melt temperature rise as a function of screw speed,* $\Delta T_{max}$*, for different barrel temperatures and formulation.*

In addition to the $\Delta T_{max}$ evaluation, contour plots of maximum and die-exit melt temperatures confirm a broader design space with less dependency on screw speed for the TEL / TW80 / COP formulation (Figure 5.12). For the maximum melt temperature, the contours are close together at low barrel temps and screw speeds, indicating a high influence of these two variables in these ranges, irrespective of the formulation. The contours are more vertical for the TEL / COP formulation, indicating higher sensitivity to screw speed than for the TEL / TW80 / COP formulation. Overall, within this design space, the maximum melt temperature for the TEL / COP formulation is higher than for the TEL / TW80 / COP formulation. On the other hand, the die-exit melt temperature contours within the same range of barrel temperatures and screw speeds is slightly higher for the TEL / COP formulation and the contours are again slightly more vertical for the TEL / COP formulation. In this case, the contours are evenly spaced throughout the design space studied.

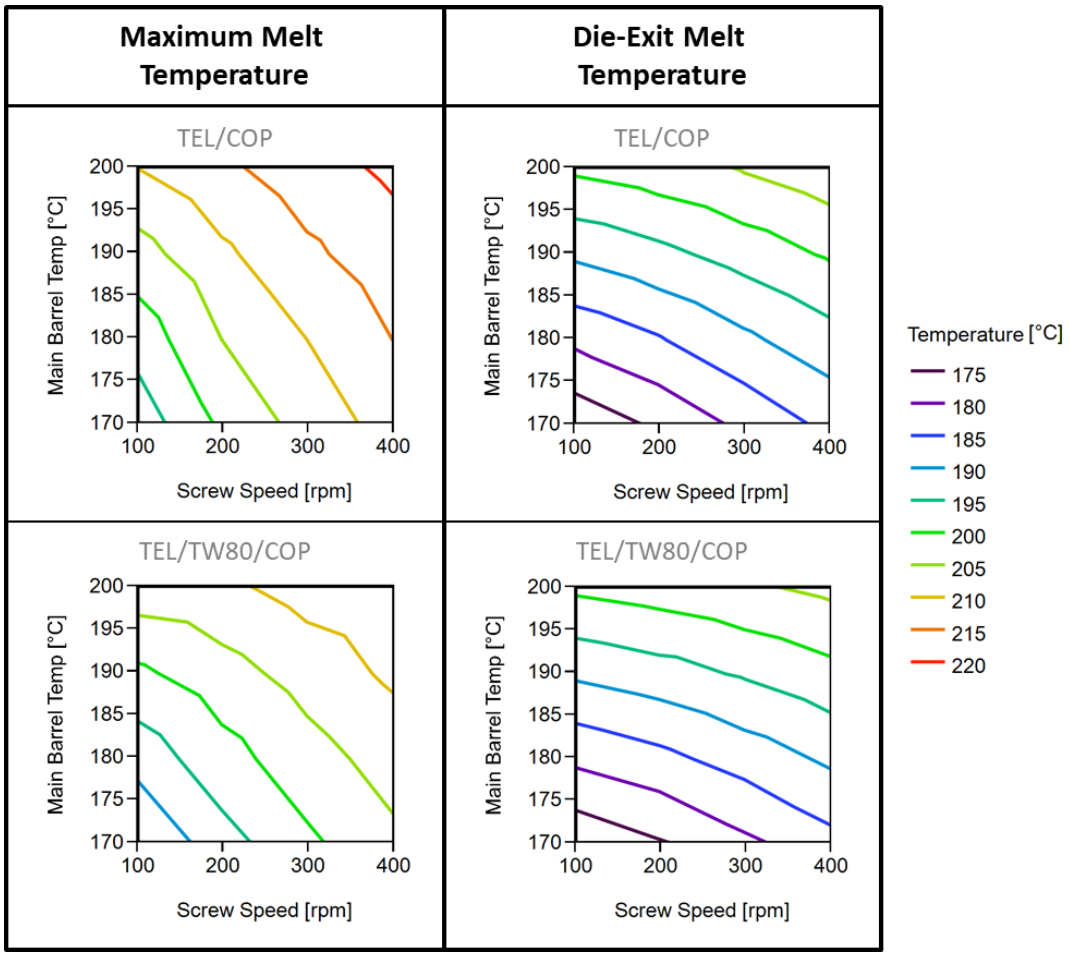


Figure 5.12. *Contour plots for maximum and die-exit melt temperatures from simulated full-factorial experiment.*

### 5.4.3.3 Impact of Matrix Melt Viscosity on Extruder and Process Energetics

The global process energetics, specifically the dissipated, mechanical, conducted and product energies, are strong functions of the process conditions as well as formulation matrix melt viscosity. The temperature rise, as a function of formulation and screw speed, is in part related to the total dissipated energy in the screw, a quantity accessible by simulation (Figure 5.13). Higher values were computed for the un-plasticized formulation TEL / COP than for the TEL / TW80 / COP formulation for all processing conditions, although the difference decreases with increasing barrel temperature. For both formulations, higher screw speed generally led to higher dissipated energy, except for at the lowest temperature; here, the lower screw speed yielded a higher dissipated energy. Related to dissipated energy, slightly higher levels of shear stress were also computed in the second mixing zone for the un-

plasticized formulation (data not shown). The specific mechanical energy showed the same relationships to the processing conditions and formulations as the total dissipated energy and was generally higher for the TEL / COP formulation.

For both formulations, the total conducted energy became more positive with increasing barrel temperatures. For a given processing condition, the total conducted energy was much lower for the TEL / COP formulation than for the TEL / TW80 / COP formulation. At roughly 200 °C barrel temperature, the total conducted energy for the TEL / COP formulation approached 0 kJ/kg, indicated by a darker gray horizontal line in the third row of plots, while the total conducted energy approached 0 kJ/kg at lower barrel temperature for the TEL / TW80 / COP formulation (180 to 190 °C). Negative values for the total conducted energy indicate barrel cooling will be required while positive values indicate that the barrels will need to heat the product. The total conducted energy for the TEL / COP formulation also showed a temperature-dependent effect for screw speed, as indicated by the cross-over point around 180 °C in the plots for total dissipated energy, specific mechanical energy and again total conducted energy. Within the temperature range studied, the TEL / TW80 / COP formulation showed a straightforward relationship with screw speed: higher screw speeds lead to more negative values of total conducted energy.

The total product energy (TPE), a global value equivalent to the sum of the specific mechanical energy and the total conducted energy, was nearly the same for both formulations, increasing with increasing barrel temperature and increasing screw speed ($4^{th}$ row of plots in Figure 5.13). When the two formulations were considered independently, the total product energy correlated well with the residual crystallinity, with both regression equations yielding high $r^2$ values (0.89 for un-plasticized and 0.98 for plasticized) (Figure 5.14). The residual crystallinity decreased as more energy was applied. However, for the same level of TPE, the amount of residual crystallinity was slightly higher for the TEL / TW80 / COP formulation.

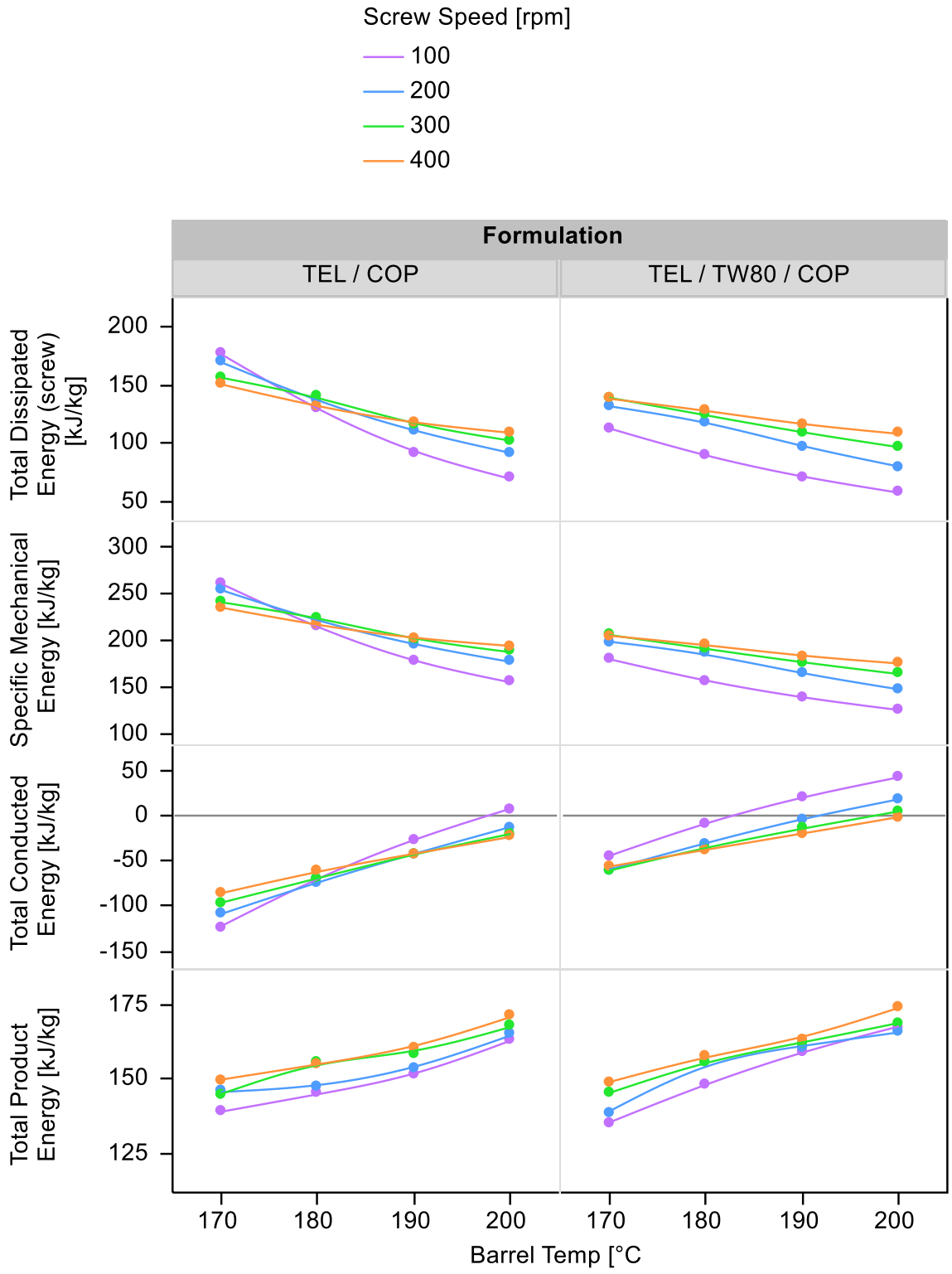


Figure 5.13 *Global process energetics as a function of processing condition and formulation. Note: Barrel Temp is the set temperature.*

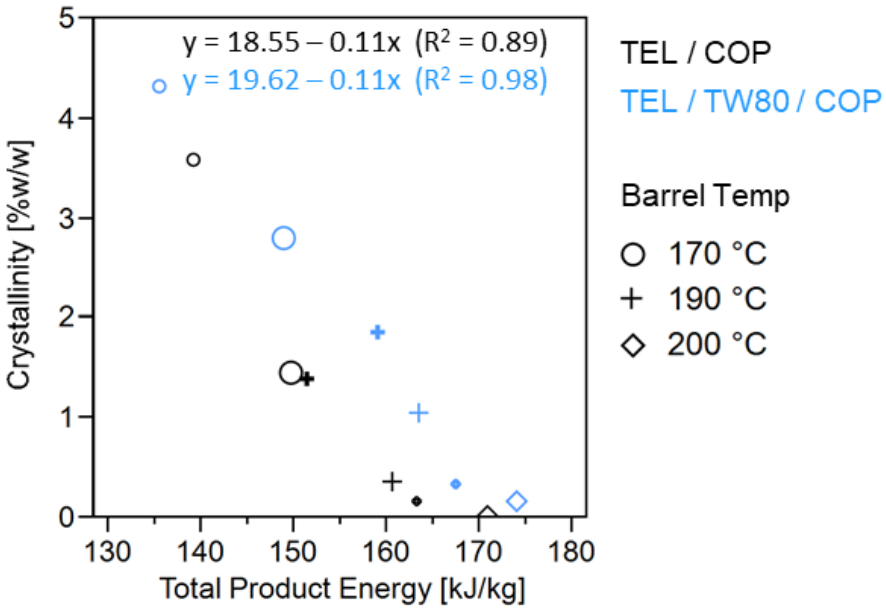


Figure 5.14 *Relationship between residual crystallinity and total product energy as a function of formulation and process conditions. Note: small symbols are low screw speed while large symbols are high screw speed.*

## 5.5 Discussion

Telmisartan in copovidone is an informative model system for studying the relationship between formulation material properties and HME processing characteristics for ASD formation. Selection of the process parameters was informed by the API-polymer matrix solubility phase diagram so as to achieve a measurable level of the CQA, residual crystallinity. By processing near to or below TEL's solubility temperature at 10 %w/w, and far below its melting temperature of 269 °C, TEL dissolves incompletely into the polymer matrix. In addition, it is thermo-stable and exhibits non-plasticizing behavior at 10 %w/w drug loading in COP. With such material properties, selected by design, the effect of the matrix melt viscosity on processing design space could be studied, with and without the addition of a plasticizing surfactant, TW80.

Several steps were carried out to ensure comparability of the two formulations. First, the TW80 / COP matrix was pre-extruded in order to isolate the study of the dissolution of TEL into the already homogeneously plasticized matrix and to facilitate comparison with the COP matrix formulation. Second, as a result of the prior processing of the TW80 / COP matrix, the material was dehydrated, eliminating the

plasticizing effect of moisture. Correspondingly, the COP raw material was also dehydrated. By dehydrating both matrices, the melt rheological behavior was simplified and made to be more similar with the material measured with the rheometer; in fact, rheological studies are most reliable when performed in the absence of water, especially in the temperature regions of interest here. Third, the pre-extruded TW80 / COP matrix was milled to similar particle size distribution as the raw COP material with the intention of maintaining blend bulk density and therefore fill volume in the extruder constant. Further studies are needed to determine if these precautions were absolutely necessary.

One of the goals of this study was to evaluate the significance of melt rheology, in particular the plasticization and apparent shear thinning behavior of a surfactant, on ASD formation. The formation of the ASD, namely the dissolution of the API, as measured by residual crystallinity, is a function of the independent process parameters, e.g. barrel temperature, screw speed, feed rate, as well as the resultant process performance, e.g. product temperature, melt viscosity, shear rate. However, the process performance is in turn dependent on the properties of the material being processed, e.g. matrix melt viscosity. These inter-dependent relationships were simultaneously considered using process simulation.

First, simulation was used to investigate the sensitivity of the melt temperature rise as a function of screw speed and barrel temperature for materials with different rheological characteristics, $\eta_0$ and $n$. As mentioned in the introduction to this chapter, these parameters can vary for different material compositions and, depending on the shear rate range of the process, either or both of these parameters can influence the resulting melt viscosity. However, the results indicated that the overall plasticization described by $\eta_0$ is the dominating factor (Figure 5.6). Within the shear rate range explored, the melt viscosity profile essentially shifts vertically along the melt viscosity axis, with $\eta_0$ exhibiting a greater shift than $n$ (Figure 5.1, Figure 5.5). While intrinsic shear thinning behavior described by $n$ does contribute to melt viscosity reduction, decreased viscous dissipation and therefore lower heat rise, it was less substantial in this case. However, HME process simulations can and should be used to evaluate the relative significance of the melt viscosity parameters in other systems as well. This example also highlights the applicability of the model developed by the working

group of K.G. Wagner to estimate melt viscosity by a straightforward $T_g$ measurement (80,81,110), but also that further work is needed to extend the model for matrices which exhibit different non-Newtonian behavior.

Second, simulation was used to retrospectively gain insight into the experimental results. After validating the model by obtaining correlation between the measured and simulated die-exit melt temperatures, the additional results that only simulation can produce, maximum melt temperature and the process energetics, were correlated with the CQA, residual crystallinity. In this way, process conditions and material properties were again simultaneously taken into consideration. Through analysis of the $\Delta T_{max}$ and contour diagrams, melt temperature rise as a function of formulation melt viscosity, barrel temperature and screw speed showed that the design space as a function of screw speed is broader for the plasticized formulation. In this study, this behavior was shown with TW80 as a surfactant in COP, and in a related publication, the same behavior with a sorbitan monolaurate (Span® 20)-COP system was observed (119). Further, the narrow spacing of the maximum melt temperature contours in the low temperature and low screw speed region (Figure 5.12) corroborates the finding that the residual crystallinity is a strong function of screw speed at low temperatures (Figure 5.8a). Additional analysis of the die-exit melt temperature contour diagrams, along with the measured melt temperature (Figure 5.7 & Figure 5.8), highlights the insufficiency of correlating the absolute residual crystallinity with die-exit melt temperature. The total product energy, which along with the die-exit melt temperature, showed strong correlation with residual crystallinity, was also insufficient for explaining the difference in residual crystallinity between the two formulations. By the time that the melt reaches the die-exit, it may experience heat loss to the barrels if they are set to lower values. Albeit the use of this value for validating the model, this method, although imperfect, was the most feasible option and utilized the most accessible experimentally measurable value, the melt temperature via IR sensor. Additional work to develop better methods for measuring the melt temperature, perhaps in a highly-filled zone such as a mixing element, are certainly justified and would improve model validation.

Despite the method of validation of the model using the die-exit melt temperature, simulation further revealed that the maximum melt temperature within the extruder

was found to strongly correlate with residual crystallinity. Residual crystallinity approached zero as the simulated maximum melt temperature was close to the solubility temperature given by the API solubility phase diagram for the given drug loading, differentiating between the formulations with differing intrinsic melt viscosity (Figure 5.9). As Moseson and Taylor recently described theoretically and demonstrated practically using a small conical twin-screw extruder, the thermodynamics and use of API-polymer matrix phase diagrams clearly and scientifically explain the requirement of reaching the solubility temperature for achieving a crystal-free ASD (48). This argumentation of thermodynamic driving force for dissolution, the API solubility temperature, also explains the strong correlation between residual crystallinity, maximum melt temperature and the greater degree of TEL dissolution into the matrix for the un-plasticized TEL / COP formulation. However, it is not the only possible explanation, as kinetics is also a driving force for dissolution. As several authors have discussed previously, application of the Noyes-Whitney equation, equation 5.1, can phenomonologically elucidate the impact of temperature, screw speed and melt viscosity on the rate of API dissolution into a polymer matrix (7,26,48,131–133):

$$\frac{dC}{dt} = \frac{DA(C_S - C)}{hV} \tag{5.1}$$

where $C$ is the concentration of the API dissolved in the polymer matrix at a given time $t$, $D$ is the diffusion coefficient, $A$ is the surface area of API particles suspended in the polymer matrix, $C_S$ is the saturation solubility of the drug at a given temperature, $h$ is the diffusion boundary layer thickness, and $V$ is the volume of the molten polymer phase. The diffusion coefficient can be expressed by equation 5.2, the Stokes-Einstein equation (134):

$$D = \frac{k_B T}{6\pi\eta r} \tag{5.2}$$

where $k_B$ is the Boltzmann constant, $T$ is the temperature, $\eta$ is the melt viscosity and $r$ is the particle radius.

An increase in matrix temperature, regardless of the source, e.g. conduction from barrels warmer than the melt or from viscous dissipation, will increase the saturation solubility of the API and therefore the dissolution rate; this saturation solubility value is equivalent to the solubility temperature given in the phase diagram. In this study, the temperature rise, locally in the 2$^{nd}$ mixing zone, was higher for the formulation with higher intrinsic melt viscosity due to pronounced viscous dissipation. This heat rise was enough to increase the saturation solubility and induce more dissolution of the API in the un-plasticized system. However, at increasingly high barrel temperatures, the differences observed between the two formulations in maximum melt temperature and viscous dissipation diminished. These results were a direct reflection of the increasing similarity of the measured melt temperature and residual crystallinity between the two formulations at higher barrel temperatures. In addition, an increase in matrix temperature, either by conduction from the barrels or melt temperature rise from viscous dissipation will lead to an increase in the diffusion coefficient.

Further, a decrease in melt viscosity, from higher process set temperatures, increased shear rate, intrinsic matrix melt viscosity by incorporation of a plasticizer, or over time as a plasticizing API dissolves into the matrix (19,39,41,135) will also lead to a higher diffusion coefficient. Changing melt viscosity as a function of API dissolution was not a factor in this study because the API and matrix properties, as well as drug loading, were selected to minimize this potential effect. Conversely, an increase in melt viscosity, perhaps from the use of lower process set temperatures, lower shear rate or even anti-plasticization by APIs with amorphous $T_g$ greater than that of the matrix, will decrease the diffusion coefficient, but can also lead to an increase in viscous dissipation, and therefore temperature rise and increased diffusion coefficient. Interestingly, this phenomenon is exemplified by the discrepancy in dissipated energy for the un-plasticized formulation at 100 rpm and 170 °C (Figure 5.13) in which the highest dissipated energy condition did not directly translate into the highest melt temperature or lowest observed residual crystallinity. Here, the shear rate and melt temperature were so low that insufficient shear thinning occurred, resulting in a high value for melt viscosity, leading to higher dissipated energy. However, this high viscous dissipation was not enough to overcome the predominant

effect of temperature control by conduction from the barrels at this temperature setting. In addition, at this processing setting, the feed rate was relatively low, leading to longer residence times and correspondingly more time for melt temperature to equilibrate with that of the barrel wall. This type of result, highlighting different heat generation phenomena in different processing regimes, proves the value of process simulation due to consideration of all relationships between relevant material property and process parameter inputs simultaneously. Despite these inter-dependent relationships, the simulated maximum melt temperature still correlated with the CQA residual crystallinity. Furthermore, a low barrel temperature setting of 170 °C was not able to reduce the risk of temperature rise of the melt due to viscous dissipation, especially in the non-plasticized formulation. Not only was the melt temperature too low to dissolve the API, the amount dissolved was more dependent on screw speed at this low temperature, narrowing the design space. Therefore, it is more desirable to operate at low melt viscosities so as to widen the design space with respect to screw speed.

Higher shear rate can reduce the boundary layer thickness, inherently a function of melt viscosity, decrease the melt viscosity due to shear thinning, and decrease the local concentration of dissolved API near a particle surface via distributive mixing, leading to a higher local concentration gradient at the particle surface, all of which will increase the diffusion coefficient. Some of these effects are supported by the experimental results, in particular the variation of screw speed. In addition, higher shear rate, especially at high melt viscosity, can lead to higher shear stress and greater dispersive mixing (99). In this study, slightly higher levels of shear stress computed for the un-plasticized formulation may have contributed to breaking up potential aggregates of the fine TEL primary particles, which would have increased the area of contact between API particles and polymer matrix, and therefore increasing the dissolution rate (99,133). Alternatively, increased distributive mixing can homogenize the melt temperature, caused simply by a higher number of expansion and contraction events at higher screw speeds (15,99). This effect can lead to either increasing or decreasing local temperature gradients within the melt, which could both increase or decrease the dissolution rate.

A large specific surface area of the API and smaller particle size will lead to increased dissolution rates. This effect was shown by Li, *et.al.*, in which the smaller of two acetaminophen API batches led to overall more API dissolved via faster dissolution rates (33).

The impact of the overall process time, that is residence time, and another aspect of the kinetics, can be inferred, as it was not independently varied. Longer residence time in the extruder can also lead to more observed dissolution. In this study, for a given combination of feed rate and screw speed, the residence time should not be a strong function of formulation due to similar bulk density and therefore fill level. On the other hand, the residence time would have been shorter as a consequence of increasing feed rate proportionally to screw speed in order to maintain fill ratio for all conditions, consistent with published RTD characteristics for TSEs (136,137). However, more residual crystallinity was observed with low feed rates, i.e. long residence times, and therefore this cannot be the dominating factor for dissolution of TEL. Of course, a separate study in which the temperature and residence time are independently varied could be performed to confirm this inference.

Despite the complex interdependent and simultaneously evolving relationships between all of the independent process and formulation parameters (e.g. screw speed, barrel temperature, feed rate, screw configuration, material properties) and process variables (e.g. melt temperature, shear rate, melt viscosity, residence time), which can in part be accounted for by use of process simulation, the strongest evidence for less observed residual crystallinity in the un-plasticized formulation is the generally higher material temperature. After all, the residual crystallinity approached 0 %w/w when the simulated maximum melt temperature reached the solubility temperature. For more dramatically evolving systems, for example when the API itself is a strong plasticizer for the matrix, process modeling may help to explain complex processing behavior. However, the same challenges as those mentioned by Vergnes and Berzin for modeling reactive extrusion will also apply to pharmaceutical HME (138) and will need to be addressed.

While the TW80 certainly exhibited the typical behavior of a plasticizer, that is decreasing the $T_g$ and therefore overall melt viscosity profile, it also widened the

design space with respect to screw speed. This behavior offers an additional justification for including a surfactant in an ASD formulation; beyond improving bioavailability enhancement (45), the surfactant can improve processability. Of course, traditional plasticizers are typically advised for decreasing the processing temperature to avoid high temperatures which could lead to API or polymer degradation. However, this study shows that this would not help to achieve complete dissolution due to lack of a thermodynamic driving force, as has also been suggested by others (26,48). Instead, process conditions must induce a melt temperature which reaches the solubility temperature for the given drug load.

Any plasticization must also be considered in the context of the impact it can have on product stability. Reduction in the $T_g$ will lead to greater molecular mobility which can induce recrystallization (65,139–141). On the other hand, rather than having a destabilizing effect, Ghebremeskel, et.al., showed that plasticizing surfactants can increase the physical stability (121). They reasoned that the solubility of API in the polymer matrix could increase due to positive intermolecular interactions or that greater homogeneity was achieved via better mixing in the extruder in a plasticized matrix. However, by design, this was not the case in this system as TEL's solubility in COP was unaffected by 5 %w/w TW80. In addition, the reduced $T_g$ of the TW80 formulation in this study does not indicate an explanation for higher residual crystallinity. The potential for recrystallization at 10 %w/w TEL is low because the formulation $T_g$ is 92 °C, well above the recommended 50 °C above room temperature (142). In addition, the pure drug substance does not recrystallize from the amorphous state upon re-heating (data not included, see Lepek, et.al. (129)).

Last but not least, the simulated global process energetics generated insightful results which are difficult to obtain experimentally. While the specific mechanical energy can be measured, it is highly reliant on accurate measurement of torque, which can be error-prone due to energy loss between the gear box and the shafts. The conducted energy can also be estimated for a process, but it is again challenging as not all extruders are configured to access relevant heating and cooling signals and due to inaccessible measures of melt surface area contact with the barrels, for example. Therefore, there are advantages to using process simulation to obtain a comprehensive picture of the process energetics. The viscous dissipated

energy, specific mechanical energy and total conducted energy all accounted for the differences between the two formulations, especially as a function of process conditions. According to the analysis by Zecevic, *et.al.*, a total conducted energy of zero is a predictor of a quasi-adiabatic process (22). By comparing formulation matrices with differing degrees of plasticization, it is apparent that the processing conditions at which a given formulation will produce a quasi-adiabatic state are highly dependent on the matrix melt viscosity, as suggested in the literature (143). The results indicate that the quasi-adiabatic point can be achieved at lower temperatures for the plasticized formulation, and a quantitative, rather than qualitative, estimate is provided by simulation. In this study, because the extruder was not yet configured to collect and record heating and cooling events, it was not possible to confirm this observation experimentally. The lower-temperature quasi-adiabatic point could be beneficial for formulations in which thermal degradation is a concern and for which scaling needs to be performed. The advantage of an adiabatic process is that if little or no cooling or heating is required, scaling should be more straightforward and less dependent on the differing conducting surface area to volume ratio, which decreases with increasing extruder diameter. This idea is explored further in Chapter 6. In addition, as mentioned previously, the global total product energy, although it correlated with the residual crystallinity, was not sufficient to explain the difference between the two formulations; only analysis of the maximum melt temperature fully explained the difference in the extent of telmisartan dissolution.

## 5.6 Conclusions

Like the torasemide indicator system, telmisartan in copovidone is an informative model system for the study of HME QbD. It enabled the comprehensive evaluation of the relationship between formulation material properties and HME processing characteristics for ASD formation. Due to its high solubility temperature and non-plasticizing characteristic in copovidone-based polymer matrices at a concentration of 10 %w/w, the plasticizing effect of a common surfactant on the HME process and the residual crystallinity CQA could be isolated and studied. While surfactants are commonly selected to enhance the bioavailability of a drug substance, it was found that the plasticizing behavior of polysorbate 80 broadened the processing design space with respect to screw speed. Also, while plasticizers are commonly

incorporated to reduce the processing temperature, it was also found that by doing so in the case of TEL with a high API solubility temperature, the complete formation of the ASD is hindered; complete reduction of residual crystallinity is only possible if the melt temperature reaches the thermodynamic solubility temperature. Therefore, a temperature increase in kneading blocks due to viscous dissipation generated by a highly viscous melt was required to achieve a fully amorphous system. Process simulations, in which matrix melt viscosity, screw speed and barrel temperature were varied, enabled simultaneous consideration of the complex inter-dependent relationships inherent to HME, namely those between formulation material properties, independent process parameters, and process dependent variables such as melt temperature and melt viscosity and their impact on the CQA residual crystallinity. In this way, the measured melt temperature and simulated maximum melt temperature were correlated with residual crystallinity, differentiating the process behavior between plasticized and un-plasticized matrices.

# 6 Application of Telmisartan Indicator System and Process Modeling to Study Scaling of a Quasi-Adiabatic Pharmaceutical HME Process

## 6.1 Introduction

The optimization of the energy usage of an extrusion process, particularly in plastics compounding, but also food extrusion, has been the subject of research for many years. Due to the emerging importance of single screw extrusion for plastics processing in the middle of the 20$^{th}$ century, and following the development of models to better understand the process, the first theoretical analysis of adiabatic extrusion for a single screw extruder was published in 1954 (143). Plastics processing by extrusion is typically performed at large scale, e.g. up to 420 mm diameter extruders with throughputs of up to 125,000 kg/h for a twin-screw extruder. At such large scales, energy conservation is of high interest and improvements can be achieved following simple guidelines (144,145). Despite commercial pharmaceutical products being manufactured on much smaller extruders ranging in diameter from 27 to 70 mm, it is of interest to study the applicability to pharmaceutical extrusion, in particular if it is feasible for common pharmaceutical materials and if the required product quality can still be achieved given the reactive nature of the formation of an ASD.

Extruder operation, in terms of heat generation and heat transfer, has been categorized as either autogenous or isothermal (146). Autogenous or near adiabatic operation takes place when no heating or cooling of the barrels occurs because enough thermal energy is generated by mechanical work from the screws turning and shearing the processed material. Isothermal operation denotes that heating or cooling from the barrels maintains the temperature of the product.

Isothermal operation can be appropriate for low melt viscosity materials, if a material is fed pre-molten, or if the fill volume is low. However, isothermal processing of viscous materials is not practical, especially when high throughput is desired for which a high screw speed is needed in order to maintain a suitable fill level in the extruder barrel. Due to the viscous nature of polymeric materials, polymers will

generate heat from the mechanical energy imparted by turning of the screws, referred to as viscous dissipation (143). Further, because polymers are thermally insulating materials, heating or cooling them in temperature-jacketed containers is also not practical due to low thermal conductivity (16,145).

For pharmaceutical production, as in other types of polymer processing (143), the material is fed as a solid, and therefore a certain amount of thermal conduction from the barrels helps to facilitate the transition from solid to melt. As a result, the process combines both isothermal and autogenous characteristics, and therefore the term quasi-adiabatic is used. The exact quasi-adiabatic point depends on formulation melt viscosity, extruder design and screw speed (143). Depending on the material rheological properties and the thermal and energy efficiency requirements for a given product and process, the ideal combination of all factors may be difficult to identify, as was noted for single screw extrusion of pure polymers (147,148). It may also be challenging to identify the exact adiabatic point if a formulation’s melt viscosity is changing as a function of composition, for example if an API highly-plasticizes the surrounding matrix.

In addition to achieving an energetically optimized process, scaling of a process which is also energetically balanced is of interest. If quasi-adiabatic extrusion can be achieved for a given formulation, it may be advantageous or easier to scale the process. For example, if the mechanical energy per amount of material remains constant across scales, the product temperature may also remain constant, and if the barrel temperatures are simply selected to be similar to the temperature profile of the melt along the screw, then key geometric differences between scales such as the difference in surface area to volume ratio may not be important. On the other hand, an energetically unbalanced situation may be one in which the melt temperature is higher than the barrel temperature due to considerably higher mechanical energy on the larger scale and the reduced barrel surface area may not be sufficient to cool the melt. Further, heat transfer between melt and barrel, particularly in the screw channel, is inefficient due to the insulating nature of the polymeric material as well as short contact time (149). Alternatively, regardless of scale, if the melt temperature is lower than the barrel temperature, local hot spots may form high thermal gradients near the barrel walls (143). Both types of energetically unbalanced situations could

lead to uncontrolled product temperature and result in unfavorable and non-uniform product quality characterized by thermal degradation or incomplete ASD formation. In addition, if the product temperature is similar to the barrel temperature, the extruder will not need to constantly fluctuate between heating and cooling cycles, which should also improve product quality (145). When considering all of these factors, scale-up of a pharmaceutical HME process can be considered all the more challenging as well as warrants systematic study.

### 6.1.1 Simplified Criteria for Assessing Quasi-Adiabatic Processing

Two criteria were used for assessing the quasi-adiabatic state of the extrusion process. They are expressed as 1st Hypothesis and 2nd Hypothesis. The 1st hypothesis is related to temperature control of the barrels and die. If heating and cooling activity in the extruder is identical during processing in comparison to the heated but empty state, then the process can be considered quasi-adiabatic (Figure 6.1).

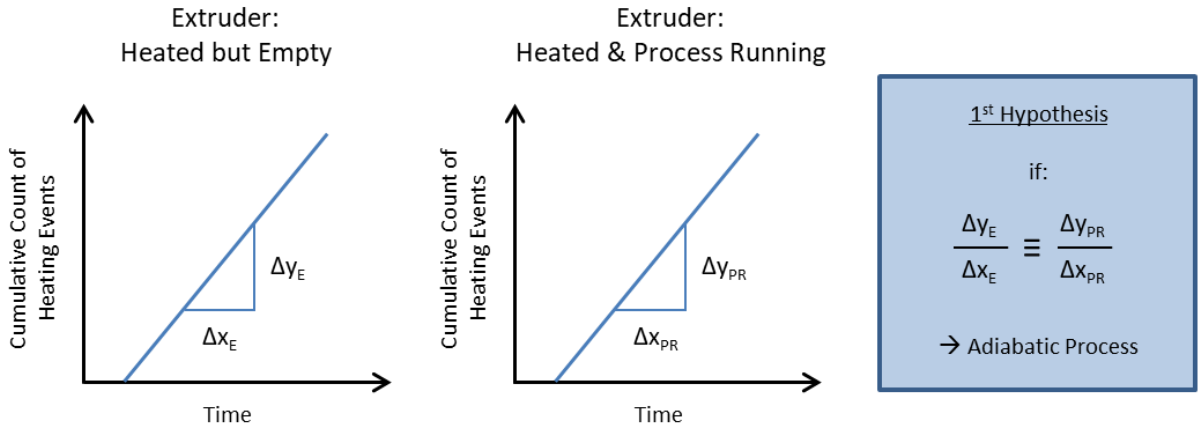


Figure 6.1 *1st Hypothesis for quasi-adiabatic processing.*

The temperature of the barrels is controlled by electrical heating cartridges and by water pumped through cooling channels while the die temperature is controlled only by electrical heating cartridges. Temperature probes are also located in each barrel and the die. The heating and cooling activity is regulated by a temperature controller. When a temperature controller detects that the temperature is less than the target temperature, the heating cartridges turn on. Likewise, when the temperature is too low, valves open to allow cooling water to enter the channels in the barrels. When turned on, the heating cartridges operate at a fixed power, the magnitude of which

can depend on the scale and vendor. For cooling power, the temperature of the water can be adjusted, as well as frequency and duration of valve opening. The primary control, however, of heating and cooling is the length of time, also called the impulse, for which the cartridges are on or the valves are open. These times are regulated by the temperature controller, typically operating under PID logic (150). This type of signal has been used successfully to monitor the energetics of single screw extrusion (16).

Heating and cooling activity is described by the controller output, expressed either as a percentage value in the range of -100% to 100%, with positive values indicating heating and negative values indicating cooling, or as the slope of the cumulative count of heating or cooling events over time. Actually, the former is in fact derived from the latter. A value of 100% or -100% indicates that the heating cartridges are on at all times or that the water valves are open at all times, respectively. Intermediate controller output values indicate periodic turning on and off or opening and closing. When expressed as a slope, a slope of zero indicates no activity while a steeper slope indicates many impulses of activity and for long periods of time. For the extruders used in this study, the 40 mm extruder (ZSK40) controller output was expressed as a percentage while the 18 mm extruder (ZSK18) controller output was expressed as a slope. For the ZSK18, separate signals were produced for heating and cooling. As an approximation, when both were active, the slope of cooling line was subtracted from the slope of the heating line. In summary, the process is considered quasi-adiabatic if the percentage value of the controller output or the slope of the controller output is identical between the “heated but empty” and “heated and process running” states.

A notable complicating factor is that extruders are composed of many independently temperature-controlled zones, all of which ideally should meet the 1$^{st}$ Hypothesis criteria. In addition, in the “heated and process running” state, heat is generated by viscous dissipation inside the screw channel, leading to an additional heat source. In reality, it is challenging to achieve a quasi-adiabatic state because of the many channels of heat flow. For example, heat can flow between the barrel segment or die and the surrounding environment, between melt and barrel segment or die, and between barrel segment-to-barrel segment and barrel segment-to-die. Considerable

differences are also present between scales: barrel outer surface areas differ, barrel inner surface area to volume ratios (SA:V) differ and shear rates can differ. Upon scaling, the combination of reduced SA:V and potentially increased viscous dissipation could result in the need for extensive cooling, so much so that the extruder may no longer be capable of controlling the temperature, resulting in constant cooling or even increasing barrel overheating over time. Because of these complications, or specifically the heat loss to the environment, it would be acceptable to define quasi-adiabatic by, instead of exactly achieving agreement between “heated but empty” and “heated and process running” controller output, the controller output at least never enters a cooling regime. A depiction of the possible thermal energy flows for both “heated but empty” and “heated and process running” is shown in Figure 6.2.

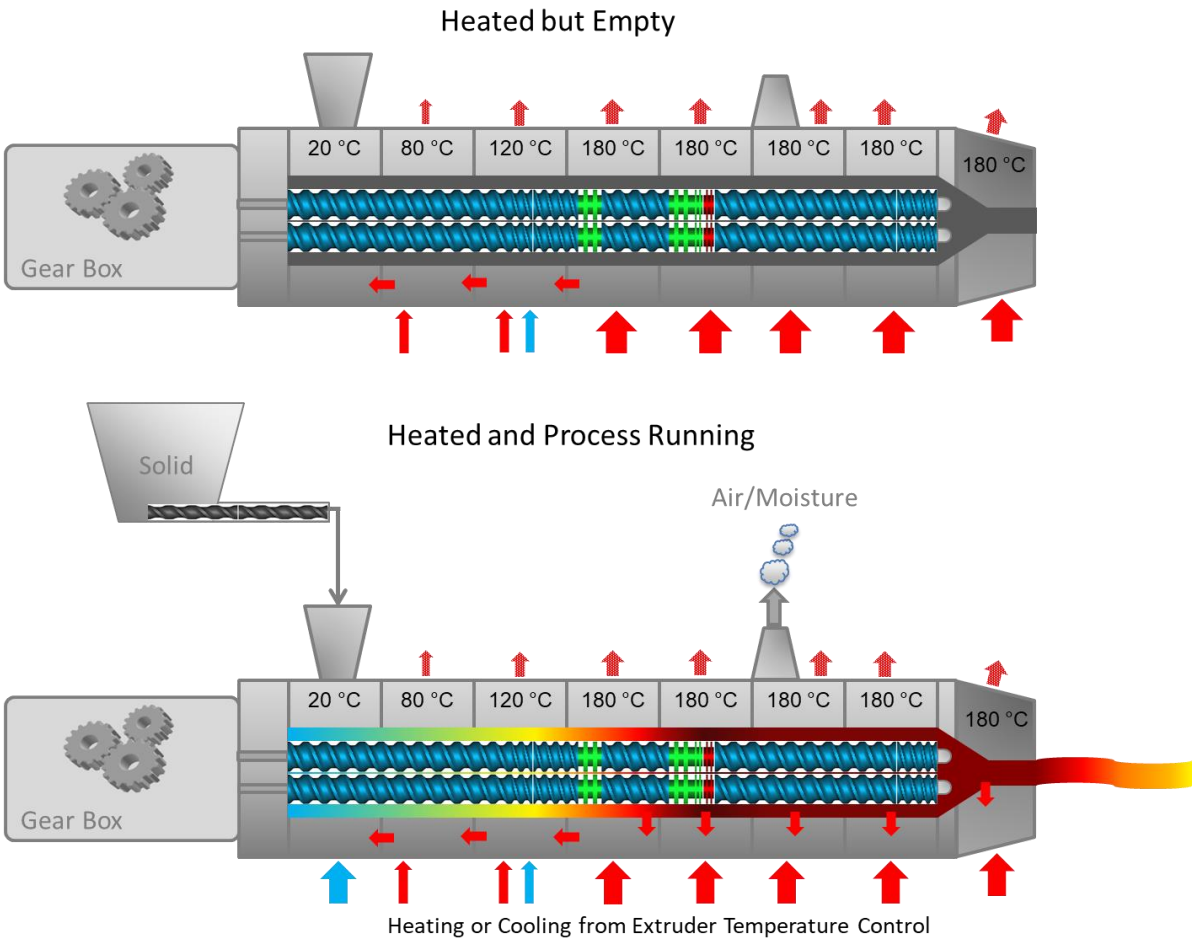


Figure 6.2 *Hypothetical thermal energy flow in an extruder. (Note: not to scale, and arrows do not indicate single points of heat transfer but are instead generalized from zone to zone).*

The temperature profile (Table 6.3) for the study discussed in this chapter was used as the basis for this depiction. Arrows below the extruder refer to heating or cooling supplied by the heating cartridges or cooling water. Arrows above the extruder indicate heat loss to the environment. Arrows within the extruder refer to heat transfer between barrels or between melt and barrel.

The 2nd hypothesis is related to the relationship between the temperature of the barrel segments or die and the temperature of the melt inside the barrel segments or die. If the difference in temperature, DeltaT, at all locations along the length of the extruder is zero, then the process can be considered quasi-adiabatic (Figure 6.3). In the figure, the DeltaT is indicated at the point of maximum melt temperature, but DeltaT can be located elsewhere as well, for example at the end of the screw or at the die exit. A positive DeltaT implies that the melt received enough energy from an additional source, in this case mechanical energy from the screw, to cause an increase in temperature. The DeltaT in the core of a screw channel for an unmixed portion of polymer has been reported to be as great as 60 °C, depending on the process parameters (151).

Based on these hypotheses, it follows that a low DeltaT should correspond to a controller output close to zero. In this study, minimizing the difference between the “heated but empty” and “heated and process running” controller output as well as minimizing the DeltaT in the portion of the extruder set to 180 °C was the primary focus, but the differences were also analyzed in the earlier, cooler sections as well.

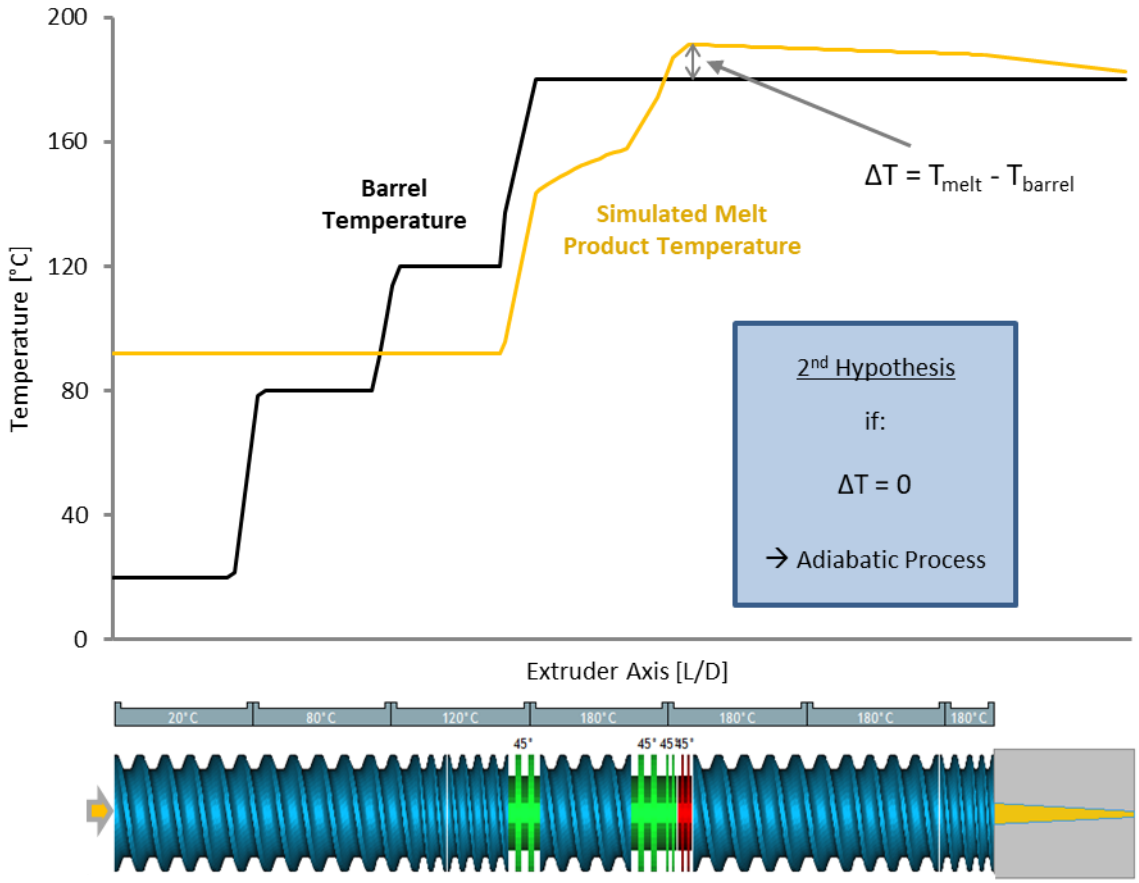


Figure 6.3 *2nd Hypothesis for quasi-adiabatic processing (note: die not to scale).*

An additional hypothesis was related to use of the results from the Ludovic® model. The question posed was: could Ludovic® guide the selection of process parameters to achieve a quasi-adiabatic state? For example, the total conducted energy (TCE), a global result and measure of how much heating or cooling occurs during steady state (Figure 7.2), could directly relate to the controller output. Evidence for this idea was present in the study performed by Zecevic, *et.al.*, in which minimal TCE corresponded with low measured DeltaT, although controller output was not monitored (22). Further, and possibly even better, the local conduction energy (LCE) as a function of extruder length could relate to the individual barrel and die controller output. In addition, the estimated difference between melt and barrel temperature can be calculated from the temperature evolution as a function of the length of the extruder, f(x), plot in Ludovic®. One uncertainty, however, is that these results are also a function of the thermal exchange coefficient (TEC), an input value in Ludovic® (Figure 7.6). Therefore, any result is always only an estimate for the real process

unless the model is tuned or validated with experimental data. Such validation is challenging if not impossible because of measurement limitations, such as temperature at all locations in the extruder.

### 6.1.2 Twin-Screw Extrusion Scaling Approaches

Transfer of a process from one scale to another, known generally as scaling, or specifically as scale-up or scale-down, aims to maintain product quality while adapting scale-specific process parameters. Scale-up may be performed to increase the overall throughput of the process or to develop a commercial-scale process while scale-down may be performed to study the large-scale process at development-scale and reduce quantities of costly raw materials while developing or troubleshooting a process.

Several important variables in TSE differ as a function of scale: barrel diameter and cross-sectional area, barrel volume and inner surface area per unit length, screw tip speed, drive power, and barrel heating and cooling capacity (146). As the diameter increases, the barrel inner surface area increases by the power of 2 while the barrel inner volume increases by the power of 3. This results in the dramatic decrease in the surface area to volume ratio as the diameter increases (22). Reduced surface area results in a decrease in the area available for heat exchange between melt and barrel. At the same time, as the diameter increases, the screw tip speed will also increase, leading to higher potential for shear heating; however, the propensity for shear heating is also a function of the screw-barrel clearance and screw-screw clearance. As a result, upon scale-up, these geometrical differences can result in reduced heat transfer and increased amount of viscous dissipated energy. The independent process parameters such as screw speed, feed rate, barrel temperature and screw configuration can be adapted in order to compensate for these fundamental differences and to obtain comparable operating conditions. Along with geometric similarity (see next paragraph), such operating conditions to keep consistent include average shear rate, fill level in the screw channels, discharge pressure, specific heating and cooling power, residence time and the heat exchange surface (15).

Numerous strategies for scaling of the extrusion process, originally intended for single-screw extruders, have been published (32,152). The strategies can be adapted to twin-screw extrusion, but the added geometric complexity and the presence of both filled and partially-filled sections along the screw channel should not be disregarded (60). In both single- and twin-screw extrusion, one typically begins with the assumption that geometric similarity exists between the two extruder scales. Geometric similarity is defined by similar extruder length:diameter ratio L/D, $D_o/D_i$, number of flights and screw helix angle (15). If geometric similarity criteria are met, the screw speed is typically maintained and the feed rate, Q, is calculated for the new scale based upon a selected scaling exponent, *x*, using equation 6.1.

$$\frac{Q_2}{Q_1} = \left(\frac{D_2}{D_1}\right)^x \tag{6.1}$$

where *D* refers to the barrel diameter and the subscripts 1 and 2 refer to the initial and second scales, respectively. The origin and derivation of this equation is outlined nicely in Dryer, *et.al*., in particular its applicability to twin-screw extrusion and geometrically similar extruders based on the assumption that flow from pressure or leakage are negligible in comparison to drag flow (60). The exponent *x* is selected from a range between 1.5 to 3 with 1.5-2 typically for comparable heat transfer and 3 for comparable mixing (32,146). Rauwendaal states that scaling for heat transfer typically results in nearly constant specific energy consumption and therefore comparable melt temperature, while the output is significantly lower and therefore the residence time much longer. On the other hand, scaling for mixing again results in constant specific energy consumption and high throughput upon scale-up, which can be detrimental if melting is required. In this case, these problems can be compensated for by altering the screw configuration, but then the geometric similarity would no longer be present. As mentioned by Dryer, *et.al.*, for both single- and twin-screw extrusion, compromises must be made, and the scaling factor should be selected based on which characteristic should be kept more constant for the particular formulation being processed.

In both scaling scenarios, the shear rate remains constant with constant screw speed, again as long as geometric similarity is maintained, in particular the $D_o/D_i$ and

leakage (15,58). If this is not the case, the shear rate can be adapted by adjusting the screw speed using equation 2.9 for shear rate in the screw channel and equation 2.10 in the screw overflight region.

Specifically in the case of adiabatic extrusion, two approaches have been suggested. The first approach outlined by Frame seeks to maintain the same viscous dissipation energy by linking the residence time, the power and screw tip speed, given that the residence time is determined in large part by the feed rate as long as the screw speed and profile are comparable (146). Since an adiabatic process is limited by the extent of viscous dissipated energy, the first approach recommends an exponent of 3 in equation 6.1 so as to increase the feed rate in accordance with increasing volume. Screw tip speed should be maintained with the assumption that it maintains constant shear rate. Equivalent power can be achieved with comparable power density or specific torque $M_d/a^3$, where $M_d$ is the torque limit of the screws and 'a' is the center line (15). It is therefore assumed that adiabatic conditions can be realized on both scales if these three parameters are kept constant. The second approach developed by Nakatani strives to maintain melt temperature upon scaling (153). Several unique parameters were included to account for heat-removal, an adiabatic index which should fall between 0 and 1, and the non-Newtonian index from modeling of rheological data. The approach acknowledges that additional work is needed to account for situations in which the barrels are heating and cooling, in which case the adiabatic index would be greater than 1 or negative, respectively. The adiabatic index can be calculated via simulation software and the resulting scale up index for throughput, *x*, in equation 6.1, can be determined.

Alternatively, scale-independent parameters such as specific energy, residence time distribution and product temperature can be held constant during scaling (24,58). However, identification of process parameters to obtain consistency in these scale-independent parameters is not straightforward due to the inter-dependent relationship between independent and dependent variables and the process responses (Figure 2.1). For example, specific mechanical energy increases with screw speed and torque, but decreases with increasing feed rate (equation 2.13). However, the torque can increase with increasing feed rate but can also decrease with increasing screw speed due to the dependency of torque on material melt

viscosity. In addition, Frame pointed out that product quality can vary even if the SME remains constant, since multiple combinations of the screw speed, torque and throughput can result in the same SME (146). For example, for constant feed rate, increased screw speed can lead to reduced fill level, reduced melt viscosity and therefore reduced torque. Fortunately, simulation tools can help to estimate the response of specific energy, residence time distribution and product temperature to changes in process variables, regardless of whether they are independently or dependently adjustable.

## 6.2 Aims of Work

The present approach to scaling was intended to be simple, tangible and visualizable. More specifically, the idea was to keep the experience of a unit volume of melt the same throughout its journey in the extruder. To do this, screw speed and feed rate were calculated such that the VSFL (equation 2.15) and the overflight shear rate were maintained constant. The difference in the barrel surface area to volume ratio was not adjusted or accounted for because it was assumed that this would be less relevant at adiabatic conditions. The step-by-step experimental approach is outlined in Figure 6.4. The specific objectives were the following:

- Study adiabatic scaling for pharmaceutical systems, in particular for extruders for which exactly matching geometric similarity was lacking but was kept as constant as was feasible, with the aim of developing a scaling approach for geometrically dissimilar extruders
- Avoid the need for cooling at large scale
- Determine if the adiabatic point is similar or the same for a given formulation at different scales when geometry is kept as similar as possible
- Estimate and identify adiabatic conditions using modeling and verify hypotheses about controller output and melt-barrel temperature difference and their correlation to simulated local and total conducted energy
- Select a formulation with material properties, specifically the melt viscosity, so as to enable the utilization of a CQA, the telmisartan residual crystallinity, to verify scaling

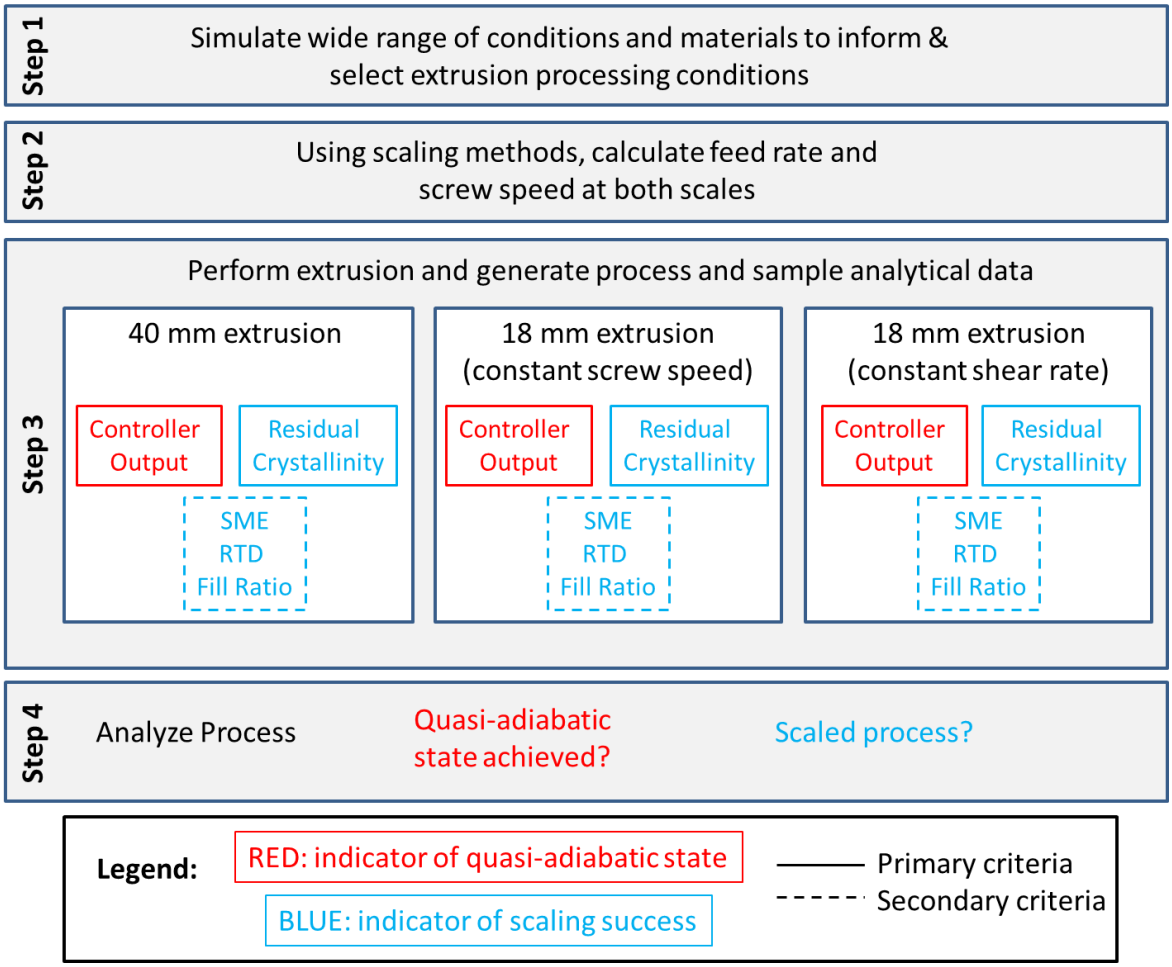


Figure 6.4 *Overview of experimental approach.*

## 6.3 Experiment Design

The inspiration for the experimental design derived from observations from the work presented in Chapter 5 with telmisartan and work published previously with dipyridamole (DPD) by Zecevic, *et.al.* (22). In the previous chapter, simulated results for total conducted energy (TCE) showed strong dependency on both formulation melt viscosity and barrel temperature (Section 5.4.3.3). In the work with DPD, the TCE also varied in a rational way with respect to variation in mechanical energy as a function of varied screw speed and feed rate for several extruder scales. In both studies, it was observed that the TCE approached zero as DeltaT approached zero. However, in the work by Zecevic, *et.al.*, the measured DeltaT was used as a surrogate for measurements of the heat flow in the extruder, and an exact measure of the success of scaling was not realized due to the absence of a measurable CQA. In fact, the main barrel set temperature of 150 °C was higher than the solubility

temperature of ~120 °C for 30 %w/w DPD in copovidone, and DPD strongly plasticizes COP (135). The focus of this work was to build upon the prior work and to connect the behavior of residual crystallinity as a CQA to better understand quasi-adiabatic extrusion processing in a pharmaceutical scaling application.

### 6.3.1 Formulation Compositions

The two formulations investigated in Chapter 5, 10 %w/w TEL in COP and 10 %w/w TEL in a 5 %w/w TW80 in COP matrix, were also investigated in the simulation study in this chapter, while only the ternary mixture was evaluated experimentally.

### 6.3.2 Laboratory Experiment Design

#### 6.3.2.1 Extruder Design

Two extruders were used in the study, with nominal diameters of 18 and 40 mm, and were relatively geometrically similar. The design characteristics of the two extruders are listed in Table 6.1. Included in the list are the make and model, geometric dimensions, heating and cooling capabilities, and motor capabilities. While the absolute screw lengths were different, the relative length in units of length divided by diameter, or L/D, was similar at 28 L/D and 25.725 L/D for the 18 mm (ZSK18) and 40 mm (ZSK40) extruders, respectively. Both extruders had an identical diameter ratio of 1.55, which is important for geometrical similarity, especially with respect to the shear rate in the screw channel (see discussion in section 6.3.2.2).

One design difference was the number of barrel segments, with the ZSK18 extruder consisting of 7 barrel segments while the ZSK40 only 6 barrel segments. Because the individual barrel segments had nearly the same length ratio of 4 L/D, the ZSK18 extruder essentially had one additional heating zone. This difference was compensated for by slightly lengthening the distance between the two mixing zones and by keeping the barrel set temperature constant in this region.

Table 6.1 *Comparison of extruder characteristics – ZSK18 vs. ZSK40.*

| | **18 mm Extruder** | **40 mm Extruder** |
|---|---|---|
| **Vendor** | Coperion | Coperion |
| **Model** | ZSK18 MegaCompounder | ZSK40 MegaCompounder |
| **Screw Diameter [mm]** | 18 | 40 |
| **Diameter Ratio $D_o/D_i$** | 1.55 | 1.55 |
| **Total Screw Length [mm]** | 504 | 1029 |
| **Total Screw Length [L/D]** | 28 | 25.725 |
| **Number of Barrels** | 7 (plus a passively-heated die plate) | 6 (plus a passively-heated die plate) |
| **Barrel Length [mm]** | 72 | 162 |
| **Barrel Length [L/D]** | 4 | 4.05 |
| **Die Plate Length [mm]** | 25 | 57 |
| **Barrel Diameter [mm]** | 18.25 | 40.3 |
| **Center Line [mm]** | 15.0 | 33.4 |
| **Screw-Barrel Clearance [mm]** | 0.1 | 0.2 |
| **Free Cross-Sectional Area [$mm^2$]** | 188 | 872 |
| **Barrel Free Volume without Die [$dm^3$]** | 0.095 | 0.8865 |
| **Barrel Surface Area to Volume Ratio [1/cm]** | 4.79 | 2.38 |
| **Die Plate Length [mm]** | 58 | 25 |
| **Die Free Volume [$cm^3$]** | 9.1 | 116 |
| **Die Outlet Dimensions** | 10 mm diameter | 5 mm x 60 mm |
| **Heating Cartridges per Barrel** | 4 x 200 W | 4 x 800 W |
| **Maximum Barrel Temperature [°C]** | 250 | 270 |
| **Barrel Cooling Medium** | water | water |
| **Heating Cartridges per Die and Power** | 1 x 160 W | 4 x 550 W |
| **Location of Heating Cartridges** | adjacent to die lip, near surface of die | 2 internal near melt flow<br>2 adjacent to die lip |
| **Location of Die Thermocouples** | adjacent to die lip, near surface of die | (upper, middle, lower) |
| **Power Drive [kW]** | 10 | 64 |
| **Maximum Screw Speed [rpm]** | 1024 | 250 |
| **Max Torque/shaft [N·m]** | 38 | 500 |

The screw configurations were designed such that the functional zones remained constant (Figure 6.5). Considerations included the number and type of mixing zones, the barrel temperature profile, use and placement of the vacuum port, and placement of the mixing zones with respect to the temperature profile, vacuum port, and die exit. For example, the first mixing element was placed within the temperature transition region between 120 °C and 180 °C, while the second mixing section was placed just before the vacuum port. The kneading blocks used at both scales were identically geometrically scaled, meaning that the number of disks per element, the element length in L/D, the disk L/D, and offset angle were the same (Table 6.2).The pitch of conveying elements was also kept constant as much as was feasible. For example,

large pitch elements were used at the powder entry, pitch was decreased leading up to the first mixing element, pitch was increased in the venting section, and pitch was again decreased prior to the die.

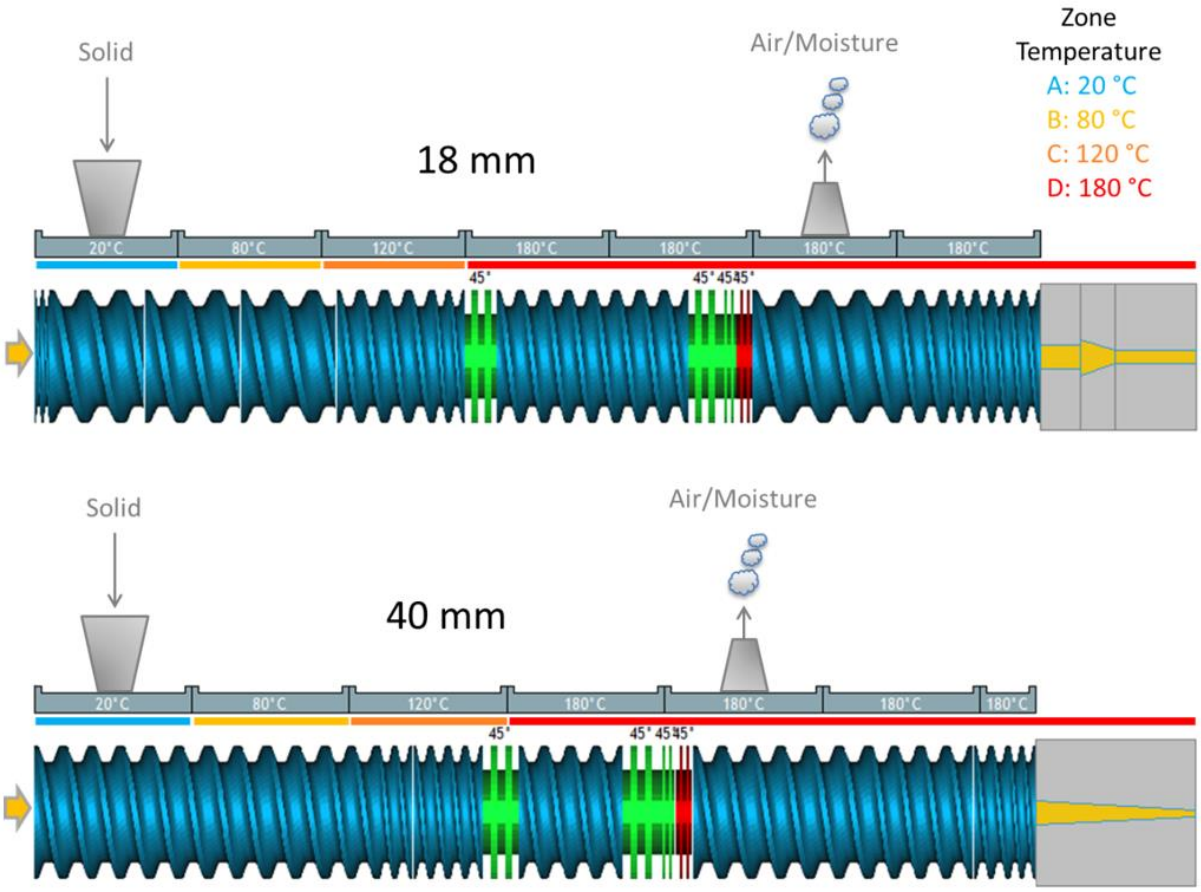


Figure 6.5 *Schematic of extruder configurations (note: drawings are not to scale). For further details, see Table 6.2.*

Table 6.2 *Comparison of screw configurations – ZSK18 vs. ZSK40.*

| 18 mm ZSK18 Extruder | | | | | 40 mm ZSK40 Extruder | | | | |
|---|---|---|---|---|---|---|---|---|---|
| **Element Type** | **Length [mm]** | **Pitch [mm] or # of Disks / Offset Angle [°]** | **Length L/D [-]** | **Pitch L/D [-]** | **Element Type** | **Length [mm]** | **Pitch [mm] or # of Disks / Offset Angle [°]** | **Length L/D [-]** | **Pitch L/D [-]** |
| Conveying – FW | 8 | 8 | 0.44 | 0.44 | Conveying – FW | 60 | 60 | 1.5 | 1.5 |
| Conveying – FW | 48 | 36 | 2.67 | 2 | Conveying – FW | 60 | 60 | 1.5 | 1.5 |
| Conveying – FW | 48 | 36 | 2.67 | 2 | Conveying – FW | 60 | 60 | 1.5 | 1.5 |
| Conveying – FW | 48 | 36 | 2.67 | 2 | Conveying – FW | 60 | 60 | 1.5 | 1.5 |
| - | - | - | - | - | Conveying – FW | 60 | 60 | 1.5 | 1.5 |
| Conveying – FW | 48 | 24 | 2.67 | 1.33 | Conveying – FW | 54 | 54 | 1.35 | 1.35 |
| - | - | - | - | - | Conveying – FW | 36 | 36 | 0.9 | 0.9 |
| - | - | - | - | - | Conveying – FW | 36 | 36 | 0.9 | 0.9 |
| Conveying – FW | 16 | 16 | 0.89 | 0.89 | Conveying – FW | 36 | 36 | 0.9 | 0.9 |
| Kneading – FW | 16 | 5 / 45° | 0.89 | - | Kneading – FW | 36 | 5 / 45° | 0.9 | - |
| Conveying – FW | 48 | 24 | 2.67 | 1.33 | Conveying – FW | 54 | 54 | 1.35 | 1.35 |
| Conveying – FW | 48 | 24 | 2.67 | 1.33 | Conveying – FW | 54 | 54 | 1.35 | 1.35 |
| Kneading – FW | 16 | 5 / 45° | 0.89 | - | Kneading – FW | 36 | 5 / 45° | 0.9 | - |
| Kneading – FW | 8 | 5 / 45° | 0.44 | - | Kneading – FW | 18 | 5 / 45° | 0.45 | - |
| Kneading – BW | 8 | 5 / -45° | 0.44 | - | Kneading – BW | 18 | 5 / -45° | 0.45 | - |
| Conveying – FW | 36 | 36 | 2 | 2 | Conveying – FW | 60 | 60 | 1.5 | 1.5 |
| Conveying – FW | 36 | 36 | 2 | 2 | Conveying – FW | 60 | 60 | 1.5 | 1.5 |
| Conveying – FW | 24 | 24 | 1.33 | 1.33 | Conveying – FW | 60 | 60 | 1.5 | 1.5 |
| Conveying – FW | 16 | 16 | 0.89 | 0.89 | Conveying – FW | 54 | 54 | 1.35 | 1.35 |
| Conveying – FW | 16 | 16 | 0.89 | 0.89 | Conveying – FW | 54 | 54 | 1.35 | 1.35 |
| Conveying – FW | 16 | 16 | 0.88 | 0.89 | Conveying – FW | 36 | 36 | 0.9 | 0.9 |
| - | - | - | - | - | Conveying – FW | 27 | 27 | 0.675 | 0.675 |
| **Total** | **504** | **-** | **28** | **-** | **Total** | **1029** | **-** | **25.725** | **-** |

FW = Forward
BW = Backward

#### 6.3.2.2 Process Parameter Selection

Observations and learnings from the prior experiments and findings discussed in Chapter 5 on the 18 mm scale, as well as the simulation experiment discussed in Sections 6.3.3 and 6.4.1, informed selection of the process parameters for the experiments performed in this scaling study. The magnitude of the screw speeds and feed rates were chosen based upon the scaling methods under investigation.

For the barrel temperature heating profile, the same temperature gradient in the first three barrel segments was used as in the previous study (Table 6.3). These first three barrel segments are also referred to as Zones A, B and C, respectively, and were set to 20, 80 and 120 °C. The remaining barrels, collectively known as Zone D, were set to a constant temperature of 180 °C. Within Zone D, there are four barrel segments on the ZSK18 extruder, three barrel segments on the ZSK40 extruder, and a die on each. The die plates on both extruders are not included in the list because they were not independently temperature-controlled.

Table 6.3 *Extruder heating profile and barrel-die description.*

| | | **18 mm Extruder** | **40 mm Extruder** |
|---|---|---|---|
| **Zone** | **Temperature Setting** | **Barrel Designation** | |
| Zone A | 20 °C | 20 °C Barrel | 20 °C Barrel |
| Zone B | 80 °C | 80 °C Barrel | 80 °C Barrel |
| Zone C | 120 °C | 120 °C Barrel | 120 °C Barrel |
| Zone D | 180 °C | Barrel 1a | Barrel 1 |
| | | Barrel 1b | n/a |
| | | Barrel 2 | Barrel 2 |
| | | Barrel 3 | Barrel 3 |
| | | Die | Die Upper/Middle/Lower |

Calculation of the average shear rates as a function of screw speed in the screw channel and overflight regions, according to equations 2.9 and 2.10, respectively, showed no difference in the screw channel and a slight difference in the overflight region (Figure 6.6). No difference was present in the screw channel because the extruders were designed to have the same $D_o/D_i$ ratio. However, the difference in the shear rate in the overflight region is different between the two extruders because of the differences in clearance, 0.1 mm for the ZSK18 and 0.2 for the ZSK40, and because of the significant difference in diameter leading to different tip speeds. The

differences here are notable because the shear rate present in the overflight region is roughly 1.5 orders of magnitude greater than in the screw channel. From a scaling perspective, and because this work deals with viscous polymers, this difference can result in substantial viscous dissipation and increase in melt temperature (15).

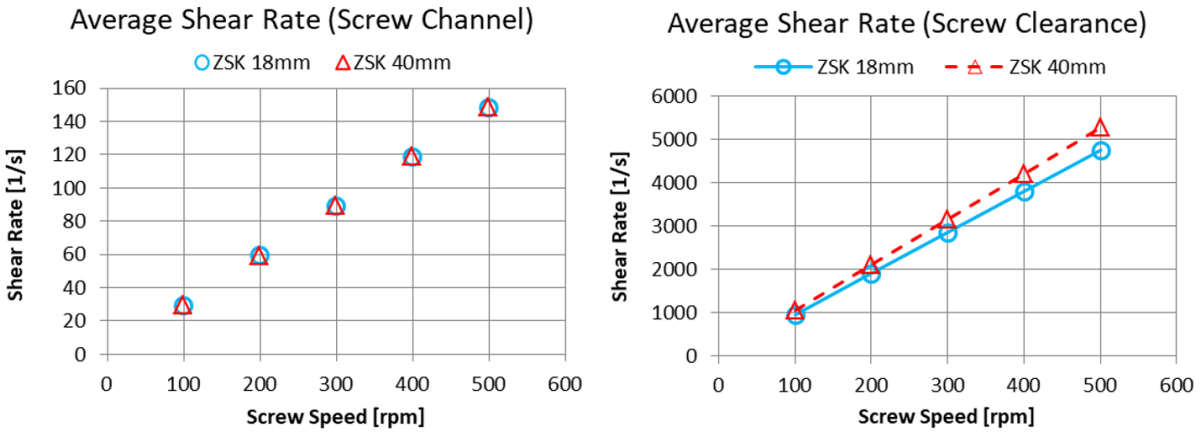


Figure 6.6 *Shear rate in screw channel (left) and in clearance region (right) as a function of screw speed for ZSK18 and ZSK40 extruders.*

The process parameters, namely the screw speed and feed rate, for the 40 mm scale experiments are listed in Table 6.4. Each combination of screw speed and feed rate resulted in a different VSFL, the value of which is also listed in the table. The VSFL was calculated using equation 2.15. All combinations of feed rate and screw speed were run on the ZSK40 extruder.

Table 6.4 *ZSK40 process settings and resulting volume specific feed load.*

| **ZSK40 Extruder** | **Volume Specific Feed Load [g/rev/dm³]** | | |
|---|---|---|---|
| | **Feed Rate [kg/h]** | | |
| **Screw Speed [rpm]** | **17** | **20** | **23** |
| **175** | 1.83 | 2.15 | 2.47 |
| **200** | 1.60 | 1.88 | 2.16 |
| **225** | 1.42 | 1.67 | 1.92 |

Note: Colored text corresponds to color coding in Figure 6.16 and Figure 6.22.

For scaling with the ZSK18 extruder, the VSFL was kept constant. Based on the shear rate differences in the overflight region between the two extruders, two approaches were tested for selection of the screw speed: the “constant screw speed” approach and the “constant shear rate” approach. As is commonly recommended for geometric scaling, the first approach employed the same screw speed in units of revolutions per minute. Alternatively, in order to keep the shear rate in the overflight

region constant, the screw speed was adjusted, and in this case, increased (Table 6.5). Accordingly, the feed rate, in combination with the screw speed, was back-calculated for each value of VSFL (Table 6.6 and Table 6.7). Because higher screw speeds were needed for the “constant shear rate” method on the ZSK18, the feed rates were also correspondingly higher. By testing two methods for scaling the screw speed, the significance of the shear rate in the clearance region and its effect on viscous dissipation was tested. Lastly, since experiments were performed first on the ZSK40 extruder, and because two methods for down-scaling to the ZSK18 extruder were tested, only the center point and corner points were run on the 18 mm scale. Interestingly, the feed rates calculated using the present scaling approaches are similar to those calculated with the geometric scaling equation, equation 6.1, when an exponent of 2.68 for the “constant shear rate” method and an exponent of 2.8 for the “constant screw speed” method, values not shown.

Table 6.5 *Comparison of shear rates in screw channel and clearance region for ZSK18 and ZSK40 extruders as a function of screw speed.*

| | **Shear Rate in Screw Channel [1/s]** | | **Shear Rate in Clearance Region [1/s]** | |
|---|---|---|---|---|
| **Screw Speed [rpm]** | **ZSK18** | **ZSK40** | **ZSK18** | **ZSK40** |
| 175[1] | 52.1 | 52.0 | 1668[1] | 1846 |
| 194[2] | 57.8 | n/a | 1846[2] | n/a |
| 200[1] | 59.6 | 59.4 | 1906[1] | 2110 |
| 221[2] | 65.8 | n/a | 2110[2] | n/a |
| 225[1] | 67.0 | 66.9 | 2144[1] | 2374 |
| 249[2] | 74.2 | n/a | 2374[2] | n/a |

[1] “Constant Screw Speed” Method
[2] “Constant Shear Rate” Method
n/a indicates process condition not tested

Table 6.6 *ZSK18 process settings for “Constant Screw Speed” scaling method and resulting volume specific feed load.*

| **ZSK18 Extruder** | **Volume Specific Feed Load [g/rev/dm³]** | | |
|---|---|---|---|
| | **Feed Rate [kg/h]** | | |
| **Screw Speed [rpm]** | **1.82** | **2.14** | **2.46** |
| **175** | 1.83 | n/a | 2.47 |
| **200** | n/a | 1.88 | n/a |
| **225** | 1.42 | n/a | 1.92 |

n/a indicates process condition not tested
Colored text corresponds to color coding in Figure 6.16 and Figure 6.22.

Table 6.7 *ZSK18 process settings for "Constant Shear Rate" scaling method and resulting volume specific feed load.*

| ZSK18 Extruder | Volume Specific Feed Load [g/rev/dm$^3$] | | |
|---|---|---|---|
| | Feed Rate [kg/h] | | |
| **Screw Speed [rpm]** | **2.02** | **2.37** | **2.73** |
| **194** | 1.83 | n/a | 2.47 |
| **221** | n/a | 1.88 | n/a |
| **249** | 1.42 | n/a | 1.92 |

n/a indicates process condition not tested
Colored text corresponds to color coding in Figure 6.16 and Figure 6.22.

### 6.3.2.3 Experimental Manufacturing and Analytical Procedure

The experiments performed as part of the quasi-adiabatic scaling study are shown schematically in a process train diagram (Figure 6.7). See section 7.2.2.2 for more information about experimental details.

Firstly, as with the experiments in the previous chapter with TEL, the TW80 / COP formulation matrix was pre-extruded. In this case, the composition of the matrix was 6 %w/w TW80 in COP. Prior extrusion of the matrix was performed for two reasons. First, it was intended to study the dissolution of TEL into a pre-formed matrix rather than, for example, first into a liquid phase of TW80 and then later into a mixture of TW80 and COP. In fact, the exact formation, presence and behavior of such multi-phase systems inside extruders is not well understood and accurate models for the phase transition from solid to melt are insufficient as initial melting is neglected (15,154). Therefore, in this way, uncertainty was reduced by simplifying the system. The melt viscosity of the matrix was also more uniform, being a function of only temperature and shear rate, rather than also composition. Second, it was intended to dehydrate the matrix to minimize potential processing issues like clogging in the feed section and to simplify the melt viscosity behavior by minimizing the effect of plasticization by water. Melt viscosity and $T_g$ characterization measurements for simulation input were also performed with dried samples. In this fashion, material characterization, extrusion processing and simulation were kept as similar to one another as possible. When preparing the placebo matrix, many combinations of feed rate, screw speed and barrel temperature were tested. The results of these placebo extrusion experiments are not discussed in this thesis. The placebo extrudate

prepared at several process settings was assumed identical and milled to a particle size roughly equivalent to unprocessed COP.

Secondly, a blend used for extrusion at both the 18 and 40 mm scales was prepared. Because the same blend was used for extrusion at both scales, no difference in performance can be attributed to this step in the experiment. The milled TW80 / COP extrudate was mixed with TEL at a concentration of 10 %w/w. A blending-delumping-blending procedure was used to ensure a uniform blend. The flowability of the powder blend was measured by ring shear cell to confirm feasibility of feeding at high feed rates, especially on the 40 mm scale, results not shown.

Lastly, the blend was extruded on the 40 mm scale, processing conditions listed in Table 6.3 and Table 6.4, as well as on the 18 mm scale, processing conditions listed in Table 6.6 and Table 6.7. The residual crystallinity of all extrudate samples was measured by XRPD.

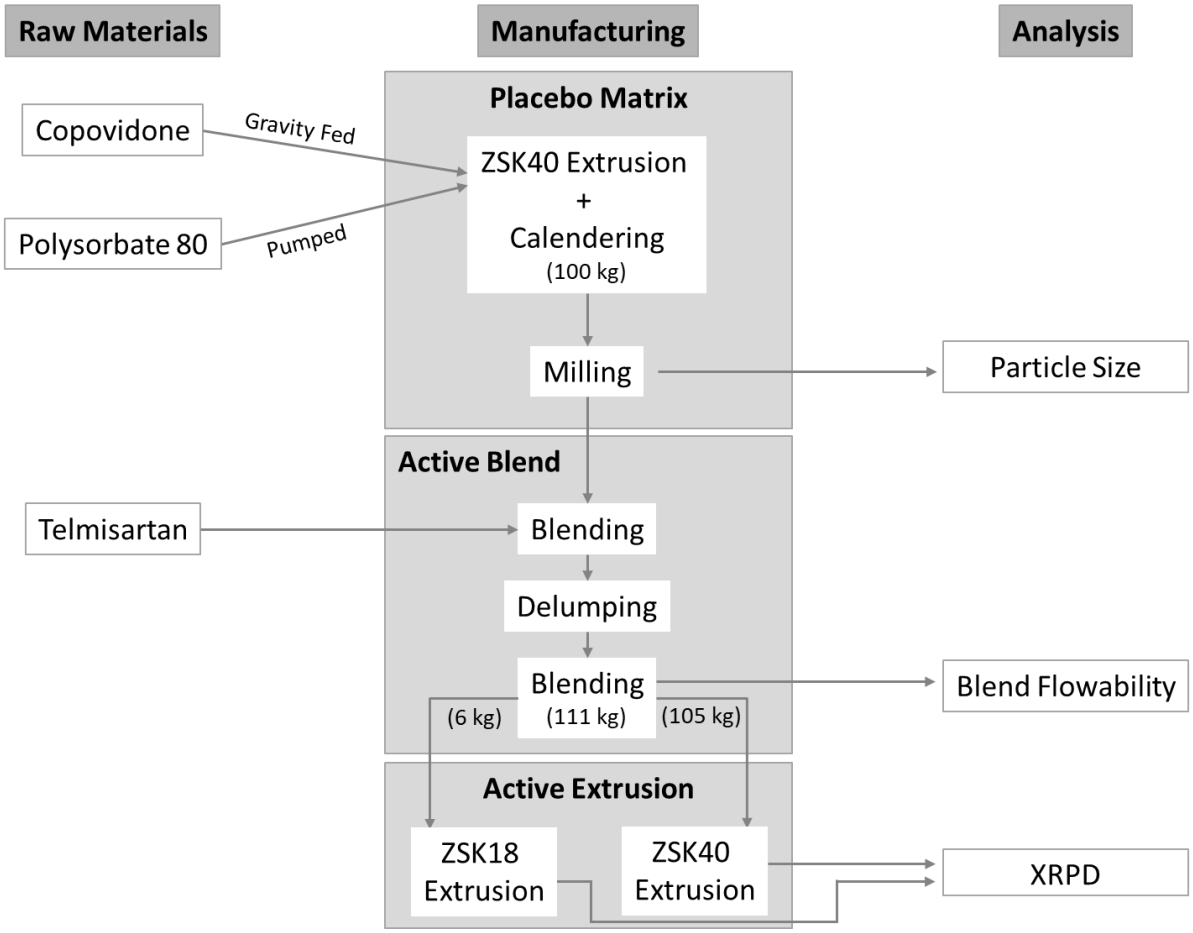


Figure 6.7 *Experimental processing train and corresponding analysis.*

### 6.3.3 Simulation Experiment Design

A full factorial design of simulation experiments was performed to guide the selection of barrel temperatures (Table 6.8). Ranges of feed rate and screw speed were chosen based on prior experiments with placebo, the results of which are not discussed. Both extruders, ZSK18 and ZSK40, were included in the experiment. Two formulations, identical to those processed in the previous study, with differing zero-shear rate viscosity were also included (Figure 5.5b). As always, the extruders were represented geometrically as similarly to the laboratory extruders as was possible.

Table 6.8 *Variables for simulated full factorial DOE.*

| **Extruder Scale** | **18 mm Extruder** | **40 mm Extruder** |
|---|---|---|
| **Screw Speed [mm]** | 175, 200, 225 | |
| **Feed Rate [kg/h]** | 1.8, 2.15, 2.5 | 17, 20, 23 |
| **Zone A Temperature [°C]** | 20 °C | |
| **Zone B Temperature [°C]** | 80 °C | |
| **Zone C Temperature [°C]** | 120 °C | |
| **Zone D Temperature [°C]** | 160, 170, 180, 190, 200 | |
| **Formulation** | TEL-COP, TEL-TW80-COP | |

## 6.4 Results & Discussion

### 6.4.1 Selection of Formulation and Barrel Temperatures for Laboratory Experiments via Supportive Simulation

In addition to learnings from numerous process settings tested empirically with placebo (results not presented), findings from simulation discussed in this section informed and supported the selection of the process parameters for extrusion experiments with TEL. The findings from simulation also confirmed the decision to select the TEL / TW80 / COP formulation for empirical scaling.

Based on the assumption that the 1$^{st}$ and 2$^{nd}$ Hypotheses would lead to a quasi-adiabatic state, and also that zero TCE would be related to this, process conditions were virtually identified that exhibited these characteristics. The simulations were performed for both formulations, namely with and without TW80, so as to confirm the findings from section 5.4.3.3 on both the 18 mm and 40 mm scales. Independent of extruder scale and with less substantial influence from screw speed and feed rate, simulation results showed that the TCE was near to zero when the TW80 formulation

was processed at a Zone D temperature of 180 °C whereas 200 °C was needed for the formulation without TW80 (Figure 6.8 and Figure 6.9). Within each Zone D temperature setting, the screw speed and feed rate also influenced the TCE, but to a lesser extent than did the temperature. Also interesting is that the range of TCE for the ZSK40 is roughly half that of the ZSK18, even though the process parameters were selected for similar VSFL and screw speed. This difference may result from the 2-fold difference in surface area to volume ratio for the two extruders (Table 6.1).

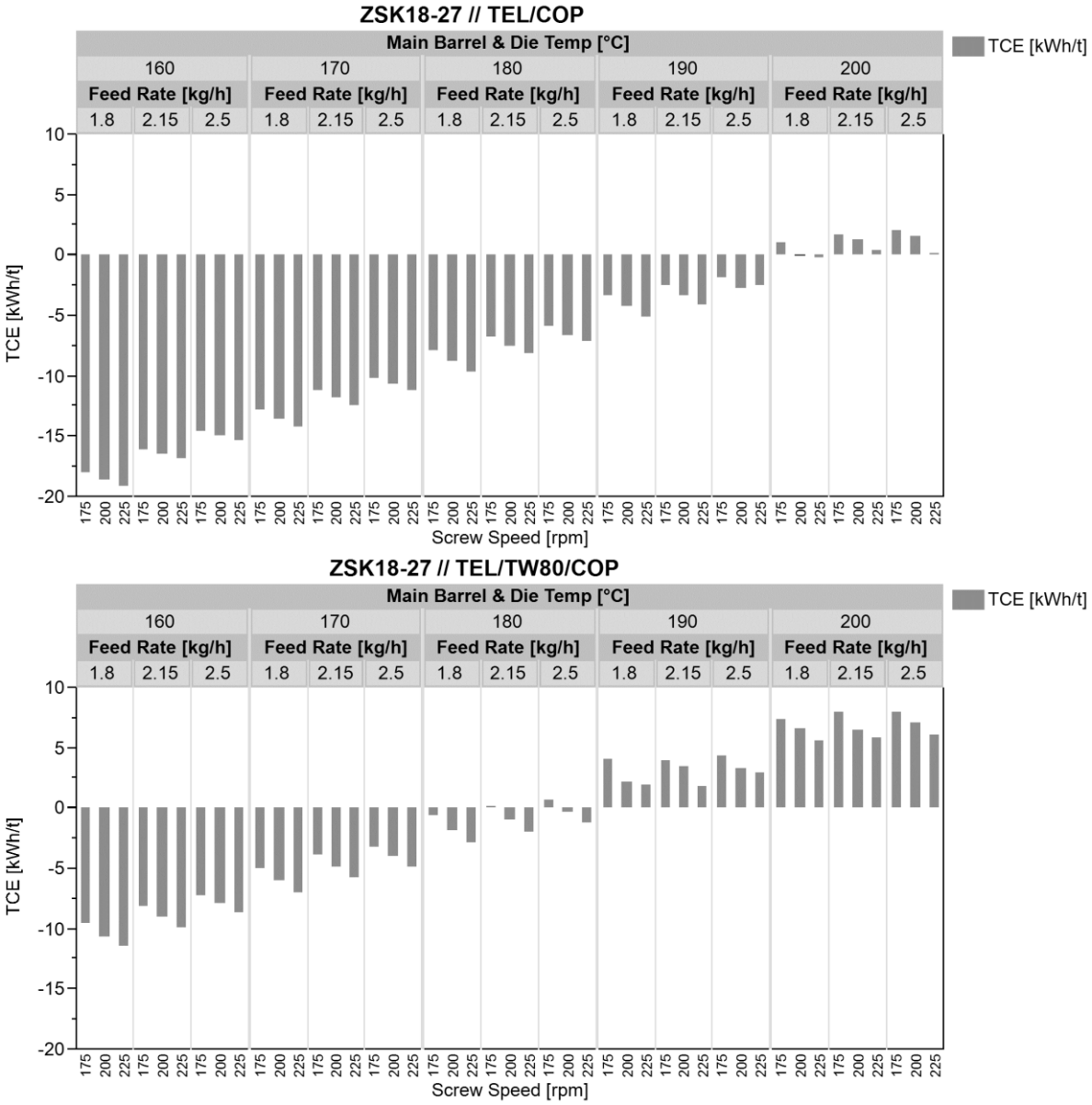


Figure 6.8 *Relationship of simulated TCE to barrel temperature as a function of formulation and processing conditions (feed rate and screw speed) for ZSK18.*

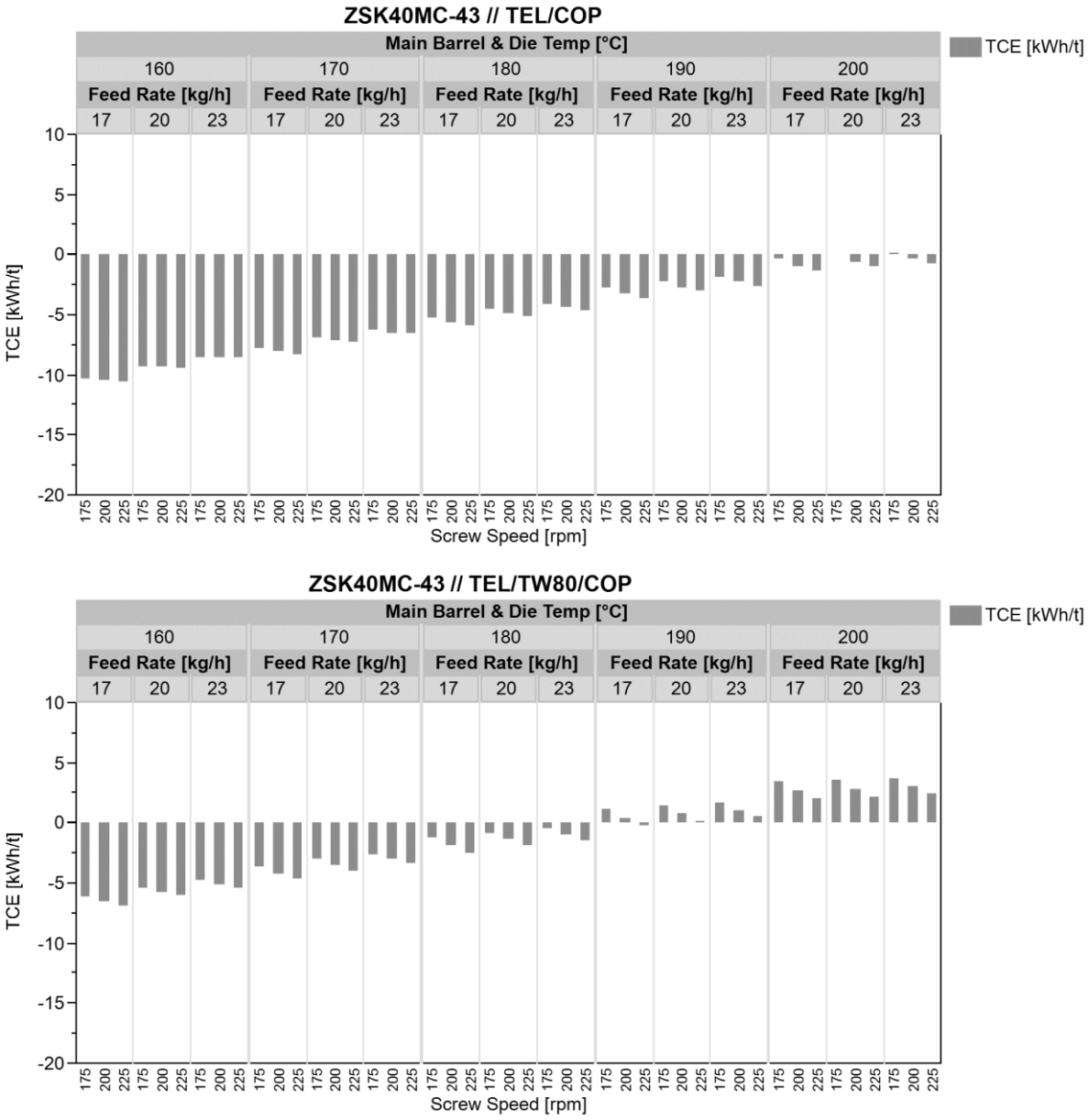


Figure 6.9 *Relationship of simulated TCE to barrel temperature as a function of formulation and processing conditions (feed rate and screw speed) for ZSK40.*

The simulated DeltaT between the maximum melt temperature and the Zone D temperature decreased as Zone D was increased (Figure 6.10). Within the range of barrel temperatures tested, the DeltaT approached zero for the TEL / COP formulation, while the DeltaT became negative (aka melt temp was lower than barrel temp setting) for the TEL / TW80 / COP formulation at high barrel temperatures. For both formulations, the DeltaT was around 10 °C when the TEC was zero. Interestingly, the DeltaT vs. TCE relationship for both extruder scales was most

similar (cross-over point) when the TCE was near to zero. For the TEL / COP formulation, this cross-over point occurred when the Zone D temperature was between 190 to 200 °C, while for the TEL / TW80 / COP formulation the cross-over occurred at around 180 °C. More simulations would be needed to confirm if this cross-over relationship holds for other extruder scales. If this proved to be true, this relationship may be a good guide for quasi-adiabatic scaling.

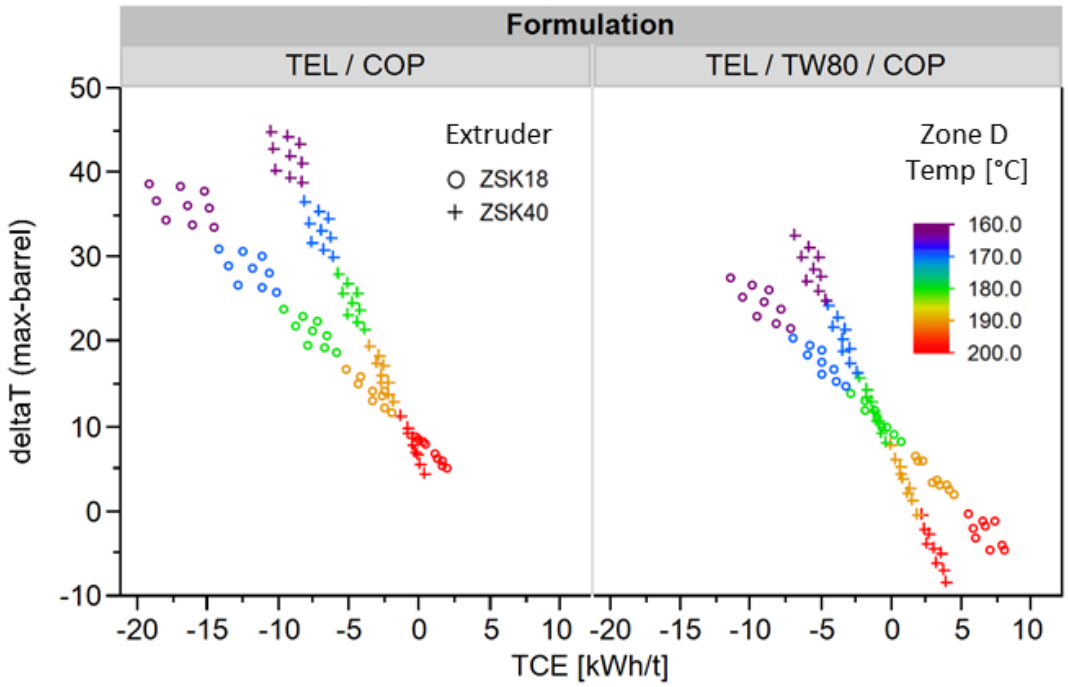


Figure 6.10 *Simulated DeltaT vs. TCE as a function of formulation, Zone D temperature and extruder scale. (Note: individual data points within each Zone D temperature are different combinations of screw speed and feed rate).*

Based on these findings, one could say that a coarse adjustment to energy and resulting melt temperature can be made by varying the barrel temperature while a fine adjustment can be made by varying the screw speed and feed rate. Accordingly, barrel temperature was fixed at 180 °C for the TW80 formulation scaling experiments, and the screw speed and feed rate were adjusted to tune the TCE close to zero.

Taking into account the phase diagram for the two formulations (Figure 5.4) and the relationship between residual crystallinity and melt temperature for extruded samples (Figure 5.8), the expected level of residual TEL crystallinity would be too low to

potentially distinguish between process settings in the TEL / COP formulation at barrel temp of 200 °C. Therefore, the TEL / TW80 / COP formulation was selected for scaling studies so as to enable both use of TEL as an indicator substance as well as study adiabatic scaling.

### 6.4.2 Process Analysis and Assessment of Energy Balance

#### 6.4.2.1 Baseline Controller Output for Heated but Empty ZSK18 and ZSK40

The controller output of each temperature-controlled barrel and die zone, measured for a heated but empty extruder, was similar for both extruder scales due to selection of the same set points in the temperature profile. The temperature profile used was similar to that listed in Table 6.3, except that Zone D was varied from 150 to 210 °C for the ZSK18 and from 140 to 180 °C for the ZSK40. The temperature of Zones A, B and C was held constant. Zone D was varied in order to assess the impact of its magnitude on heating and cooling requirements in other zones. In addition, the data was generated in order to have the baseline values in case, during the experiments with the process running, adjustment of the Zone D temperature was required in order to achieve a more acceptable quasi-adiabatic state. The results obtained did not vary as a function of room temperature within the range of 20-28 °C.

The controller output for the heated but empty ZSK18 extruder, expressed in units of counts/s, for each barrel segment and the die was plotted as a function of Zone D temperature (Figure 6.11). No heating or cooling was required to hold Zone A at 20 °C. As for the other zones, the most heating took place in the die due to probe placement, followed by the first barrel segment in Zone D. Zone B also required a considerable amount of heating, while Zone C fluctuated between heating and cooling, especially as the Zone D temperature was increased, due to barrel segment-to-segment heat transfer from the adjacent cooler and warmer segments. As the temperature of Zone D was increased, cooling activity in Zone C increased. At the same time, most of the individual barrel segments within Zone D needed increasingly more heating activity to hold their temperature due to the temperature differential between the barrel and the environment and resulting heat loss over time. Interestingly, both the first barrel segment in Zone D and the die exhibited maxima in their heating requirements as a function of Zone D temperature.

The controller output for the heated but empty ZSK40 extruder, expressed in units of percentage, for each barrel segment and the die was plotted as a function of Zone D temperature (Figure 6.12). In this case, full cooling power was required to hold Zone A at 20 °C. Aside from this, no other zone required cooling, regardless of Zone D temperature. As was seen with the ZSK18, the most heating was required for the die, followed by the first barrel segment in Zone D. Again, Zone B also required relatively a lot of heating. Zone C required less and less heating as the Zone D temperature was increased, but in comparison to the ZSK18, it never required cooling. However, this could be due to the fact that Zone D temperature range investigated was narrower for the ZSK40. Also, as was observed with the ZSK18, as the Zone D temperature was increased, all barrel segments in Zone D required increasingly more heating activity to hold their temperature. In comparison to the ZSK18, the die on the ZSK40 contained 3 temperature probes and therefore 3 controller output values. The upper and lower probes were located closer to the surface of the die while the middle probe was located closer to the center of the die. Due to their placement and proximity to the surface of the die where heat loss can rapidly occur, the upper and lower probes required correspondingly large amounts of heating. Due to an insulating effect provided by the upper and lower heating elements, the middle section of the die required much less heating, although its heating activity did increase with increasing Zone D temperature.

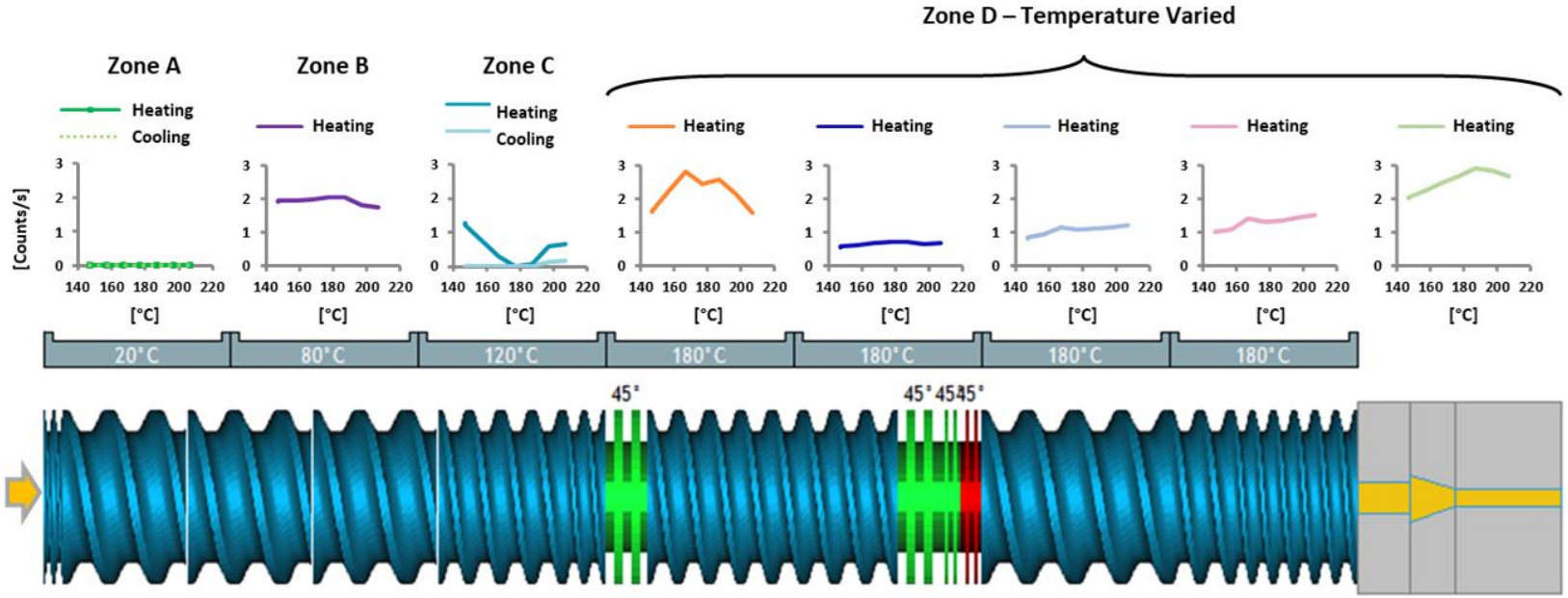


Figure 6.11 *Baseline ZSK18 barrel and die controller output – heated but empty (x-axis of mini-plots is Zone D temperature, die volume not to scale).*

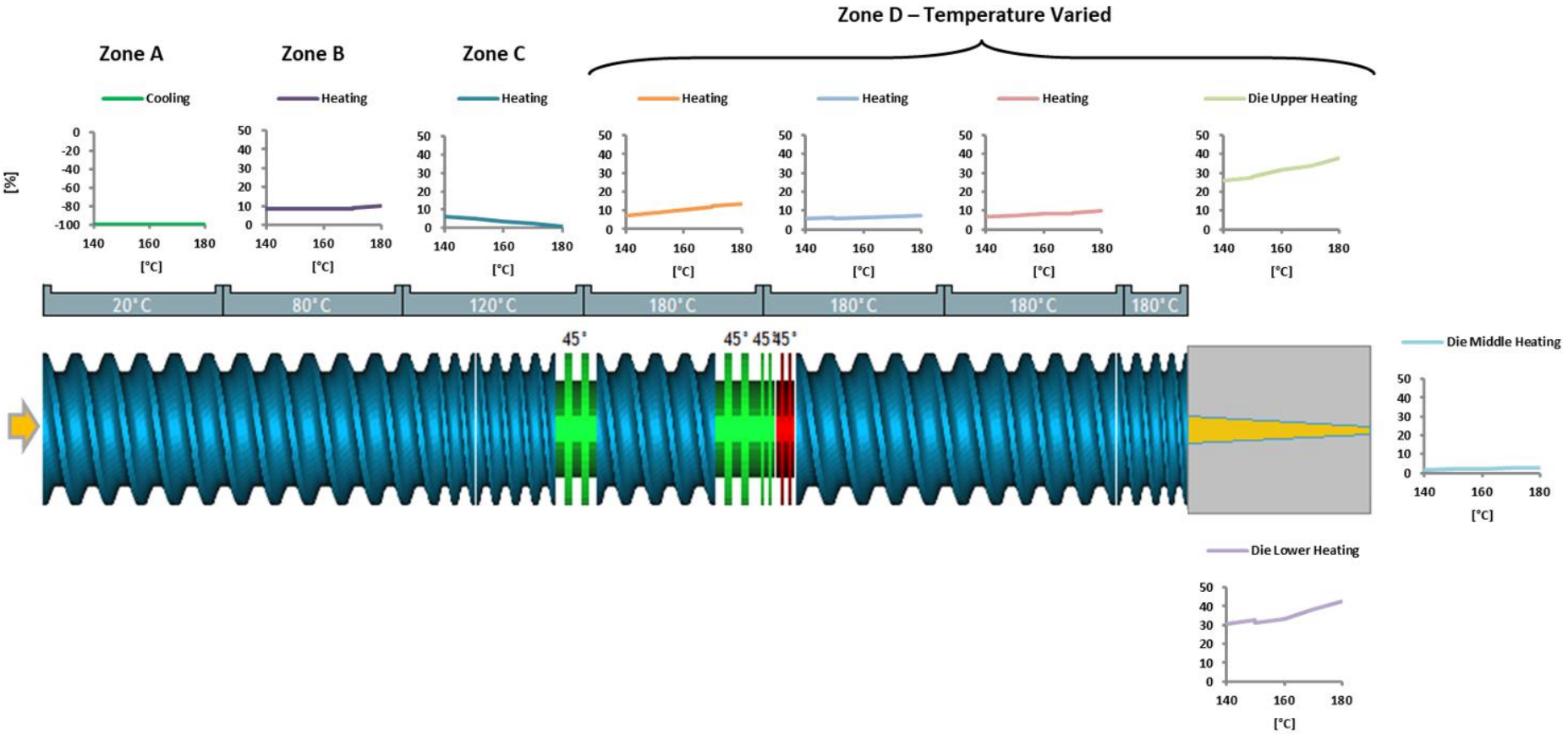


Figure 6.12 *Baseline ZSK40 barrel and die controller output – heated but empty (x-axis of mini-plots is Zone D temperature, die volume not to scale).*

### 6.4.2.2 Temperature Difference between Melt and Barrel

At both scales, the measured die exit melt temperature was higher than the Zone D barrel set temperature (Figure 6.13), with the melt temperature at the ZSK40 overall 4-6 °C higher than at the ZSK18, for comparable processing conditions. The higher melt temperature at screw exit for the ZSK40 was observed for simulated data as well (Figure 6.14). In addition, simulation indicated that the maximum melt temperature, located in the second mixing zone (see example in Figure 6.3), was approximately the same for both extruders (Figure 6.14). Because the barrel temperature was not varied in this study, the DeltaT was also higher for the ZSK40 than for the ZSK18, both measured and simulated (Table 6.9). For both scales, the temperature increased with increasing screw speed while the impact of feed rate or fill level was unclear from experimental data. For simulated data, higher screw speed led to higher melt temperatures while lower VSFL led to higher melt temperatures. The melt temperature may be higher on the ZSK40 for several reasons: better cooling and/or melt temp homogenization on ZSK18, and possibly more locally intense shear on the ZSK40 due to differing tip speed which may not have been accounted for in the use of the simple shear rate models for scaling, as described in Kohlgrüber (15).

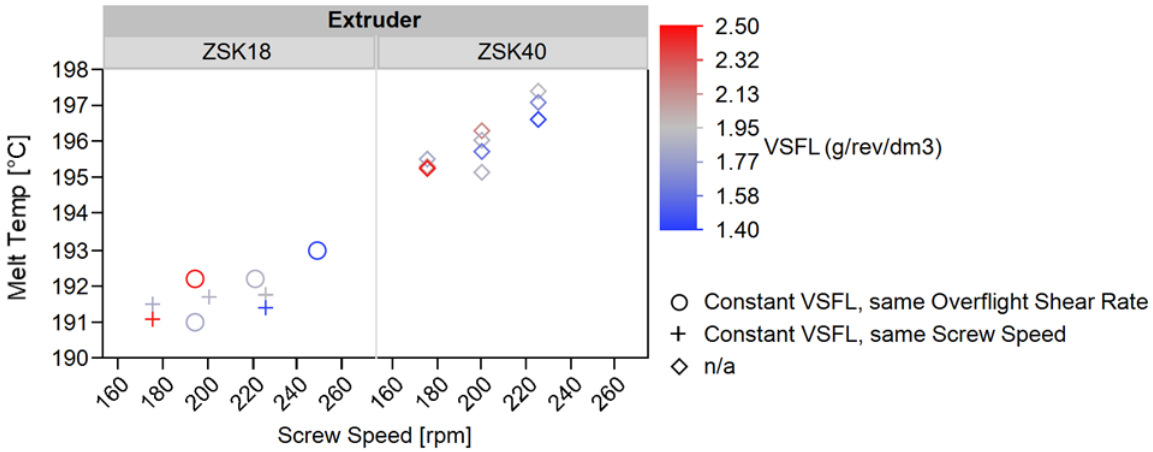


Figure 6.13 *Experimental die exit melt temperature vs. processing conditions.*

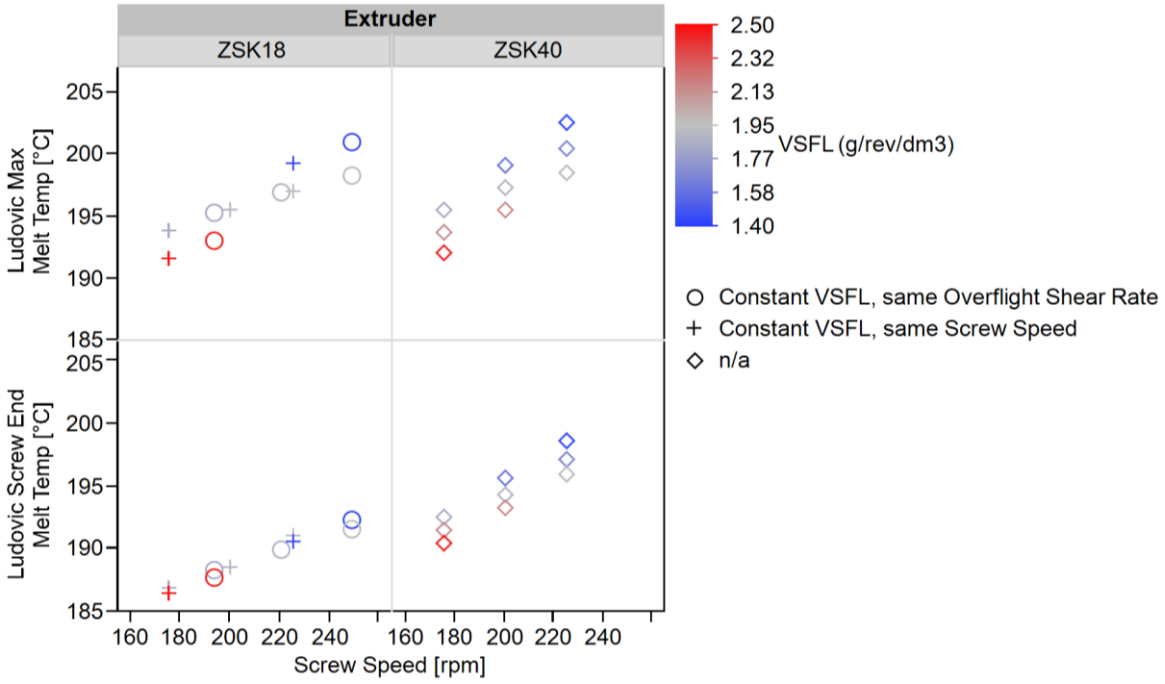


Figure 6.14 *Simulated maximum melt temperature and melt temperature at screw exit vs. processing conditions.*

Table 6.9. *Range of experimental and simulated DeltaT.*

| Extruder Scale | Range of DeltaT [°C] | |
|---|---|---|
| | Measured (Die Exit) | Simulated (Screw Exit) |
| ZSK18 | 11-13 | 6-12 |
| ZSK40 | 15-17 | 10-18 |

### 6.4.2.3 Controller Output when Heated and Process Running

The controller output behaved similarly for both extruder scales due to similar barrel temperature profile. In addition, the Zone D for both extruders required less heating than in the empty state. The controller output was found to correlate with simulated total conducted energy and simulated local conducted energy, and all of these tended to correlate with variation in SME via changes in screw speed and feed rate.

As was observed in the “heated but empty” state, similarities were also observed when comparing the controller output between scales when the extruder was heated and the process was running (Figure 6.15). In the figure, individual data points indicate the controller output for a given screw speed and VSFL. In the array of plots, the controller output for the “heated but empty” extruder state, with temperature

profile listed in Table 6.3, is indicated by a thin horizontal line. The bold horizontal lines serve to differentiate between each temperature zone and to guide the eye.

Overall, the screw speed had the predominant effect on controller output in each zone. In comparison, the feed rate or corresponding fill level had little effect, within the range tested. In addition, if the zone needed cooling or less heating than when empty, less heating was required with higher screw speeds. This agrees with the relationships described by the equation to calculate SME (equation 2.13), namely that SME increases with increasing screw speed and decreasing feed rate.

Cooling was required to keep Zone A at 20 °C. Both extruders required less heating than in the “heated but empty” state to keep Zone B at 80 °C, possibly due to a high level of powder friction or the powder beginning to melt in this region. Depending on the processing conditions, heating or cooling was required in Zone C to hold the 120 °C temperature. Interestingly, more heating was required at higher screw speeds on the ZSK18 while the opposite was true for the ZSK40. In fact, the highest SME process condition with high screw speed and low feed rate resulted in the first instance of cooling (red dot at about –8% encircled and indicated with an asterisk *). The other two gray dots between –4% and –8% were run after the extruder entered the cooling state in this zone, and because material was limited, the extruder could not overcome this transition and reach a new steady state within the allocated processing time. However, with the last set of low SME process conditions at low screw speed and high feed rate, Zone C recovered and no longer needed cooling (data not explicitly shown). This observation reinforced the critical influence that mechanical energy from varied screw speed and feed rate can have on heating and cooling requirements. In addition, it is notable that the first mixing zone is located in or near to Zone C, potentially adding substantial mechanical energy, especially because this is where the polymer will undergo a solid-to-liquid phase transition, contributing thermal energy to the overall system due to more intensive shear than in conveying elements. This aspect of plasticating extrusion is noted in the analysis by McKelvey, in which he hypothesized that adiabatic operation in the early zones in the extruder may not be feasible (143).

The first barrel segment in Zone D, designated Barrel 1a, required either a slight bit of heating or cooling depending on the processing parameters. Again, as in Zone C, more heating was required at higher screw speeds on the ZSK18 while the opposite was true for the ZSK40. However, within the ranges tested, and considering the theory of SME, the observation on the ZSK18 is likely negligible while the observation on the ZSK40 is likely true. For all remaining barrel segments in Zone D, less heating was required to hold the temperature of 180 °C than in the empty state. Lastly, it was observed that the controller output for Barrel 2 in Zone D on the ZSK40 fluctuated substantially under the same processing conditions as when Zone C began to require cooling. Barrel 2 remained in this unstable state until the processing conditions were returned to the lowest SME state.

As for the die, the upper section of the ZSK40 die required either more or less heating than in the empty state, depending on the processing condition. Less heating was required when higher screw speeds were used. The lower section of the ZSK40 die always required less heating than in the empty state. Interestingly, more heating than in the empty state was required to hold the die at the set temperature of 180 °C for the ZSK18. The same was observed for the middle section of the die on the ZSK40. Given the fact that the melt is warmer than the barrel set temperature and given that the middle of the die on the ZSK40 extruder was insulated by the other two zones, this result is counterintuitive.

These observations of controller output agree with the dependency of the SME on the terms in the equation for its calculation (equation 2.13). Higher screw speeds and lower feed rates lead to higher SME. The higher the SME, the higher will be the viscous dissipation, leading to higher melt temperature and a higher contribution of heat coming from the melt. Thus, at high SME conditions, there will be a lower requirement for heating the barrel segments, and in extreme cases of very high SME, the barrel segments may need to cool.

The controller output values for each individual temperature zone also correlate well with the Ludovic® simulated local conduction energy (LCE) (Figure 6.16) given in units of energy per mass per unit length. A positive LCE, indicating heating is required, located in Zone C and at the beginning of Zone D, corresponded with

observations of controller output with values near the “heated but empty” controller output. Likewise, a negative LCE, indicating either cooling or perhaps heating less than when empty because Ludovic® does not consider heat loss to the environment, occurring in the majority of Zone D, corresponded with observations of controller output less than values needed when empty. The rank ordering with respect to SME is also in agreement with experimental values. The magnitude of local conducted energy corresponding to cooling is greater for the ZSK18 than for the ZSK40. To compare the absolute values of the LCE between scales, one must correct for the length of the extruder. When this correction is made, and the resulting cumulated conduction energy is compared, the values at each scale are more comparable although still indicative of more cooling occurring on the ZSK18 (results not shown). Note that Ludovic® calculates the LCE only where it assumes melt is located, in this case beginning at the first kneading block.

A more precise minimization of DeltaT and LCE along the length of the extruder might be obtained by further adjustment of each zone temperature. Depending on the screw design, especially near the mixing zones, the Zone D temperature could be broken down further into multiple temperature steps, instead of using one constant temperature for all barrel segments. If possible, a detailed energy or mass balance could be performed on each section of the extruder, taking into consideration the potential endothermic and exothermic processes occurring along the screw (146).

The dependency of total conducted energy on VSFL and screw speed is in agreement with that of the controller output (Figure 6.17). In addition, as reasoned above, the TCE decreases as SME increases (Figure 6.18), confirming experimental observations. Although the TCE values for this study are negative, they may actually account for the energy lost to the environment at the barrel-air interface. Exact calibration of this “gray-zone” could be an area of future research and would be highly dependent on extruder scale and model. Also of note in Figure 6.18 is the similarity in magnitude of the SME and TCE for both scales and between experiment and simulation.

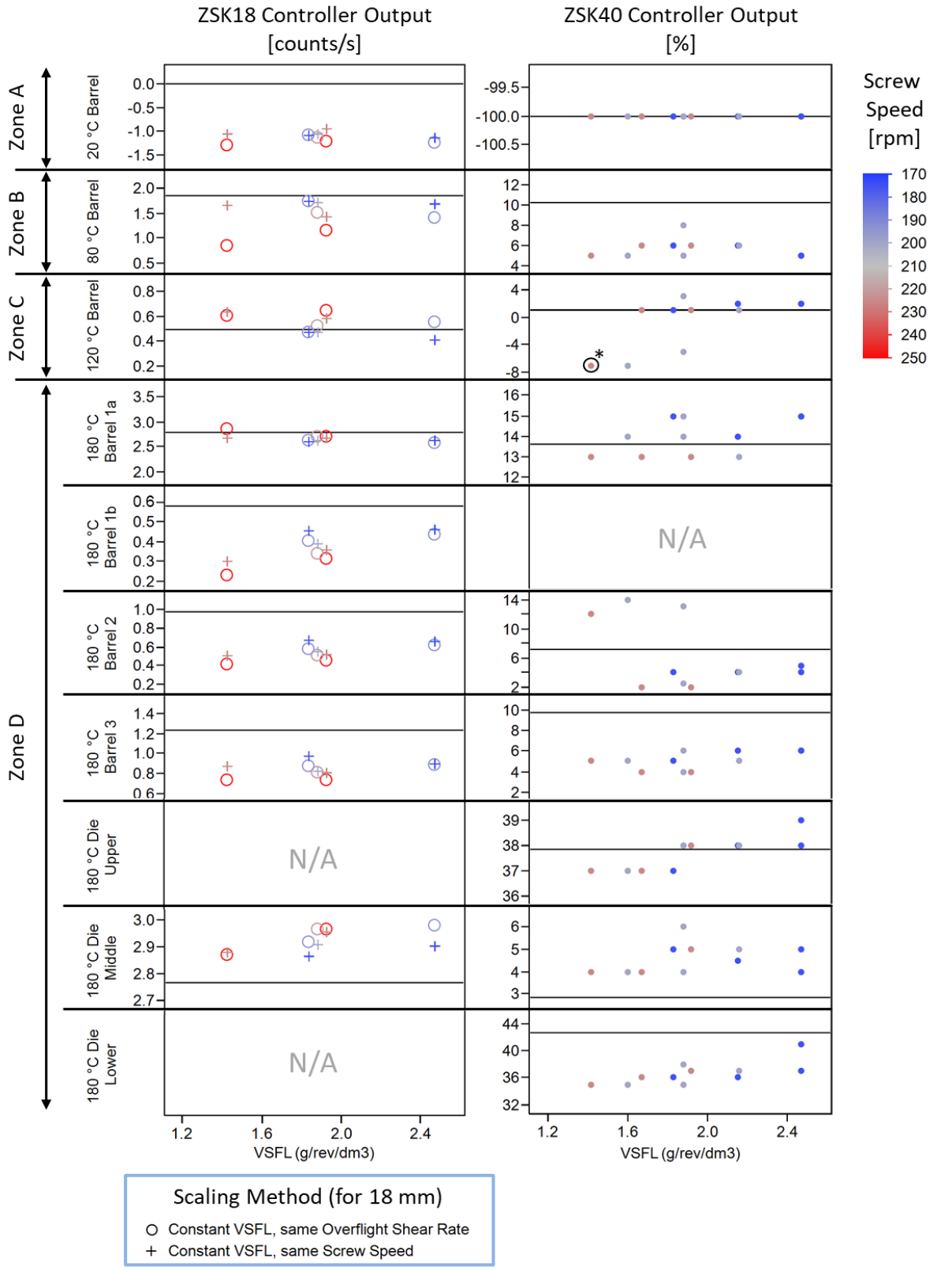


Figure 6.15 *ZSK18 & ZSK40 barrel and die controller output – heated & process running.*

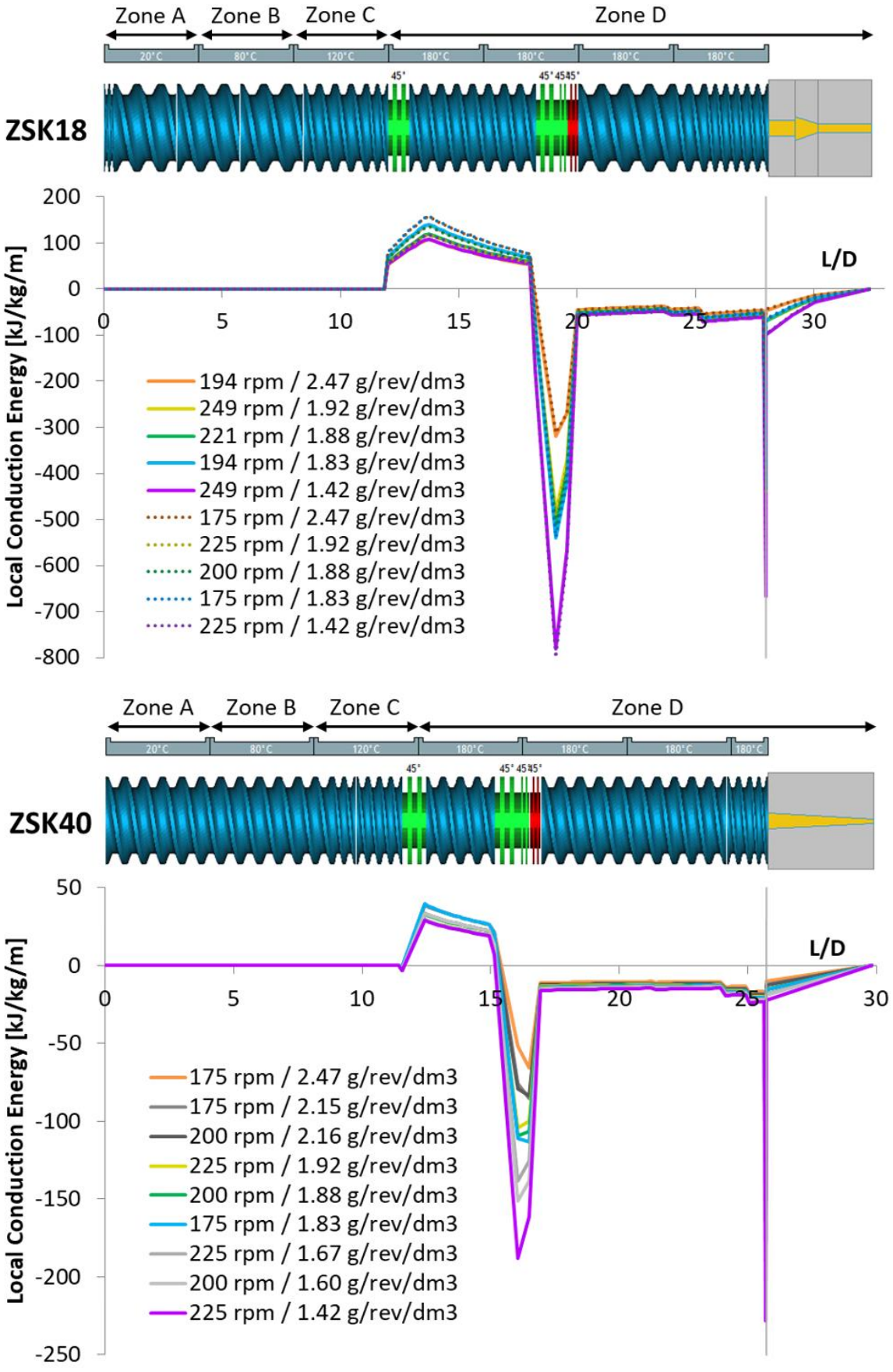


Figure 6.16 *ZSK18 & ZSK40 simulated local conduction energy vs. L/D.*

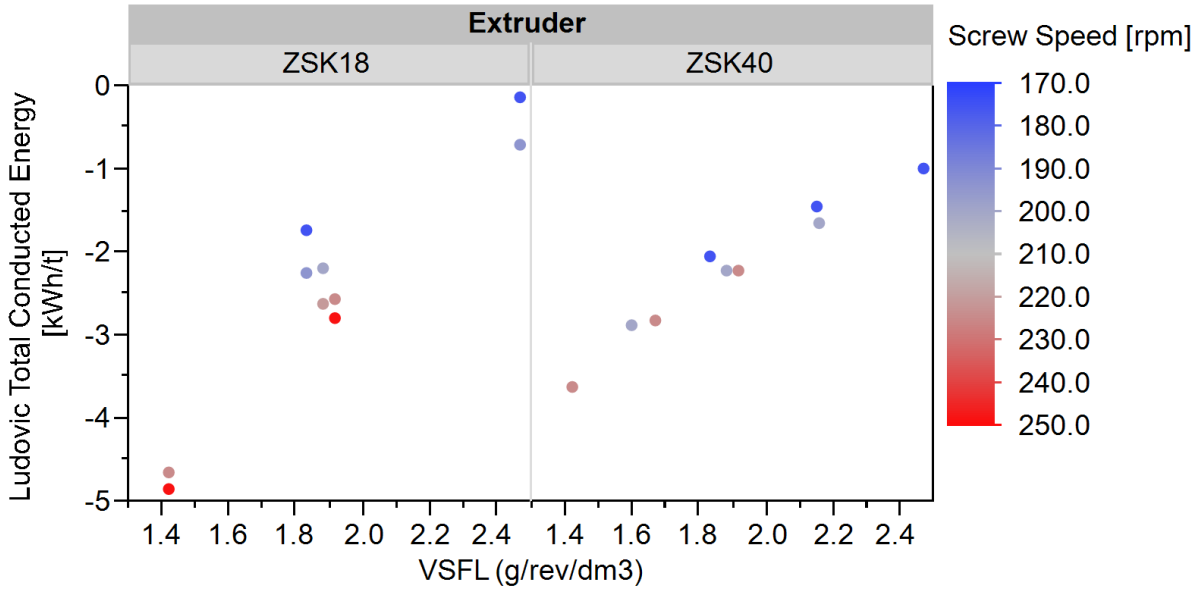


Figure 6.17. *Total conducted energy vs. VSFL and screw speed.*

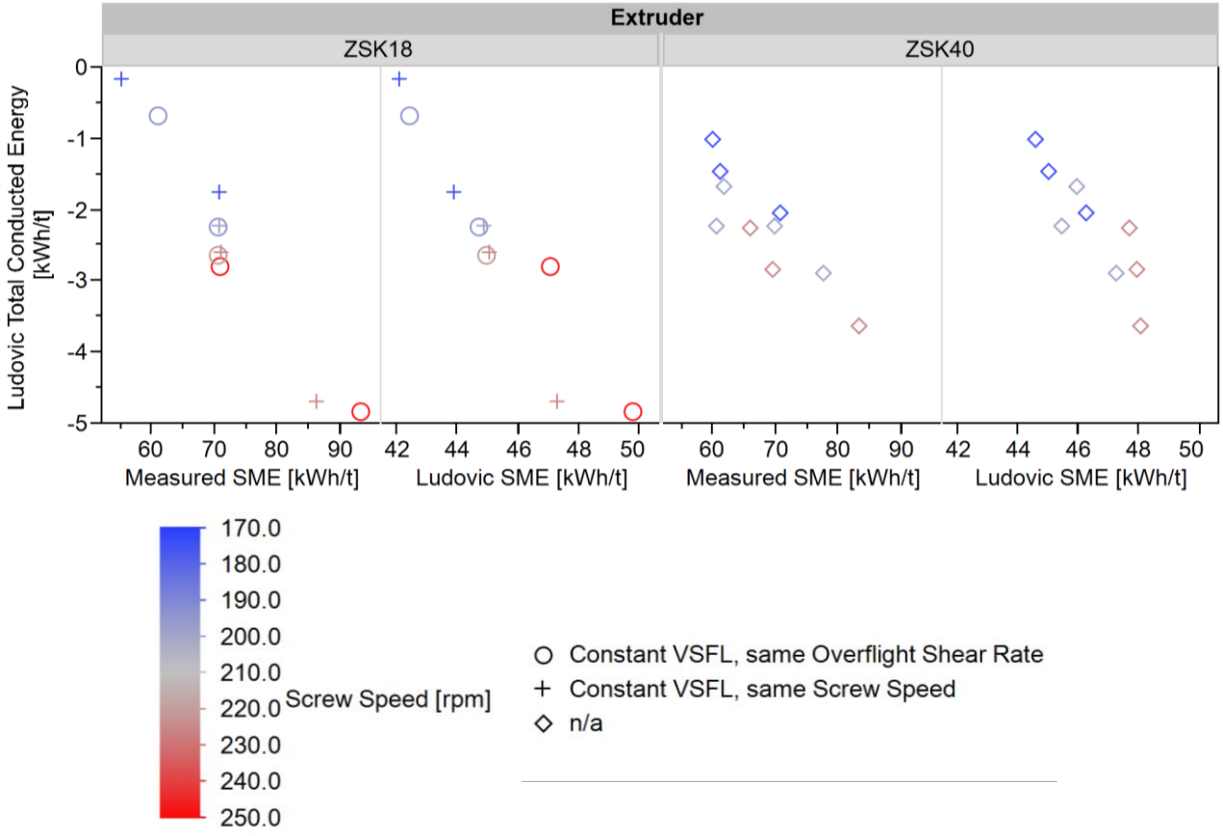


Figure 6.18. *Total conducted energy vs. measured and simulated SME*.

### 6.4.3 Assessment of Scaling via CQA Indicator Substance

The amount of residual crystallinity, a common CQA in hot-melt extrusion, was used as the key marker for assessing the agreement between extruder scales. For both scales, the residual crystallinity decreased as a function of increasing screw speed. The residual crystallinity varied less as a function of feed rate, reflected by the VSFL (Figure 6.19). Despite the approach to keep the fill level and either screw speed or shear rate constant between scales, the residual crystallinity was markedly lower at the ZSK40 than at the ZSK18. From this representation of the data, the decrease in residual crystallinity with increasing screw speed is also steeper at the ZSK40. The residual crystallinity also shows an inverse relationship with measured melt temperature, with a strong correlation coefficient $R^2$ of 0.88 (Figure 6.20). Considering only one Zone D temperature was tested in this scaling study, the regression equation is likely not suitable for predicting residual crystallinity at different Zone D temperatures. However, as shown in section 6.4.2.2, the measured die exit melt temperature and simulated screw exit melt temperature were also higher for the ZSK40 than at the ZSK18 (Figure 6.13 and Figure 6.14).

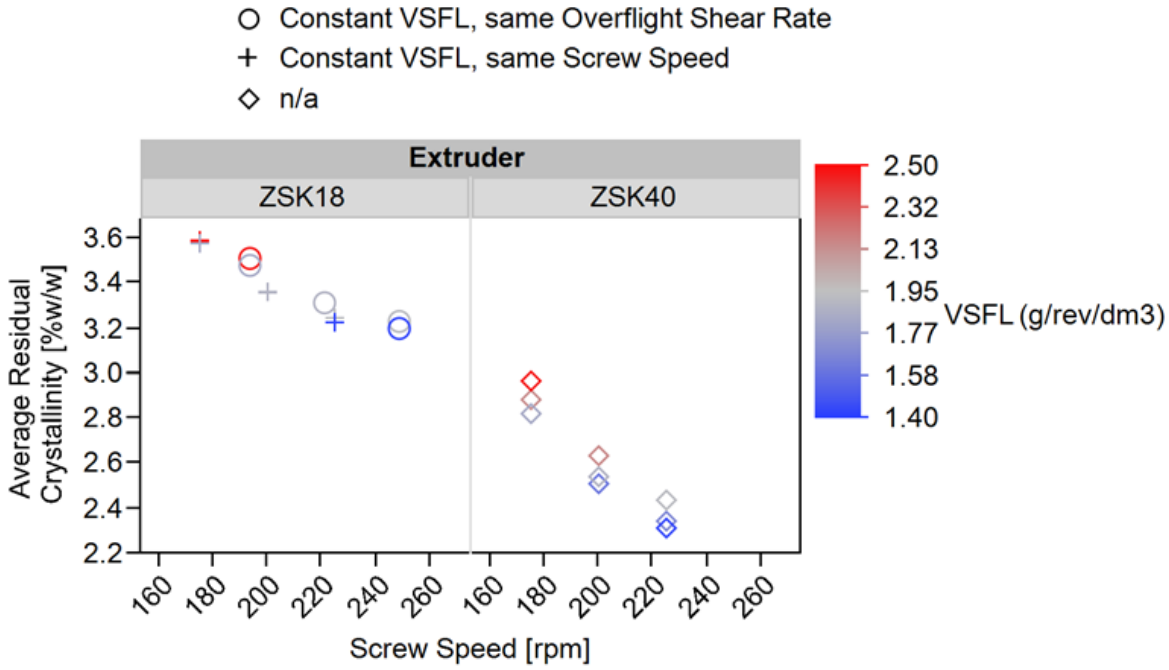


Figure 6.19 *Dependency of residual crystallinity on extruder scale and process parameters.*

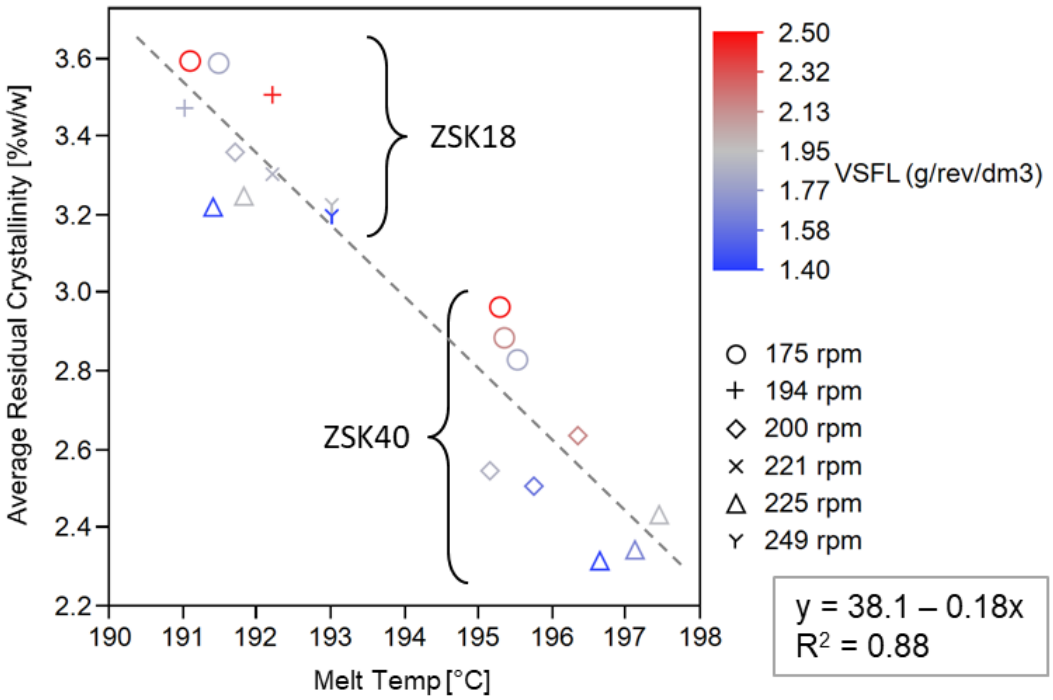


Figure 6.20 *Dependency of residual crystallinity on measured melt temperature at die exit.*

The measured residence time at both scales does not explain the discrepancy in measured residual crystallinity. The measured RTD varied in accordance with the well-known influence of varied screw speed and feed rate (136,137) and was similar for both extruders (Figure 6.21), with the MRT slightly higher at the ZSK18 than at the ZSK40. The distributions were also broader at the ZSK18 than at the ZSK40 (Figure 6.22). Due to experimental limitations on the ZSK18 extruder (too little telmisartan blend remaining after ZSK40 experiments), the RTD was only measured for the “same shear rate” scaling method. Simulation results supported the decision to not measure the RTD for all conditions due to the observation that the simulated MRTs from this scaling method were more similar to the ZSK40 MRTs than for the other scaling method (lower half of Figure 6.21). The apparent lack of influence of the RTD on residual crystallinity is supported by the CQA’s strong correlation with melt temperature (Figure 6.20) and, in the previous study, also independently of varying the feed rate and screw speed (Figure 5.8a). However, confirmation of these relationships would require a different experimental design with the possibility to independently vary the melt temperature and RTD.

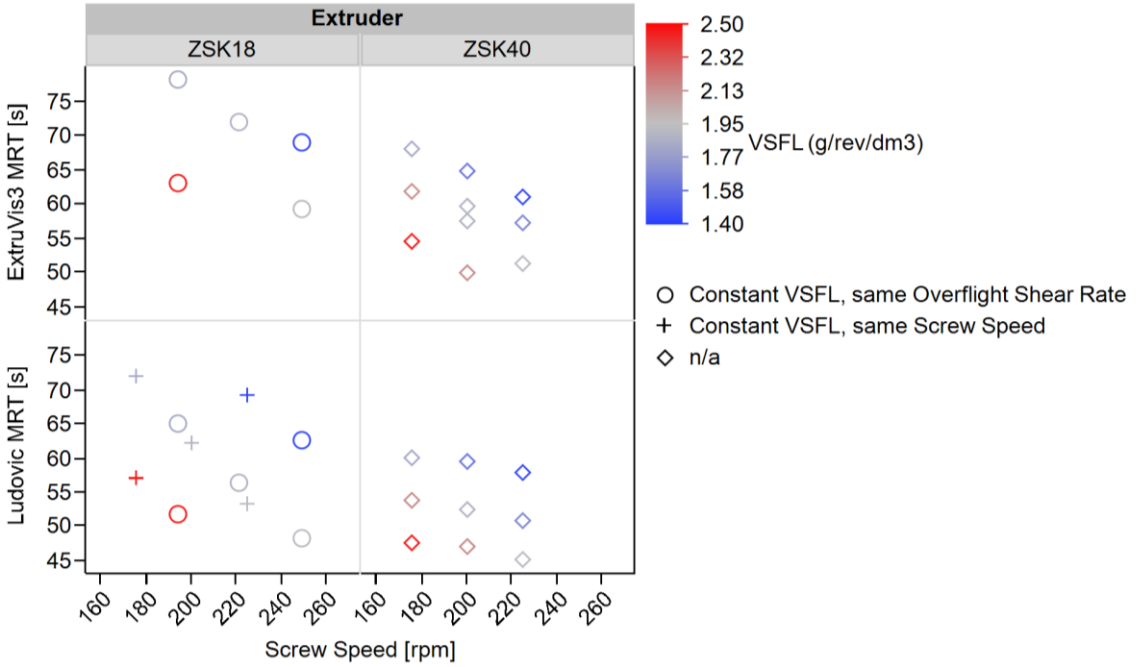


Figure 6.21 *Experimental and simulated MRT vs. processing conditions.*

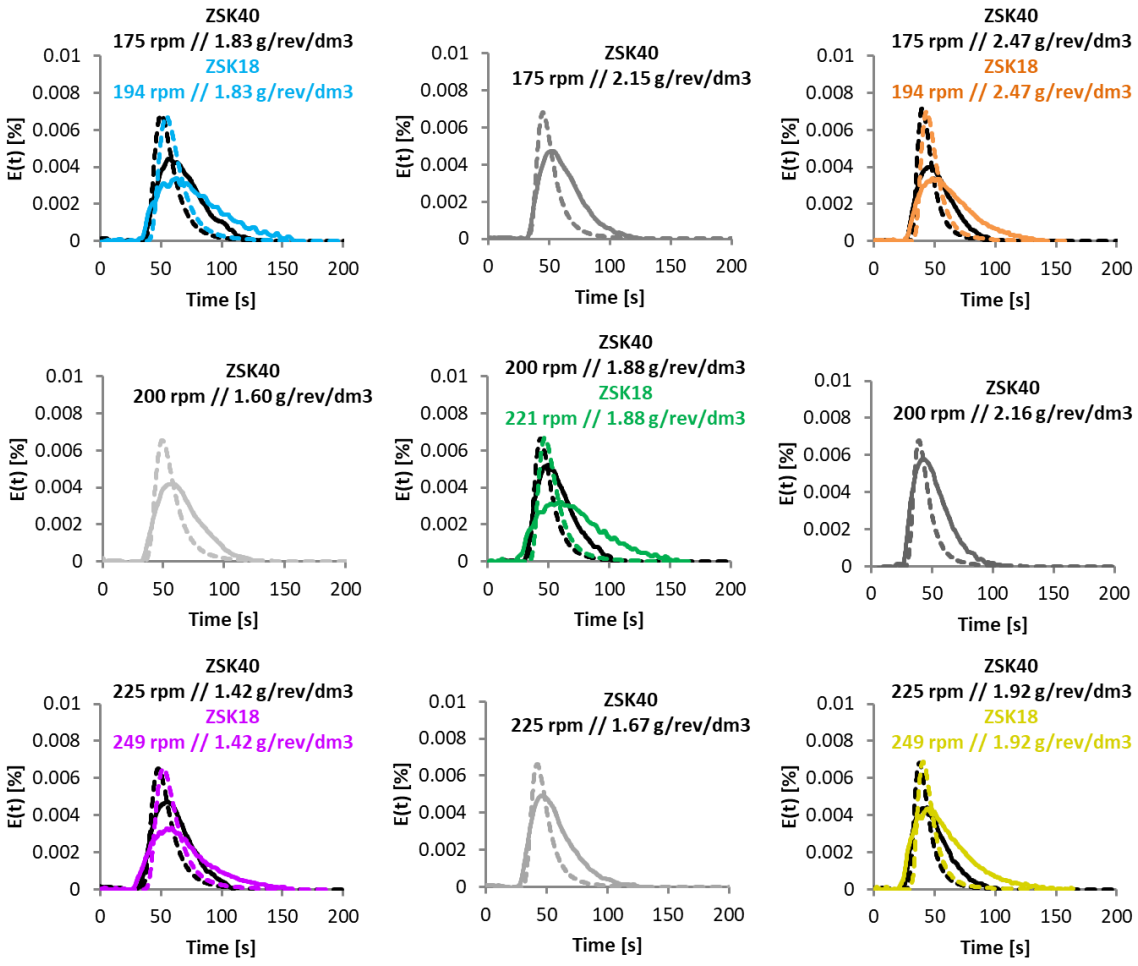


Figure 6.22 *Experimental and simulated RTD (dashed lines are simulated).*

The fill level, using a simple calculated approximation (equation 2.16), was higher for the ZSK18 than for the ZSK40 (Figure 6.23). Because the fill level in the extruder is challenging to measure directly due to its variation along the length of the extruder (60), although recent advancements have been made (155), and because this was not the primary focus of this study, this simple estimate was used. The exact reason for the discrepancy is not clear, but it could be related to the fact that the volume of the die was neglected in the calculation of the extruder volume, while at the same time, the die was included in the measurement of the RTD and subsequent calculation of MRT. However, the fill level could be related to the effective surface area for cooling; if at one scale relatively more melt is in contact with the inner barrel surface due to greater fill, and the SA:V ratio is greater, then more melt can be effectively cooled. Nevertheless, the relationship between fill level and residual crystallinity is not directly obvious and therefore this discrepancy is simply an observation. In addition, higher fill level in a smaller extruder can support scaling as the surface area to volume ratio changes. For example, perhaps an effective strategy could be to maintain the surface area to fill volume ratio constant.

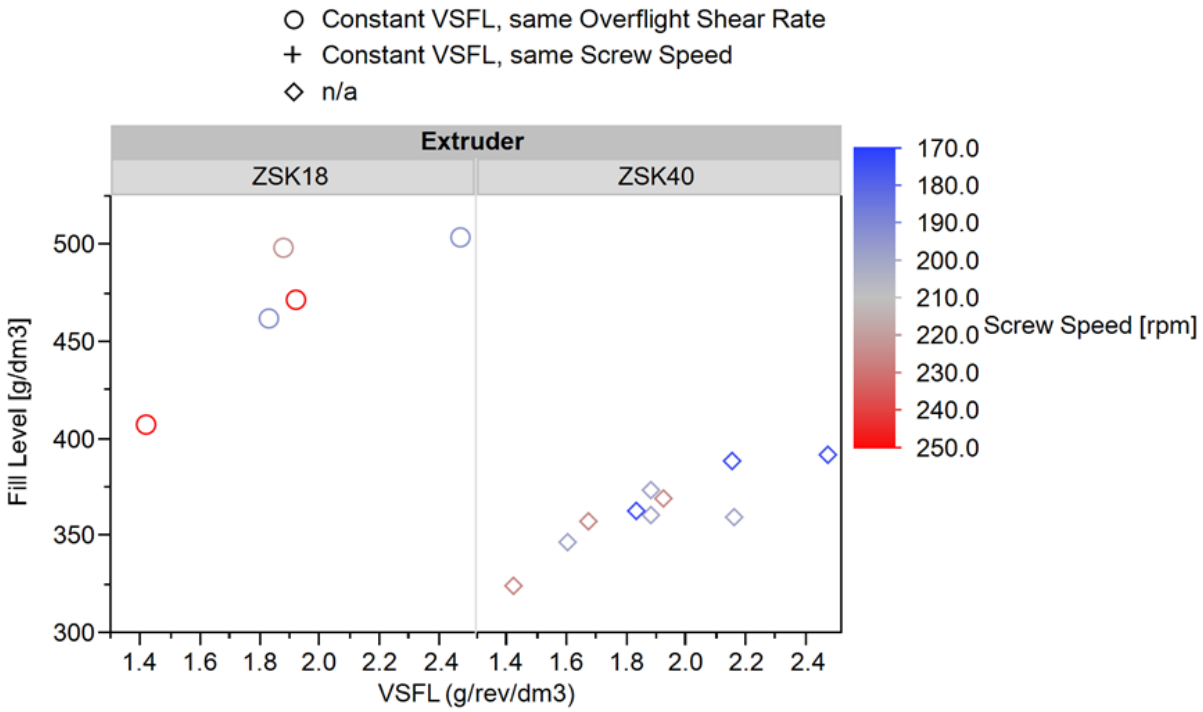


Figure 6.23 *Extruder fill level vs. VSFL and screw speed.*

The magnitude of measured and simulated SME is similar independent of extruder scale but the range of measured SME is much broader than for that of the simulated (Figure 6.24). Despite this, the two versions of SME are in the same order of magnitude and correlate similarly with VSFL and screw speed. Although the magnitude of simulated SME is similar for both scales, the range is narrower for the ZSK40 (Figure 6.24 and Figure 6.25). In addition, the melt temperature rise in the most intense shear region of the screw configuration, in this case the 2nd mixing zone, designated as “DeltaT max-barrel,” is similar for both extruder scales. However, the temperature rise is more sensitive to changes in simulated SME on the ZSK40 than on the ZSK18, as seen by the steeper slope for the ZSK40 (Figure 6.25). Despite this difference in sensitivity, which may be more substantial outside the presently explored design space, the similarity in SME at both scales indicates that mechanical energy is not the explanation for differing melt temperatures and resulting differences in residual crystallinity.

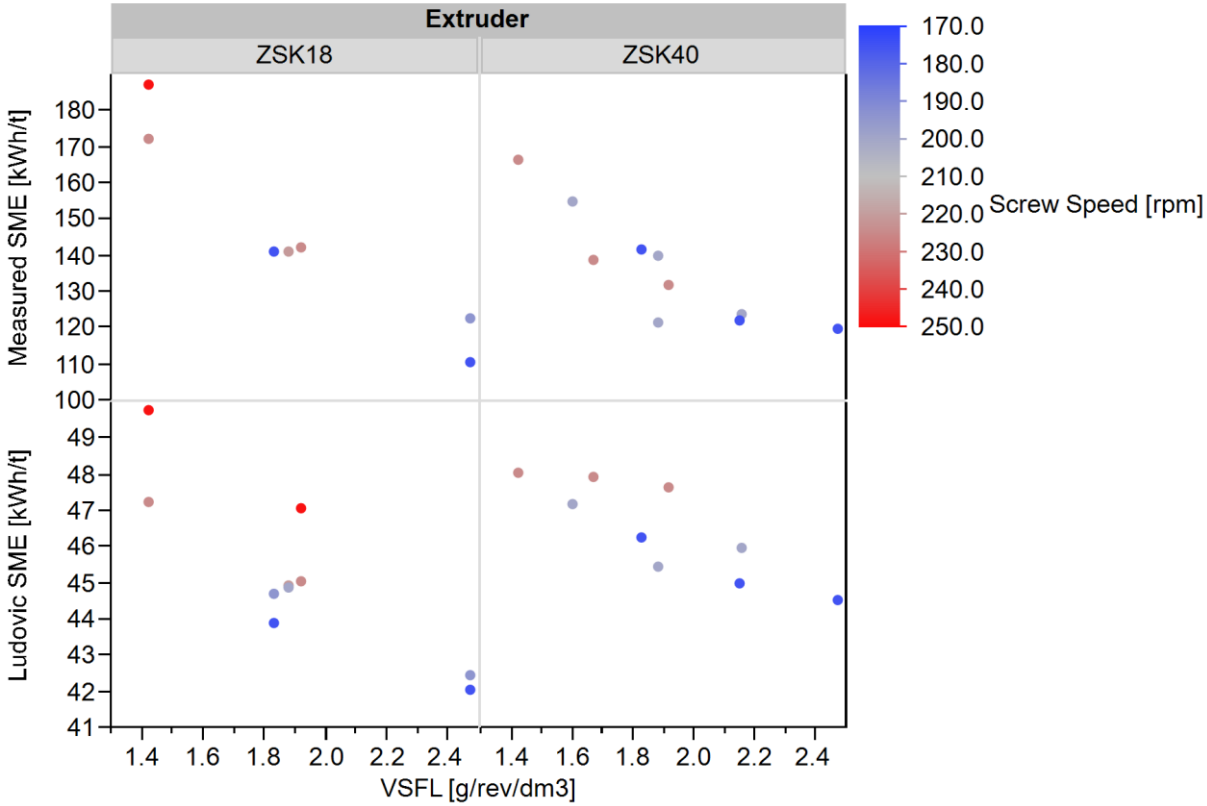


Figure 6.24 *Experimental and simulated SME vs. VSFL and screw speed.*

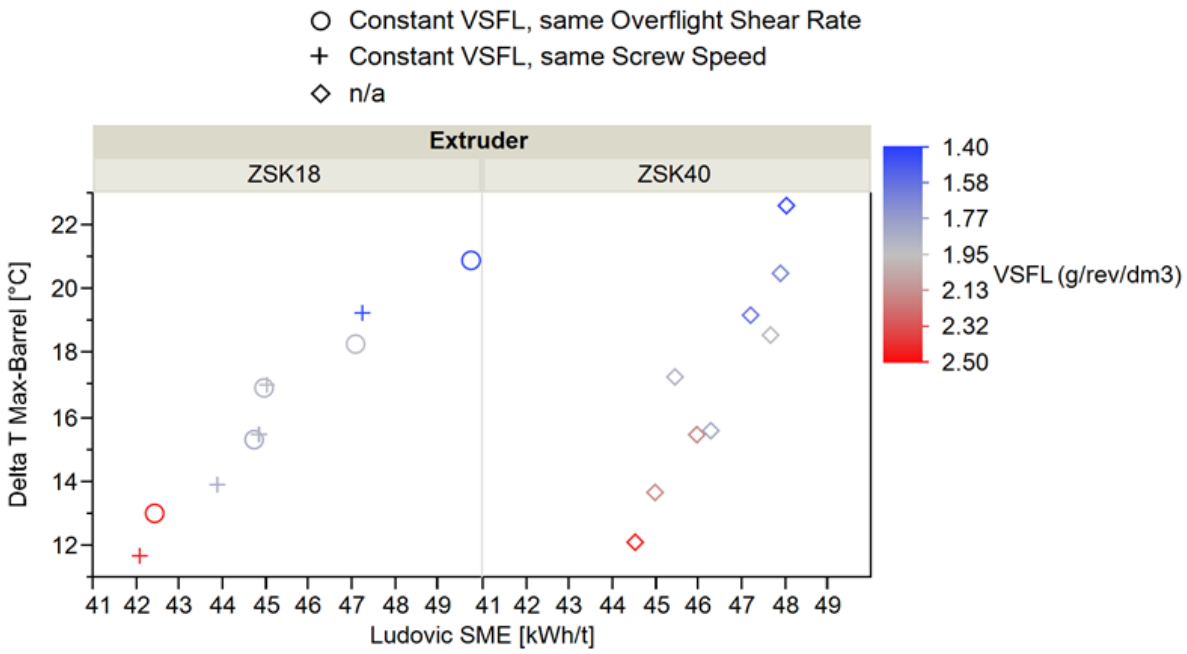


Figure 6.25 Simulated *DeltaT vs. simulated SME for various processing conditions.*

The combination of some of the scale-dependent differences may explain the difference in melt temperature and residual crystallinity. While the simulated maximum melt temperature was similar for both scales (Figure 6.14), the simulated screw exit (Figure 6.14) and measured melt temperatures (Figure 6.13) were higher and the MRT was shorter and distribution was narrower for the ZSK40 (Figure 6.21 and Figure 6.22). In addition, the available contact area per unit volume for cooling the melt was lower for the ZSK40 (Table 6.1). Also, both the fill level (Figure 6.23) and the magnitude of simulated cooling conducted energy (Figure 6.16) was greater for the ZSK18. Putting this all together, perhaps the greater surface area and slightly longer residence time on the ZSK18 allowed for greater cooling of the melt, limiting the extent of telmisartan dissolution.

Finally, one simple explanation for differences between scales could be that the real barrel temperature in contact with the melt may differ from the set point. In fact, depending on the location of heating elements in relation to the screw channel and the barrel temperature control thermocouples, the metal closest to the screw channel can vary from the set point. This discrepancy has been observed for the ZSK18 extruder used in this study; in particular, the inner part of the barrel is typically measured to be 7 °C hotter than the set point by inserting melt temperature

thermocouples into the sensor bores. Because of this, the barrel set point was adjusted accordingly, although slight offsets of this type could potentially lead to experimental error. On the other hand, this is again likely not the explanation for the temperature discrepancy because the simulated temperature was also different for both scales.

Depending on the sensitivity of a given CQA to melt temperature in a given formulation, the observed difference of 4-6 °C in melt temperature upon scaling may or may not be problematic. In the case of telmisartan, this temperature difference was great enough to result in a measurable difference in residual crystallinity. However, at process settings intense enough to eliminate residual crystallinity, such as higher barrel temperatures and higher mechanical energy, the design space may be broader, as was seen in Chapter 5. On the other hand, if a system is thermo-labile or exhibits fast degradation kinetics following dissolution, as was seen with torasemide and other systems (31,128,156), this difference in temperature may not be tolerable. If a narrow temperature range is required for a particular pharmaceutical product, for example one prone to thermal degradation, some options for adjusting the melt temperature could be to adjust the barrel temperature, the screw speed (146), or the volume of material in the extruder, for example, in accordance with the change in surface area available for conduction, as suggested earlier.

The methodology employed here for identifying the quasi-adiabatic point for a formulation for a given hardware setup, i.e. screw configuration, using simulation, and then and using simple scaling approaches coupled with simulation to select ranges for screw speed and feed rate to more precisely inform experimental design could be used to guide scaling approaches in other systems which seek to maintain constant CQAs and simultaneously balance the extruder thermal energy. The two ideas are not mutually exclusive and the relationships between all factors should still hold. Use of a phase diagram plus knowledge of the degradation propensity can support identification of the target melt temperature which will enable meeting the CQA ranges. Simulation can then be used to identify and build a process around the quasi-adiabatic point. Due to all of the inter-dependent and related factors which can affect the melt temperature, and because simulation accounts for these factors, simulation is a promising and useful tool to design a scale-up or -down study. If the

quasi-adiabatic point is too high, or too low, to achieve the required CQAs for a given drug substance, the formulation can be adjusted by addition of a plasticizer or anti-plasticizer, or the screw configuration could be adapted. The feed rate and screw speed, considering their individual impact on the SME, can then be adjusted to tune the process to the quasi-adiabatic point. As was highlighted in Chapter 5, the formulation is not just critical for bio-performance; formulation material properties are also critical to achieve ideal processing performance.

## 6.5 Conclusions

This investigation aimed to study the scaling of adiabatic processes using an indicator substance, the API itself, with support from simulation, and to avoid the need for cooling at large scale. Simulation helped to identify the best formulation for processing to both achieve adiabatic state and have a measurable CQA. Simulation also helped to identify the target barrel temperature that would result in an adiabatic state.

Quasi-adiabatic states were observed for both scales. In particular, a balance was achieved in which the DeltaT was positive due to some viscous dissipation but, on the whole, the extruder required less heating than in the empty state to maintain barrel set temperatures. Cooling in one barrel was required on the 40 mm scale in only one extreme high SME condition. The controller output correlated with both simulated total and local conducted energy, indicating that this simulated value is a good predictor of an adiabatic state. Use of the simplified scaling approaches of maintaining VSFL and shear rate resulted in slightly higher melt temperature and slightly less residual crystallinity at large scale. The telmisartan indicator system was sensitive enough to indicate that the slight difference in melt temperature between the two scales was too substantial. However, this melt temperature difference between scales may be insignificant in other cases in which the CQA is less sensitive to temperature. The agreement across scale in extruder conducted energy profile, melt temperature, residence time and SME indicate that the approach investigated in this study is appropriate for scaling an adiabatic process.

# 7 Materials and Methods

## 7.1 Materials

The materials used in the experiments are listed in Table 7.1. All materials were used as supplied unless otherwise noted. All materials were purchased except for Soluplus® which was kindly donated by BASF.

Torasemide API particle size was $d_{90}$ < 36 µm according to the material certificate of analysis. SOL was chosen for its relatively low processing temperature, beginning at 135 °C on the 10 mm diameter extruder based on torque limitations. PEG 1500 was chosen as a plasticizer for SOL based on its chemical similarity to the side chains of the SOL polymer as well as for its waxy-solid state at room temperature for ease of processing.

Telmisartan API displayed needle shaped morphology with primary particle size less than 50 µm. Agglomerates were present in the bulk API powder. COP and TW80 were chosen for their thermal stability and melt viscosity properties.

Table 7.1 *Material utilization.*

| **Material Name** | **Abbreviation** | **Function** | **Supplier** | **Modification prior to use** |
|---|---|---|---|---|
| Torasemide, anhydrous, polymorphic form I | TOR | API indicator substance | Arevipharma GmbH, Radebeul, Germany | none |
| Telmisartan, polymorphic form A | TEL | API indicator substance | Molekula GmbH, Munich, Germany | none |
| Polyvinyl caprolactam-polyvinyl acetate-polyethylene glycol graft copolymer (Soluplus®) | SOL | Matrix polymer | BASF Chemical Co., Ludwigshafen, Germany (donated) | none |
| vinylpyrrolidone-vinyl acetate copolymer (copovidone, Kollidon® VA 64) | COP | Matrix polymer | BASF SE, Ludwigshafen, Germany | dried or as received |
| Polyethylene glycol 1500 | PEG 1500 | Plasticizer | Carl Roth GmbH & Co. KG, Karlsruhe, Germany | milled and screened to <500 µm |
| polysorbate 80 Ph.Eur./NF (Tween® 80) | TW80 | Surfactant / plasticizer | Merck KGaA, Darmstadt, Germany | none |
| triethyl citrate | TEC | plasticizer | Merck KGaA, Darmstadt, Germany | none |
| Red iron(III) oxide Sicovit® Red 30 E172 | n/a | RTD tracer substance | BASF Chemical Co., Ludwigshafen, Germany | none |
| Two-component adhesive | n/a | Embedding matrix for microtome | Stanger PV GmbH & Co. KG, Espelkamp, Germany | none |
| Wacker® AK 10000 silicone fluid | n/a | Refractive index-matching fluid | Wacker Chemie AG, Munich, Germany | none |

Molecular structures of the two APIs, torasemide and telmisartan, which were used as indicator substances for the HME process are shown in Figure 7.1.

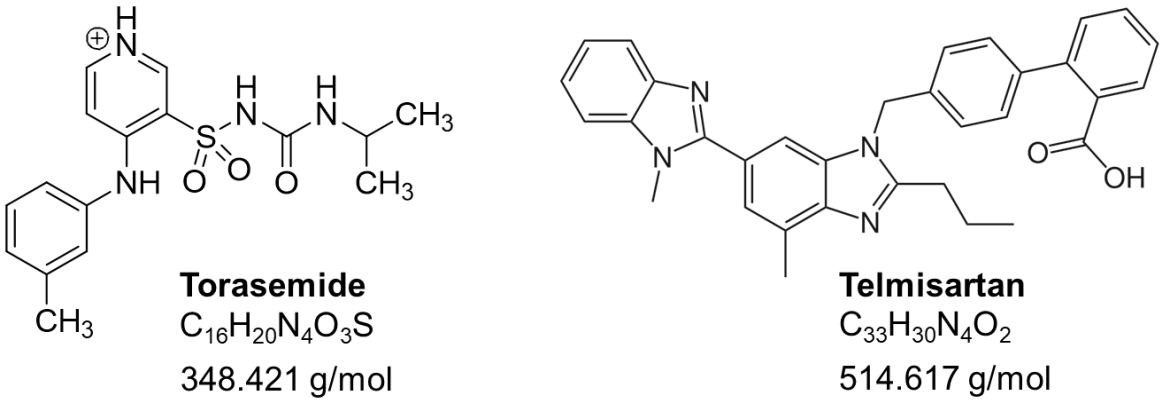


Figure 7.1 *Molecular structures for model APIs used as indicator substances.*

## 7.2 Methods

### 7.2.1 Equipment and Software

All equipment which were used to generate, analyze or characterize samples and/or data are listed in Table 7.2. All software programs which were used to generate, analyze or simulate data are listed in Table 7.3.

Table 7.2 *Equipment utilization.*

| Type | Name or Model | Manufacturer |
|---|---|---|
| **Sample Preparation** | | |
| Cryomill | Sample Prep Freezer/mill 6770 | Spex, Stanmore, UK |
| Vacuum oven | VDL 115 | Binder GmbH, Tuttlingen, Germany |
| Shaker-mixer blender | Turbula® T2F | Willy A. Bachofen AG – Maschinenfabrik Muttenz, Switzerland |
| Bin Blender | LM 40 or PM 400 | L. B. Bohle Maschinen + Verfahren GmbH, Ennigerloh, Germany |
| Sieving machine | BTS 200 | L. B. Bohle Maschinen + Verfahren GmbH, Ennigerloh, Germany |
| Impact mill | UPZ100 | Alpine Bau GmbH, Wals bei Salzburg, Austria |
| Conical twin screw extruder | Haake® Minilab | Thermo Fisher Scientific, Karlsruhe, Germany |
| 10 mm extruder | MicroLab | Rondol Industrie, Strasbourg, France |
| 18 mm extruder | ZSK18 MegaCompounder | Coperion GmbH, Stuttgart, Germany |
| 26 mm extruder | ZSK26 MegaCompounder | Coperion GmbH, Stuttgart, Germany |
| 40 mm extruder | ZSK40 MegaCompounder | Coperion GmbH, Stuttgart, Germany |
| **Analytical Sample Preparation** | | |
| texture analyzer | TA-XT2 | Stable Micro Systems, Surrey, United Kingdom |
| Microtome | Leica SM2500E | Leica Microsystems, Wetzlar, Germany |
| Ball mill | MM 400 | Retsch GmbH, Haan, Germany |
| Coffee grinder mill | Rotor GT95 | Rotor Lips AG, Uetendorf, Switzerland |
| Vacuum compression molding | MeltPrep | MeltPrep GmbH, Graz, Austria |
| **Process Characterization** | | |
| Adjustable focus thermal imager | Testo 882 | Testo SE & Co. KGaA, Lenzkirch, Germany |
| RTD instrument | ExtruVis 2 or ExtruVis 3 | ExtruVis, Riedstadt, Germany |
| **Sample Characterization/Analysis** | | |
| TGA | TGA/DSC 1 | Mettler-Toledo, GmbH, Giessen, Germany |
| TGA cooler | Ministat 125 | Huber Kältemaschinenbau AG, Offenburg, Germany |
| DSC | DSC1 | Mettler-Toledo, GmbH, Giessen, Germany |
| DSC immersion cooler | TC100 | Huber Kältemaschinenbau AG, Offenburg, Germany |
| Modulated DSC | TA Q2000 | TA Instruments, Eschborn, Germany |
| HPLC | Agilent 1100 series | Agilent Technologies, Waldbronn, Germany |
| HPLC column | Gemini NX-C18 | Phenomenex, Torrence, CA, USA |
| XRPD | Empyrean | PANalytical, Almelo, the Netherlands |
| Moisture analyzer | HB43-S | Mettler-Toledo GmbH, Giessen, Germany |
| Polarized light microscope | Leica DM2500M | Leica Microsystems, Wetzlar, Germany |
| Microscope digital color camera | Leica DFC295 | Leica Microsystems, Wetzlar, Germany |
| Digital microscope | VH-X | Keyence Deutschland GmbH, Neu-Isenburg, Germany |
| Optical transparency instrument | Haze-gard i | BYK-Chemie GmbH, Wesel, Germany |
| Oscillatory rheometer | Haake® MARS® II | Thermo Scientific, Karlsruhe, Germany |
| Laser diffraction for PSD | Mastersizer 3000 | Malvern Instruments GmbH, Herrenberg, Germany |

Table 7.3 *Software utilization.*

| Type | Name | Supplier |
|---|---|---|
| **Software** | | |
| TSE process simulation | Ludovic® v.6.1 or v.6.2 beta | Sciences Computers Consultants, Saint Etienne, France |
| DSC & TGA (data collection and analysis) | STAR$^e$ Software version 11.00a | Mettler-Toledo, GmbH, Giessen, Germany |
| Modulated DSC | Advantage™ | TA Instruments, Eschborn, Germany |
| HPLC (data collection and analysis) | Agilent OpenLAB CDS ChemStation Edition | Agilent Technologies, Waldbronn, Germany |
| XRPD (data collection) | X'Pert Data Collector version 5.2a | PANalytical, Almelo, the Netherlands |
| XRPD (data analysis) | X'Pert High Score version 4.1 | PANalytical, Almelo, the Netherlands |
| Melt viscosity measurements | RheoWin Job Manager and Data Manager, respectively, version 4.61.0003 | Thermo Scientific, Karlsruhe, Germany |
| Melt viscosity modeling | OriginLab version 8.5 | Originlab Corporation, Northampton, MA, USA |
| Residence time distribution | ExtruVis 2 Excel® analysis spreadsheet V06 or ExtruVis 3 software V1.0.0.22 | ExtruVis, Riedstadt, Germany |
| General data analysis | JMP® v.10 | SAS Institute Inc., Cary, NC, USA |

### 7.2.2 Sample Preparation

#### 7.2.2.1 Physical Mixtures

*Torasemide*

Physical mixtures were prepared for DSC analysis. Samples were prepared in the composition of 10 %w/w torasemide, 10 %w/w PEG 1500, 80 %w/w SOL and cryomilled using a Sample Prep Freezer/mill 6770. Milling program began with 5 min temperature equilibration in a liquid nitrogen bath followed by 2 min of milling at 10 cycles per second. Batch size was 200 mg in an ~5 mL stainless steel tube.

*Telmisartan*

Physical mixtures for the API solubility phase diagram generation were cryomilled using a Sample Prep Freezer/mill 6770 with 5 min pre-cooling and 1 minute milling at 10 cycles per second. Batch size was 200 mg in an ~5 mL stainless steel tube.

#### 7.2.2.2 Extrudates

*Torasemide*

Extrudate production involved preparation of blends, extrusion, and ball milling of extrudates for analysis. Blending involved de-lumping the torasemide by passing it through a 500 µm screen followed by blending it with the PEG 1500 and SOL (dispensed amount was adjusted for moisture) in a Turbula® blender for 5 min. Blends and extrudates were stored refrigerated at 5 °C. Blends were prepared in 500 g quantities in 2 L containers.

Extrusion experiments were conducted with a 10 mm (actual 10.9 mm) co-rotating twin-screw extruder. The extruder was fed via a volumetric feeder with two co-rotating feeding screws with adjustable speed; feed rate was controlled in this way and throughput was measured as mass exiting the die per time. Samples of extrudate were collected only during steady state, defined by a constant torque reading. The processing zone of the extruder contained 4 temperature zones: zone 1 was cooled by recirculating water set to 10 °C, zone 2 was set to 80 °C, and zone 3, composed of the last two temperature-controlled regions, was varied. The die was also heated and was set to the same temperature as zone 3; collectively they are referred to as “main barrel and die temperature” (Figure 4.2). The die geometry is known as an 8-0 shape with the following dimensions: 22.9 mm length, 11 mm inlet diameter, 2 mm outlet diameter, and 9 mm centerline for inlet portion. Four screw configurations were used (Figure 4.2, Table 7.4). Note that die geometry, designated in yellow, is not to scale. Extrusion experiments were conducted in 2 separate studies, details explained in Table 4.1).

The three venting configurations listed in Table 4.1 were selected to produce extremes in moisture removal from the extruder. The early closed-end closed configuration enabled a high-moisture process while the two early open configurations enabled lower-moisture containing processes, and especially with moisture removal prior to intense mixing. A fourth option, early closed-end open, was not included in the study because it represents an intermediate moisture-level condition. In this way, high and low moisture content environments were created to look at the effect on the evolution of the different degradant species.

Table 7.4 *Screw configurations. Note: all elements are double-flighted.*

| Screw Element # | 1mix5disk60degFW | 2mix5disk60degFW | 2mix5disk60degFWBW | 2mix5disk60degFW-5disk60degFWBW |
|---|---|---|---|---|
| 1 | C / FW / 18.92 / 18.92 | C / FW / 18.92 / 18.92 | C / FW / 18.92 / 18.92 | C / FW / 18.92 / 18.92 |
| 2 | C / FW / 18.92 / 18.92 | C / FW / 18.92 / 18.92 | C / FW / 18.92 / 18.92 | C / FW / 18.92 / 18.92 |
| 3 | C / FW / 18.92 / 18.92 | C / FW / 18.92 / 18.92 | C / FW / 18.92 / 18.92 | C / FW / 18.92 / 18.92 |
| 4 | C / FW / 18.92 / 18.92 | C / FW / 18.92 / 18.92 | C / FW / 18.92 / 18.92 | C / FW / 18.92 / 18.92 |
| 5 | C / FW / 13.51 / 13.51 | C / FW / 13.51 / 13.51 | C / FW / 13.51 / 13.51 | C / FW / 13.51 / 13.51 |
| 6 | C / FW / 13.51 / 13.51 | C / FW / 13.51 / 13.51 | C / FW / 13.51 / 13.51 | C / FW / 13.51 / 13.51 |
| 7 | K / FW / 13.51 / 5 / 60° | K / FW / 13.51 / 5 / 60° | K / FW / 13.51 / 5 / 60° | K / FW / 13.51 / 5 / 60° |
| 8 | C / FW / 13.51 / 13.51 | C / FW / 13.51 / 13.51 | K / BW / 13.51 / 5 / -60° | C / FW / 13.51 / 13.51 |
| 9 | C / FW / 13.51 / 13.51 | C / FW / 13.51 / 13.51 | C / FW / 13.51 / 13.51 | C / FW / 13.51 / 13.51 |
| 10 | C / FW / 13.51 / 13.51 | C / FW / 13.51 / 13.51 | C / FW / 13.51 / 13.51 | C / FW / 13.51 / 13.51 |
| 11 | C / FW / 13.51 / 13.51 | C / FW / 13.51 / 13.51 | K / FW / 13.51 / 5 / 60° | K / FW / 13.51 / 5 / 60° |
| 12 | C / FW / 13.51 / 13.51 | K / FW / 13.51 / 5 / 60° | K / BW / 13.51 / 5 / -60° | K / BW / 13.51 / 5 / -60° |
| 13 | C / FW / 18.92 / 18.92 | C / FW / 18.92 / 18.92 | C / FW / 18.92 / 18.92 | C / FW / 18.92 / 18.92 |
| 14 | C / FW / 13.51 / 13.51 | C / FW / 13.51 / 13.51 | C / FW / 13.51 / 13.51 | C / FW / 13.51 / 13.51 |
| 15 | C / FW / 13.51 / 13.51 | C / FW / 13.51 / 13.51 | C / FW / 13.51 / 13.51 | C / FW / 13.51 / 13.51 |
| 16 | C / FW / 8.10 / 8.10 | C / FW / 8.10 / 8.10 | C / FW / 8.10 / 8.10 | C / FW / 8.10 / 8.10 |
| 17 | C / FW / 8.10 / 8.10 | C / FW / 8.10 / 8.10 | C / FW / 8.10 / 8.10 | C / FW / 8.10 / 8.10 |
| 18 | C / FW / 8.10 / 8.10 | C / FW / 8.10 / 8.10 | C / FW / 8.10 / 8.10 | C / FW / 8.10 / 8.10 |
| 19 | C / FW / 11.00 / 11.00 | C / FW / 11.00 / 11.00 | C / FW / 11.00 / 11.00 | C / FW / 11.00 / 11.00 |
| Notation for Conveying elements I: direction / length / pitch<br>Notation for Kneading elements (K): direction / length / number of disks / staggering angle | | | | |

*Telmisartan (Chapter 5)*

*Preparation of the Matrices*

Copovidone powder, approximately 2 kg, was dried in a vacuum oven VDL 115 at 40 °C for approximately 3 days to reduce the moisture content prior to blend preparation. This dried material was used to prepare the binary TEL / COP blend which was used for extrusion.

A placebo mixture of 5.5 %w/w TW80 in COP was prepared using a 26 mm, 24 L/D co-rotating twin screw extruder with vacuum vent prior to die, screw configuration composed of conveying and kneading disk elements with two mixing-zones, calender and cooling belt. Approximately 20 kg of calendered extrudate was produced but not

used in full. The concentration of TW80 reduced to approximately 5 %w/w when 10 %w/w TEL was added to the extruded matrix.

The calendered material was milled using an Alpine impact mill with rotor speed 12000 rpm, 1 mm round-hole screen. To ensure particle size distribution similarity to the dried COP, the milled extrudate was further sieved and only the fraction less than 200 µm was used for further processing. To confirm similarity in matrix particle size, the particle size distribution (PSD) of both the COP and milled and screened TW80 / COP extrudate were measured using a Mastersizer 3000 laser diffraction instrument with dry powder dispersion module. Approximately 2-5 g of material was measured 3 times for 30 s each, fed using the vibratory feeder and dispersed with 2 bar air pressure keeping the obscuration level between 2-8%, and measurements were analyzed according to the Fraunhofer approximation and averaged.

*Blending of the Materials for Extrusion*

Blends of 10 %w/w TEL in either dried COP or milled and sieved TW80 / COP extrudate were prepared by a blending-sieving-blending process to produce a uniform blend and minimize agglomerates of the API observed in the neat drug substance. The mixtures, 2 kg batch size, were blended for 2 minutes at 15 rpm in a 10 L bin, discharged and hand sieved through a 500 µm screen, re-charged to the bin and blended for a further 10 minutes at 15 rpm.

The moisture content of the blends was measured prior to extrusion via loss-on-drying (LOD) using a HB43-S moisture analyzer. Approximately 5.5-6 g of blend was heated to 105 °C and held until mass was constant within ± 1 mg for 100 s. The bulk density of the blends was also calculated from the mass and bulk volume occupied by the aerated powder filled into a 250 mL graduated cylinder.

*Extrusion of Telmisartan Blends*

Both blends were extruded under a set of identical processing conditions (Table 5.1) using a ZSK18 18 mm, 28 L/D co-rotating twin screw extruder. The screw configuration contained two zones with forward (green) and reverse (red) 60° kneading disks (Figure 5.3, Table 7.5) and vacuum vent ports prior to 1$^{st}$ mixing zone

and prior to the die. The second vacuum port pressure was set to 900 mbar. The extruder barrel was composed of 7 barrel segments or temperature zones plus die set to 20/80/120/T/T/T/T/T °C, with T meaning target temperature. The target temperature was varied together in the experiment and is referred to as “barrel temperature.” The screw speed and feed rate were varied together in order to maintain the same degree of fill in the extruder barrel using the simple specific feed load equation, equation 2.14 of mass flow rate divided by screw speed (62).

Thin strands of extrudate were collected, separated from one another, and allowed to cool to room temperature before storage in air tight bottles. Samples were stored at room temperature prior to further processing.

Table 7.5 *Screw configurations. Note: all elements are double-flighted.*

| Screw Element # | Screw Element Description | Screw Element # | Screw Element Description |
|---|---|---|---|
| 1 | C / FW / 8.00 / 8.00 (spacer element) | 11 | C / FW / 24.00 / 24.00 |
| 2 | C / FW / 48.00 / 36.00 | 12 | K / FW / 24.00 / 5 / 60° |
| 3 | C / FW / 48.00 / 36.00 | 13 | K / BW / 24.00 / 5 / -60° |
| 4 | C / FW / 36.00 / 24.00 | 14 | C / FW / 36.00 / 36.00 |
| 5 | C / FW / 36.00 / 24.00 | 15 | C / FW / 24.00 / 24.00 |
| 6 | C / FW / 24.00 / 24.00 | 16 | C / FW / 24.00 / 24.00 |
| 7 | C / FW / 24.00 / 24.00 | 17 | C / FW / 12.00 / 12.00 |
| 8 | K / FW / 24.00 / 5 / 60° | 18 | C / FW / 12.00 / 12.00 |
| 9 | C / FW / 24.00 / 24.00 | 19 | C / FW / 12.00 / 12.00 |
| 10 | C / FW / 24.00 / 24.00 | 20 | C / FW / 16.00 / 16.00 |
| Notation for Conveying elements I: direction / length / pitch<br>Notation for Kneading elements (K): direction / length / number of disks / staggering angle | | | |

*3 %w/w Triethyl Citrate in COP*

A mixture of 3 %w/w triethyl citrate in COP was prepared in a coffee grinder type mill and extruded at 160 °C and 100 rpm using a Minilab co-rotating conical screw extruder. The extrudates were milled again in a coffee grinder type mill and stored at ambient conditions prior to further testing.

*Telmisartan (Chapter 6)*

The process flow diagram for sample preparation is shown in Figure 6.7.

*Preparation of the Matrix*

A mixture of 6 %w/w TW80 in COP was prepared using a 40 mm, 25.725 L/D co-rotating twin screw extruder with vacuum vent prior to die at 500 mbar, 2 mixing-zone screw composed of conveying and kneading disk elements (Figure 6.5, Table 6.2), calender and cooling belt. Approximately 100 kg was prepared.

The calendered material was milled using an impact mill using a 2-step procedure. First the calendered material was milled with rotor speed 12000 rpm, 1.3 mm conidur screen to form a coarse granulate. Second, the granulate was milled with rotor speed 11000 rpm and 0.8 mm conidur screen to ensure similarity to the dried COP and milled placebo extrudate used in Chapter 5. To confirm similarity in matrix particle size, the extrudate was measured identically as described in methods for Chapter 5.

*Blending of the Materials for Extrusion*

A blend of 10 %w/w TEL in milled TW80/COP extrudate were prepared by a blending-sieving-blending process to produce a uniform blend and minimize agglomerates of the API observed in the neat drug substance. The blend, about 110 kg in two portions due to blender container fill volume, was blended for 10 minutes at 6 rpm in a Bohle MCL 200 L container, discharged and de-lumped through a 1.5 mm screen installed in a Bohle BTS 200 sieving machine, collected in a second Bohle MCL 200 L container and blended for a further 10 minutes at 6 rpm. Blending was performed using a Bohle PM 400 machine.

*Extrusion with Telmisartan*

The blend was extruded according to scaled conditions using both 18 mm and 40 mm extruders. The extruder characteristics are listed in Table 6.1, schematics of the extruder configurations are shown in Figure 6.5, the screw configurations are listed and compared in Table 6.2, and the barrel and die temperature profile is listed in Table 6.3. The feed rate and screw speed process parameters for the 40 mm scale are listed in Table 6.4, while those for the two scaling methods run on the 18 mm scale are listed in Table 6.6 and Table 6.7. The vacuum port pressure was set to 500 mbar. The experiment design is explained in section 6.3 and selection of the process

parameters is explained in section 6.3.2.2. Approximately 100 kg of blend was extruded at the 40 mm scale while less than 10 kg remained for the 18 mm scale.

Thin strands of extrudate were collected, separated from one another in metal bowls, and allowed to cool to room temperature before collection in air tight bottles. Samples were stored at room temperature prior to further processing.

### 7.2.3 Process Characterization

#### 7.2.3.1 Melt Temperature

The melt temperature of the extrudate was measured at the exit of the die using a Testo 882 adjustable focus thermal imager. The hottest temperature recorded on the extrudate strand in the focused image was taken as the melt temperature. A literature value of 0.9 was used for the thermal emissivity (56).

#### 7.2.3.2 Residence Time Distribution (RTD)

Experiments discussed in section 4.4.2 were measured with the ExtruVis 2 and accompanying analysis spreadsheet. Experiments discussed in section 4.4.3 and in Chapter 6 were measured using the ExtruVis 3 and accompanying software. Mean residence times (MRT) were determined using the algorithms described in the equipment documentation literature. Red iron(III) oxide was used as a tracer substance and added as a pulse in quantities <1/100 of the throughput.

#### 7.2.3.3 Controller Output

The controller output on the ZSK18 consisted of a cumulative count of heating or cooling events at least 150 ms in duration. This accumulation was plotted over time and the slope was taken as the controller output signal. When both heating and cooling events were occurring in a given temperature zone, aka barrel segment or die, during steady state, both slopes were calculated and summed. For the ZSK40, the controller output, expressed as either a positive or negative percentage, was used directly.

### 7.2.4 Analytical Sample Preparation

Torasemide extrudates were ball milled using 50 mL jars and 20 mm diameter balls for 10 s at 30 Hz, followed by collection of powder <500 µm via sieving. Milled extrudates were stored refrigerated at 5 °C prior to further analysis and characterization.

Telmisartan extrudates were milled in a coffee grinder type mill and sieved <500 µm. Powder was stored at room temperature in air-tight bottles prior to further analysis and characterization.

### 7.2.5 Sample Characterization/Analysis

TGA experiments for all samples were performed using a TGA/DSC 1 with a Ministat 125 under nitrogen gas flow. All conventional DSC experiments were performed using a DSC 1 with auto-sampler with a TC100 immersion cooler under nitrogen gas flow. Calibration of the DSC was performed with zinc and indium standards.

#### 7.2.5.1 Torasemide

*TGA*

TGA was used to characterize the degradation temperature of a neat unprocessed torasemide sample. A sample mass of 33.5 mg was filled in a 100 µL aluminum pan and was heated from 25 to 250 °C at a heating rate of 10 K/min under nitrogen gas flow.

*DSC*

A DSC was used as an oven for controlled heating studies on the micro-scale as well as for heat flow characterization. Measurements were conducted under nitrogen gas flow.

*Controlled Heating of Neat Torasemide and Physical Mixtures*

DSC pans, 40 µL aluminum, containing approximately 5 mg of sample were heated from room temperature to various end temperatures at a heating rate of 10 K/min.

The end temperature range for neat torasemide was 100-180 °C while a range of 40-160 °C was used for physical mixtures. Both lid-pierced, with 3 large vent holes, and hermetically sealed pans were prepared for each end temperature to study the effect of moisture. Samples were removed from the DSC via the auto-sampler and were allowed to cool at ambient conditions.

*Determination of Torasemide Dissolution Starting Temperature in Soluplus® / PEG 1500 Matrix*

An 8.5 mg sample of extrusion blend, dried in a vacuum oven to remove moisture, was heated in a 40 µL aluminum pan with pierced lid from 25-180 °C at a heating rate of 10 K/min. The dissolution endotherm was visible from the thermogram, but the exact point of dissolution onset was identified via the first derivative of the original curve.

*HPLC*

HPLC was conducted to identify the presence and relative amounts of degradation products of torasemide formed during DSC studies and extrusion processing, as well as to quantify the total amount of torasemide in the extrudates, i.e. crystalline plus dissolved. Analysis was performed using an Agilent 1100 series. The chromatographic separation was performed on a Gemini NX-C18 analytical column (150 mm long, 2.1 mm diameter, 3 µm particle size, 110 Å pore size). The mobile phase was water with 0.1 %v/v trifluoroacetic acid (85%) (mobile phase A) and acetonitrile with 0.05 %v/v trifluoroacetic acid (85%) (mobile phase B) with linear gradient elution: 0 min, B 10%; 5 min, B 15%; 15 min, B 65%; 17 min, B 80%; 18 min, B 10% (total time 25 min). The flow rate was 0.4 mL/min, the injection volume was 2 µL, and the detection was performed at 280 nm. All reagents were of HPLC grade.

Standard solutions of neat torasemide in 1+1 (v/v) acetonitrile (I) + water were prepared at 0.1 mg/mL. Ball-milled extrudate samples were dissolved at concentrations of approximately 5 mg of extrudate per 50 mL 1+1 (v/v) acetonitrile + water. Samples prepared in DSC pans containing approximately 5 mg of analyte were dissolved in 50 mL 1+1 (v/v) I + water.

Typical chromatograms showed 1-3 peaks, depending on their composition and how they were processed. The molecular structure of the species present in each peak was investigated by mass spectrometry. For details, please see Appendix 10.1. The first eluent at retention time (RT) 2.8 min is a thermal degradant, m/z 290, the second at RT 6.5 min is a hydrolysis degradant, m/z 264, identical to R2 described in (101), and the third at RT 11.6 min is torasemide, m/z 349. Most results are reported as sum of degradants in units of peak area percent (PA%), and in extrudate samples, this value is the sum of the thermal and hydrolysis degradant PA%. Total torasemide as %w/w of the original extrusion blend was calculated via a calibration standard curve. The amount of dissolved torasemide as %w/w was calculated by subtracting the residual crystallinity in %w/w measured by XRPD from the total torasemide. An estimate of the weight fraction of degradants was calculated by subtracting the total torasemide from the theoretical extrusion blend concentration of 10 %w/w. Note that 10 %w/w is the maximum value that these values can have based upon the 10 %w/w drug loading of the original extrusion blend.

*X-ray Powder Diffraction (XRPD)*

Residual crystallinity was quantified using X-ray powder diffraction (XRPD). Samples were measured using an Empyrean system using Cu $K_\alpha$ radiation (45 kV and 40 mA), a step size of 0.026° 2θ over an angular range of 24-26° 2θ. Background subtraction was performed on all diffraction patterns. Calibration was performed with samples ranging from 0.1 to 10 %w/w spiked crystalline torasemide in extruded placebo, and the reflex height at 24.5° 2θ was used for back calculation of the %w/w crystalline torasemide in extruded samples. Residual crystallinity is reported as %w/w of sample, and all formulations contained a nominal or initial concentration of 10 %w/w crystalline torasemide.

*Blend Moisture Content*

The moisture content of SOL and extrusion blends was measured via loss-on-drying using a HB43-S moisture analyzer. Samples were heated to 105 °C and held until the mass was constant within +/- 1 mg for 100 seconds. The typical SOL moisture content was 2.5-3 %w/w and for blends was 2-2.5 %w/w.

*Polarized Light Microscopy (PLM)*

Residual crystallinity present in extrudates was qualitatively visualized in the form of thin sections. Extrudates were prepared by embedding them in two-component adhesive for support. The two-component adhesive was prepared in a 1:1 mass ratio of resin to accelerator, which produced a non-brittle matrix suitable for cutting. This composite sample was sliced to 50 µm thick using a Leica SM2500E microtome. The thin sections were submerged in silicone fluid between glass slide and cover slip to minimize the presence of cut marks and then imaged using a Leica DM2500M microscope equipped with a Leica DFC295 color digital camera. The samples were imaged using crossed polars and Koehler illumination.

*Extrudate Optical Appearance*

Extrudate strands were flattened between two slides to a thickness of 1 mm using a TA-XT2 texture analyzer equipped with an oven set to 100 °C. These extrudates were placed on 1 mm grid paper and photographed using a digital microscope VH-X. The turbidity of the samples was quantified using the haze value reported by the Haze-gard i optical transparency instrument. The haze value is a measure of the diffuse scattering of transmitted light in all directions, and this is detected by an integrating sphere with the forward directed light being excluded by a light trap.

*Melt Rheology*

The melt viscosity of pure Soluplus® and selected extrudates was measured and fitted to the Carreau-Yasuda equation with WLF temperature dependency, as described previously (135), with slight modifications: a Haake® MARS® II oscillatory rheometer was used with a gap height of 1.5 mm and amplitude of 5%. Temperature ranged from 110 to 170 °C, depending on formulation.

*Thermal Properties for Simulation*

The heat capacity of milled TOR extrudates with less than 1 %w/w residual crystallinity was measured by modulated DSC TA Q2000. Approximately 4 mg was placed in a pierced Tzero hermetic aluminum pan and heated to 100 °C, held for 2 min, cooled to 10 °C, held for 5 min, and then heated to 170 °C with a heating rate

of 2 K/min with modulation ±1 °C every 120 s. The instrument was temperature calibrated with gallium, indium, tin and bismuth standards. Calibration of the heat capacity was performed with a sapphire calibration standard. The thermal conductivity for both solid and liquid phases was assumed to be temperature independent and a literature value similar to other amorphous polymers was used (157). The $T_g$ of the respective formulation was used at the input value for melt temperature.

*Density Characterization for Simulation*

The solid density input parameter required for simulation was taken to be the bulk density of the starting blend, method described in section 7.2.2.2. The melt density was taken as the room temperature density calculated from cylindrically shaped pieces of cooled extrudate of uniform diameter.

7.2.5.2 Telmisartan

*DSC Experiments*

Basic thermal analysis such as melting temperature ($T_m$) and glass transition temperature, ($T_g$), were performed. The $T_m$ of TEL, taken as the peak of the melting endotherm, was confirmed using DSC by heating 4 mg of substance in 20 µL pierced aluminum pans and heated from room temperature to 280 °C at 10 K/min under nitrogen gas flow. The $T_g$, taken as the midpoint in the transition, was measured in the second heating after the $T_m$ determination, holding the sample above the melting point for 1 minute, then rapidly cooling at 50 K/min to -40 °C, and re-heating to the melting temperature at 10 K/min.

In addition, the solubility phase diagram of TEL in binary and ternary mixtures of COP and TW80 according to method in Kyerematen, *et.al.*, was also generated (102). The $T_g$ of various mixtures was calculated using the Fox equation (158). The onset dissolution temperature of TEL into the two matrices was measured using DSC and extrudates with > 3 %w/w residual crystallinity by heating the milled extrudates to 120 °C at 10 K/min, holding for 2 minutes to dehydrate the sample, cooling to -40 °C at 50K/min, and finally heating to 220 °C at 10 K/min.

The $T_g$ of a 3 %w/w TEC in COP milled extrudate sample was measured using the DSC1 by heating the sample to 150 °C at 10 K/min, holding for 2 minutes to remove moisture, cooling rapidly at 50 K/min to -40 °C and heating again to 150 °C at 10 K/min.

*TGA Experiments*

Thermal decomposition of TEL and TW80 was determined by thermogravimetric analysis (TGA) in 40 µL aluminum pans with 5-20 mg of substance, heating from room temperature to 300 °C with a heating rate of 10 K/min under nitrogen gas flow.

*X-Ray Powder Diffraction (XRPD)*

The residual crystalline TEL in milled extrudate samples was measured using an Empyrean system using Cu $K_\alpha$ (45 kV and 40 mA), over an angular range of 5-8° 2θ with a step size of 0.026° 2θ. Data was analyzed using X'Pert High Score v4.1, including background subtraction on all diffraction patterns. Peak intensities at 6.75° 2θ were compared to those measured in a calibration set of samples with spiked crystallinity concentrations ranging between 0-10 %w/w. The residual crystallinity is reported as %w/w of sample, and aside from the calibration samples, a nominal concentration of 10 %w/w TEL was used in all samples.

*Thermal Properties for Simulation*

The heat capacity, $c_p$, of milled TEL extrudates with less than 1 %w/w residual crystallinity was measured by modulated DSC TA Q2000. Approximately 4 mg was placed in a pierced Tzero hermetic aluminum pan and heated to 100 °C, held for 2 min, cooled to 10 °C, held for 5 min, and then heated to 230 °C with a heating rate of 2 K/min with modulation ±1 °C every 120 s. The instrument was temperature calibrated with gallium, indium, tin and bismuth standards. Calibration of the heat capacity was performed with a sapphire calibration standard. The thermal conductivity for both solid and liquid phases was assumed to be temperature independent and a literature value similar to other amorphous polymers was used (157). The $T_g$ of the respective formulation taken from the phase diagram was used as the input value for melt temperature in the Ludovic® simulation.

*Density Characterization for Simulation*

The solid density input parameter required for simulation was taken to be the bulk density of the starting blend, method described in section 7.2.2.2. The melt density was taken as the room temperature density calculated from disks made with a 20 mm diameter vacuum compression molding device (159).

*Melt Rheology*

Melt viscosity of copovidone and the two TEL-containing formulations was measured using small angle oscillatory shear (SAOS) rheometry according to the method described by Bochmann, *et.al.*, with minor modifications (135) noted here for the TEL-containing formulations. Using milled extrudates with less than 1 %w/w residual crystallinity, sample disks were prepared using the 20 mm diameter vacuum compression molding device to a thickness of 2 mm. An oscillatory rheometer was used with a 20 mm diameter plate-plate geometry and gap height of 2 mm. The melt viscosity was measured over a range of 150-180 °C, frequency sweep data was subsequently processed by time temperature superposition (TTS) to generate master curves. The master curves and obtained TTS data were fitted using the Carreau-Yasuda (C-Y) and Williams-Landel-Ferry (WLF) equations. The parameters from the fit to the reference temperature of 170 °C were then used as inputs to the Ludovic® simulation software. The master curves are presented as a function of angular frequency, which is equivalent to shear rate because the Cox-Merz relation has been found to apply to particle-free COP-based melts (135,160)

The melt viscosity of the 3 %w/w triethyl citrate in COP mixture was modeled using the equation developed by Bochmann, et.al. (110) based on the free-volume theory relating $T_g$ and melt viscosity (52,161). The modeling procedure is as follows. One begins with the C-Y equation coefficients $n$, $a$, $\eta_0$ and $\lambda$ for COP at a certain reference temperature, here 170 °C. The zero-shear rate viscosity for the new formulation, $\eta_{0,new}$, is calculated using equation 7.1 by inserting the $T_g$, measured by DSC:

$$\eta_{0,new} = 4.91E^{-5}e^{0.17351T_g} \quad (7.1)$$

Please note that this equation is valid only for COP and at a reference temperature of 170 °C. A shift factor, *SF* is then calculated from the $\eta_0$ and the $\eta_{0,new}$ in order to also adjust the characteristic time $\lambda$ for the new formulation, $\lambda_{new}$. They are calculated using equations 7.2 and 7.3:

$$SF = \frac{\eta_{0,new}}{\eta_0} \tag{7.2}$$

$$\lambda_{new} = SF * \lambda \tag{7.3}$$

The WLF equation coefficients $C_1$ and $C_2$ of COP are used un-changed.

### 7.2.6 Process Simulation

#### 7.2.6.1 Numerical Simulation

*The Ludovic® Model*

Ludovic® is a 1D numerical simulation software representing the polymer flow in a hot-melt co-rotating twin-screw extrusion process. The extruder geometry, polymer material properties and extrusion process parameters are all inputs for the computation. The Ludovic® model, its development and working principles have been summarized elsewhere (22,27,80). Briefly, computation of the temperature and pressure occurs locally in discretized c-shaped chambers and proceeds backward from the die until the convergence criteria of product temperature equals the defined melting or softening temperature, the pressure is equal to zero, and no further restrictive elements are present upstream. The numerical computations are performed iteratively, beginning at the exit because the fill volume is unknown for starve-fed extruders. The iteration begins with a user-defined exit temperature, in this case chosen to be that of the die temperature. Melting or softening of the matrix is assumed by default to occur at the first restrictive element, although this position can be adjusted by the user.

Results are computed and categorized according to global values, residence time distribution, f(x) results, and f(t) results (Table 7.6). Global values are either averages or summations of local values for the entire process, but which are in some cases

only relevant for certain locations in the extruder (Figure 7.2). The f(x) results are local values which are a function of the position in the extruder. The f(t) results are normalized local values which have been transformed to a time scale by plotting them against the mean residence time reached at a given location on the screw (38).

Table 7.6 *Results computed by the Ludovic® model (those in bold were found to be relevant to the work in this thesis)*

| | |
|---|---|
| **Global Results** | • Mean residence time<br>• **Dissipated Energy (viscous dissipation – screw)**<br>• Dissipated Energy (viscous dissipation – die)<br>• Solid Transport Energy<br>• Melting Energy<br>• **Specific Mechanical Energy**<br>• **Total Conduction Energy**<br>• **Total Product Energy**<br>• Total Extruder Energy<br>• Engine Power<br>• **Torque per Shaft** |
| **RTD Results** | • Minimum or onset residence time<br>• Peak residence time<br>• **Mean residence time**<br>• Variance in the residence time distribution<br>• **Residence time distribution profile** (E(t)) |
| **Local Results f(x)** | • **Temperature**<br>• Pressure<br>• Filling Ratio<br>• Local and Cumulated Residence Time<br>• Shear Rate<br>• **Melt Viscosity**<br>• **Local and Cumulated Dissipated Energy**<br>• **Local and Cumulated Conduction Energy**<br>• Strain per C Chamber<br>• Cumulated Strain<br>• **Barrel Temperature** |
| **Local Results f(t)** | • **Temperature**<br>• Pressure<br>• Time above threshold temperature<br>• **Integral of temperature-time profile above the threshold temperature** |

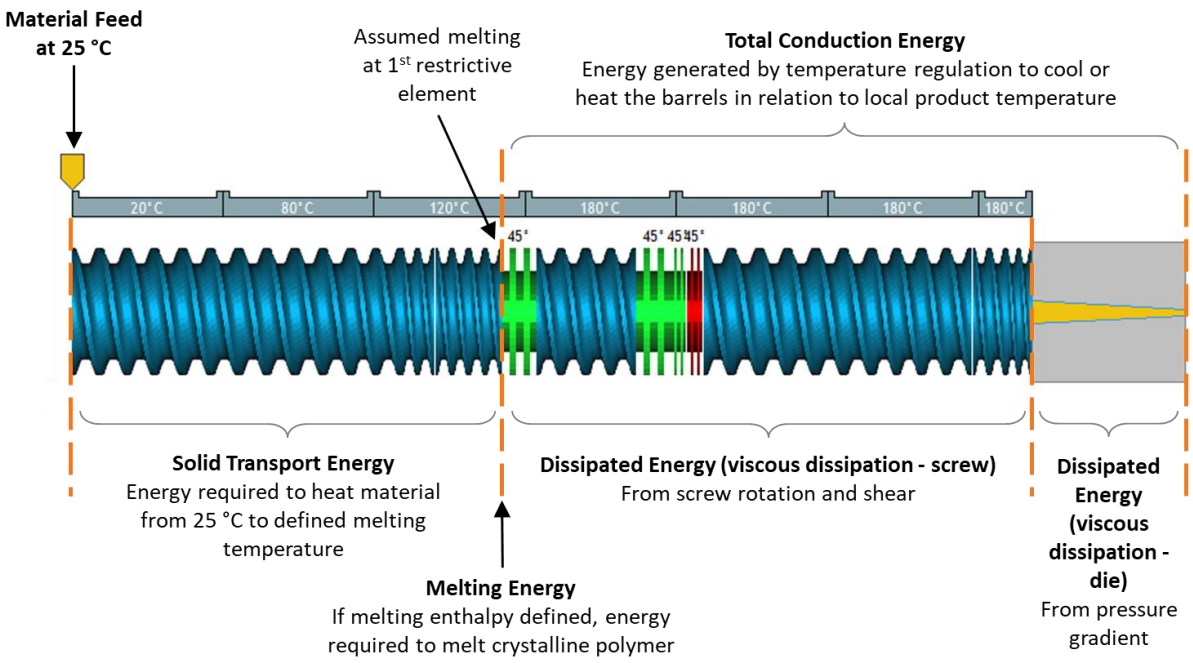


Figure 7.2 *Global energy results in Ludovic® as a function of location (adapted from Ludovic®, basic training documentation by Sciences Computers Consultants).*

*Sensitivity Analysis of the Ludovic® Model*

Sensitivity analysis is a useful exercise to better understand a model. It involves the systematic variation of the various input parameters and can enhance the understanding of the relationships between the input and output variables. The learnings can, for example, be applied to guide the generation or acquisition of input values, especially for material property data which may be time-consuming or challenging to obtain, and to assist with the validation of the model, i.e. which high-uncertainty input values impact the results most appreciably. Sensitivity analysis was performed for input parameters for which:

- some degree of uncertainty was present (e.g. clearance, feed location, material properties, thermal exchange coefficients)
- some degree of options were available (e.g. kneading block types)
- a high degree of effort was required to obtain the input value (e.g. material properties)

- perceived variation in the value could greatly impact the process (e.g. barrel or die temperature, screw speed, feed rate).

If an input parameter had little impact on the simulation results, then an estimate was used for real simulation purposes. A high-level summary is shown in Table 7.7.

The most informative sensitivity analysis studies were the ones in which material properties, process parameters and thermal exchange coefficients were varied and results are presented in greater detail. In the presentation of the results, primary focus is placed on the melt temperature evolution along the screw; any change in energy will manifest itself in product temperature change. The ranges selected for analysis are based upon a survey of typical and reasonable expected variation (Table 7.8 and Table 7.9).

The material $T_m$ or $T_g$ and the melt viscosity show direct relationships and strong impact on the melt temperature while the liquid phase heat capacity and density have lesser impact as well as inverse relationships with melt temperature (Figure 7.3). The other properties had no impact on the melt temperature. Among the values for the material properties tested, only the melt density affected the residence time (data not shown).

Not surprisingly, the process parameters also have a strong influence on the melt temperature and residence time distribution. The Ludovic® model shows the expected relationships that melt temperature increases with increasing screw speed and decreases to a lesser extent with increasing feed rate Figure 7.4. The residence time decreases and becomes a narrower distribution with increasing feed rate at constant screw speed, while the screw speed, at constant feed rate, simply shifts the time to earlier or later. An increase in barrel temperature generally leads to an increase in melt temperature (Figure 7.5), with no impact on residence time (data not shown).

Table 7.7 *Summary of Ludovic® sensitivity analysis.*

| | | | Extruder Geometry | Material Properties | Process Parameters | Thermal Exchange Coefficients |
|---|---|---|---|---|---|---|
| Outputs | Global Results | Mechanical Energy | • Screw Configuration<br>• Clearance | • $c_{pS}$, $c_{pL}$<br>• Melt Viscosity<br>• $T_m/T_g$<br>• Melt Density | • Feed Rate<br>• Screw Speed<br>• Set Temp | • Barrel TEC<br>• Die TEC* |
| | | Conducted Energy | • Screw Configuration<br>• KB Type | • $c_{pL}$<br>• Melt Viscosity<br>• $T_m/T_g$<br>• Melt Density | • Feed Rate<br>• Screw Speed<br>• Set Temp | • Barrel TEC<br>• Die TEC* |
| | | Torque | • Screw Configuration<br>• KB Type | • $c_{pL}$<br>• Melt Viscosity<br>• $T_m/T_g$<br>• Melt Density | • Feed Rate<br>• Screw Speed<br>• Set Temp | • Barrel TEC<br>• Die TEC* |
| | Residence Time Distribution | | • Screw Configuration<br>• KB Type Screw<br>• Die Geometry* | Melt Density | • Feed Rate<br>• Screw Speed | n/a |
| | f(x) Results | Product Temperature | • Screw Configuration<br>• KB Type Screw | • Melt Viscosity<br>• $T_m/T_g$<br>• $c_{pL}$<br>• Melt Density | • Feed Rate<br>• Screw Speed<br>• Set Temp | • Barrel TEC<br>• Die TEC* |
| | | Filling Ratio | • Screw Configuration<br>• KB Type | • Melt & Solid Density<br>• Melt Viscosity | Feed Rate:Screw Speed Ratio | n/a |
| | | Shear Rate | Screw element type (conveying vs. KB) | n/a | Screw Speed | n/a |

Note: Only those inputs which had an impact are listed
* Only affects result in the die, not along the screw

Red: strong impact
Orange: moderate impact

The thermal exchange coefficient also strongly impacts the melt temperature and as an input parameter has a high degree of uncertainty (Figure 7.6). The TEC describes the effectiveness of heat transfer between barrel and melt and depends on several extremely challenging-to-measure quantities such as fill volume, contact surface area and surface roughness. It typically varies between 100 and 1000 $W/m^{2 \cdot}K$ (162,163). Low values lead to poor control of the melt temperature by the barrels while large values lead to good melt temperature control. Because melt temperatures tend to be greater than the barrel temperature in viscous systems such as the ones under consideration here, a high TEC leads typically results in a cooler melt, seen both for the last sections of barrels as well as separately for in the die (Figure 7.6 inset).

The impact of extruder geometry, especially screw configuration and die geometry, is considerable, but also too complex to represent via simple sensitivity analysis. A change in configuration leads simultaneously to changes in many dependent variables and is best looked at on a case-by-case basis.

Table 7.8 *Ranges of material properties tested in sensitivity analysis.*

| **Material Property** | **Low** | **Reference** (copovidone) | **High** |
|---|---|---|---|
| Solid phase heat capacity [J/kg/°C] | 800 | 1200 | 1800 |
| Solid phase density [$kg/m^3$] | 200 | 560 | 1200 |
| Solid phase thermal conductivity [W/m·K] | 0.15 | 0.2 | 0.25 |
| Liquid phase heat capacity [J/kg/°C] | 1200 | 1800 | 2700 |
| Liquid phase density [$kg/m^3$] | 1000 | 1200 | 1400 |
| Liquid phase thermal conductivity [W/m·K] | 0.15 | 0.2 | 0.25 |
| Melting/glass transition temperature [°C] | 50 | 107 | 160 |
| Zero-shear rate viscosity ($T_0$ = 170 °C) [Pa·s] | 400 | 3843 | 40000 |

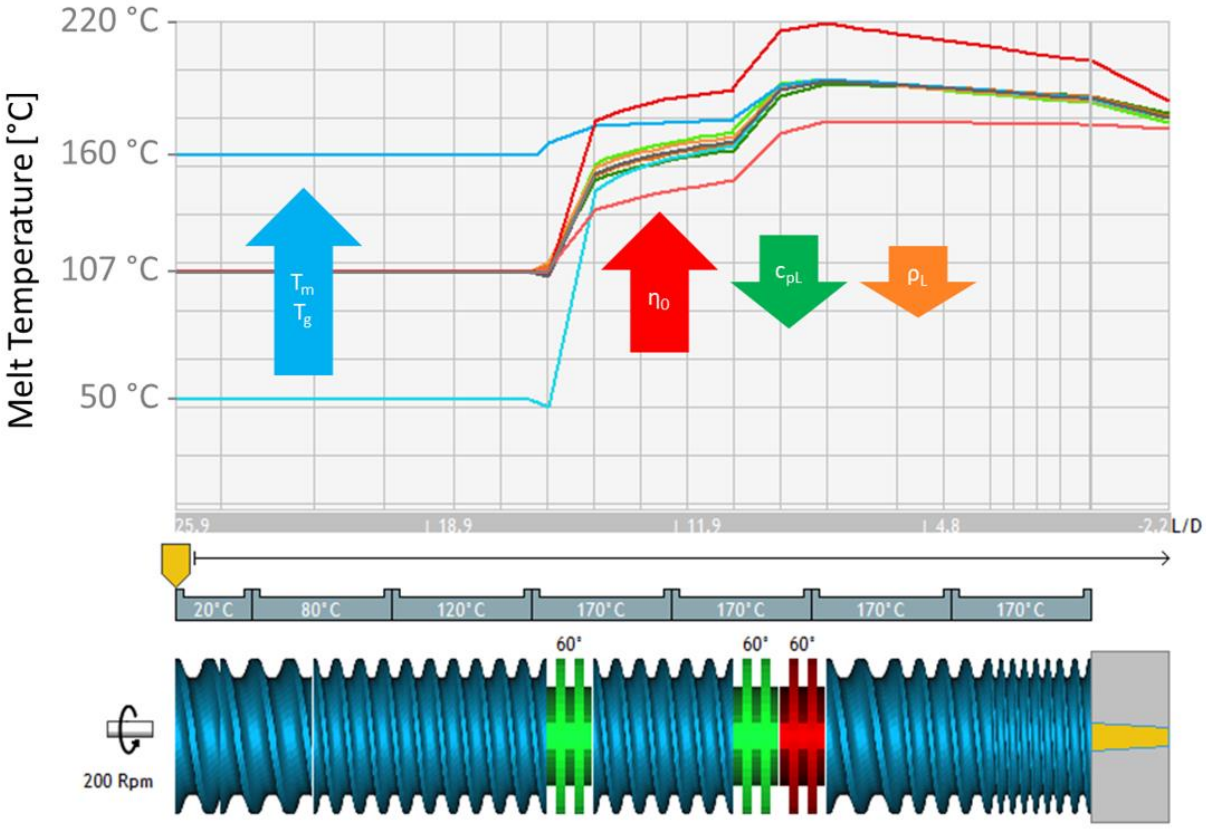


Figure 7.3 *Impact of material properties on simulated melt temperature evolution.*

Table 7.9 *Ranges of process parameters and TECs tested in sensitivity analysis.*

| Process Parameter / TEC | Low | Reference | High |
|---|---|---|---|
| Screw speed [rpm] | 100 | 200 | 300 |
| Feed Rate [kg/h] | 200 | 560 | 1200 |
| Main Barrel and Die Temperature [°C] | 0.15 | 0.2 | 0.25 |
| Feed rate:Screw speed ratio [kg/h*rpm] | 0.0075 (0.75/100) | 0.0075 (1.5/200) | 0.0075 (2.25/300) |
| Thermal Exchange Coefficient (Barrels-Die) [W/m$^2$·K] | 100-100<br>100-500<br>100-1000 | 500-100<br>500-500<br>500-1000 | 1000-100<br>1000-500<br>1000-1000 |

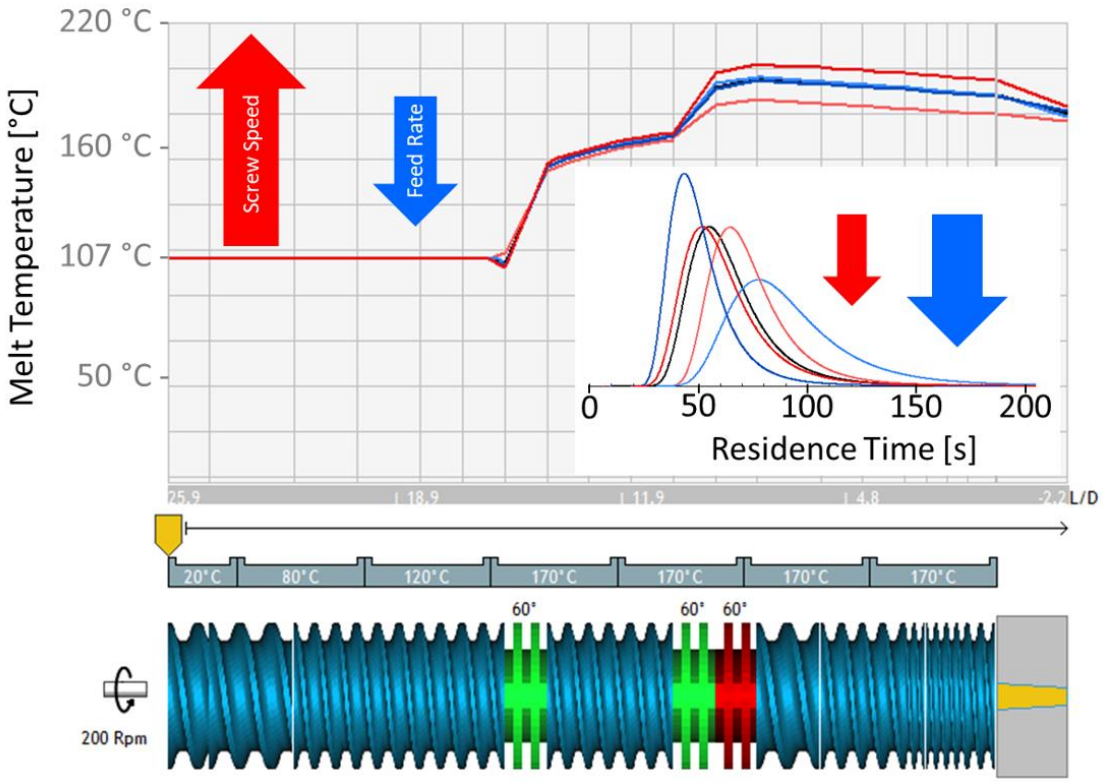


Figure 7.4 *Impact of feed rate and screw speed on melt temperature and RTD.*

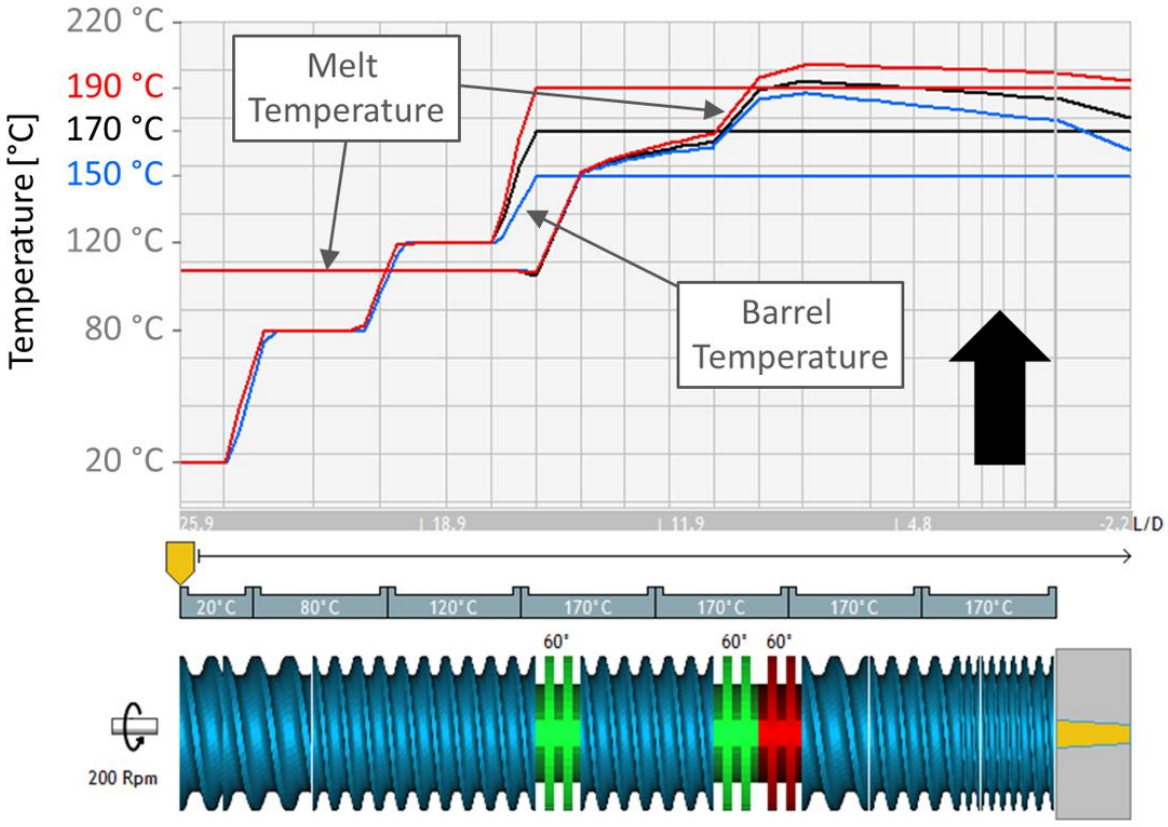


Figure 7.5 *Impact of barrel temperature on simulated melt temperature evolution.*

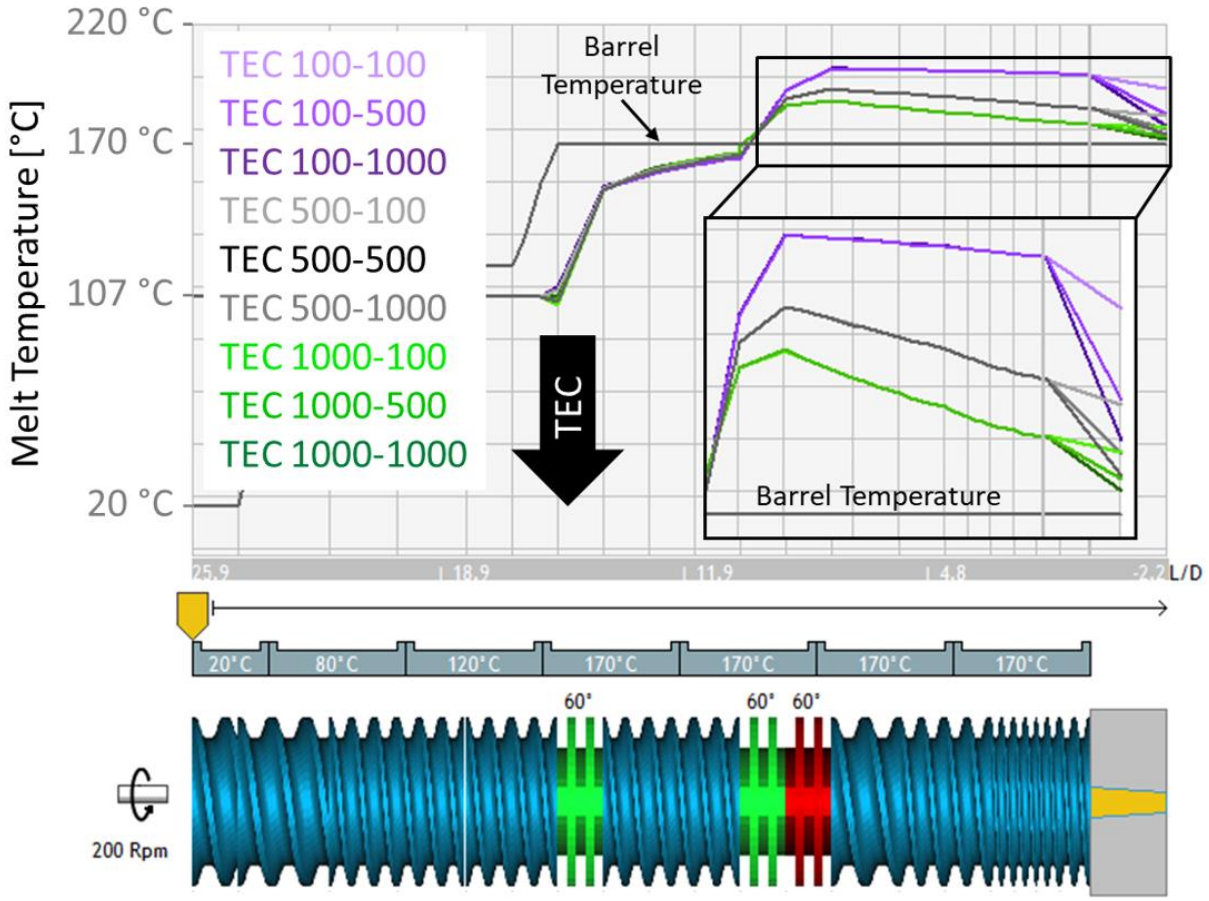


Figure 7.6 *Impact of thermal exchange coefficient (TEC) on simulated melt temperature evolution (Legend note: first number is the TEC for the barrels, second number is the TEC for the die).*

*Describing the HME Process to the Ludovic® Model*

Use of the Ludovic® model for pharmaceutical applications requires a few assumptions. The model was originally designed for processing of single-component crystalline thermoplastic polymers, although it has subsequently been utilized for filled polymer systems, semi-crystalline polymers, natural polymers such as starch and reactive systems. However, at least in the work described in this thesis, amorphous polymers comprise the matrix. In addition, while pharmaceutical systems are also reactive, given that crystalline API particles melt or dissolve into the surrounding matrix, potentially changing the properties of the matrix, experimental data regarding the kinetics and location of these reactions are lacking. Therefore, a few approximations and assumptions must be made. First, the glass transition temperature of the fully-formed ASD is used as the input value for the requested

melting temperature. Second, the temperature and pressure dependency of the melt density was assumed to be negligible; the density of the cooled melt was used as a surrogate. Third, based on the sensitivity analysis and analysis of literature as well as unpublished data, the thermal conductivity was assumed to be approximately 0.2 W/m·K. Fourth, the material properties are assumed to not change as a function of the location in the extruder, at least in terms of definition or composition. This assumption impacted primarily the definition of the heat capacity, $T_g$ and melt viscosity. Finally, the moisture content of the materials was neglected due to the inability to measure the properties as a function of the moisture content within the relevant process temperature range, i.e. above 100 °C.

As for extruder geometry, a few adaptations were made to the geometrical description. First, beginning of the simulated screw was shortened so that defined feeding location in Ludovic® aligns with the center of the feeding port in the first barrel of the extruder. Second, because the extruder dies are typically complex combinations of geometrical shapes, the most similar available shape in Ludovic® was selected, and the dimensions were entered so that the die volume and outlet dimensions matched.

Regarding the process description, the only assumption made was that, if vacuum was applied experimentally, this was not described to Ludovic®. While the location of the vent port and vacuum pressure are easy to define, there is uncertainty in the experimental flow rate of gas and vapor exiting the process, which is the value Ludovic® requires.

*Model Validation*

The approach used to validate the Ludovic® model is outlined in Figure 7.7. The goal of model validation is to obtain agreement between experimental and simulated results. Depending on the availability of experimental data, as many outputs as possible should be compared with simulated outputs. Although it is undesirable to adjust input parameters such as the melt viscosity, there are inherent uncertainties in the experimental data due to, for example, moisture content. Moisture may be present during extrusion but is likely absent during melt viscosity measurements.

Uncertainties in extruder geometrical definition may also occur due to wear and tear, e.g. clearance could be larger than specification, or the die geometry may be complex and challenging to describe to the model.

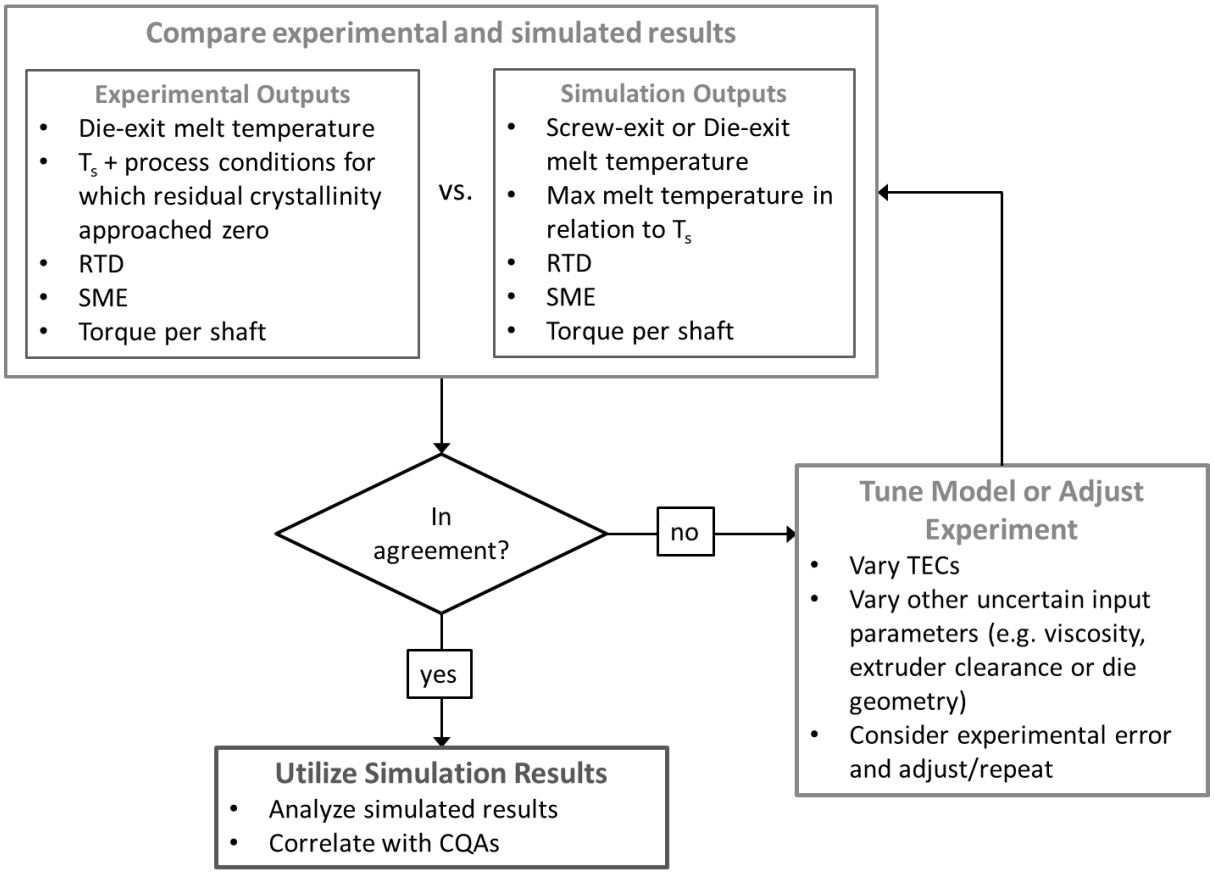


Figure 7.7 *General method and decision tree for model validation.*

### 7.2.6.2 Torasemide Simulation

Process simulations were performed using Ludovic® v.6.2 beta. This version is a test version based on v.6.1 with the additional feature of automatic integration of the temperature vs. time curve when a threshold temperature is given to the software. The model is described in section 7.2.6.1.

Additional parameters describing the extruder needed for simulation are: center line of 9 mm, screw/barrel leakage of 0.35 mm, and 2 mm diameter die opening. The screw configuration 2mix5disk60degFW-5disk60degFWBW, composed of conveying elements of various pitch, forward 60 degree kneading blocks shown in green and reverse kneading block shown in red, is displayed at the bottom of Figure 4.2 and all elements are listed in Table 7.4.

Process simulations at conditions identical to the experimental extrusion conditions were performed to validate the model for torasemide-containing formulations. The model was validated by correlating 1) the measured and simulated melt temperature at die exit and 2) the measured and simulated residence time distribution and mean residence time. The thermal exchange coefficients used were 500 W/m$^2$·K in the first two barrels, 300 W/m$^2$·K in the last two barrels, and 50 W/m$^2$·K in the die.

#### 7.2.6.3 Telmisartan Simulation

*Chapter 5*

Process simulations of the laboratory experiments on the ZSK18 were performed using Ludovic® v.6.1 software. The model is described in section 7.2.6.1.

Additional parameters describing the ZSK18 extruder needed for simulation are: center line of 15 mm, screw/barrel leakage of 0.14 mm, and 10 mm diameter die opening. The screw configuration, composed of conveying elements of various pitch, forward 60° kneading blocks shown in green and reverse kneading block shown in red, is displayed at the bottom of Figure 5.3 and elements listed in Table 7.5.

Sensitivity analysis of the Ludovic® model with varied rheological parameters, $n$ and $\eta_0$ in the Carreau-Yasuda equation, were performed to determine the relative impact of $n$ and $\eta_0$ on melt temperature evolution. Copovidone was used as the baseline material with $n$ and $\eta_0$ ranges selected within that of previously measured values when the formulation was varied by addition of surfactant. Copovidone at a reference temperature of 150 °C has $n$ = 0.577 and $\eta_0$ = 61000 Pa·s. The extruder and screw geometry used for this study was the same as for all other simulations of the ZSK18 extruder. The barrel temperature was varied along with the screw speed, and the feed rate was adjusted in combination with the screw speed to maintain constant fill level. The thermal exchange coefficients used were 500 W/m$^2$·K in the barrels and 500 W/m$^2$·K in the die.

Process simulations at conditions identical to the TEL experimental extrusion conditions were performed to validate the model for TEL-containing formulations. The model was validated by correlating the melt temperature at die exit, measured

experimentally, with that of the simulated value. The thermal exchange coefficients used were 300 W/m$^2$·K in the barrels and 100 W/m$^2$·K in the die.

Thereafter, a full factorial simulated experimental design was employed thanks to the resource-sparing nature of simulation work. The parameters varied in the simulation experiment are listed in Table 5.2. The thermal exchange coefficients used were 300 W/m$^2$·K in the barrels and 100 W/m$^2$·K in the die. Contour plots of resulting simulated data were generated using JMP® v.10 software.

In addition to the simulated melt temperature at die exit, the maximum melt temperature along the screw, the total viscous dissipated energy from the screw, the specific mechanical energy, the total conducted energy, the total product energy (Figure 7.2) and local shear stress were analyzed. The total viscous dissipated energy in the screw is calculated by Ludovic® as the sum of the viscous dissipated energy computed in each c-shaped chamber, utilizing the local values of computed shear rate, melt viscosity, discretized volume and local residence time for computation. The local shear stress can be calculated by multiplying the local values for melt viscosity and shear rate in each c-shaped chamber.

*Chapter 6*

Process simulations were performed using Ludovic® v.6.2 beta. The model is described in section 7.2.6.1.

Two sets of simulations were performed: 1) pre-experiment full factorial design to select the best formulation and also the barrel temperature and 2) post-experiment to analyze the process. The simulation parameters for the first set are listed in Table 6.8 while the simulation parameters for the second set were identical to the experimental parameters described in section 7.2.2.2. Material property inputs were identical to those used in Chapter 5 simulations. Thermal exchange coefficients were 500/300/50 W/m$^2$·K for zones A-C/zone D/die for the both extruder scales. The Ludovic® model was validated by comparing the empirically measured temperature with the simulated melt temperature at screw exit in this study.

# 8 Summary and Outlook

Hot-melt extrusion is a well-established process for the production of pharmaceutical products. Nevertheless, some aspects of process development are not straightforward to ascertain and are poorly understood, such as assessing the correlation of CQAs with process performance or achieving a scaled and energy-balanced process. These challenges are primarily due to the lack of accurate measures of the process. In order to gain deeper process understanding, a surrogate approach combining the use of indicator substances with process simulation can be used.

In this work, two APIs, torasemide and telmisartan, were identified which, when combined with the appropriate matrix and processed at appropriate conditions, behaved like highly sensitive indicator substances. With these indicator substances, two relevant CQAs for the HME process, degradation and residual crystallinity, were correlated with both empirical and simulated process performance. Customized formulations were developed for both APIs in order to target the relevant process and CQA design spaces. Formulations were developed to minimize the impact of the API dissolution into the matrix on melt viscosity or thermal properties by minimizing the difference between the $T_g$ of the API and that of the matrix.

Both APIs were processed below their single-component melting points as well as below their solubility temperatures in the matrix system. By doing so, the APIs were forced to dissolve into the surrounding matrix rather than first melt and then disperse and distribute. As a result, for the given drug loading, dissolution was never complete and residually crystalline material was always present after extrusion. The amount of residually crystalline material present was correlated to both melt temperature and residence time in the case of torasemide while for telmisartan was highly correlated with melt temperature.

In order to realize the full benefit of torasemide as an indicator substance, a formulation with 10 %w/w TOR, 10 %w/w PEG 1500 in Soluplus® was used. Soluplus® was chosen for its relatively low temperature processing window and because its $T_g$ of 70 °C was similar to that of TOR, 80 °C. PEG 1500 was chosen as

a plasticizer for the system because PEG was already present in the Soluplus® polymer side chains. Addition of the plasticizer allowed processing at barrel temperatures below the onset temperature of dissolution of TOR in Soluplus®, 115 °C. Solid-state characterization tools and a 10 mm diameter lab-scale co-rotating TSE were used to study the system. It was found that TOR first dissolved into the matrix and then degraded. Based on this mechanism, within the processing space of varied barrel temperatures and residence times explored, both degradation and residual crystallinity were observed and were highly correlated to both time and temperature. In addition, because torasemide is sensitive to both thermal- and hydrolysis-induced degradation, the indicator system was used to study the effect of moisture on the process by way of various venting conditions. Also, because of the dissolve-then-degrade mechanism, the residual crystallinity and total degradation were highly correlated, independent of the processing conditions applied. This relationship was further quantified by use of simulated results, namely the integral of the melt temperature evolution over time for which the melt temperature was greater than the onset dissolution temperature of the API in the polymer, 115 °C. In this way, utilization of torasemide as a highly-sensitive process indicator enhanced the understanding of the dynamic thermal environment inside an extruder and elucidated the inter-dependent yet cumulative thermal and hydrolysis effects of the processes occurring within HME.

The telmisartan indicator system was developed specifically with the intention of studying the relationship between melt viscosity and processing performance and its relevance for pharmaceutical extrusion coupled with process simulation. Two formulations containing 10 %w/w TEL in either a pure COP matrix or one containing 5.5 %w/w polysorbate 80 were extruded at various barrel temperatures and screw speeds, keeping fill volume in the barrel constant, on an 18 mm screw diameter extruder. The polysorbate 80 was included as a plasticizing component, while the presence of dissolved telmisartan had a negligible effect on $T_g$ at the investigated drug loading. The presence of polysorbate 80 did not impact the solubility of TEL in the matrix. It was hypothesized and also confirmed by process simulation that the design space with respect to screw speed was broader for the plasticized formulation. In addition, the amount of residual crystallinity was more sensitive to

screw speed at low barrel temperatures than at higher barrel temperatures. The residual crystallinity was found to be highly correlated with melt temperature but differed for the two formulations. Uniquely, the simulated maximum melt temperature at which residual crystallinity approached zero was very similar to the solubility temperature of telmisartan in the matrix determined by DSC, therefore explaining the difference in residual crystallinity between the two formulations. In this way, simulation enabled a deeper understanding of the relationship between process performance and CQAs.

Based on these results with telmisartan and a surfactant acting as a plasticizer, the conventionally proposed recommendation for using a plasticizer should be reconsidered. While the decision to use a plasticizer is typically centered around lowering the processing temperature to avoid thermal degradation, consideration should be made in relation to the inherent need to achieve an ASD, which can only be done by processing above the solubility temperature for a given drug concentration. Use of a plasticizer to simply process below an API's degradation temperature is only one factor for consideration. While it will enable processing at a lower barrel temperature, doing so may prevent the full dissolution of the API into the polymeric matrix for high solubility temperature APIs. Alternatively, the benefit in broadening the design space with respect to shear rate is a rational reason to introduce a plasticizer. The decision to use a surfactant in an ASD formulation can also be based not only on bioavailability enhancement but also on process performance. If the API's in-vitro or in-vivo release behavior benefits from the inclusion of a surfactant in the formulation, a surfactant's plasticizing behavior will also broaden the design space.

Use of the telmisartan indicator system and process simulations also enabled quantitative analysis of scaling and adiabatic conditions between two twin-screw extruders 18 mm and 40 mm in diameter. The scaling approach of maintaining VSFL and either the screw speed or the overflight shear rate resulted in almost identical quantitative energetic states, namely same SME, same conduction energy profile, same quasi-adiabatic state, and melt temperature was also similar. However, the TEL system is so sensitive that the difference in melt temperature, measured at die exit, resulted in a different amount of residual crystallinity between the two scales.

For some systems, this degree of similarity in melt temperature and process energetics may be sufficient for scaling, while in others not.

Despite the reasonable findings and correlations between simulated results and CQAs obtained, validation of the Ludovic® model in this work was dependent on an imperfect measure of the process, namely the melt temperature at the die exit. Even better models could be developed with the help of enhanced measures of the process such as the melt temperature measurement in a maximum temperature zone, for example in a mixing element with high or complete degree of fill. If temperature could be measured more accurately, especially maximum temperature and not just the die-exit temperature, then the thermal exchange coefficients could be more precisely adjusted to obtain a greater degree of confidence in experiment-simulation agreement.

Further work is also needed to calibrate the Ludovic® model with respect to the “gray-zone” of total conducted energy because the model does not consider heat loss to the environment in the energy balance. This heat loss would differ from extruder to extruder, and therefore would need to be analyzed on a case-by-case basis. One way to investigate this could be to extrude a matrix polymer and vary the melt viscosity by either gradually adjusting barrel temperature or plasticizer content to quantitatively identify the threshold of total conducted energy magnitude which correlates to real cooling, aka a negative controller output.

Additional experiments are also needed to confirm some of the findings, those for which slight indications or tendencies were observed. Because the present experiments were designed to study other hypotheses, perhaps a screening DOE to determine main effects would be useful, for example to confirm observation of the temperature dependency of TEL, seen both Chapters 5 and 6, and rule out the observation that the residual crystallinity is independent of residence time. On the other hand, it may be tricky to design such an experiment due to the extent of interactions between the independent variables in an extrusion process.

An additional aspect of the process which was not fully explored in these studies is kinetics, both that of dissolution of the API into the polymer and that of API

degradation. Study of the dissolution kinetics of an API into the molten polymer would require development of either new methods and/or sensors. For example, an off-line device to replicate in a controlled fashion the thermal-temporal-mechanical environment of molten polymer in an extruder with off-line sample analysis could be used to study the kinetics of dissolution. Alternatively, on-line sensors could be used to quantify the rate of dissolution if a signal could be identified as specific to the dissolved or undissolved state of the API. Further, if dissolution and degradation kinetics could be quantified, the Ludovic® model could be used to simulate and estimate the CQAs for a given process setting as has been done for polymerization reactions.

Lastly, the use of these or other indicator substances could be used to study other aspects of the HME process such as the impact of screw configuration or mixing element design, die geometry, moisture as a plasticizer or other plasticizers on the outcome of the process. In addition, new models could be developed and validated based on the use of indicator substances. The benefit of using the API as the indicator substance for pharmaceutical applications is that the response is directly related to relevant CQAs for the given unit operation.

# 9 Publications

Parts of this work are already published or submitted as:

**Articles:**

- Evans, R.C., Kyerematenga, S.O., Asmus, L., Degenhardt, M., Rosenberg, J., Wagner, K.G.; *Development and Performance of a Highly Sensitive Model Formulation Based on Torasemide to Enhance Hot-Melt Extrusion Process Understanding and Process Development*; AAPS PharmSciTech 2018; doi:10.1208/s12249-018-0970-y
- Evans, R.C., Bochmann, E.S., Kyerematenga, S.O., Gryczke, A., Wagner, K.G.; *Holistic QbD Approach for Hot-Melt Extrusion Process Design Space Evaluation: Linking Materials Science, Experimentation and Process Modeling*; submitted.

**Abstracts/Posters (Conference participation):**

- Evans, R.C., Kyerematenga, S., Asmus, L., Degenhardt, M., Rosenberg, J., Wagner, K.G.; *Improved HME Process Understanding Facilitated by API-as-Indicator Substance and Simulation*; AAPS Annual Meeting, San Diego, California, USA, November 2017.
- Evans, R.C., Kyerematenga, S., Degenhardt, M., Wagner, K.G.; *Influence of Surfactant+Polymer Rheological Properties on Hot-Melt Extrusion Design Space – Investigation via Process Simulation*; 11th PBP World Meeting, Granada, Spain, March 2018.

**AbbVie Poster Sessions**

- Rachel C. Evans, Lutz Asmus, Samuel Kyerematenga, Matthias Degenhardt, Jörg Rosenberg, Karl G. Wagner *Enhancing Hot Melt Extrusion Process Understanding – Development of a Highly Sensitive Model to Facilitate Rational Process Understanding* (Ludwigshafen – AbbVie Celebration of Science 2015)
- John Strong, Rachel C. Evans, Maxx Capece, Sean Garner, David O'Brien, Divya Sunkara, Connie Skoug, Ping Gao, Samuel Kyerematenga, Lutz Asmus, Matthias Degenhardt, Jörg Rosenberg, Karl G. Wagner *Formulation Development and Process Understanding Facilitated by Simulation and Modeling* (Lake County – AbbVie Celebration of Science 2016)

# 10 Appendix

## 10.1 Mass Spectrometry Characterization for Torasemide Study

HPLC mass spectrometry (HPLC-MS) was conducted to identify the chemical structure of the three peaks observed in standard HPLC sample analysis. HPLC-MS was performed with an Agilent 1260 series (Agilent Technologies, Germany) HPLC with a binary pump (G1313B), column compartment (G1316C), DAD detector (G4212B), and HIP sampler (G1367E) coupled to a Bruker AmaZon x ion trap mass spectrometer (Brucker, USA). The amaZon x was controlled by ESI Compass 1.7 trapControl software Version 7.2, data were collected using HyStar software, version 3.2, and data were processed using Bruker Compass DataAnalysis Version 4.2 (Bruker Daltonik GmbH, Bremen, Germany).

The chromatographic separation was performed using the same column as standard HPLC-UV and with column temperature of 25 °C. The mobile phase was water with 0.1 %v/v trifluoroacetic acid (85%) (mobile phase A) and acetonitrile with 0.05 %v/v trifluoroacetic acid (85%) (mobile phase B). Chromatographic separation was conducted using gradient elution: 0 min, B 5%; 5 min, B 10%; 15 min, B 40%; 17 min, B 80%; 18 min, B 5%; 25 min, B 5%. The flow rate was 0.4 mL/min and the injection volume was 5 µL for both LC-DAD and LC-MS analysis. UV-detection was performed at 249 nm and 279 nm.

LC-MS analysis utilized electrospray ionization (ESI) operating in positive ionization mode. The following MS parameters, optimized for the corresponding analysis, were applied: flow rate drying gas ($N_2$) = 8.0 mL/min, nebulizer gas pressure = 20 psig, temperature drying gas ($N_2$) = 220 °C, capillary voltage = 4500 V, collision gas = Helium. The mass spectrometer was operated in full scan mode in the range from 100 to 1000 m/z. Tuning of the ion trap mass spectrometer was performed with Agilent ESI tune mix (G2431A). The tune solution was infused with a syringe pump at a flow rate of 180 µL/h. A torasemide standard solution at a concentration of 500 µg/mL was used as control standard to verify the collision energy. The target mass was 350 m/z and the compound stability 100% for SPS tune.

Mass spectrometry data for the three peaks observed in torasemide physical mixture and extrudate samples, along with a corresponding UV chromatogram, are shown in

Figure 10.1. Due to the slight difference in the gradients used for HPLC-UV analysis and HPLC-MS analysis, the retention times for the three species are slightly shifted. The peaks in the HPLC-MS chromatogram elute somewhat later than in the HPLC-UV chromatogram because the gradient was less steep. For clarification, the peak at 2.8 min in the HPLC-UV chromatogram corresponds to the peak at 5.7 min in HPLC-MS chromatogram, the peak at 6.5 min to the peak at 10.3 min and the peak at 11.6 min to the peak at 12.7 min.

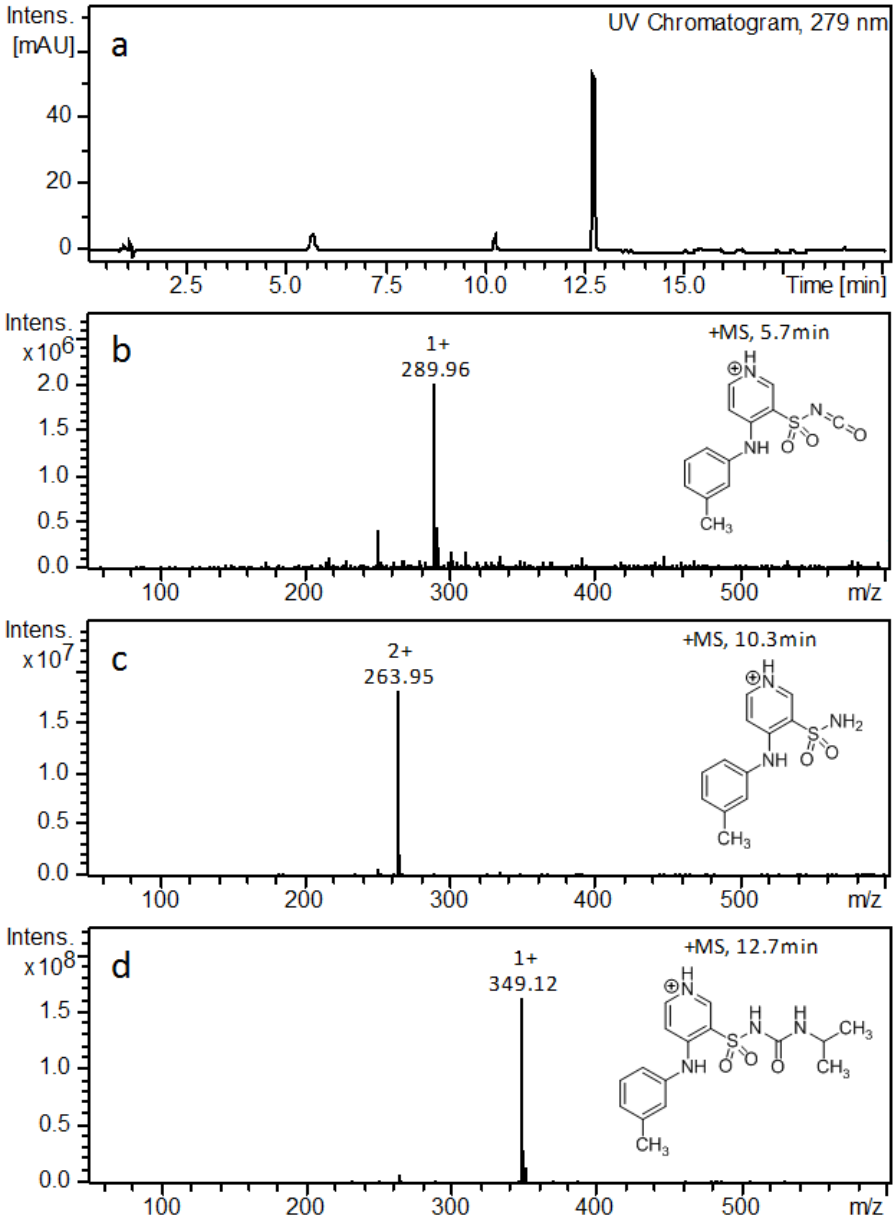


Figure 10.1 *HPLC chromatogram (a) and mass spectra for the 3 peaks found in samples: thermal degradant (b), hydrolysis degradant (c) and torasemide (d).*

## 10.2 Determination of Telmisartan Degradation

The extent of degradation of telmisartan within the extrusion processing range was determined by lab-scale extrusion and HPLC analysis.

### 10.2.1 Sample Preparation

A blend of 10 %w/w TEL in COP was prepared via mixing in a Turbula® blender for 5 min (Willy A. Bachofen AG - Maschinenfabrik Muttenz, Switzerland). Extrudates were prepared by extruding using a Haake® MiniLab conical twin-screw extruder (Thermo Fisher Scientific, Karlsruhe, Germany) at 100 rpm and barrel temperatures of 180 °C and 220 °C. The extrudates were milled to <500 µm using a coffee grinder type mill.

### 10.2.2 HPLC Analysis

HPLC was conducted to identify the presence and relative amounts of degradation products of telmisartan formed during extrusion feasibility studies.

Analysis was performed using an Agilent 1100 series (Agilent Technologies, Waldbronn, Germany). The chromatographic separation was performed on an Agilent Poroshell 120 SB-C18 analytical column (100 mm long, 3 mm diameter, 2.7 µm particle size, 120 Å pore size) with column temperature of 40 °C. The mobile phase was 10 mM ammonium acetate in water (mobile phase A) and acetonitrile (mobile phase B) with linear gradient elution: 0 min, B 15%; 5 min, B 20%; 25 min, B 100%; 30 min, B 100%; 30.1 min, B 15%; 35 min, B 15%. The flow rate was 1.0 mL/min, the injection volume was 10 µL, and the detection was performed at 292 nm, slit 4 nm. Agilent OpenLAB CDS ChemStation Edition software was used for data collection and analysis. All reagents were of HPLC grade. Results are presented as peak area percent.

Diluent for both neat telmisartan standard and milled extrudate samples was composed of 1+1 (v/v) methanol + water. Both the standard and sample solutions were prepared at 200 µg/mL concentration.

### 10.2.3 Results

Impurity content in API standard and extruded samples is shown in Table 10.1. Minor levels of impurities were observed in the sample extruded at 220 °C while no impurities were observed in the standard or sample extruded at 180 °C.

Table 10.1 *Telmisartan and impurity content in peak area %. Dashes indicate no peak present.*

| | **Peak Area [%]** | | |
|---|---|---|---|
| **Retention Time [min]** | **Standard** | **Extrudate at 180 °C** | **Extrudate at 220 °C** |
| 1.724 | - | - | 0.027 |
| 10.187 | - | - | 0.031 |
| 10.57 | - | - | 0.032 |
| 10.814 | - | - | 0.039 |
| 11.364 | 100 | 100 | 99.872 |

# 11 References

1. Breitenbach J. Melt extrusion: from process to drug delivery technology. Eur J Pharm Biopharm. 2002 Sep;54(2):107–17.

2. Crowley MM, Zhang F, Repka MA, Thumma S, Upadhye SB, Kumar Battu S, et al. Pharmaceutical Applications of Hot-Melt Extrusion: Part I. Drug Dev Ind Pharm. 2007 Jan 1;33(9):909–26.

3. Stanković M, Frijlink HW, Hinrichs WLJ. Polymeric formulations for drug release prepared by hot melt extrusion: application and characterization. Drug Discov Today. 2015 Jul;20(7):812–23.

4. Theil F, Anantharaman S, Kyerematen SO, van Lishaut H, Dreis-Kühne SH, Rosenberg J, et al. Frozen in Time: Kinetically Stabilized Amorphous Solid Dispersions of Nifedipine Stable after a Quarter Century of Storage. Mol Pharm. 2017 Jan 3;14(1):183–92.

5. Patil H, Tiwari RV, Repka MA. Hot-Melt Extrusion: from Theory to Application in Pharmaceutical Formulation. AAPS PharmSciTech. 2016;17(1):20–42.

6. Jermain SV, Brough C, Williams RO. Amorphous solid dispersions and nanocrystal technologies for poorly water-soluble drug delivery – An update. Int J Pharm. 2018 Jan 15;535(1):379–92.

7. Repka MA, Bandari S, Kallakunta VR, Vo AQ, McFall H, Pimparade MB, et al. Melt extrusion with poorly soluble drugs – An integrated review. Int J Pharm. 2018 Jan 15;535(1):68–85.

8. Newman A, editor. Pharmaceutical Amorphous Solid Dispersions. New Jersey: John Wiley & Sons, Inc.; 2015.

9. Gryczke A. Hot-Melt Extrusion Process Design Using Process Analytical Technology. In: Melt Extrusion. 1st ed. New York: Springer-Verlag; 2013. (AAPS Advances in the Pharmaceutical Sciences; vol. 9).

10. Treffer D, Wahl P, Markl D, Koscher G, Roblegg E, Khinast J. Hot Melt Extrusion as a Continuous Pharmaceutical Manufacturing Process. In: Repka MA, Langley N, DiNunzio J, editors. Melt Extrusion. 1st ed. New York: Springer-Verlag; 2013. (AAPS Advances in the Pharmaceutical Sciences; vol. 9).

11. Lang B, McGinity JW, Williams RO. Hot-melt extrusion – basic principles and pharmaceutical applications. Drug Dev Ind Pharm. 2014 Sep 1;40(9):1133–55.

12. Repka MA, Langley N, DiNunzio J. Melt Extrusion. 1st ed. New York: Springer-Verlag; 2013. 474 p. (AAPS Advances in the Pharmaceutical Sciences; vol. 9).

13. Brown EC, Kelly AL, Coates PD. Melt temperature field measurement in single screw extrusion using thermocouple meshes. Rev Sci Instrum. 2004 Nov 1;75(11):4742–8.

14. Emin MA, Teumer T, Schmitt W, Rädle M, Schuchmann HP. Measurement of the true melt temperature in a twin-screw extrusion processing of starch based matrices via infrared sensor. J Food Eng. 2016 Feb;170:119–24.

15. Kohlgrüber K. Co-Rotating Twin-Screw Extruders - Fundamentals, Technology and Applications. Munich: Carl Hanser Verlag; 2008.

16. Deng J, Li K, Harkin-Jones E, Price M, Karnachi N, Kelly A, et al. Energy monitoring and quality control of a single screw extruder. Appl Energy. 2014;113:1775–85.

17. Heil C, Hirsch J. Improved process understanding and control of a hot-melt extrusion process with near-infrared spectroscopy. In: Hot-Melt Extrusion: Pharmaceutical Applications. John Wiley & Sons, Ltd; 2012. p. 333–52.

18. Hitzer P, Bäuerle T, Drieschner T, Ostertag E, Paulsen K, van Lishaut H, et al. Process analytical techniques for hot-melt extrusion and their application to amorphous solid dispersions. Anal Bioanal Chem. 2017 Jul 1;409(18):4321–33.

19. Siepmann F, Le Brun V, Siepmann J. Drugs acting as plasticizers in polymeric systems: A quantitative treatment. J Controlled Release. 2006 Oct 27;115(3):298–306.

20. Ghebremeskel AN, Vemavarapu C, Lodaya M. Use of surfactants as plasticizers in preparing solid dispersions of poorly soluble API: Selection of polymer–surfactant combinations using solubility parameters and testing the processability. Int J Pharm. 2007 Jan 10;328(2):119–29.

21. Gogos CG, Liu H, Wang P. Laminar Dispersive and Distributive Mixing with Dissolution and Applications to Hot-Melt Extrusion. In: Hot-Melt Extrusion: Pharmaceutical Applications [Internet]. John Wiley & Sons, Ltd; 2012. p. 261–84. Available from: http://dx.doi.org/10.1002/9780470711415.ch12

22. Zecevic DE, Evans RC, Paulsen K, Wagner KG. From benchtop to pilot scale–experimental study and computational assessment of a hot-melt extrusion scale-up of a solid dispersion of dipyridamole and copovidone. Int J Pharm. 2018 Feb 15;537(1):132–9.

23. Dreiblatt A. Technological Considerations Related to Scale-Up of Hot-Melt Extrusion Processes. In: Hot-Melt Extrusion: Pharmaceutical Applications [Internet]. John Wiley & Sons, Ltd; 2012. p. 285–300. Available from: https://doi.org/10.1002/9780470711415.ch13

24. Lowinger M. Process Development: Scaling a Melt Extrusion Process from Conception to Commercialization. Am Parmaceutical Rev. 2011 Mar 1;

25. Hughey JR, DiNunzio JC, Bennett RC, Brough C, Miller DA, Ma H, et al. Dissolution Enhancement of a Drug Exhibiting Thermal and Acidic Decomposition Characteristics by Fusion Processing: A Comparative Study of Hot Melt Extrusion and KinetiSol® Dispersing. AAPS PharmSciTech. 2010;11(2):760–74.

26. Boersen N, Brown C, DiNunzio J, Johnson D, Marsac P, Meyer R, et al. Hot-Melt Extrusion: The Process-Product-Performance Interplay. In: Templeton AC, Byrn SR, Haskell RJ, Prisinzano TE, editors. Discovering and Developing Molecules with Optimal Drug-Like Properties [Internet]. New York, NY: Springer New York; 2015. p. 345–81. Available from: https://doi.org/10.1007/978-1-4939-1399-2_11

27. Vergnes B, Valle GD, Delamare L. A global computer software for polymer flows in corotating twin screw extruders. Polym Eng Sci. 1998 Nov 1;38(11):1781–92.

28. Eitzlmayr A, Khinast J. Co-rotating twin-screw extruders: Detailed analysis of conveying elements based on smoothed particle hydrodynamics. Part 1: Hydrodynamics. Chem Eng Sci. 2015 Sep 29;134:861–79.

29. Eitzlmayr A, Khinast J. Co-rotating twin-screw extruders: Detailed analysis of conveying elements based on smoothed particle hydrodynamics. Part 2: Mixing. Chem Eng Sci. 2015 Sep 29;134:880–6.

30. Sun Changquan Calvin. Materials science tetrahedron—A useful tool for pharmaceutical research and development. J Pharm Sci. 2008 Sep 9;98(5):1671–87.

31. Vigh T, Drávavölgyi G, Sóti PL, Pataki H, Igricz T, Wagner I, et al. Predicting final product properties of melt extruded solid dispersions from process parameters using Raman spectrometry. J Pharm Biomed Anal. 2014 Sep;98:166–77.

32. Rauwendaal C. Polymer Extrusion [Internet]. Hanser; 2001. (SPE books). Available from: https://books.google.de/books?id=pT3MIAAACAAJ

33. Li M, Gogos CG, Ioannidis N. Improving the API dissolution rate during pharmaceutical hot-melt extrusion I: Effect of the API particle size, and the co-rotating, twin-screw extruder screw configuration on the API dissolution rate. Int J Pharm. 2015 Jan 15;478(1):103–12.

34. Chokshi RJ, Sandhu HK, Iyer RM, Shah NH, Malick AW, Zia H. Characterization of physico-mechanical properties of indomethacin and polymers to assess their suitability for hot-melt extrusion processs as a means to manufacture solid dispersion/solution. J Pharm Sci. 2005 Nov 1;94(11):2463–74.

35. Dudhedia Mayur S., Agrawal Anjali M. Rheological study of copovidone and solid dispersion blend used for hot melt extrusion. J Appl Polym Sci [Internet]. 2015 Dec 24 [cited 2018 Apr 30];133(14). Available from: https://doi.org/10.1002/app.43278

36. Yang F, Su Y, Zhang J, DiNunzio J, Leone A, Huang C, et al. Rheology Guided Rational Selection of Processing Temperature To Prepare Copovidone–Nifedipine Amorphous Solid Dispersions via Hot Melt Extrusion (HME). Mol Pharm. 2016 Oct 3;13(10):3494–505.

37. Aho J, Boetker JP, Baldursdottir S, Rantanen J. Rheology as a tool for evaluation of melt processability of innovative dosage forms. Potential 2D 3D Print Pharm Dev. 2015 Oct 30;494(2):623–42.

38. Zecevic DE, Wagner KG. Rational development of solid dispersions via hot-melt extrusion using screening, material characterization, and numeric simulation tools. J Pharm Sci. 2013 Jul 1;102(7):2297–310.

39. Chan S-Y, Qi S, Craig DQM. An investigation into the influence of drug–polymer interactions on the miscibility, processability and structure of polyvinylpyrrolidone-based hot melt extrusion formulations. Spec Issue Contin Manuf Process Anal Tools". 2015 Dec 30;496(1):95–106.

40. Solanki N, Gupta SS, Serajuddin ATM. Rheological analysis of itraconazole-polymer mixtures to determine optimal melt extrusion temperature for development of amorphous solid dispersion. Eur J Pharm Sci. 2018 Jan 1;111:482–91.

41. Sarode AL, Sandhu H, Shah N, Malick W, Zia H. Hot melt extrusion (HME) for amorphous solid dispersions: Predictive tools for processing and impact of drug–polymer interactions on supersaturation. Eur J Pharm Sci. 2013 Feb 14;48(3):371–84.

42. Dukeck R, Sieger P, Karmwar P. Investigation and correlation of physical stability, dissolution behaviour and interaction parameter of amorphous solid dispersions of telmisartan: A drug development perspective. Eur J Pharm Sci. 2013 Jul 16;49(4):723–31.

43. Williams III RO. Technologies to enhance the delivery of poorly water soluble drugs. 11th PBP World Meeting; 2018 Mar 20; Granada, Spain.

44. Williams III RO. Formulating Poorly Water Soluble Drugs - Importance of Process Selection. AAPS PharmSci360; 2018 Nov 7; Washington D.C.

45. DiNunzio JC, Miller DA. Formulation Development of Amorphous Solid Dispersions Prepared by Melt Extrusion. In: Melt Extrusion. 1st ed. New York: Springer-Verlag; 2013. (AAPS Advances in the Pharmaceutical Sciences; vol. 9).

46. Verreck G. The Influence of Plasticizers in Hot-melt Extrusion. In: Hot-Melt Extrusion: Pharmaceutical Applications [Internet]. John Wiley & Sons, Ltd; 2012. p. 93–112. Available from: https://onlinelibrary.wiley.com/doi/abs/10.1002/9780470711415.ch5

47. LaFountaine JS, McGinity JW, Williams RO. Challenges and Strategies in Thermal Processing of Amorphous Solid Dispersions: A Review. AAPS PharmSciTech. 2016;17(1):43–55.

48. Moseson DE, Taylor LS. The application of temperature-composition phase diagrams for hot melt extrusion processing of amorphous solid dispersions to prevent residual crystallinity. Int J Pharm. 2018 Dec 20;553(1):454–66.

49. Cross MM. Rheology of non-Newtonian fluids: A new flow equation for pseudoplastic systems. J Colloid Sci. 1965 Jun 1;20(5):417–37.

50. Carreau PJ. Rheological Equations from Molecular Network Theories [Ph.D. thesis]. [Madison, Wisconsin]: University of Wisconsin, Madison; 1968.

51. Yasuda K. Investigation of the analogies between viscometric and linear viscoelastic properties of polystyrene fluids [Ph.D. thesis]. [Cambridge]: MIT; 1979.

52. Williams ML, Landel RF, Ferry JD. The temperature dependence of relaxation mechanisms in amorphous polymers and other glass-forming liquids. J Am Chem Soc. 1955;77:3701–7.

53. Fried JR. Polymer Science and Technology. 2nd ed. New Jersey: Prentice Hall; 2003.

54. Brown C, DiNunzio J, Eglesia M, Forster S, Lamm M, Lowinger M, et al. HME for Solid Dispersions: Scale-Up and Late-Stage Development. In: Shah N, Sandhu H, Choi DS, Chokshi H, Malick AW, editors. Amorphous Solid Dispersions: Theory and Practice [Internet]. New York, NY: Springer New York; 2014. p. 231–60. Available from: https://doi.org/10.1007/978-1-4939-1598-9_7

55. Brown C, DiNunzio J, Eglesia M, Forster S, Lamm M, Lowinger M, et al. Hot-Melt Extrusion for Solid Dispersions: Composition and Design Considerations. In: Shah N, Sandhu H, Choi DS, Chokshi H, Malick AW, editors. Amorphous Solid Dispersions: Theory and Practice [Internet]. New York, NY: Springer New York; 2014. p. 197–230. Available from: https://doi.org/10.1007/978-1-4939-1598-9_6

56. Gay FP. Polymer emissivity. J Polym Sci Polym Phys Ed. 1973 Nov;11(11):2227–35.

57. Levenspiel O. Chemical Reaction Engineering. 3rd ed. New York: John Wiley & Sons, Inc.; 1999.

58. Hughey JR. A Practical Guide to Hot-Melt Extrusion Scale-Up for Pharmaceutical Applications. Pharmaceutical Technology. 2014 Apr 15;2014(1):24–9.

59. Maniruzzaman M, Nokhodchi A. Continuous manufacturing via hot-melt extrusion and scale up: regulatory matters. Drug Discov Today. 2017 Feb 1;22(2):340–51.

60. Dryer B, Fukuda G, Webb J, Montemayor K, Bigio DI, Andersen P, et al. Comparison of scale-up methods for dispersive mixing in twin-screw extruders. Polym Eng Sci. 2017 Mar 1;57(3):345–54.

61. Rauwendaal C. Understanding Extrusion. In: Understanding Extrusion [Internet]. Carl Hanser Verlag GmbH & Co. KG; 2018 [cited 2018 Nov 27]. p. I–XII. Available from: https://doi.org/10.3139/9781569906996.fm

62. Kolter K, Karl M, Gryczke A. Hot-Melt Extrusion with BASF Pharma Polymers. 2nd ed. Ludwigshafen, Germany: BASF SE; 2012.

63. Swanborough A. A Practical Approach to Scale-up from Bench-top Twin-screw Extruders. 2006; ThermoFisher Scientific.

64. Thiry J, Krier F, Evrard B. A review of pharmaceutical extrusion: Critical process parameters and scaling-up. Int J Pharm. 2015 Feb 1;479(1):227–40.

65. Lehmkemper K, Kyerematen SO, Heinzerling O, Degenhardt M, Sadowski G. Long-Term Physical Stability of PVP- and PVPVA-Amorphous Solid Dispersions. Mol Pharm. 2017 Jan 3;14(1):157–71.

66. Kremer DM, Hancock BC. Process simulation in the pharmaceutical industry: A review of some basic physical models. J Pharm Sci. 2006 Mar 1;95(3):517–29.

67. Markarian J. Compounders look to simulation software for savings in time and costs. Plast Addit Compd. 2005 Mar 1;7(2):34–7.

68. Potente H., Bastian M., Flecke J. Design of a compounding extruder by means of the SIGMA simulation software. Adv Polym Technol. 1999 Apr 20;18(2):147–70.

69. White JL, Keum J, Jung H, Ban K, Bumm S. Corotating Twin-Screw Extrusion Reactive Extrusion-Devolatilization Model and Software. Polym-Plast Technol Eng. 2006 May 1;45(4):539–48.

70. Banu I, Puaux J-P, Bozga G, Nagy I. Modeling of L-lactide Polymerization by Reactive Extrusion. Macromol Symp. 2010 Mar 26;289(1):108–18.

71. Farahanchi A, Sobkowicz MJ. Kinetic and process modeling of thermal and mechanical degradation in ultrahigh speed twin screw extrusion. Polym Degrad Stab. 2017 Apr 1;138:40–6.

72. Dubey PS, Abhyankar AH, Marchante V, Brighton LJ, Blackburn K, Temple C, et al. Modelling and Validation of Synthesis of Poly Lactic Acid Using an Alternative Energy Source through a Continuous Reactive Extrusion Process. Polymers. 2016;8(4).

73. Carneiro OS, Covas JA, Vergnes B. Experimental and theoretical study of twin-screw extrusion of polypropylene. J Appl Polym Sci. 2000;78(7):1419–30.

74. Berzin F, Tara A, Tighzert L, Vergnes B. Importance of coupling between specific energy and viscosity in the modeling of twin screw extrusion of starchy products. Polym Eng Sci. 2010 Aug 16;50(9):1758–66.

75. Berzin F, Tara A, Tighzert L, Vergnes B. Computation of starch cationization performances by twin-screw extrusion. Polym Eng Sci. 2007 Jan 17;47(2):112–9.

76. Balakrishnan N. Validation of residence stress distribution methodology using 1-D computer simulations [Master of Science]. [College Park]: University of Maryland;

77. Emin MA. Modeling extrusion processes. In: Bakalis S, Knoerzer K, Fryer PJ, editors. Modeling Food Processing Operations [Internet]. Woodhead Publishing; 2015. p. 235–53. Available from: http://www.sciencedirect.com/science/article/pii/B978178242284600009X

78. Redl A, Morel MH, Bonicel J, Vergnes B, Guilbert S. Extrusion of Wheat Gluten Plasticized with Glycerol: Influence of Process Conditions on Flow Behavior, Rheological Properties, and Molecular Size Distribution. Cereal Chem. 1999 May 15;76(3):361–70.

79. Domenech T, Peuvrel-Disdier E, Vergnes B. The importance of specific mechanical energy during twin screw extrusion of organoclay based polypropylene nanocomposites. Compos Sci Technol. 2013 Feb 11;75:7–14.

80. Bochmann ES, Steffens KE, Gryczke A, Wagner KG. Numerical simulation of hot-melt extrusion processes for amorphous solid dispersions using model-based melt viscosity. Eur J Pharm Biopharm. 2018 Mar 1;124:34–42.

81. Bochmann ES, Gryczke A, Wagner KG. Validation of Model-Based Melt Viscosity in Hot-Melt Extrusion Numerical Simulation. Pharmaceutics. 2018;10(3).

82. Eitzlmayr A, Koscher G, Reynolds G, Huang Z, Booth J, Shering P, et al. Mechanistic modeling of modular co-rotating twin-screw extruders. Int J Pharm. 2014 Oct 20;474(1–2):157–76.

83. Eitzlmayr A, Khinast J, Hörl G, Koscher G, Reynolds G, Huang Z, et al. Experimental characterization and modeling of twin-screw extruder elements for pharmaceutical hot melt extrusion. AIChE J. 2013 Jun 27;59(11):4440–50.

84. Eitzlmayr A, Matić J, Khinast J. Analysis of flow and mixing in screw elements of corotating twin-screw extruders via SPH. AIChE J. 2016 Dec 10;63(6):2451–63.

85. Reitz E, Podhaisky H, Ely D, Thommes M. Residence time modeling of hot melt extrusion processes. Eur J Pharm Biopharm. 2013 Nov 1;85(3, Part B):1200–5.

86. Schittny A, Ogawa H, Huwyler J, Puchkov M. A combined mathematical model linking the formation of amorphous solid dispersions with hot-melt-extrusion process parameters. Eur J Pharm Biopharm. 2018 Nov 1;132:127–45.

87. Chokshi R, Zia H. Hot-Melt Extrusion Technique: A Review. Iran J Pharm Res. 2010;Volume 3(Number 1):3–16.

88. Tadmor Z, Gogos CG. Principles of Polymer Processing. 2nd ed. New Jersey: Wiley; 2006.

89. Verreck G, Decorte A, Heymans K, Adriaensen J, Liu D, Tomasko D, et al. Hot stage extrusion of p-amino salicylic acid with EC using CO2 as a temporary plasticizer. Int J Pharm. 2006 Dec 11;327(1–2):45–50.

90. Guo Z, Lu M, Li Y, Pang H, Lin L, Liu X, et al. The utilization of drug–polymer interactions for improving the chemical stability of hot-melt extruded solid dispersions. J Pharm Pharmacol. 2014 Feb 1;66(2):285–96.

91. Lakshman JP, Cao Y, Kowalski J, Serajuddin ATM. Application of Melt Extrusion in the Development of a Physically and Chemically Stable High-Energy Amorphous Solid Dispersion of a Poorly Water-Soluble Drug. Mol Pharm. 2008 Dec 1;5(6):994–1002.

92. Liu X, Lu M, Guo Z, Huang L, Feng X, Wu C. Improving the Chemical Stability of Amorphous Solid Dispersion with Cocrystal Technique by Hot Melt Extrusion. Pharm Res. 2012;29(3):806–17.

93. Ghosh I, Vippagunta R, Li S, Vippagunta S. Key considerations for optimization of formulation and melt-extrusion process parameters for developing thermosensitive compound. Pharm Dev Technol. 2012 Aug 1;17(4):502–10.

94. Munjal M, Stodghill SP, ElSohly MA, Repka MA. Polymeric systems for amorphous Δ9-tetrahydrocannabinol produced by a hot-melt method. Part I: Chemical and thermal stability during processing. J Pharm Sci. 2006 Aug 1;95(8):1841–53.

95. Haser A, Huang S, Listro T, White D, Zhang F. An approach for chemical stability during melt extrusion of a drug substance with a high melting point. Int J Pharm. 2017 May 30;524(1–2):55–64.

96. DiNunzio JC, Brough C, Hughey JR, Miller DA, Williams III RO, McGinity JW. Fusion production of solid dispersions containing a heat-sensitive active ingredient by hot melt extrusion and Kinetisol® dispersing. Eur J Pharm Biopharm. 2010 Feb;74(2):340–51.

97. Surasarang SH, Keen JM, Huang S, Zhang F, McGinity JW, Williams RO. Hot melt extrusion versus spray drying: hot melt extrusion degrades albendazole. Drug Dev Ind Pharm. 2016 Sep 12;1–15.

98. Kulthe VV, Chaudhari PD. Effectiveness of Spray Congealing to Obtain Physically Stabilized Amorphous Dispersions of a Poorly Soluble Thermosensitive API. AAPS PharmSciTech. 2014;15(6):1370–7.

99. Liu H, Zhu L, Wang P, Zhang X, Gogos CG. Effects of screw configuration on indomethacin dissolution behavior in Eudragit E PO. Adv Polym Technol. 2012 Dec 1;31(4):331–42.

100. Flanagan F, Hein E, Choi R, Yang F, McQuade M, Neu C, et al. Measurement of hot melt extrusion thermal residence distributions. In Indianapolis, Indiana, USA: Society of Plastics Engineers; 2016. p. 806–11. Available from: www.4spe.org

101. Jovic Z, Zivanovic L, Protic A, Radisic M, Lausevic M, Malesevic M, et al. Forced Degradation Study of Torasemide: Characterization of its Degradation Products. J Liq Chromatogr Relat Technol. 2013 May 1;36(15):2082–94.

102. Kyerematen SO, Pudlas M, Woehrle GH. A Fast and Reliable Empirical Approach for Estimating Solubility of Crystalline Drugs in Polymers for Hot Melt Extrusion Formulations. J Pharm Sci. 2014 Sep 1;103(9):2847–58.

103. Pharmaceutical Development Annex to Q8(R2) [Internet]. ICH; 2009. Available from: http://www.ich.org/fileadmin/Public_Web_Site/ICH_Products/Guidelines/Quality/Q8_R1/Step4/Q8_R2_Guideline.pdf

104. Unlu E, Faller JF. RTD in twin-screw food extrusion. J Food Eng. 2002 Jun;53(2):115–31.

105. Filić D, Dumić M, Klepić B, Danilovski A, Tudja M. Amorphous torasemide modification. US 6,767,917, 2004.

106. Alshahrani SM, Morott JT, Alshetaili AS, Tiwari RV, Majumdar S, Repka MA. Influence of degassing on hot-melt extrusion process. Eur J Pharm Sci. 2015 Dec 1;80:43–52.

107. Wagner, Jr JR, Mount III EM, Giles, Jr. HF. Extrusion: The Definitive Processing Guide and Handbook. 2nd. ed. Waltham, MA: William Andrew; 2014. (Plastics Design Series).

108. Yalçinyuva T, Kamal MR, Lai-Fook RA, Özgümüs S. Hydrolytic Depolymerization of Polyethylene Terephthalate by Reactive Extrusion. Int Polym Process. 2000 May 1;15(2):137–46.

109. Lim L-T, Auras R, Rubino M. Processing technologies for poly(lactic acid). Prog Polym Sci. 2008 Aug;33(8):820–52.

110. Bochmann ES, Üstüner EE, Gryczke A, Wagner KG. Predicting melt rheology for hot-melt extrusion by means of a simple Tg-measurement. Eur J Pharm Biopharm. 2017 Oct;119:47–55.

111. Vlachopoulos J, Polychronopoulos N. Basic concepts in polymer melt rheology and their importance in processing. In: Applied Polymer Rheology: Polymeric Fluids with Industrial Applications. 1st ed. John Wiley & Sons, Ltd; 2012. p. 1–26.

112. Kachrimanis K, Nikolakakis I. Polymers as Formulation Excipients for Hot-Melt Extrusion Processing of Pharmaceuticals. In: Handbook of Polymers for Pharmaceutical Technologies. Scrivener Publishing LLC; 2015. p. 121–50.

113. Maru SM, de Matas M, Kelly A, Paradkar A. Characterization of thermal and rheological properties of zidovidine, lamivudine and plasticizer blends with ethyl cellulose to assess their suitability for hot melt extrusion. Eur J Pharm Sci. 2011 Nov 20;44(4):471–8.

114. Gupta SS, Parikh T, Meena AK, Mahajan N, Vitez I, Serajuddin ATM. Effect of carbamazepine on viscoelastic properties and hot melt extrudability of Soluplus®. Int J Pharm. 2015 Jan 15;478(1):232–9.

115. Yang F, Su Y, Zhu L, Brown CD, Rosen LA, Rosenberg KJ. Rheological and solid-state NMR assessments of copovidone/clotrimazole model solid dispersions. Int J Pharm. 2016 Mar 16;500(1):20–31.

116. Repka MA, Gerding TG, Repka SL, McGinity JW. Influence of Plasticizers and Drugs on the Physical-Mechanical Properties of Hydroxypropylcellulose Films Prepared by Hot Melt Extrusion. Drug Dev Ind Pharm. 1999 Jan 1;25(5):625–33.

117. Desai D, Sandhu H, Shah N, Malick W, Zia H, Phuapradit W, et al. Selection of Solid-State Plasticizers as Processing Aids for Hot-Melt Extrusion. J Pharm Sci. 2018 Jan 1;107(1):372–9.

118. Aho J, Van Renterghem J, Arnfast L, De Beer T, Rantanen J. The flow properties and presence of crystals in drug-polymer mixtures: Rheological investigation combined with light microscopy. Int J Pharm. 2017 Aug 7;528(1):383–94.

119. Evans RC, Kyerematen SO, Degenhardt M, Wagner KG. Influence of Surfactant+Polymer Rheological Properties on Hot-Melt Extrusion Design Space - Investigation via Process Simulation. In Granada, Spain: APV International Association for Pharmaceutical Technology; 2018.

120. Verreck G, Decorte A, Li H, Tomasko D, Arien A, Peeters J, et al. The effect of pressurized carbon dioxide as a plasticizer and foaming agent on the hot melt extrusion process and extrudate properties of pharmaceutical polymers. J Supercrit Fluids. 2006 Oct 1;38(3):383–91.

121. Ghebremeskel AN, Vemavarapu C, Lodaya M. Use of Surfactants as Plasticizers in Preparing Solid Dispersions of Poorly Soluble API: Stability Testing of Selected Solid Dispersions. Pharm Res. 2006 Aug 1;23(8):1928–36.

122. De Brabander C, van den Mooter G, Vervaet C, Remon JP. Characterization of Ibuprofen as a Nontraditional Plasticizer of Ethyl Cellulose. J Pharm Sci. 2002 Jul 1;91(7):1678–85.

123. Repka MA, McGinity JW. Influence of Vitamin E TPGS on the properties of hydrophilic films produced by hot-melt extrusion. Int J Pharm. 2000 Jul 20;202(1):63–70.

124. Wu C, McGinity JW. Non-traditional plasticization of polymeric films. Int J Pharm. 1999 Jan 15;177(1):15–27.

125. Yang M, Wang P, Suwardie H, Gogos C. Determination of acetaminophen’s solubility in poly(ethylene oxide) by rheological, thermal and microscopic methods. Int J Pharm. 2011 Jan 17;403(1–2):83–9.

126. Wu C, McGinity JW. Influence of ibuprofen as a solid-state plasticizer in eudragit® RS 30 D on the physicochemical properties of coated beads. AAPS PharmSciTech. 2001 Dec 1;2(4):35–43.

127. Zhu Y, Shah NH, Malick AW, Infeld MH, McGinity JW. Solid-state plasticization of an acrylic polymer with chlorpheniramine maleate and triethyl citrate. Int J Pharm. 2002 Jul 25;241(2):301–10.

128. Evans RC, Kyerematen SO, Asmus L, Degenhardt M, Rosenberg J, Wagner KG. Development and Performance of a Highly Sensitive Model Formulation Based on Torasemide to Enhance Hot-Melt Extrusion Process Understanding and Process Development. AAPS PharmSciTech [Internet]. 2018 Feb 27; Available from: https://doi.org/10.1208/s12249-018-0970-y

129. Lepek P, Sawicki W, Wlodarski K, Wojnarowska Z, Paluch M, Guzik L. Effect of amorphization method on telmisartan solubility and the tableting process. Eur J Pharm Biopharm. 2013 Jan 1;83(1):114–21.

130. Jamadar S, Pore Y, Sayyad F. Formation of Amorphous Telmisartan Polymeric Microparticles for Improvement of Physicochemical Characteristics. Part Sci Technol. 2014 Sep 3;32(5):512–9.

131. Noyes AA, Whitney WR. THE RATE OF SOLUTION OF SOLID SUBSTANCES IN THEIR OWN SOLUTIONS. J Am Chem Soc. 1897 Dec 1;19(12):930–4.

132. Wurster DE, Taylor PW. Dissolution rates. J Pharm Sci. 1965 Feb;54(2):169–75.

133. Liu H, Wang P, Zhang X, Shen F, Gogos CG. Effects of extrusion process parameters on the dissolution behavior of indomethacin in Eudragit® E PO solid dispersions. Int J Pharm. 2010 Jan 4;383(1):161–9.

134. Bird RB, Stewart WE, Lightfoot EN. Transport Phenomena. New York: John Wiley & Sons, Inc.; 1960.

135. Bochmann ES, Neumann D, Gryczke A, Wagner KG. Micro-scale prediction method for API-solubility in polymeric matrices and process model for forming amorphous solid dispersion by hot-melt extrusion. Eur J Pharm Biopharm. 2016 Oct;107:40–8.

136. Poulesquen A, Vergnes B. A study of residence time distribution in co-rotating twin-screw extruders. Part I: Theoretical modeling. Polym Eng Sci. 2004 Apr 7;43(12):1841–8.

137. Puaux J., Bozga G, Ainser A. Residence time distribution in a corotating twin-screw extruder. Chem Eng Sci. 2000 May;55(9):1641–51.

138. Vergnes B, Berzin F. Modeling of reactive systems in twin-screw extrusion: challenges and applications. Modif Dégrad Stabilisation PolymèresPolymer Modif Degrad Stabilisation. 2006 Nov;9(11–12):1409–18.

139. Kothari K, Ragoonanan V, Suryanarayanan R. Influence of Molecular Mobility on the Physical Stability of Amorphous Pharmaceuticals in the Supercooled and Glassy States. Mol Pharm. 2014 Sep 2;11(9):3048–55.

140. Matsumoto T, Zografi G. Physical Properties of Solid Molecular Dispersions of Indomethacin with Poly(vinylpyrrolidone) and Poly(vinylpyrrolidone-co-vinyl-acetate) in Relation to Indomethacin Crystallization. Pharm Res. 1999 Nov 1;16(11):1722–8.

141. Lauer EM, Maurer R, De Paepe TA, Stillhart C, Jacob L, James R, et al. A Miniaturized Extruder to Prototype Amorphous Solid Dispersions: Selection of Plasticizers for Hot Melt Extrusion. Pharmaceutics. 2018;10(2).

142. Hancock BC, Shamblin SL, Zografi G. Molecular Mobility of Amorphous Pharmaceutical Solids Below Their Glass Transition Temperatures. Pharm Res. 1995 Jun 1;12(6):799–806.

143. McKelvey JM. Theory of Adiabatic Extruder Operation. Ind Eng Chem. 1954;46(4):660–4.

144. Frankland J. Extrusion: Run Your Chevy Volt with Extruder Energy Savings - Part 1 [Internet]. Plastics Technology - Columns - Extrusion. 2011 [cited 2018 Nov 4]. Available from: https://www.ptonline.com/columns/extrusion-run-your-chevy-volt-with-extruder-energy-savingspart-i

145. Frankland J. Extrusion: Reducing Energy, Part II: “Adiabatic” Extrusion [Internet]. Plastics Technology - Columns - Extrusion. 2011 [cited 2018 Nov 4]. Available from: https://www.ptonline.com/columns/extrusion-reducing-energy-part-ii-adiabatic-extrusion

146. Frame ND. Operational characteristics of the co-rotating twin-screw extruder. In: Frame ND, editor. The Technology of Extrusion Cooking [Internet]. Boston, MA: Springer US; 1994. p. 1–51. Available from: http://dx.doi.org/10.1007/978-1-4615-2135-8_1

147. Vera-Sorroche J, Kelly AL, Brown EC, Gough T, Abeykoon C, Coates PD, et al. The effect of melt viscosity on thermal efficiency for single screw extrusion of HDPE. Chem Eng Res Des. 2014 Nov 1;92(11):2404–12.

148. Abeykoon C, Kelly AL, Vera-Sorroche J, Brown EC, Coates PD, Deng J, et al. Process efficiency in polymer extrusion: Correlation between the energy demand and melt thermal stability. Appl Energy. 2014 Dec 15;135:560–71.

149. Rauwendaal C. Heat transfer in twin screw compounding extruders. AIP Conf Proc. 2016 Oct 31;1779(1):030014.

150. Rauwendaal C. Instrumentation and Control. In: Understanding Extrusion [Internet]. Carl Hanser Verlag GmbH & Co. KG; 2018 [cited 2018 Nov 27]. p. 19–52. Available from: https://doi.org/10.3139/9781569906996.002

151. Rauwendaal C. How an Extruder Works. In: Understanding Extrusion [Internet]. Carl Hanser Verlag GmbH & Co. KG; 2018 [cited 2018 Nov 27]. p. 77–121. Available from: https://doi.org/10.3139/9781569906996.005

152. Carley JF, McKelvey JM. Extruder Scale-Up Theory and Experiments. Ind Eng Chem. 1953 May 1;45(5):989–92.

153. Nakatani M. Scale-Up Theory for Twin-Screw Extruder, Keeping the Resin Temperature Unchanged. Adv Polym Technol. 1998;17(1):19–22.

154. Knieper A, Beinert C. Plastification of polymers in twin-screw-extruders: New visualization technic using high-speed imaging. AIP Conf Proc. 2014 May 15;1593(1):48–51.

155. Taki K, Sugiyama T, Ohara M, Umemoto S, Tanifuji S, Murata J, et al. Online Monitoring of the Degree of Fill in a Rotating Full-Flight Screw of a Corotating Twin-Screw Extruder. AIChE J [Internet]. 2018 Aug 16 [cited 2018 Oct 28];0(0). Available from: https://doi.org/10.1002/aic.16382

156. Huang S, O'Donnell KP, Delpon de Vaux SM, O'Brien J, Stutzman J, Williams RO. Processing thermally labile drugs by hot-melt extrusion: The lesson with gliclazide. Eur J Pharm Biopharm. 2017 Oct 1;119:56–67.

157. Mark JE. Physical Properties of Polymers Handbook. 2nd ed. New York: Springer Science+Business Media, LLC; 2007.

158. Fox TG. Influence of Diluent and of Copolymer Composition on the Glass Temperature of a Polymer System. In: Bulletin of the American Physical Society. New York City: American Physical Society; 1956.

159. Treffer D, Troiss A, Khinast J. A novel tool to standardize rheology testing of molten polymers for pharmaceutical applications. Int J Pharm. 2015 Nov 10;495(1):474–81.

160. Cox WP, Merz EH. Rheology of polymer melts - A correlation of dynamic and steady flow measurements. In: Committee D-20, editor. Int Symp Plast Test Stand [Internet]. 100 Barr Harbor Drive, PO Box C700, West Conshohocken, PA 19428-2959: ASTM International; Available from: http://dx.doi.org/10.1520/STP44206S

161. Doolittle AK. Studies in newtonian flow. II. The dependence of the viscosity of liquids on free-space. J Appl Phys. 1951;22(12):1471–5.

162. White JL, Kim EK, Keum JM, Jung HC, Bang DS. Modeling heat transfer in screw extrusion with special application to modular self-wiping co-rotating twin-screw extrusion. Polym Eng Sci. 2001 Aug 1;41(8):1448–55.

163. Derezinski SJ. Heat Transfer Coefficients in Extruder Melt Sections. In: SPE Conference Papers. Indianapolis, Indiana, USA: Society of Plastics Engineers; 1996. p. 417–21.